PL-TR-91-2130

# AD-A240 859

SOURCE CONTRIBUTIONS AT REGIONAL DISTANCES

Karl Koch
William Soroka
Brian Stump

Southern Methodist University
Department of Geological Sciences
Dallas, TX 75275-0395

14 May 1991

**DTIC**
**ELECTE**
**SEP 24 1991**
**S** **B** **D**

Final Report
9 August 1988-31 May 1991

# 91-11278

This technical report has been reviewed and is approved for
publication.


JAMES F. LEWKOWICZ
Contract Manager
Solid Earth Geophysics Branch
Earth Sciences Division

JAMES F. LEWKOWICZ
Branch Chief
Solid Earth Geophysics Branch
Earth Sciences Division


DONALD H. ECKHARDT, Director
Earth Sciences Division

# REPORT DOCUMENTATION PAGE

| 1a. REPORT SECURITY CLASSIFICATION<br>Unclassified | | 1b. RESTRICTIVE MARKINGS | | | |
|---|---|---|---|---|---|
| 2a. SECURITY CLASSIFICATION AUTHORITY | | 3 DISTRIBUTION/AVAILABILITY OF REPORT<br>Approved for public release;<br>distribution unlimited | | | |
| 2b. DECLASSIFICATION/DOWNGRADING SCHEDULE | | | | | |
| 4. PERFORMING ORGANIZATION REPORT NUMBER(S)<br>SMU G-9 | | 5 MONITORING ORGANIZATION REPORT NUMBER(S)<br>PL-TR-91-2130 | | | |
| 6a. NAME OF PERFORMING ORGANIZATION<br>Southern Methodist University | 6b OFFICE SYMBOL<br>*(If applicable)* | 7a. NAME OF MONITORING ORGANIZATION<br>Phillips Laboratory | | | |
| 6c. ADDRESS (City, State, and ZIP Code)<br>Department of Geological Sciences<br>Dallas, Texas 75275-0395 | | 7b. ADDRESS (City, State, and ZIP Code)<br>Hanscom AFB, MA 01731-5000 | | | |
| 8a. NAME OF FUNDING/SPONSORING<br>ORGANIZATION<br>DARPA/NMR? | 8b. OFFICE SYMBOL<br>*(If applicable)* | 9. PROCUREMENT INSTRUMENT IDENTIFICATION NUMBER<br>F19628-88-K-0038 | | | |
| 8c ADDRESS (City, State, and ZIP Code)<br>1400 Wilson Blvd.<br>Arlington, VA 22209 | | 10 SOURCE OF FUNDING NUMBERS | | | |
| | | PROGRAM<br>ELEMENT NO.<br>62714E | PROJECT<br>NO<br>8A10 | TASK<br>NO.<br>DA | WORK UNIT<br>ACCESSION NO.<br>AQ |

11 TITLE (Include Security Classification)

Source Contributions at Regional Distances

12. PERSONAL AUTHOR(S)
Karl Koch, William Soroka, Brian Stump

| 13a. TYPE OF REPORT<br>Final Report | 13b. TIME COVERED<br>FROM 09AUG88 TO 31MAY91 | 14 DATE OF REPORT (Year, Month, Day)<br>1991 May 14 | 15. PAGE COUNT<br>238 |
|---|---|---|---|

16. SUPPLEMENTARY NOTATION

| 17 | COSATI CODES | | 18 SUBJECT TERMS (Continue on reverse if necessary and identify by block number) |
|---|---|---|---|
| FIELD | GROUP | SUB-GROUP | Regional Seismograms, Basin and Range, broadband, discrimi-<br>nation, yield, synthetic seismograms, explosion, spall, Lg,<br>coda Q, scattering, teleseismic P waves. |
| | | | |
| | | | |

19 ABSTRACT (Continue on reverse if necessary and identify by block number)

In order to quantify the effects of different components of the explosion source function on far regional seismograms (900-2000km) a one-dimensional velocity model is developed for seismic waves traveling across the Basin and Range. This model is constrained by broadband data recorded at the Lajitas seismic station. Complete synthetic seismograms are developed for the model utilizing the extended reflectivity technique. Pg, Pn, mantle P, Lg and surface waves are included in the data as well as in the synthetics. The P velocity model follows closely that of Olsen et al. (1980,1) developed from shorter offset data. The lack of Sn in the observational data requires a thin mantle S lid not included in these earlier models. The complete set of synthetics replicate the transition of crustal P energy to mantle P around 900km, the rapid decay of Pg beyond 1000km, the lack of Sn energy, and the lower frequency content of Lg relative to the body wave arrivals.

| 20. DISTRIBUTION/AVAILABILITY OF ABSTRACT<br>☐ UNCLASSIFIED/UNLIMITED ☐ SAME AS RPT ☐ DTIC USERS | 21. ABSTRACT SECURITY CLASSIFICATION<br>Unclassified | |
|---|---|---|
| 22a. NAME OF RESPONSIBLE INDIVIDUAL<br>James Lewkowicz | 22b TELEPHONE (Include Area Code)<br>(617) 377-3222 | 22c. OFFICE SYMBOL<br>PL/LWH |

**DD FORM 1473,** 84 MAR

83 APR edition may be used until exhausted
All other editions are obsolete.

This wave propagation model is used to quantify the source effects from an explosion and spall source function. The explosion source is much less sensitive to depth of burial differences than the spall source. Spall and explosion source parameters constrained by near source data indicate that the importance of spall to the Lg phase is source time function dependent. If the peak of the spall source falls outside the low frequency window for Lg, then it has negligble contribution to the regional waveforms.

The final section of this report documents a recent study of long time window (up to 700 sec) P coda at teleseismic distances. The P coda is modeled in terms of a multiple scattering process where coda Q, turbidity, and source excitation can in some instances be recovered. High frequency RSTN data with bandwidths as high as 7 Hz are analyzed. The coda Q values are found to be in general agreement with Lg coda Q estimates from the same regions. The analysis indicates the strong affect of multiple scattering near the receivers. The source functions recovered from this analysis provide a new way of comparing different size explosion or earthquake events.

| Accession For | |
|---|---|
| NTIS GRA&I | ☑ |
| DTIC TAB | ☐ |
| Unannounced | ☐ |
| Justification | |

By_____
Distribution/

| Availability Codes | |
|---|---|
| | Avail and/or |
| Dist | Special |
| A-1 | |

# Wave propagation to far-regional distances in the Western United States

Karl Koch, Brian Stump
Southern Methodist University
Department of Geological Sciences
Dallas, TX 75275

## 1. Introduction

Recent work in the field of discrimination, verification, and yield estimation has been directed towards utilization of regional seismograms for a number of reasons. First, these data may be considered as the basis for verification in the context of a reduced threshold test ban treaty. Second, one regional phase, Lg, has proven to be not only a stable measure for yield (Nuttli 1986; Patton 1988), but is itself a useful waveform feature, as it is often associated with the largest amplitudes observed in regional seismograms. This is particularly true for small events, where Lg in many cases (Hansen et.al. 1990) is the only phase that can be identified from seismic observations.

Using regional phases for discrimination and yield estimation has been quite successful in recent studies. Nuttli (1986a,b; 1988; Patton 1988) found that Lg is a very stable yield estimator and that the $m_{b_{Lg}}$ yield estimator can be easily transported to different geological settings. Taylor & Randall (1988) reported the usefulness of spectral measurement from regional phase (spectral ratios) for discrimination purposes. Other authors (Pomeroy et al. 1982; Bennett & Murphy

1986) identify amplitude as well as spectral ratios among different regional phases as useful discriminants. All these empirical results demand a more thorough theoretical evaluation of wave propagation to regional distances in order to provide a physical understanding for these measures as well as separate the source contributions from the propagation path effects. The work by Lilwall (1988) addressed this problem by studying different discriminants with synthetic models of regional seismograms. Barker et.al (1990) used a similar approach to investigate the source contributions for a variety of source types on particular regional phases, especially the relative excitation of these phases. Neither of these authors, however, matched regional seismograms to observed recordings. This study however will try to fill this gap by attempting to attribute as much as possible of observed waveforms characteristics to propagation path effects. Following this study we will address differences in regional phases that are related to different source representation accompanying the nuclear explosion.

The distance range for the regional data of this study is from 800-2000 km across the Basin and Range province (Western United States), which is effectively what can be expected for the station spacing in host countries under a verification scenario. This distance range implies that the region illuminated by waves travelling from the source to the receiver is the crust extending into the upper mantle. A number of velocity models for crustal and upper mantle propagation have been developed for the Western United States. Many of these models have been derived by analysis of long-period body waves (Archambeau et al 1969, Johnson 1967, Wiggins & Helmberger 1973, Burdick & Helmberger 1978, Helmberger & Engen 1974) and from surface waves (Priestley & Brune 1978, Patton & Taylor 1984). None of these modeling studies have tried to incorporate complete waveforms extending from the body waves to the surface waves. The

2

focus of this study will be to integrate all the observed phases in the regional seismograms.

The characteristics of previous models include a simple crust, with upper crustal compressional wave velocities around 6 km/s and a lower crust with a P velocity of about 6.5 km/s. The thickness of the crust is 35±5 km. The upper mantle is often associated with a high-velocity structure below the Moho, underlain by a low velocity region (both in compressional and shear wave velocity). This low velocity region extends for P waves frequently to a depth of about 150, while for shear waves the zone of low S velocities extends to somewhat greater depth. Most P models incorporate a discontinuous decrease of velocity into the low velocity zone followed by a large positive gradient, while the S wave speed in the low velocity zone is characterized by an almost constant velocity throughout the region. As is indicated by our data, the velocity model below about 250 km is not important in terms of wave propagations effects for the distance range considered.

Since Olsen et al. (1980, 1983) dealt with crustal and upper mantle wave propagation to distances between 600 and 900 km, we use these velocity models as the starting point in synthesizing the characteristics of observed waveforms which will be discussed in the following section. The analysis of the far-regional waveforms will focus on the major regional phases, which include body wave arrivals as well as the surface wave contributions. In characterizing these waveforms we will prepare the ground for the section on synthetic seismograms at far regional distances where the goal will be to realistically model the observed wavefield. If it is possible to model the shape of these waveforms even with

3

relatively simple assumptions, effects of source contributions to regional seismograms can be quantified.


## 2. Observed waveforms

The observations used in this study are seismograms from Nevada Test Site (NTS) nuclear explosions and earthquakes in the California/Gulf of California region. The seismograms were recorded at theLajitas (LTX) seismic station in the Big Bend area of southwest Texas. One supplementary observation of an NTS explosion recorded at Albuquerque is included. Station and epicenter locations are shown in Fig.1, which also displays the great circle paths for the waves crossing the Basin and Range province. Additional information on each event is summarized in Table I. LTX is part of the GSETT experiment (Golden & Herrin 1989) and includes a set of 3-component velocity transducers and a set of 3-component broadband accelerometers. The eigenfrequency of the velocity instruments is 1 Hz, the broadband instruments are flat in acceleration response between DC and 20 Hz. The data were originally sampled at 120 Hz (SP) and 10 Hz (BB). For the purpose of data reduction and consistency between short-period and broadband seismograms, the SP records were subsequently decimated to a sampling rate of 10 Hz, as most of the seismograms contained no energy above 5 Hz. The effective bandwidth for data from both instruments extends to 3-4 Hz (Fig.2).

A total of 15 events were selected for the waveform analysis that follows (see Table I). These events had magnitudes between 4.7 and 5.9, smaller events could be identified, but a signal to noise ratio of between 1:2 to 1:3 rendered them

4

unusable for detailed spectral analysis and modeling. Six of the recordings were from nuclear explosions at NTS. Using both earthquake and explosion recordings we hoped to minimize source bias in our modelling. In some respects, however, waveforms from explosions and earthquakes often showed quite similar waveform patterns, as will be discussed below.

Fig.2a and b display the vertical data for all events recorded by SP (2a) and BB (2b) instruments. The event closest to the receiver is at 836 km while the most distant event is at 2224 km. Although sorted in ascending order with distance, the records are not displayed in a reduced time-distance section, because of the uneven distance spacing, with quite a large number of seismograms in the 1300-1500 km distance interval mainly from NTS. The first arrivals of the records (either $P_n$ (< 1000 km) or mantle P waves (> 1000 km) ) are aligned with a time offset of 20 sec. The record length was chosen as 600 seconds in order to include all body and surface wave contributions in the seismograms.

As Koch & Stump (1989) discussed, these waveforms are characterized by an emergent Pn phase, strong Pg and Lg phases for distances less than 1000 km. Beyond 1200 km, both P phases mentioned before can no longer be identified and are replaced by mantle P waves. This arrival along with Lg dominates the seismograms. Lg is further emphasized in this distance range by the broadband recordings, because of its lower frequency content relative to the P waves. Surface waves are particularly strong for the earthquakes, again emphasized in the broadband data (Fig.2b). It should also be pointed out that there is a lack of any mantle S phases. These phases should precede the Lg wave, which appears to be the only identifiable S arrival.

The transition from crustal to mantle propagation for P waves is even more evident in fig.3, where the P wave segmen of a few seismograms is enlarged. Pn is very emergent for distances less than 1000 km, and may be seen as a small arrival just in front of the mantle P wave for distances beyond 1200 km. In order to demonstrate the frequency content of the data, we calculated sonograms from the short-period data for 2 events in Fig.4. This figure shows that the main energy for the regional seismograms is in the 0.2 to 1.5 Hz range, with a characteristic frequency decrease from P to Lg and the surface waves.

As surface waves are often used as discriminants between earthquakes and explosions, we filtered the data of Fig.2 with a low pass filter at 0.1 Hz to enhance and separate the surface wave contributions. The filtered traces are shown in Fig.5 (a,b). Due to the strong roll-off for the SP instruments below the eigenperiod, there is considerable high frequency energy remaining in the seismograms, while the broadband data are characterized by the long-period surface wave components. Earthquake as well as explosion seismograms show considerable surface wave energy. Comparing the surface waves from both sources in the distance range between 1336-1468 km, there are no obvious differences that may give rise to a successful discrimination between events. Either the generation and propagation of surface waves from explosions within the Basin and Range is favorably enhanced compared to other geologic areas, or the bandwidth of the data is not large enough with respect to long periods to differentiate between nuclear and tectonic events. Most explosions showed transverse surface waves, that are in phase with the Rayleigh waves observed on vertical and radial components (Koch & Stump 1989). The Loves waves from earthquakes show higher phase velocities, as predicted by the dispersion curves derived by Priestley & Brune (1978) from their surface wave model.

6

The major difference in the surface wave observations is that the explosions show considerably more higher frequency surface wave contributions trailing the fundamental mode arrivals (see Figs.4,5a). It can be hypothesized that this energy is trapped in shallow layers of the crust due to the near-surface source. This effect may be reinforced by the Western U.S. crustal model which is topped by a sedimentary layer with low seismic velocities. Unfortunately the signal to noise ratio does not allow a more detailed analysis of this pattern.


## 3. Synthetic seismogram modelling

Since our goal is to model the complete far-regional seismograms with as simple a velocity model as possible, we used the reflectivity method (Müller 1985), which allows us to calculate synthetic seismograms including all body and surface waves for plane layered structures. We focused on both amplitude information as well as waveform shape. The velocity models were further examined by travel time calculations to facilitate the identification of particular phases and to constrain the depth range where arrivals were propagating. For the reflectivity calculations throughout this study, we used an explosion source model with a impulsive time function, the frequency range for the seismograms was chosen from 0.05 to 2 Hz, based on the bandwidth of the data (Fig.4).

For the Western U.S a number of velocity models exist describing the structure for the crust and upper mantle. These models were derived primarily from long period body waves as well as surface waves, and, in general, include the depth range between 0-500 km. Some of these models are summarized in Fig.6, where

7

P (6a) and S (6b) models are reproduced. In order to adequately describe body and surface wave contributions, we tried to combine these models, as no one by itself was able to satisfactorily model our observed data. We focused on the models by Burdick and Helmberger (1978), derived from P wave analysis, and Priestley and Brune (1978), which inverted surface waves for velocity structure (P and S model). These two models were previously combined and extended by Olsen et al. (1980) to study wave propagation in the eastern Basin and Range for distances between 700 and 900 km. As we started our modelling effort based on these models, a brief discussion of their characteristics is included.

The Burdick & Helmberger (BH) model (1978) consists of a simple crust containing two layers with P velocities of 6.0 and 6.5 km/s, respectively, underlain by high-velocity region below the Moho. This depth range, with P wave velocities between 7.95 and 8.05 km/s has a small, positive velocity gradient. Below the so-called "mantle lid" is a low velocity layer with a strong negative velocity jump to 7.70 km/s, after which the velocity increases slightly with depth. At 120 - 150 km a stronger velocity increase can be seen. Below this depth, the velocity is again moderately increasing. The Priestley and Brune (PB) model (1978) (P wave part) also has a fairly simple crustal structure, comparable to the BH model, except for a shallow sedimentary layer at the surface. In contrast to the BH model, the P wave velocities in the PB model are constant from the Moho to a depth of 120 km. Below, the velocity increases with a moderate gradient to depth greater than 300 km. The P wave part of the PB model is not considered as an adequate model, as the traveltimes calculated from this model are too large by more than 5 sec. As Olsen et al. (1980) pointed out, the mantle lid in the BH model is not well constrained by their data, as stronger

8

mantle arrivals for distances shorter than 800 km are not adequately modeled. Therefore, they removed the mantle lid by a zone with a small negative gradient.

The S wave part of the PB model basically follows the P velocities in the crust with a Poisson's ratio near 0.25. Below the Moho a constant velocity layer (4.5 km/s) with a thickness of about 30 km follows with the same P to S ratio. At greater depth they introduced a region with significantly lower velocities of 4.05 to 4.10 km/s. At a depth of 200 km a jump in velocity to 4.4 km/s occurs and a fairly constant velocity gradient extends this model to greater depth.

Previous work has focused on the analysis of P waves or surface waves at regional distances. Few paper dealt with constraining the S wave structure as well. Olsen et al. (1980), for example, used the S wave model of Priestley and Brune (1978) in their reflectivity calculations solely to obtain higher accuracy in their P wave calculations, modifying this model in a more intuitive way. This study however tries to constrain the S wave structure as well, in order to gain a more thorough insight into the physical aspects of Lg wave propagation. We also tried to constrain some surface wave properties, although this might be hampered by the simple assumption of a one-dimensional structure for the Basin and Range. Surface waves are quite sensitive to the top sedimentary layers, which are expected to vary greatly within our distance range.

### 3.1 P phase

As Olsen et al. (1980) pointed out, the BI1 model for P waves was derived for NW or SE propagation paths across the Basin & Range. As our propagation paths were also in the SE direction (Fig.1), we calculated synthetic seismograms for

both the BH/PB models, i.e. using the P wave model from Burdick & Helmberger (1978) and the S velocity model from Priestley & Brune (1978), as well as for Olsen et al.'s (1980) A10 model. The synthetic seismograms from these calculations are shown in Figs. 7 and 8. We focus first on the P part of the waveforms. This part of the synthetics for the BH model shows very impulsive Pn phases for all distances from its onset between 200 and 300 km to 900 km, where Pn is the first arrival. Starting between 800 and 900 km, a secondary phase can be identified coming out of the upper mantle. This prominent secondary phase is not observed in the Lajitas data nor is the Pn an impulsive arrival (Fig.3).

The Olsen A10 model in contrast gives an emergent Pn throughout the modeled distance range, with Pg as the dominant phase out to a distance of 900 km. Beyond 1000 km, the mantle P phase becomes the strongest arrival. This indicates that the A10 model is better in terms of the P wave portion of our far-regional seismograms at Lajitas for events that propagate across the Basin and Range.

The Qp values used in the reflectivity calculations were selected for the BH model as 200 for the upper crust and 500-550 for the lower crust and upper mantle. For the A10 model Q was taken according to the figures given by these authors. Therefore we selected 200 in the upper crust and 1000 in the lower crust/upper mantle, except for the depth range 117-156 km, where Olsen et al. (1980) introduced a Qp value of 100. These Q values and the synthetic seismograms, which were normalized to the maximum amplitude of each trace, indicate that the observed waveform characteristics are primarily dominated by the velocity structure with minor effects from the Q model.

In order to better fit the observations we refined the velocity structure according

10

to a model that is compatible with the A10 model right below the Moho and includes smoother gradients to greater depths (Fig.6a). The synthetic seismograms resulting from this revised model are presented in Fig. 9, now only for the distance range from 600-1400 km, which is more appropriate for our observation range. The new model shows again an emergent Pn phase and the transition from crustal to upper mantle propagation between 900 and 1000 km. This model also gives a good overall fit to the diminishing of Pg for distances larger than 1000 km. Q values for the crust were here 400 while in the upper mantle we used a Qp between 300 and 350.

### 3.2 Constraints from S waves and surface waves

In our effort to represent the entire wavefield, the models of PB (S wave part) and Olsen et a.(1980) do a very poor job. In Fig. 7, which used the former S velocity model, there is considerable energy arriving with a phase velocity of 4.5 km/s, the velocity of the high-velocity layer underneath the Moho. This mantle phase is not seen at all in the observed data. Also the Lg phase, with a velocity of about 3.5 km/s is only a small arrival, although it is the dominant waveform in the observations. The A10 model with respect to S velocity is only slightly different from the PB model, and therefore gives essentially the same waveform pattern. The Qs values used were 250 throughout the crust, and 450 in the upper mantle assuming values of about half of Qp. For the low Qp of the asthenospheric layer, the Qs value was decreased to 75. The very weak Lg arrival is therefore not primarily due to the Qs values selected, but due to the leakage of the energy into the upper mantle. The crustal Q values are consistent with Q values of about 200-300 determined by Patton &Taylor (1984) from surface wave analysis at about 1 Hz, as our calculations were done for frequencies up to 2 Hz.

In order to minimize the discrepancy between the S observations and the reflectivity synthetic seismograms, we developed a new S velocity structure to explain the two basic features, seen for the propagation of S waves across the Basin & Range: (1) the dominance of the Lg phase over the entire distance range of the observations (800-2000 km); and (2) the apparent lack of mantle S arrivals similar to the P wave portion of the observed waveforms. The use of a constrained S wave model relative to the P wave model (i.e. for a Poisson's ratio of 0.25), gave a result similar to the other authors.

We perturbed the S velocity in the crust of Priestley & Brune (1978) to a constant velocity of 3.5 km/s. A high-velocity lid below the Moho was introduced , which was expected to act as a strong reflector to avoid the leakage of energy out of the crustal waveguide. The synthetic seismograms from this model still showed considerable mantle S energy. This S energy presumably is propagating in the waveguide formed by the crust-mantle boundary and the low velocity layer beneath the high-velocity lid. By systematic decrease of the thickness of the S lid we could decrease the mantle S wave contributions only to a certain degree. The inclusion of a strong negative gradient at the bottom of the lid as a transition to the low velocity layer resulted in a further decrease of these mantle S arrivals. In addition, a low Qs value of 75 was required for the region below the lid, with Qs values inside the lid of 90-100.

In order to increase the duration of the Lg phase as well as the velocity contrast across the crust and mantle boundary, a laminated structure for S was introduced within the lower crust. This is similar to the approach taken by Sandmeier & Wenzel (1986) to explain reverberations following crustal P wave arrivals. The synthetic seismograms of this model are shown in Fig.9, where now Lg is indeed

the anticipated very long lasting waveform as well as the strongest S arrival. The weak arrivals coming in before Lg are the residual contributions from the S wave lid which might be hidden by the P wave coda in the observational data. These arrivals are still large, if the Qs in and below the mantle lid are above 100,. In this case the S waves leaking out of the crust and the lid are not satisfactorily attenuated.


## 4. Discussion and conclusions

In order to study the effects of different sources on the major regional phases we have developed a one dimensional velocity model which describes in both a qualitative and quantitative way the propagation path effects for seismic waves travelling across the Basin and Range from events in Nevada and South-Central California to the Lajitas seismic station in the Big Bend of Texas. This model was developed for both P and S broadband data in an observation range larger than used in previous studies (Olsen et al. 1980, 1983). Previous models were based on long-period observations, which may be responsible for the inability to resolve fine structures in the crust and upper mantle. When comparing the BH and PB models with our new model, it becomes obvious that these earlier structures are smoothed version of the latter. As an example the mantle lid in the BH model was turned up-side down, i.e. the small positive velocity gradient was changed to a small negative gradient, in order to obtain emergent Pn arrivals throughout our observation range. If the new model is further compared to the P model given by Priestley & Brune (1978) it appears, that the upper 100 km below the Moho is essentially the average of the velocities in our model with values ranging between 7.7 and 8.0 km/s. Also, the S velocity model, that these authors

13

proposed is quite similar if our thin mantle S lid averaged over a larger depth range. Furthermore there is a striking similarity of our S model for the uppermost mantle to the S structure proposed by Priestley & Brune (1982) for the Northern Volcanic Plateau. In their comparison of different provinces within the Basin and Range or adjacent areas they found a thin mantle S lid with a thickness of 10 km and an average S velocity of 4.3 km/s correlating with our results.

The main difference remaining between our modelled synthetic seismograms and the observations is the amplitude of the Lg wave. This difference may result from the fact that the dominant source frequency in the observations was considerably less than 2 Hz. Using a source function with lower frequencies would reduce the higher frequency P wave amplitudes in the synthetic seismograms, but also transfer energy to Lg. This fact is documented by the seismograms shown in Fig. 10, where the dominant source frequency was reduced from 2 Hz to 0.5 Hz. This is also in accordance with the observed Lg at Lajitas, which shows, that the main Lg contributions are near 0.5 Hz , while the P waves have the largest amplitudes in the 1.0-1.5 Hz range (Fig.4).

Other explanations for the strong Lg waves observed are related to source contributions from different secondary sources. As the synthetic data were generated for a explosion source model, further S wave contributions might result from spall and tectonic stress release. Barker et al. (1990) consider spall as the ultimate source of Lg from nuclear explosions. On the other hand, our calculations show that Lg can be effectively generated by an isotropic source due to conversion of the primary P waves. Further, the transfer of seismic energy into Lg is more pronounced the lower the dominant source frequency.

14

# 5. References

Archambeau, C.B., E.A.Flinn & D.G.Lambert (1969): Fine structure of the upper mantle, J.Geophys.Res., **74**, 5825-5865

Barker, T., S.Day, K.McLaughlin, B.Shkoller & J.Stevens (1990): An analysis of the effects of spall on regional and teleseismic waveforms using two-dimensional numerical modeling of underground explosions, **Air Force Geophysics Lab**, Report GL-TR-90-0126, ADA 226921

Bennett & Murphy (1986): Analysis of seismic discrimination using regional data from Western United States events, **Bull.Seism.Soc.Am**, **76**, 1069-1086

Burdick, L.J. & D.V.Helmberger (1978): The upper mantle P velocity structure of the Western United States, **J.Geophys.Res.**, **83**, 1699-1712

Golden,P. & G.Herrin (1989): Development of an intelligent seismic facility and preparation for participation in the conference on disarmament group of scientific experts technical test, **Tech.Rep.DARPA-SMU-R-89-125**

Hansen, R., F.Ringdahl & P.Richards (1990): The stability of the RMS Lg measurements and their potential for accurate estimation of the yields of Soviet underground nuclear explosions, **Bull.Seism.Soc.Am**,80,2106-2126

Helmberger, D.V. & G.R. Engen (1974): Upper mantle shear structure, **J.Geophys. Res**, **79**, 4017-4028

Johnson,L.R. (1967): Array measurements of P velocities in the upper mantle, **J.Geophys.Res.**, **72**, 6309-6324

Koch, K. & B.Stump (1989): Waveform analysis and synthetic modeling of far-regional seismograms from nuclear explosions and earthquakes, **EOS**, **70**, 1197

Lilwall, R.C. (1988): Regional mb:Ms, Lg/Pg amplitude ratios and Lg spectral ratios as criteria for distinguishing between earthquakes and explosions: a theoretical study, **Geophys.J.**, **93**, 137-147

Müller, G. (1985): The reflectivity method: a tutorial, J.Geophys., 58, 153-174

Nuttli, O.W. (1986): Lg magnitudes of selected east Kazakhstan underground explosions, Bull.Seism.Soc.Am, 76, 1241-1251

Nuttli, O.W. (1986): Yield estimates of Nevada Test Site explosions obtained from seismic Lg waves, J.Geophys.Res., 91, 2137-2151

Nuttli, O.W. (1988): Lg magnitudes and yield estimates for underground Novaya Zemlya nuclear explosions, Bull.Seism.Soc.Am, 78, 873-884

Olsen, K., L.Braile & P.Johnson (1980): Seismic velocity and Q-structure of the upper mantle lid and low velocity zone for the eastern Great Basin, Geophys. Res.Lett., 12, 1029-1032

Olsen, K. & L.Braile & J.Stewart (1983): Modeling short-period crustal phases ($\bar{P}$, Lg) for long-range refraction profiles, Phys.Earth Planet.Int., 31, 334-347

Patton, H.(1988): Application of Nuttli's method to estimate yield of Nevada Test Site explosions recorded on Lawrence Livermore National Laboratory's digital seismic system, Bull.Seism.Soc.Am, 78, 1759-1772

Patton, H. & S.Taylor (1984): Q structure of the Basin and Range from surface waves, J.Geophys.Res., 89, 6929-6940

Pomeroy, P., W.Best & T.McEvilly (1982): Test ban treaty verification with regional data - a review, Bull.Seism.Soc.Am, 72, S89-S129

Priestley, K. & J. Brune (1978): Surface waves and the structure of the Great Basin of Nevada and western Utah, J.Geophys.Res., 83, 2265-2272

Priestley, K. & J. Brune (1982): Shear wave structure of the southern Volcanic Plateau of Oregon and Idaho and the northern Great Basin of Nevada from surface wave dispersion, J.Geophys.Res., 87, 2671-2675

Sandmeier, K.-J. & F.Wenzel (1986): Synthetic seismograms for a complex crustal model, Geophys.Res.Lett., 13, 22-25

Taylor, S. & G.Randall (1988): The effect of spall on regional seismograms, Geophys. Res.Lett., 16, 211-214

Wiggins,R.A. & D.V.Helmberger (1973): Upper mantle structure of the western United States, J.Geophys.Res., 78, 1870-1880

## Table I: Summary of event parameters

| No. | Date | Origin Time | Lat. | Long. | Depth | $M_B$ | $M_{sz}$ | Range‡ | Remarks (from QED's) |
|---|---|---|---|---|---|---|---|---|---|
| 1 | 1988230 | 170000.0 | 37.297N | 116.307W | 0 | 5.4 | | 1468 | SOUTHERN NEVADA. <KEARSARGE> |
| 1 | —— | same event as above | | | | | | 923 | (to ABQ) |
| 2 | 1988244 | 164516.0 | 31.789N | 115.796W | 5 | 4.9 | | 1193 | BAJA CALIFORNIA. ML 5.1 (PAS). |
| 3 | 1988287 | 140000.0 | 37.089N | 116.049W | 0 | 5.9 | 4.2 | 1436 | SOUTHERN NEVADA. <DALHART> |
| 4 | 1988300 | 061043.4 | 27.053N | 111.803W | 10 | 4.7 | | 836 | GULF OF CALIFORNIA |
| 5 | 1988315 | 050800.1 | 37.357N | 121.868W | 5 | 4.7 | | 1907 | CENTRAL CALIFORNIA. ML 4.7 |
| 6 | 1988325 | 053926.8 | 33.461N | 118.145W | 5 | 5.1 | | 1448 | SOUTHERN CALIFORNIA. |
| 7 | 1988338 | 113825.0 | 34.151N | 118.139W | 10 | 4.5 | 4.2 | 1468 | SOUTHERN CALIFORNIA. ML 5.0 |
| 8 | 1988345 | 203000.0 | 37.199N | 116.209W | 0 | 5.1 | | 1455 | SOUTHERN NEVADA. <MISTY ECHO>. |
| 9 | 1988351 | 055303.5 | 33.984N | 116.695W | 5 | 4.9 | | 1336 | SOUTHERN CALIFORNIA. ML 4.8 |
| 10 | 1989019 | 065328.0 | 33.922N | 118.629W | 10 | 5.2 | | 1504 | SOUTHERN CALIFORNIA. ML 5.0 |
| 11 | 1989068 | 140500.0 | 37.143N | 116.067W | 0 | 5.0 | | 1440 | SOUTHERN NEVADA. < INGOT > |
| 12 | 1989291 | 000415.2 | 37.036N | 121.883W | 19 | 6.6 | 7.1 | 1896 | CENTRAL CALIFORNIA. <GS-P>. ML 7.0 (BRK). |
| 13 | 1990005 | 182658.1 | 18.674N | 106.856W | 33 | 5.4 | 5.6 | 1223 | OFF COAST OF JALISCO, MEXICO. |
| 14 | 1990016 | 200820.2 | 40.150N | 124.232W | 10 | 5.1 | 5.5 | 2223 | NEAR COAST OF NORTHERN CALIF. |
| 15 | 1990069 | 160000.0 | 37.113N | 116.055W | 0 | 5.1 | | 1438 | SOUTHERN NEVADA. < METROPOLIS >. |

‡)     Epicentral distance to Lajitas, TX (LTX)

18

**Figure captions**


Figure 1:   Basin and Range sketch map showing study area and locations of
            station(s) and epicenters with corresponding great circle paths.


Figure 2:   (a) Short period velocity data in the distance range 800-2000 km

            (eigenfrequency of transducer - 1 Hz)

            (b) Broadband acceleration data for the same distance range

            (bandwidth 0-5 Hz)

            ( O indicates an explosion)

Figure 3:   P wave segments of selected events showing Pn and Pg for the top 2

            traces and mantle P for the lower traces. The weak precursor to the

            mantle P waves is Pn

Figure 4:   Sonograms for an earthquake and explosion at far-regional distances

            that illustrate the bandwidth of different phases in the seismograms


Figure 5:   Low-pass filtered results (10 sec) of the data shown in Fig. 2 designed

            to emphasize surface wave contributions


Figure 6:   One-dimensional Basin & Range velocity models: (a) P, and (b) S

            [Burdick & Helmberger 1978; Priestley & Brune 1978; Olsen et al. 1980;

            Engen & Helmberger 1974]


Figure 7:   Synthetic reflectivity seismograms at regional distances (200-1400 km)

            for a velocity structure incorporating the P model of Burdick &

            Helmberger (1978) and the S wave model of Priestley & Brune (1978).

Figure 8:    Synthetic seismograms for ve'ocity models given by Olsen et al. (1980)

Figure 9:    Synthetic reflectivity seismograms at far-regional distances (600-1400 km) for the velocity structure derived in this study (see Fig. 6)

Figure 10:   Same as Fig. 9 with lower frequency source excitation.
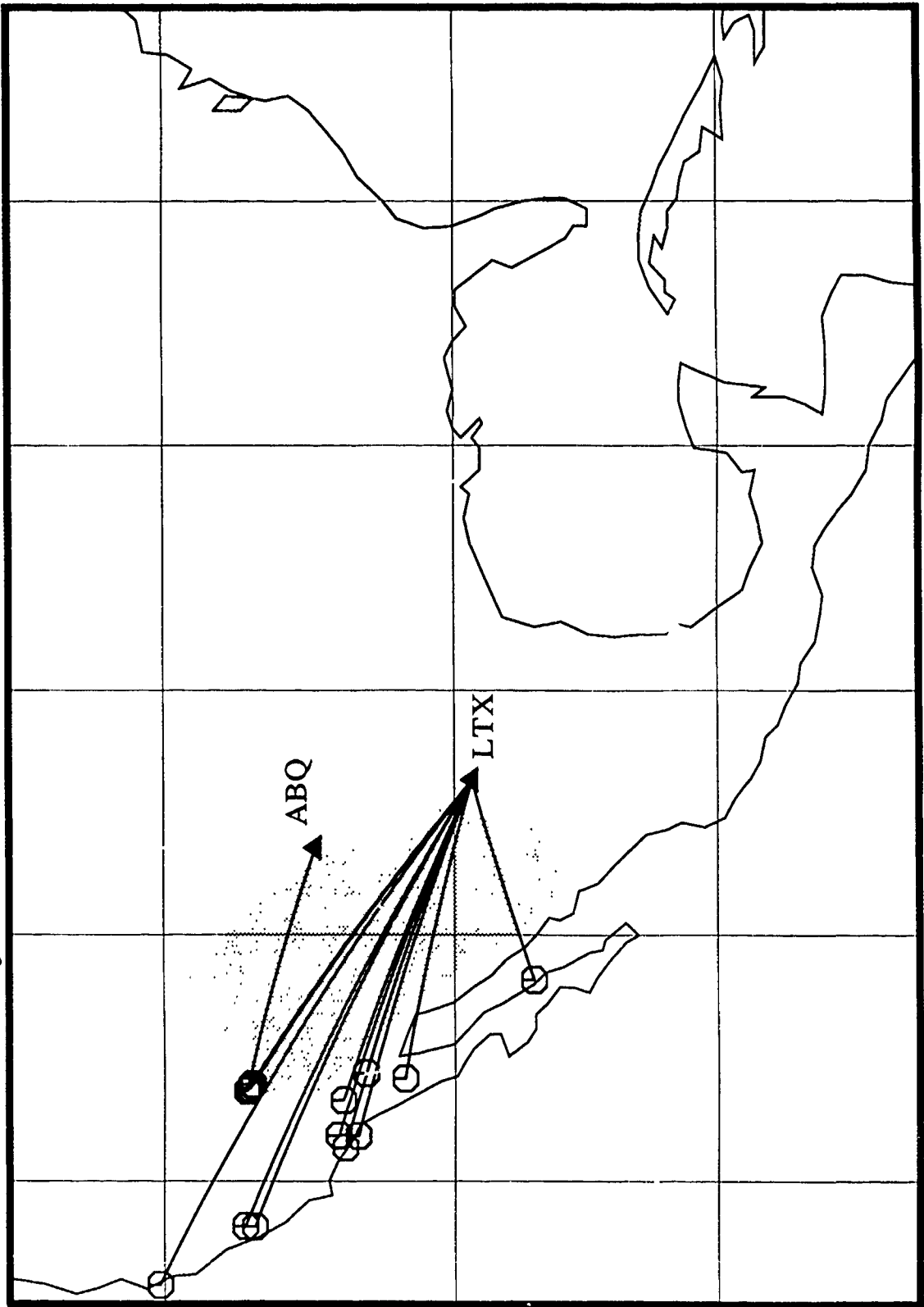
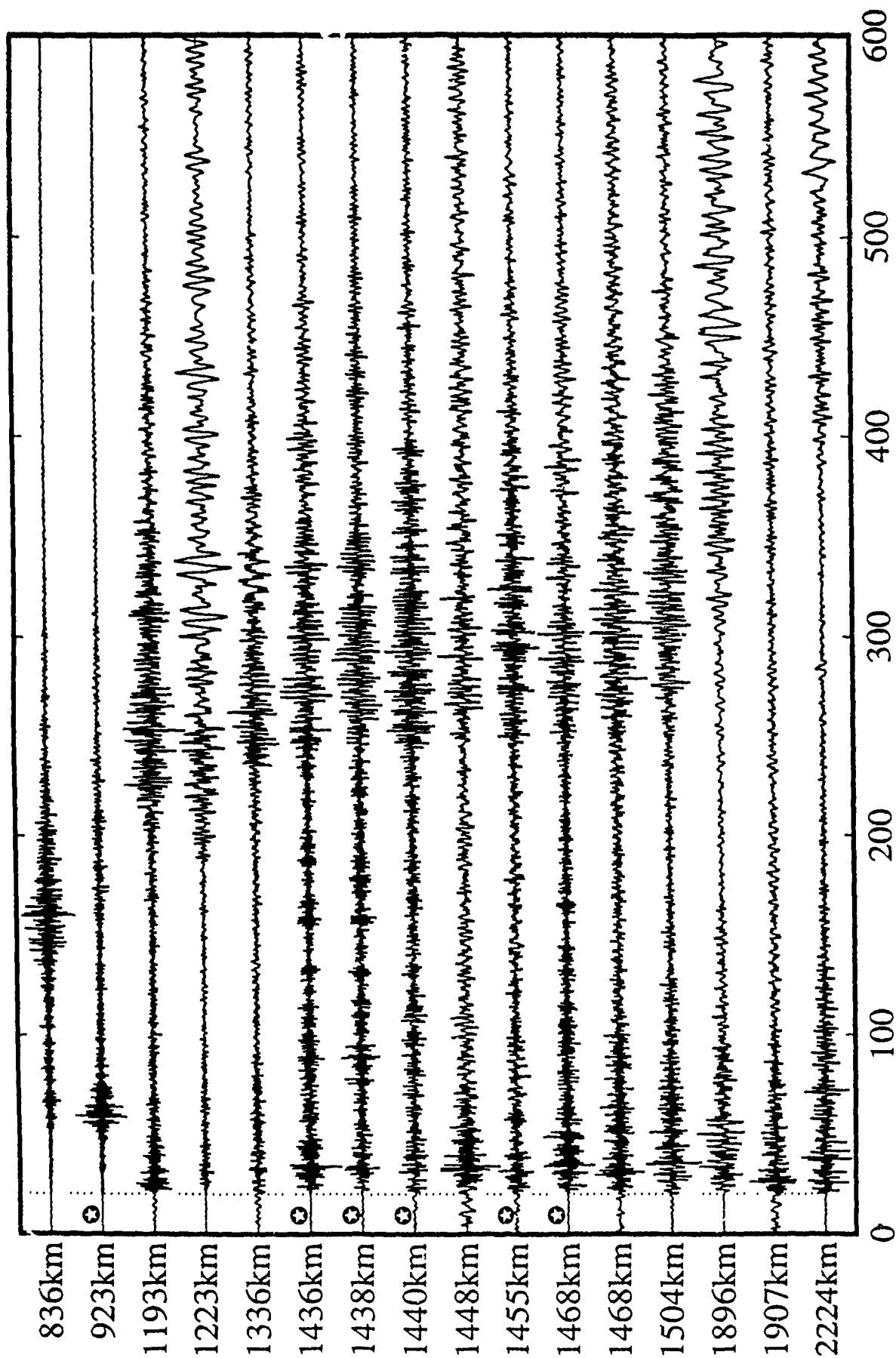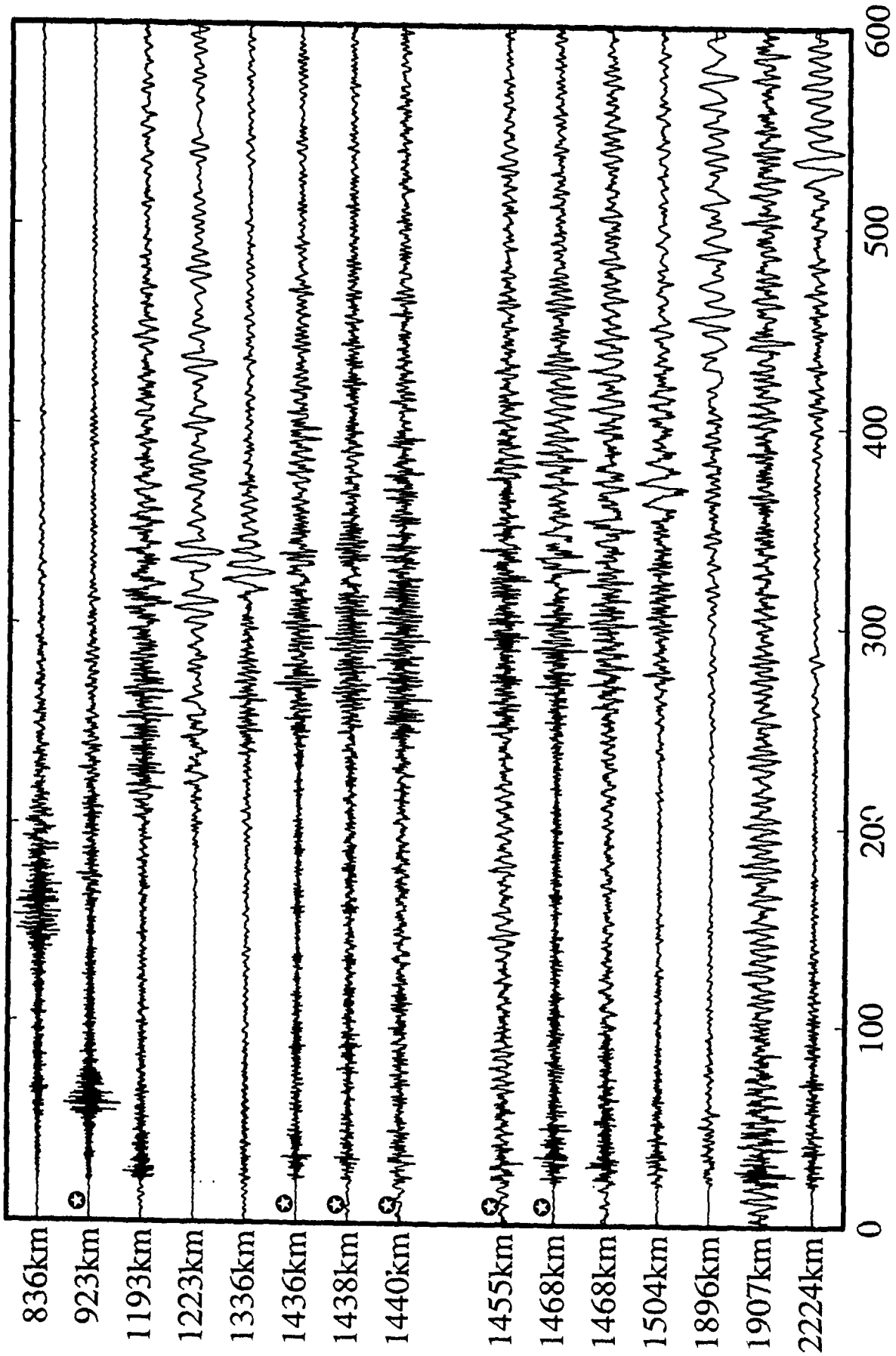MERCATOR Projection

ABQ

LTX

FIGURE 1

21

Vertical Component [SP]

836km
923km
1193km
1223km
1336km
1436km
1438km
1440km
1448km
1455km
1468km
1468km
1504km
1896km
1907km
2224km

0    100    200    300    400    500    600

Time (sec)

FIGURE 2a

22

Vertical Component [BB]

836km
923km
1193km
1223km
1336km
1436km
1438km
1440km
1455km
1468km
1468km
1504km
1896km
19071km
2224km

0   100   200   300   400   500   600

Time (sec)

FIGURE 2b

23

Vertical Component [SP]

Vertical Component [BB]

836 km

923 km

1193 km

1436 km

1468 km
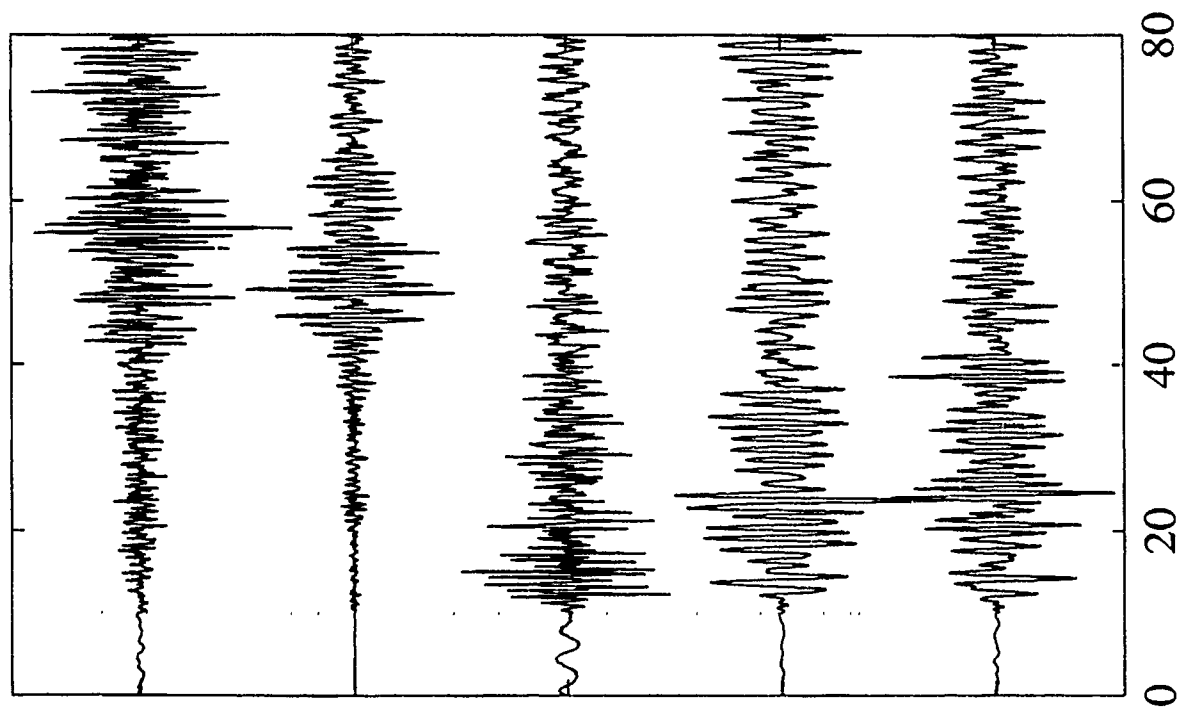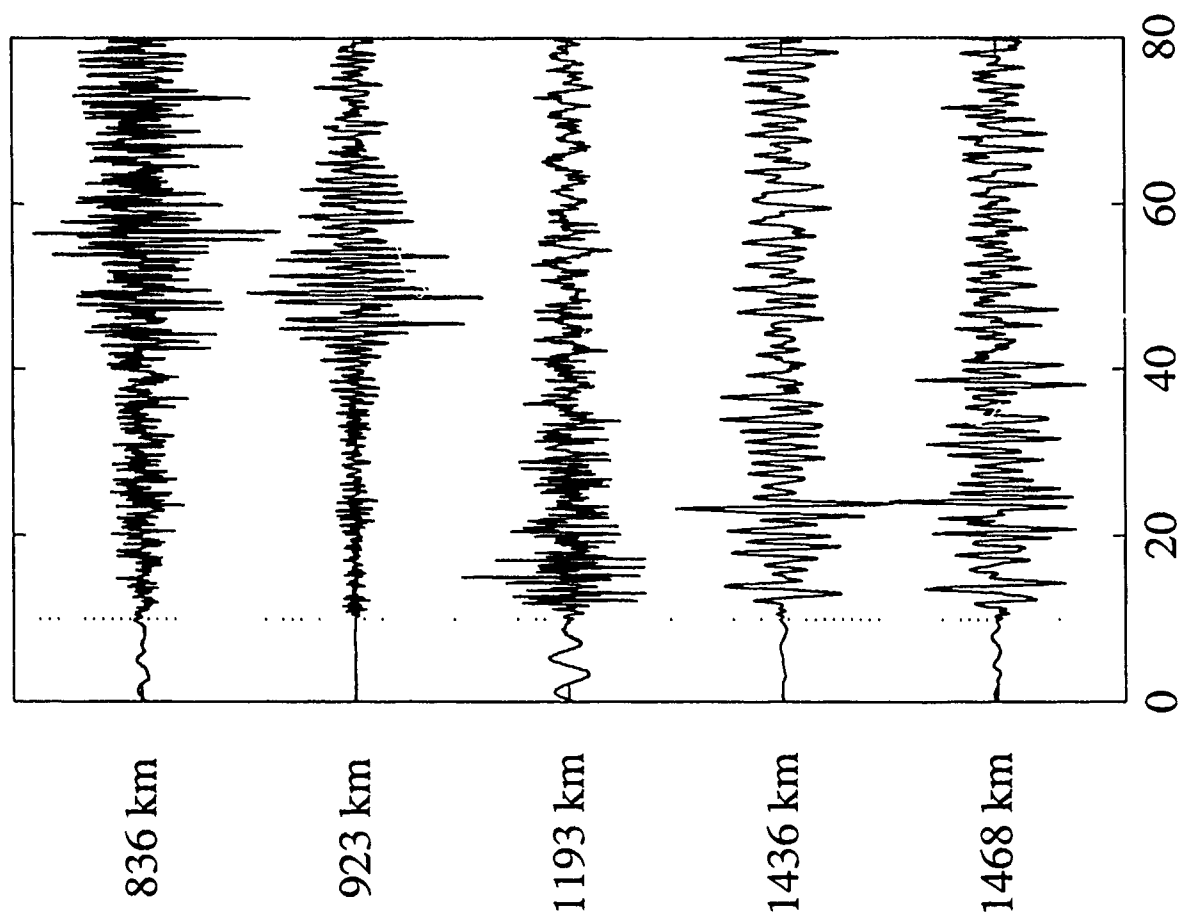
Time (sec)

Time (sec)

FIGURE 3

24

# Sonogram for event at 1336 km



# Sonogram for event at 1468 km
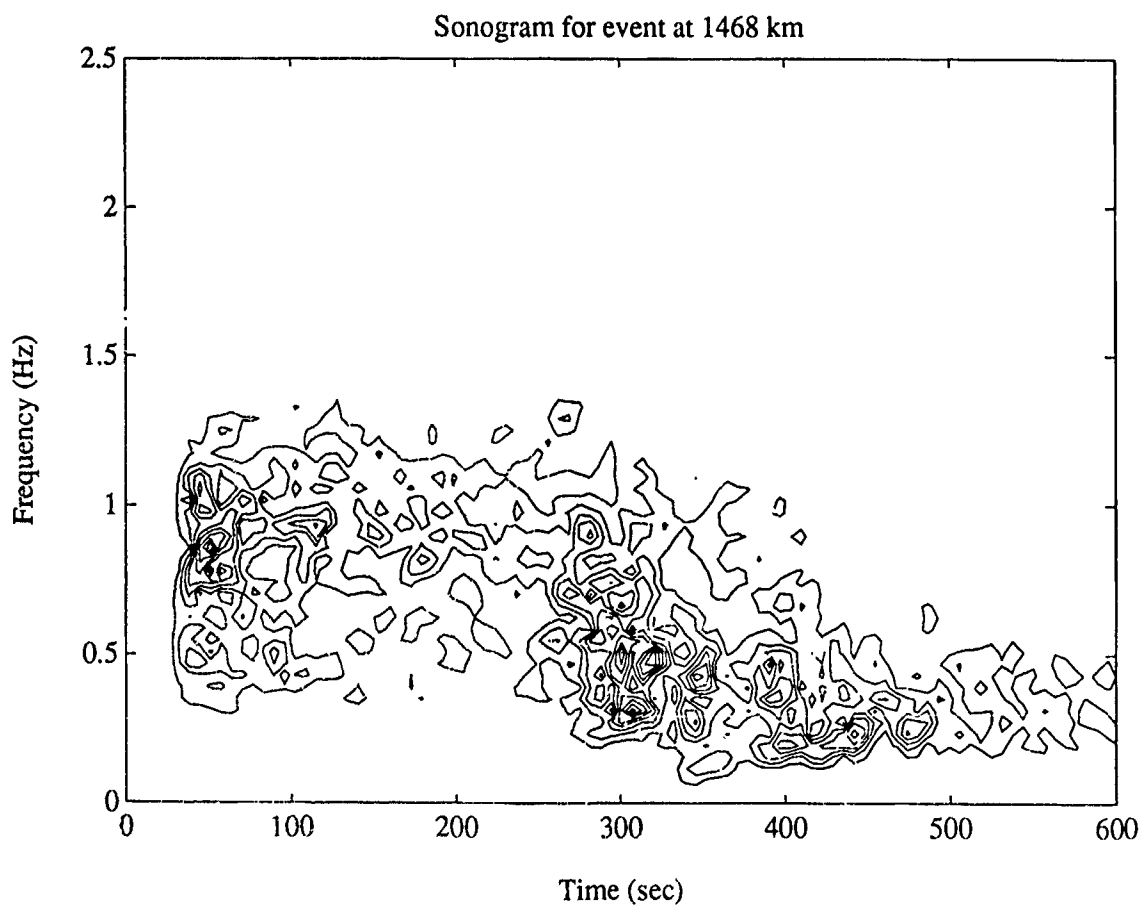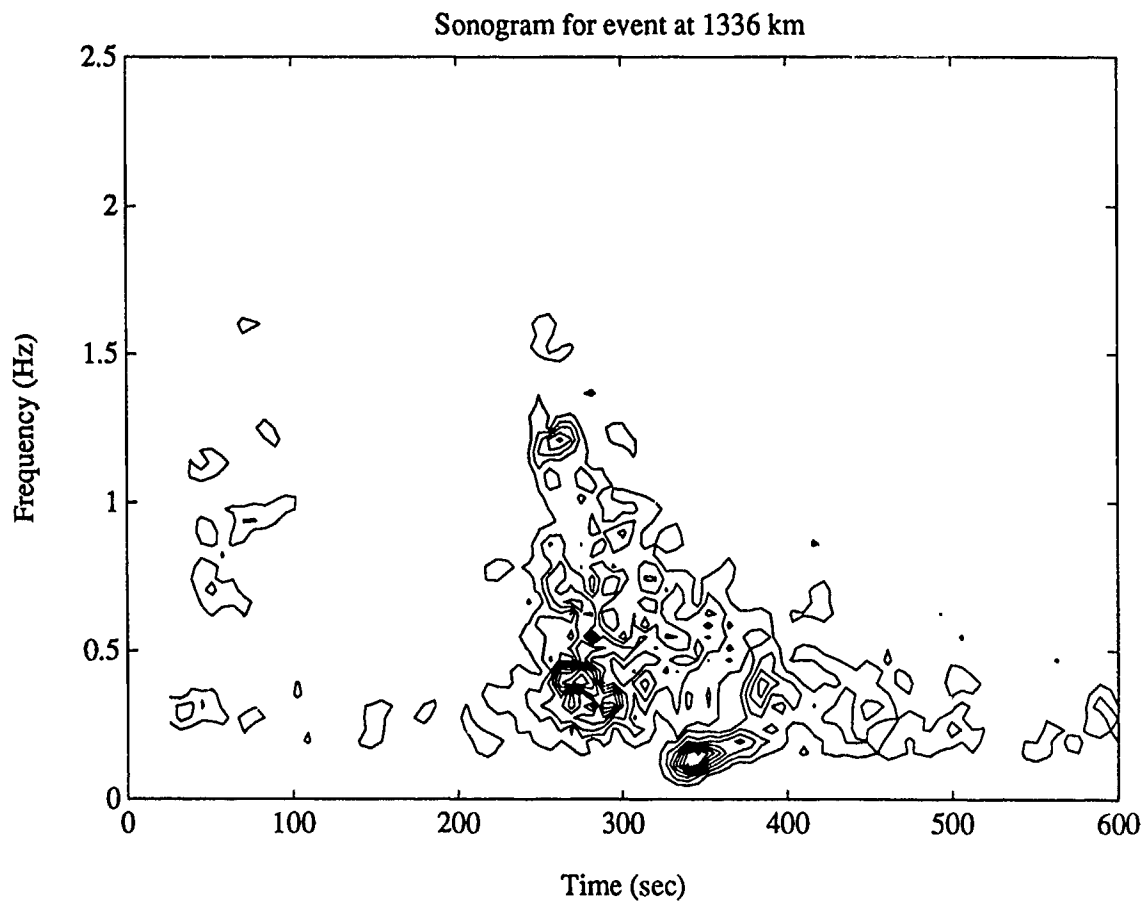


FIGURE 4

Vertical Component [SP] / LP 0.1 Hz

Time (sec)

FIGURE 5a

836km
923km
1193km
1223km
1336km
1436km
1438km
1440km
1448km
1455km
1468km
1468km
1504km
1896km
1907km
2224km

26

Vertical Component [BBJ] / LP 0.1 Hz

836km
923km
1193km
1223km
1336km
1436km
1438km
1440km
1455km
1468km
1468km
1504km
1896km
1907km
2224km

0    100    200    300    400    500    600

Time (sec)
FIGURE 5b

27

# P velocity (km/s)



**FIGURE 6a**

# S velocity (km/s)



FIGURE 6b

**This study**
**Priestley & Brune 1978**
**Helmberger & Engen 1974**
**Olsen et al. 1980**
**Koch & Stump 1989**

29

VERTICAL

Range (km)

FIGURE 7

Red.Time (sec)

Depth (km)

Velocity (km/s)

30

FIGURE 8

VERTICAL

Range (km)

Red.Time (sec)

Depth (km)

Velocity (km/s)

31

VERTICAL

Red.Time (sec)

Range (km)

**FIGURE 9**

32

VERTICAL

Depth (km): 0 100 200 300 400

Velocity (km/s): 3 6 9 12

Red.Time (sec): 400 350 300 250 200 150 100 50 0

Range (km): 200 400 600 800 1000 1200 1400

FIGURE 10

33

# Source Contributions in Regional Waveforms with Implications for Explosions with Spall

Karl Koch, Brian Stump
Southern Methodist University
Department of Geological Sciences
Dallas, TX 75275

## 1. Introduction

A physical understanding of source contributions at regional distances is an important tool leading to the identification and discrimination of earthquakes and explosions in the context of a reduced threshold test ban treaty. With this motivation we have analyzed seismograms from nuclear explosions and earthquakes at Lajitas, TX, covering a distance range of about 800-2000 km in an attempt to explain observed waveforms in terms of propagation path and source effects. Realistic modelling of the whole seismogram was carried out with the reflectivity method for a specific Western United States model (Koch & Stump 1991). This work focused on development of both a P and S wave model that describes wave propagation to far-regional distances across the Basin and Range for all major regional phases. Based on this work, we will explore the role different source models play in generating the regional phases.

The broadband data from Lajitas offers the opportunity to explore not only the arrival times of the dominant regional phases but their frequency content as well. A number of authors have suggested source discriminants based upon the frequency content of different regional phases (Pomeroy et al., 1982; Taylor et al., 1988; Chael, 1988; Suteau-Henson and Bache, 1988; Baumgardt and Young, 1990).

The initial deposition of seismic energy around a nuclear explosion is commonly represented as a spherically symmetric or isotropic source. This representation is commonly cast in terms of a reduced displacement potential (rdp) (Sharpe, 1942; von Seggern and Blandford, 1972; and Mueller and Murphy, 1971). The scaling of this rdp as a function of yield is responsible for the initial yield signature of the seismograms.

In near-source observations, spall, the tensile failure of shallow layers caused by interaction of the explosion pressure pulse with the free surface is a dominant source effect. As a secondary source of seismic waves it has been shown to have little contribution to long-period surface waves (Day et al. 1983), while studies of body waves have been restricted to a distance range of a few hundred kilometers (Taylor & Randall 1989, Barker et al. 1990). In recent papers it has been suggested that this secondary source may be responsible for the success of some spectral discriminants (Taylor & Randall 1989) at regional distances. This secondary source has also been suggested as a strong contributor to the Lg phase in some geologies (Barker et al. 1990).

In order to quantify source effects at far-regional distances, i.e distances of more than 1000 km, we have calculated complete seismograms from

explosion and spall sources for a variety of different source characteristics. First we want to contrast spall and explosion wavefields in terms of source depth, which may be different for a normally contained explosion and the near-surface spall phenomena. In this parametric study we use the same source time functions in order to separate depth effects from effects that may result from spectral source differences.

Near-source observations from two nuclear events at Rainier Mesa, NTS, will be incorporated in the modelling of far-regional seismograms for a range of source parameters. Both free-field and surface observations were available, which we use to constrain the source parameters of both explosion and spall components in terms of a von Seggern-Blandford explosion source model (von Seggern & Blandford 1972) and a spall source model according to Stump (1985).

## 2. Spectral analysis of observed waveforms

In order to quantify spectral effects that may be identified in regional seismograms we analyzed the data from the Lajitas, TX seismic station, which are shown in Fig.1. These data were recorded by a broadband acceleration instrument with a bandwidth from DC to 20 Hz but noise levels and anti-alias filters limit the bandwidth of the data to 3-4 Hz. These data are a subset of those used by Koch & Stump (1991) to constrain propagation path effects at far-regional distances across the Basin & Range. They are distinguished by signal to noise ratios of at least 5. Both explosion and earthquake data were used for the spectral analysis in order to discuss spectral differences. Three

explosion recordings, marked by an asterisk in Fig. 1, were compared to five earthquake recordings.

To characterize the temporal development of the spectral content in explosion and earthquake seismograms we calculated sonograms from the raw data. A time window of 2.56 sec was used for each individual spectral estimate, and for smoothing purposes, this window was moved in time by 0.64 sec for subsequent spectra, resulting in a fourfold oversampling and smoothing of each sonogram. The sonograms were plotted in 3-dimensional perspective view and as contour plots. Representative figures for two events used in our analysis are shown in Figs.2 and 3, where the first is from a NTS explosion at a distance of 1468 km ("Kearsarge" - referred to in the following as trace no.6) and the second event is an earthquake (trace no.7) in Southern California at a similar range (1504 km). Due to the proximity in epicentral distance, wave propagation effects are assumed to be similar allowing a direct comparison for these events.

The sonogram for event #6 (Fig.2) shows distinct frequency signatures for each regional phase including mantle P, Lg and surface waves. The early part of the sonogram is dominated by the mantle P wave with energy in the frequency band 0.3 to 1.5 Hz. The Lg arrival occurs at about 220-230 sec with a shift of the energy to lower frequencies, and a strong spectral maximum around 0.5 Hz. At times greater than 300 sec surface waves arrive with a further frequency shift to 0.1-0.2 Hz. As the seismograms in Fig.1 suggest, the sonogram of the earthquake record (event #7) is strongly dominated by the surface wave arrivals. This arrival begins after 300 sec and the frequency content of these wave is similar to those from the explosion. The Lg phase,

37

starting at 250 sec, again shows a dominant frequency range around 0.5 sec. The P waves, due to the dominance of the surface waves, are very small in the sonogram although they contain the highest frequencies, up to 1 Hz. This high frequency phase characterization is further supported by sonograms of short-period data recorded from these events which suppress the surface waves below 0.3-0.5 Hz.

Taylor et al. (1988) and Chael (1988) have suggested that the spectral shape for earthquake and explosion sources is different. This spectral discriminant was tested by calculating the P wave spectra of the explosions (Fig.4a) and earthquakes (Fig.4b) from the broadband seismograms. A time window of 80 - 150 sec was used in the spectral calculation incorporating all P wave contributions - $P_n$, $P_g$, mantle P. No attempt was made to separate these phases due to the following reasons: (1) the data base currently available is too small for a useful phase separation, i.e. only two seismograms show reasonable signal levels in Pn and Pg, while all other events show only mantle P waves; (2) as the focus of this work is on source effects, source contributions should be contained in all P phases and hence should also be observed in this integral measure. As we used broadband acceleration data, the spectra were corrected for instrument effects by double integration in time transforming them into displacement spectra. In order to separate the individual event spectra in the figures, they were scaled by multiple factors of 10. The spectra were not corrected for epicentral distance or anelastic attenuation, nor were they normalized with respect to source strength.

While the earthquakes (Fig.4a) show a clear spectral plateau for low frequencies, the explosions (Fig.4b) are characterized by a decrease of spectral

amplitudes for low frequencies, in agreement with the explosion source models of Mueller & Murphy (1971) or von Seggern & Blandford (1972). To further emphasize the spectral differences we used the closely spaced events in the 1300-1500 km distance range for spectral comparison (Fig.5). The decrease in long-period spectral amplitude for the explosions in contrast to the earthquakes is obvious. The corner frequencies of the explosions apparently are shifted to higher frequencies and the high-frequency roll-off is larger. As Taylor et al. (1988) argued, this difference in spectral amplitudes might be used as a discriminant, and they proposed the spectral ratio in the 1-2 Hz and 6-8 Hz bands. The spectra for our data indicate such a measure may be useful at far-regional distances for the frequency bands at 0.05-0.2 Hz (5-20 sec) and 0.3-1 Hz, where the explosions show the largest difference compared to the plateau for earthquakes.

## 3. Source depth effects for explosion and spall sources

Near-source ground motions (ranges to several kilometers) from nuclear explosions are dominated by the explosive source itself and the effects of spallation of near-surface layers. In order to quantify these spall effects, Day et al. (1983) developed a model to describe the tensile failure of near surface layers. Their equivalent source time function is composed of the initial impulsive failure of the near-surface layers, the relaxation during free fall of the spalled layers, and the slapdown pulse corresponding to the rejoin of the spalled mass. The driving mechanism is usually either described by a single vertical force ($f_3$) or, often applied in moment tensor inversions, by the equivalent force couple model ($m_{11}$, $m_{22}$, $m_{33}$) (Day & McLaughlin 1991). In

our modeling of far-regional seismograms we have adopted the force couple model for the spall source. The source time functions, Mueller-Murphy (1971) or von Seggern-Blandford (1972) for the explosion source, and Day et al.(1973) or Stump (1985) for the spall source, were chosen as a simple step function in order to focus on source depth effects alone. We will consider specific source time functions, along with particular source depths for primary explosion source and secondary spall source in a following section.

In order to quantify the depth dependence, we calculated synthetic reflectivity seismograms for a variety of source depths from 0 - 2 km. The depths for which synthetic seismogram calculations were performed included 0 m, 100 m, 300 m, 500 m, 750 m, 1 km and 2 km (Fig.6). Shown in this figure is the near-source velocity model consisting of a low velocity layer (2.5 km thick) with P and S wave velocities of 3.5 km/s and 2.09 km/s, followed by a typical crustal velocity structure with the corresponding velocities of 6 km/s and 3.55 km/s. All sources were placed in the top low velocity layer typical of a Basin & Range model and the NTS area. Besides the source model, the primary source effects are expected to result from the interaction of the wavefield with the free surface and the interface between the low velocity sedimentary layer and crustal layer. The explosion source was modelled by an isotropic moment tensor. The spall source, physically describing the tensile failure of the shallow layers, i.e. the opening of a horizontal crack, is theoretically represented by an isotropic moment tensor with an additional $m_{33}$ component. The ratio between the vertical and the horizontal force couples is of the order of 2-3. As our interest is in the difference between the explosion and spall event, we removed the isotropic component from the spall source model, using only the $m_{33}$ component. We therefore assume that linear

40

superposition of $m_{33}$ with the isotropic part would be appropriate, but that it provides no further information for discriminating between the spall and explosion source. Differences in these calculations for an explosion and our spall source may thus represent an upper bound for differences observed in regional seismograms.

From the synthetic data in the distance range 200-1400 km, we determined the maximum amplitudes for the major regional phases. In order to quantify depth and range effects in the synthetic seismogram sections for the various wave types, amplitude distance curves were derived from the data. Fig.7a contains amplitude distance curves for the vertical motion from explosion sources. The amplitude distance curves for LR (surface wave) show almost identical values for sources in the depth range between 0 m and 2 km, while the variability of the Lg and Pg amplitudes are a factor of 2-3, with amplitudes increasing with source depth. The 2 km deep source shows significantly higher amplitudes for the body waves which might be expected from the proximity to the underlying high velocity layers (see Fig.6). Pn and mantle P wave (Pm) are plotted as one curve, and they indicate the transition between these two waves as first arrival. In addition, these waves show a substantial depth dependency as a result of increased coupling for the deeper sources. The Pn/Pm curves clearly indicate that the transition of Pn to Pm as the prominent first arrival occurs between 900 and 1000 km, independent of source depth.

Amplitude distance curves for vertical component seismograms from the spall source are given in Fig.7b. The change in synthetic amplitudes with source depth is much greater than those observed from the explosion source.

This fact is emphasized by the amplitude distance curves, which show strongly increasing maximum amplitudes as the source is moved away from the free surface. The amplitude variations with respect to the spall source depth is of the order of 10 compared to a factor of 2-3 for the explosion sources. Due to wavenumber filtering in the synthetic seismograms, the curves for LR are not well constrained.

To further emphasize source differences, the vertical component amplitude distance curves for Pg as well as Lg for explosion and spall sources are superimposed in Fig.8a,b. Scaling of the amplitudes between the two source types is relative. Contrasting Pg amplitudes in Fig.8a, the differences for the explosion source are small except for the very deep source while the spall source differences are as large as a factor of 10. The same comparison is found for the Lg amplitudes in Fig.8b. These results indicate that body wave amplitudes for a deep spall source could be quite large in far-regional data while a shallow spall source may not be identifiable in these waveforms. As Stump (1985) showed, the spall source has its largest depth extend at ground zero and may be on the order of one half the burial depth. As the seismic moment, and hence source strength, are determined by the spalled mass and its escape velocity, the center of the spall zone may make a large contribution to the generation of significant seismic energy observable at regional distances.

## 4. Misty Echo / Mineral Quarry: A case example for near-source constraints from nuclear explosion

Modeling of regional data alone introduces ambiguities in the relative importance of the different source contributions such as the isotropic explosion and the secondary spall source. In an attempt to further quantify the source function for the regional seismograms, near-source observations can be used to constrain source parameters of the explosion and spall sources. Combined free-field (shot level) and surface data further provides separation of the different source models. Patton (1990), for example, has used surface data to constrain spall source parameters for Pahute Mesa explosions. A similar approach will be used here for the two nuclear explosions Misty Echo and Mineral Quarry at Rainier Mesa. Data from these events provide us with the opportunity for quantifying the isotropic source with free-field data and the spall source with free surface observations from within the spall zone.

The instrumentation plan for Misty Echo and Mineral Quarry are shown in Fig.9 a and b. For Misty Echo there were 8 acceleration gauges in the Rainier Mesa tunnel complex providing free-field data, in addition to 18 surface installations, which were used to map the spall zone. For Mineral Quarry, 15 instruments were emplaced in the tunnels, and more than 30 surface stations were operated.

The explosion source parameters were estimated by Min & Stump (1991) using a simultaneous inversion of near-source data for source parameters and Q. The source was either constrained to a Brune's or a von Seggern & Blandford model. While the former model was developed for earthquakes, it represents the limiting case of a von Seggern and Blandford model with no overshoot. The von Seggern-Blandford model is usually parameterized by two values B and k, where $k=2\pi \cdot f_c$ is the angular corner frequency of the

43

source spectrum, and B=(2·A+1) is the overshoot ratio. Min & Stump (1991) estimate a corner frequency of about 1 Hz for Misty Echo while the corner frequency for Mineral Quarry is 1.5 Hz, consistent for both a Brune and von Seggern & Blandford model. The overshoot value, B, was not as well constrained, as it trades off with the long-period level in their inversions. Reasonable values for B between 2 and 5 were found. In our parametric study of explosion and spall synthetics in the following section, we use a range of 1-2 Hz for $f_c$ and 1-5 for B.

Free surface acceleration records from directly above the explosion constrain the spall source parameters. These data were converted to velocity in order to determine an escape velocity estimate for the spalled mass. Fig.10 shows a typical example of the surface data, where the station was within the spall zone. It exhibits the characteristic -1g dwell during the free fall of the spalled mass. Rise time, i.e. the time for the spalled mass to detach, and dwell time, i.e. the time of free fall, were also obtained from the acceleration data. The dwell time was compared to the escape velocity for consistency:

$$T_D = \frac{2V_0}{g}$$

where $T_D$ is the dwell time, $V_0$ is the escape velocity, and g is gravitational force.

Fig. 11 compares the vertical velocities from both free-field and free surface data. In general, the velocities from the free-field data for Misty Echo are a factor 2 larger than the values observed for Mineral Quarry. In contrast, the

surface velocities inside as well as outside the spall zone are almost identical for both events. The spall radius, however, determined from the data, shows again a factor 2 difference, where we estimate a spall radius of 1000 m for Misty Echo and 500 m for Mineral Quarry. The peak velocities shown in Fig. 12 indicate a peak escape velocity of 0.2-0.3 g-s for Misty Echo and values of 0.15-0.2 g-s for Mineral Quarry. In order to bound spall momentum and determine if this secondary source can significantly contribute to the regional waveforms a range of momentum estimates for the process were made. The upper bound of these values assumes that the entire spall zone moves with the escape velocity determined at the center of the spall zone.

The dwell times are shown as a function of free surface range for Misty Echo in Fig.13. From these figures we estimate a maximum dwell time between 0.75 and 0.5 s for Misty Echo. The dwell times for Mineral Quarry, 0.375 s, are about a half as long as those for Misty Echo. From these data our estimates for the average escape velocity are 3.7 m/s for Misty Echo, and 1.9 m/s for Mineral Quarry. Both of these estimates are greater than the actual escape velocities observed and indicate that the spall process may not be totally explained by the simple ballistic model linearly linking escape velocity and dwell time.

The values independently derived are now used to calculate estimates of the spalled mass and the total momentum. They are contrasted against values, that follow from scaling relations given by Patton (1990). His scaling relations give estimates for spall extent as well as depth. The maximum range of spall is given by:

$$r_{max} = 475(\pm 60) \; W^{\; 0.26 \; (\pm 0.03)}$$

45

and the depth:

$$d_{max} = 86(\pm 12)\, W^{\,0.25\,(\pm 0.03)}$$

Following the suggestion of Patton (1990), we estimate the spall mass by two discs with lateral extent of $r_{max}$ and $r_{max}/2$, respectively, and a depth of each disc of one-half the depth extent determined for the entire spall zone, hence

$$M = \pi\, \rho_1\, r_1^2\, d_1^2 + \pi\, \rho_2\, r_2^2\, d_2^2 = \pi\, (\frac{\rho_1}{2} + \frac{\rho_2}{8})\, r_{max}^2\, d_{max},$$

and we compare it with his empirical relation for mass:

$$M = 7.3 \times 10^{10}\, W^{\,0.77}\, kg$$

for shots below the water table.

The results for the two nuclear explosions under investigation are summarized in Table 1. The scaling relations are based on $L_g$ yields reported by Patton. The $Y_{L_g}$ for Mineral Quarry is taken to be 6.1 ktons and for Misty Echo, 16.9 ktons. In the case of the bigger of the two events, Misty Echo, the total mass as predicted by the scaling relations is within 7% of that determined by the spall zone data. The Mineral Quarry spall zone data indicates a unusually small mass in comparison to the scaling relation where the difference is 70%. This difference is despite using a large estimate for spall depth in the data estimates which was set to 1/2 the depth of burial for the explosion.

## 5. Misty Echo: Regional observations and synthetic seismograms

46

As the work presented in previous sections indicated, spall as a secondary source may be important and, in some way, contribute to regional seismograms. Barker et al. (1990) used a numerical simulation approach for explosion and spall sources and found that spall can, in some instances, be a governing source for the generation of Lg waves observed at regional distances. While spall was an efficient generator of Lg waves for a high-velocity near-surface structure, similar to what is found for the Eastern Kazakhstan test site, explosion sources were poor generators of Lg waves, although capable of producing the P wave portion of regional and teleseismic seismograms. However, for a velocity structure with a low velocity surface layer, their model calculations show that Lg generation at regional distances can be attributed to either the explosion or spall source. Our goal is to use the near source information gained for the explosion and spall source models to calculate synthetic reflectivity seismograms at far-regional distances and investigate their significance on regional seismograms.

Far-regional observations from the Misty Echo explosion at Lajitas seismic station are shown in Fig.14, with a station-event distance of 1455 km. All three component, short-period seismograms are shown. As NTS is at a backazimuth of aoout 290 degrees from this station, the EW component is primarily radial, while NS is nearly transverse. The data indicate a well developed mantle P phase as well as Lg, which is the biggest arrival. What might be anticipated from the discussion in section 2 and by the seismograms, is a shift to lower frequency from P waves to Lg.

The source functions used in the synthetic seismograms, as derived from near source data, are given in Fig.15. The explosion is represented in terms of

47

a von Seggern-Blandford explosion model (top) and the spall source (bottom) follows the representation of Stump (1985). For the explosion source model, the far-field displacement, or equivalent near-field velocity, is given for a number of k values, corresponding to corner frequencies of 1, 1.5 and 2 Hz. The source time functions are scaled to a normalized static reduced displacement potential. For the spall source we have plotted the ground acceleration in g's while dwell and rise times vary between 0.375 and 0.75 s. With these source parameters we calculated regional synthetics for the distance range from 600 to 1400 km. For emplacement depth we used 500 m for the explosion, close to the actual source depth, while we used 200 km for the spall source, which we have estimated from the near source data.

Fig.16 shows reflectivity seismograms for a explosion source with no overshoot (B=1) and a dominant frequency around 1 Hz (k=6), which correspond to the results obtained from Koch & Stump (1991) for their study of wave propagation effects across the Basin and Range. As no specific source information was incorporated, this figure illustrates the partitioning of seismic energy into different regional phases that might be enhanced or blurred by source depth, source mechanism, and source time functions. A further result provided by these synthetic data is the higher frequency content for Pn, Pg and mantle P waves when compared to the Lg and surface wave parts of the seismograms.

Fig.17 shows a similar synthetic seismogram section, where the overshoot ratio was increased to B=5, thus strongly enhancing the energy around 1 Hz. As the synthetics show this results in a further enrichment of Pg and mantle

48

P energy, while the Lg as well as the surface waves remain almost the same, due to their longer period nature.

For the spall source we show the results for the distance of 1400 km with a parametric change of the dwell and rise time in the source time functions. Our estimates for these two parameters were between 0.375 and 0.5 sec for the dwell time and 0.5-0.75 sec for the rise time. We also used upper limit values twice as large to bound the effects on the regional waveforms. Fig.18 illustrates the strong dependency of the seismograms on these source parameters. Although only a qualitative examination is made, the P wave appears to be a more stable contribution to regional waveforms than either the Lg wave or surface waves. This may be related to the low frequency content of these later phases. The spall source function is peaked and moving this peak to higher frequencies strongly affects the later phases. Barker et al. (1990) argue that the peak of the spectrum for the spall source corresponds to the dwell time. In this light, spall might not be efficiently contributing to lower frequency Lg or surface waves except in the case of large dwell times (> 1.0 s).

## 6. Conclusions and Summary

In order to quantify the effects of spall on regional seismograms, which in our case are far-regional distances from several hundred to about 2000 km, we investigated data from the Lajitas seismic station. We conclude from our spectral analysis, that regional P waves across the Basin and Range show significantly higher frequencies than Lg waves, although the latter appear as strong arrivals especially in short period data.

As recent work (Barker et al. 1990) identified spall as a possible strong generator of Lg waves at regional phases, this study has focused on the explosion and spall parameters that might separate their contributions to regional seismograms and quantify their significance. We first tried to tie down the significance of source depth effects from both source types. As was demonstrated, there is a strong depth dependency for excitation of all regional phases due to the spall source, while the differences for the explosion are less distinct.

As spall is a major contribution to near source observations, we used observations of the nuclear explosions Misty Echo and Mineral Quarry to constrain explosion and spall source parameters for small to medium sized events. Using these constraints we observe that spall may not necessarily be a significant contribution to all regional seismic waves. We attribute this result to the low frequency character of observed Lg waves, which may not be generated by spall sources with short duration and vanishing momentum at longer periods.

# 7. References

Barker, T., S. Day, K. McLaughlin, B. Shkoller & J. Stevens, 1990. An analysis of the effects of spall on regional and teleseismic waveforms using two-dimensional numerical modeling of underground explosions, Air Force Geophysics Lab, **Report GL-TR-90-0126,** ADA226921

Baumgardt, D. & G. Young, 1990. Regional seismic waveform discriminants and case-based event identification using regional arrays, **Bull. Seis. Soc. Am., 80B,** 1874-1892.

Chael, E. P., 1988. Spectral discrimination of NTS explosions and earthquakes in the Southwestern United States using high-frequency regional data, **Geophys. Res. Lett., 15,** 625-628.

Day, S. & K. McLaughlin, 1991. Seismic source representation for spall, **Bull. Seism. Soc. Am., 81,** 191-201.

Day, S.M., N. Rimer & J.T. Cherry, 1983. Surface waves from underground explosions with spall: analysis of elastic and nonlinear source models, **Bull. Seism. Soc. Am., 73,** 247-264.

Koch, K. & B. Stump, 1991. Wave propagation to far-regional distances in the Western United States, this report.

Min, G. & B.Stump, 1991. Determination of explosion source parameters and Q by non-linear inversion of near source data, **Seism.Res.Lett., 62,** 17.

Mueller, R A. & J.R.Murphy , 1971. Seismic characteristics of underground nuclear explosions, Part I. Seismic spectrum scaling, **Bull. Seism. Soc. Am., 61,** 1675-1692.

Patton, H.J., 1990. Characterization of spall from observed strong ground motions on Pahute Mesa, **Bull.Seism.Soc.Am., 80,** 1326-1345.

Pomeroy, P.W., W.J. Best & T.V. McEvilly, 1982. Test ban treaty verification and regional data - A review, **Bull. Seis. Soc. Am., 72 Part B,** S89-S129.

Sharpe, J.A.,1942. The production of elastic waves by explosion pressures; I.Theory and empirical field observations, **Geophysics, 7,** 144-154.

Stump, B.W. & L.R. Johnson,1984. Near-field source characterization of contained nuclear explosions in tuff, **Bull.Seism.Soc.Am., 74,** 1-26.

Stump, B.W., 1985. Constraints on explosive sources with spall from near-source waveforms, **Bull. Seism. Soc. Am. , 75,** 361-377.

Suteau-Henson, A. & T.C. Bache, 1988. Spectral characteristics of regional phases recorded at NORESS, **Bull. Seis. Soc. Am., 78,** 708-725

Taylor, S.R., M.D. Denny, E.S. Vergino & R.E. Glaser, 1988, Regional discrimination between NTS explosions and Western U. S. earthquakes, **Bull. Seis. Soc. Am., 78,** 1563-1579.

Taylor, S. & G. Randall, 1989. The effect of spall on regional seismograms, **Geophys. Res.Lett., 16,** 211-214.

Taylor, S.R., N.W.Sherman & M.D.Denny,1988. Spectral discrimination between NTS explosions and Western U.S. earthquakes at regional distances, **Bull. Seism. Soc. Am., 78,** 1563-1579.

von Seggern, D. & R.Blandford, 1972. Source time functions and spectra for underground nuclear explosions, **Geophys.J.R astr.Soc., 31,** 83-97.

## Figure Captions

Figure 1: Far-regional seismograms (broadband acceleration data) for the distance range 800-1500 km; records from explosions are marked by the ○ symbol.

Figure 2: Sonogram for an NTS explosion at a distance of 1468 km; (top) perspective view, (bottom) contour plot. Time and frequency axes have the same scale in both plots.

Figure 3: Sonogram for an earthquake in Southern California at a distance of 1504 km; same format as Fig.2.

Figure 4: P wave spectra from (a) earthquake and (b) explosion seismograms. A window of 80-150 sec has been used in order to include the complete P wave. Spectra are offset by a factor of 10 for display purposes.

Figure 5: Comparison of P wave spectra for explosions and earthquakes at a range of 1400-1500 km.

Figure 6: Source and emplacement model used for investigating source depth effects between 0 and 2 km.

Figure 7: Amplitude distance curves for (a) explosion and (b) spall sources in the distance range 200-1400 km.

Figure 8: Comparison of Pg and Lg amplitude distance curves for different source models.

Figure 9: Map of instrument setup for near source survey for (a) Misty Echo and (b) Mineral Quarry.

Figure 10: Near surface acceleration recording and corresponding velocity seismogram calculated by integration.

Figure 11: Peak vertical velocities versus slant range for Misty Echo and Mineral Quarry using both free-field and surface data.

Figure 12: Peak vertical velocities versus free surface range for free surface data. The plots were used to constrain escape velocity and spall dimension.

Figure 13: Dwell times for spall region data from Misty Echo and Mineral Quarry

Figure 14: Three component far-regional seismogram at Lajitas (LTX) from the NTS explosion Misty Echo; epicentral distance 1455 km.

Figure 15: Source time functions constrained by near-source observations; a von Seggern-Blandford model was adopted for the explosion source with B=5 and k=6, 9 and 12; for the spall source the model of Stump (1985) was used with dwell times ranging from 0.5-0.75 sec, and rise times from 0.375-0.75 sec.

Figure 16: Far-regional synthetic seismograms for the velocity model developed by Koch & Stump (1991) from an explosion source without overshoot.

Figure 17: Far-regional synthetic seismograms for a von Seggern-Blandford explosion source with k=6 and B=5.

Figure 18: Far regional seismograms for spall sources with different source parameters (dwell time, rise time) at a distance of 1400 km.

# NEAR SOURCE SPALL ESTIMATES

## MISTY ECHO

**Data**

$r_{max}$ = 1000 m

$d_{max}$ = 200 m (1/2 dob)

$M_{ass}$ = 6.9 x $10^{11}$ kg

$V_s$ = 2.5 m/s (3.7)

$T_D$ = 0.75 s (0.5)

$R_{ise}$ $T_{ime}$ = 0.5 s

**Patton Scaling (16.9 ktons)**

$r_{max}$ = 991 m

$d_{max}$ = 174 m

$M_{ass}$ = 6.4 x $10^{11}$ kg

Total Momentum: 1.6-2.6 x $10^{12}$ Nt-s

## MINERAL QUARRY

**Data**

$r_{max}$ = 500 m

$d_{max}$ = 190 m (1/2 dob)

$M_{ass}$ = 1.7 x $10^{11}$ kg

$V_s$ = 1.7 m/s (1.9)

$T_D$ = 0.375 s (3.5)

$R_{ise}$ $T_{ime}$ = 0.25 s

**Patton Scaling (6.1 ktons)**

$r_{max}$ = 760 m

$d_{max}$ = 135 m

$M_{ass}$ = 2.9 x $10^{11}$ kg

Total Momentum: 2.9-5.5 x $10^{12}$ Nt-s

TABLE I

56

Vertical Component [BB]

836 km/254
923 km/289
1193 km/286
1336 km/295
1436 km/309
1468 km/310
1504 km/293
1896 km/301

Time (sec)

FIGURE 1

57
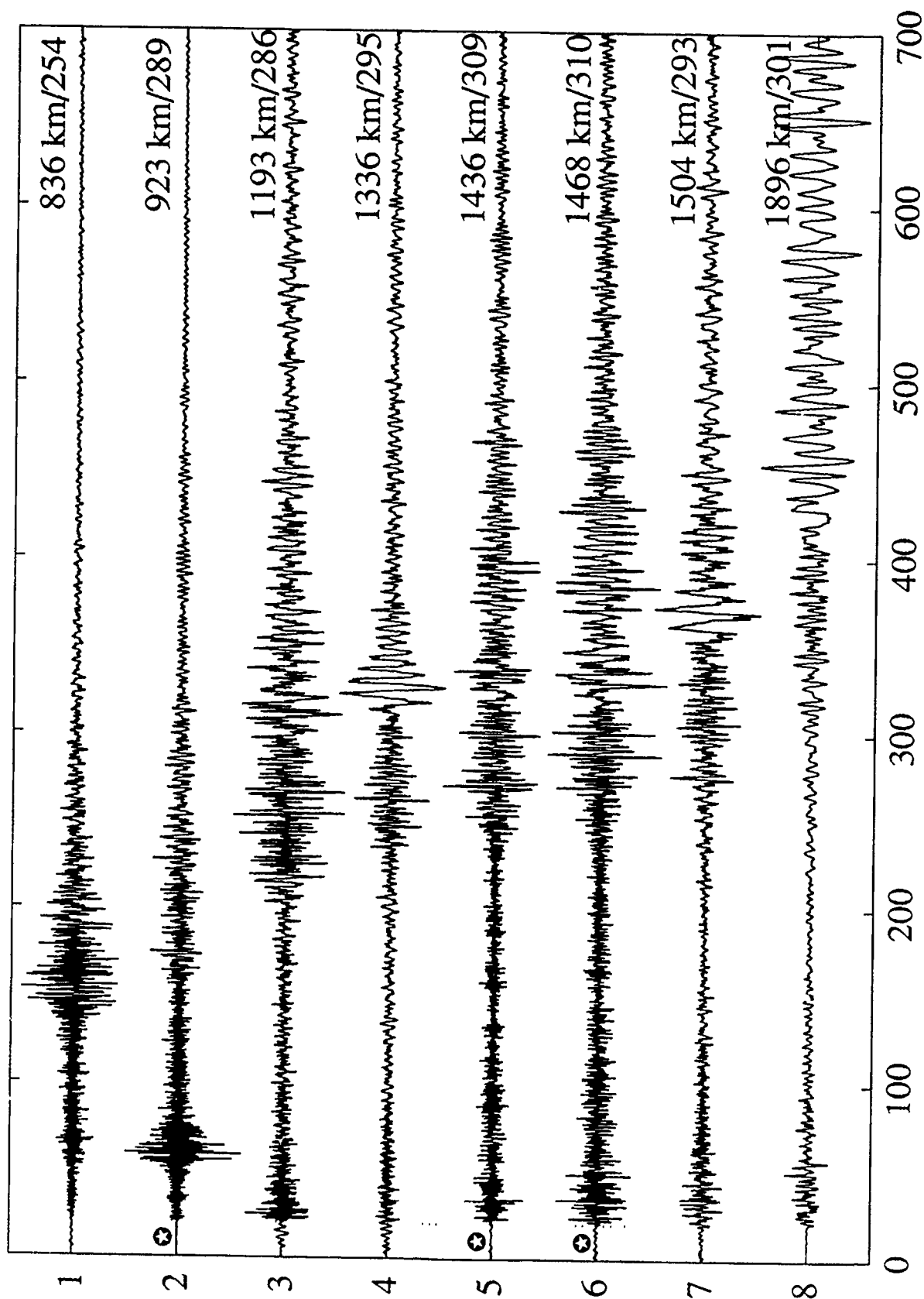
Event # 6 [Component=Z-BB]



FIGURE 2

58

Event # 7 [Component=Z-BB]



FIGURE 3

P-wave spectra
Earthquakes

Frequency (Hz)

FIGURE 4a

Amplitude

1896 km

1504 km

1336 km

1193 km

836 km

60

P-wave spectra
Explosions

1468 km

1436 km

923 km

Amplitude

Frequency (Hz)

FIGURE 4b

19

Frequency (Hz)

**FIGURE 5**

**P-wave spectra**

**⊃ Earthquakes**

**✪ Explosions**

1468 km

1436 km

1504 km

1336 km

Amplitude

62

Source model
for explosion

$$M = M_0 * \begin{pmatrix} 1 & 0 & 0 \\ 0 & 1 & 0 \\ 0 & 0 & 1 \end{pmatrix}$$

Source model
for spall used

$$M = M_0 * \begin{pmatrix} a & 0 & 0 \\ 0 & a & 0 \\ 0 & 0 & b \end{pmatrix}$$

$a = 0; b = 1$

α = 3.55
β = 2.09
ρ = 2.5

α = 6.00
β = 3.55
ρ = 3.3

FIGURE 6

63
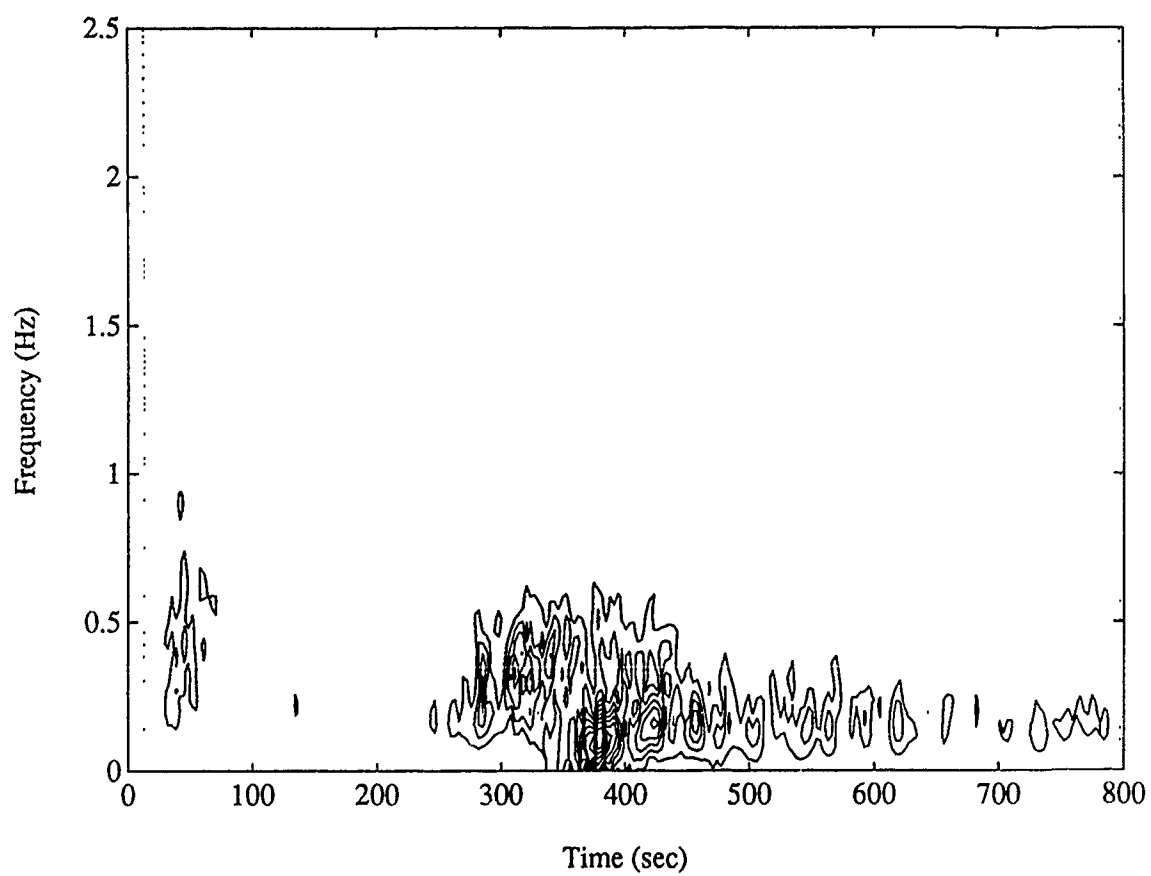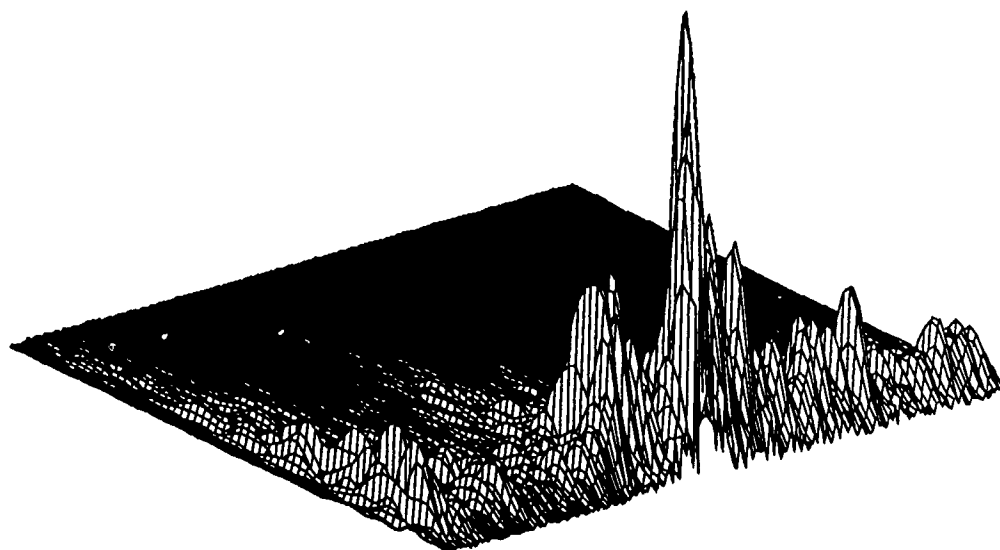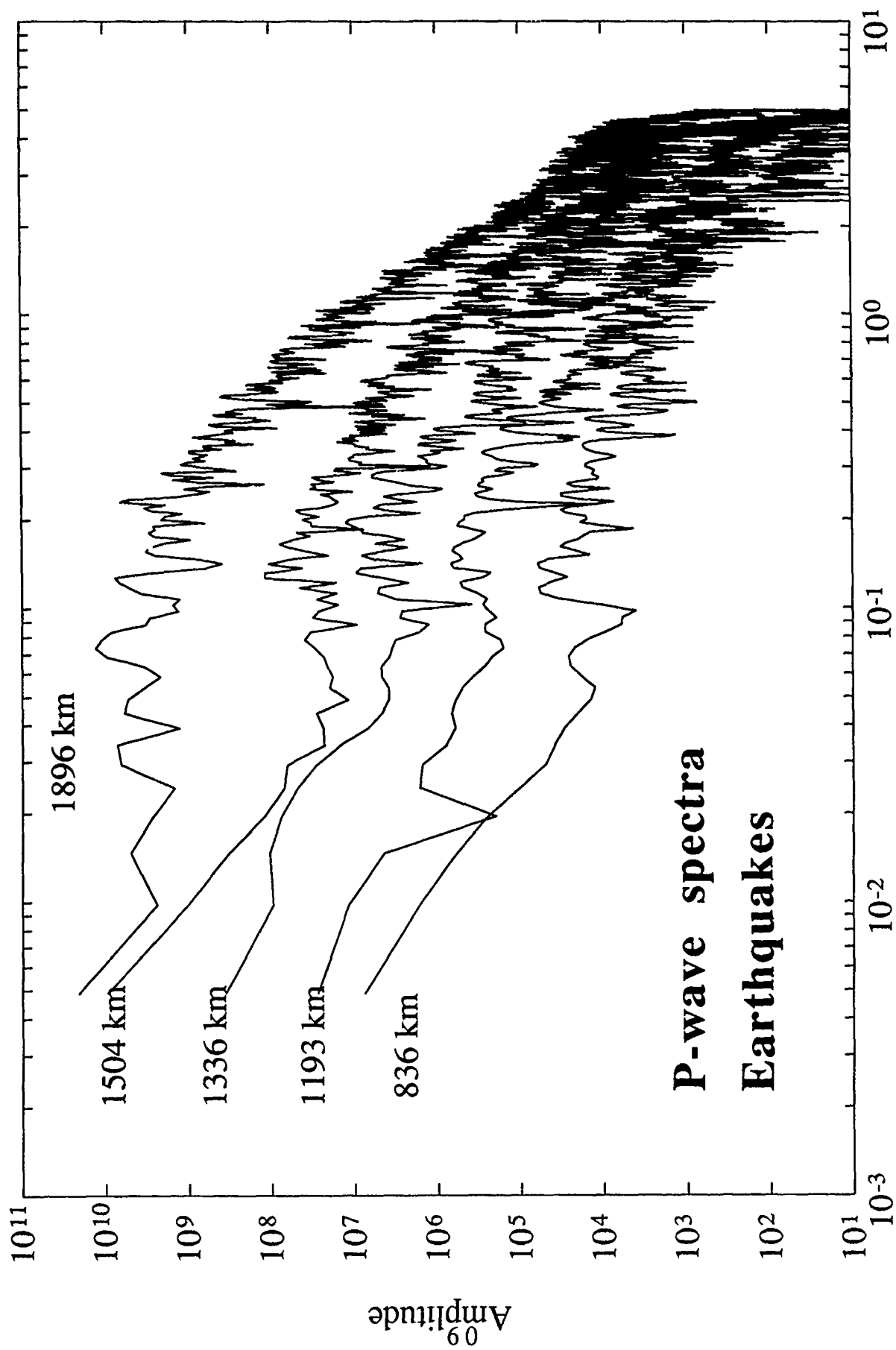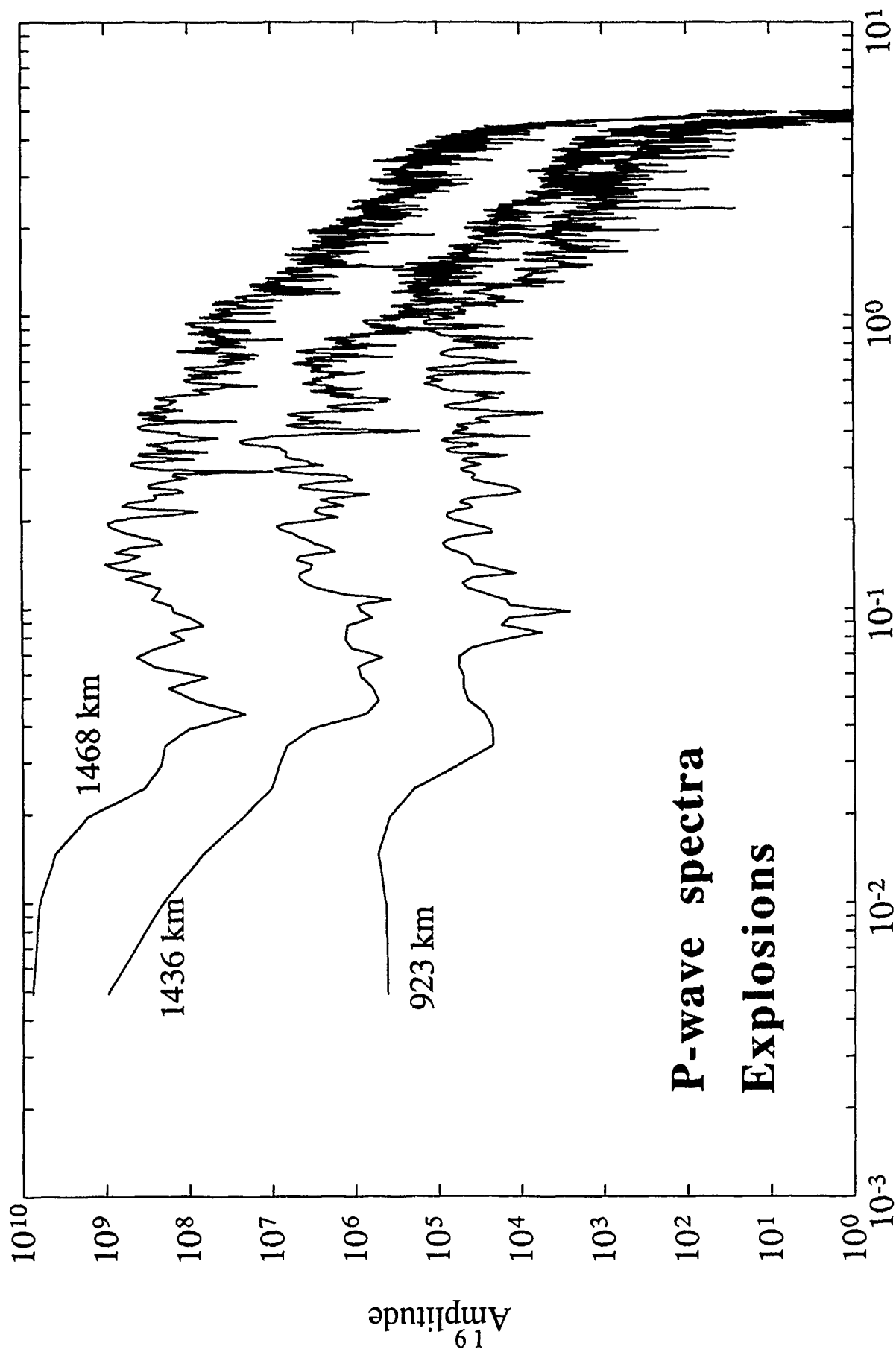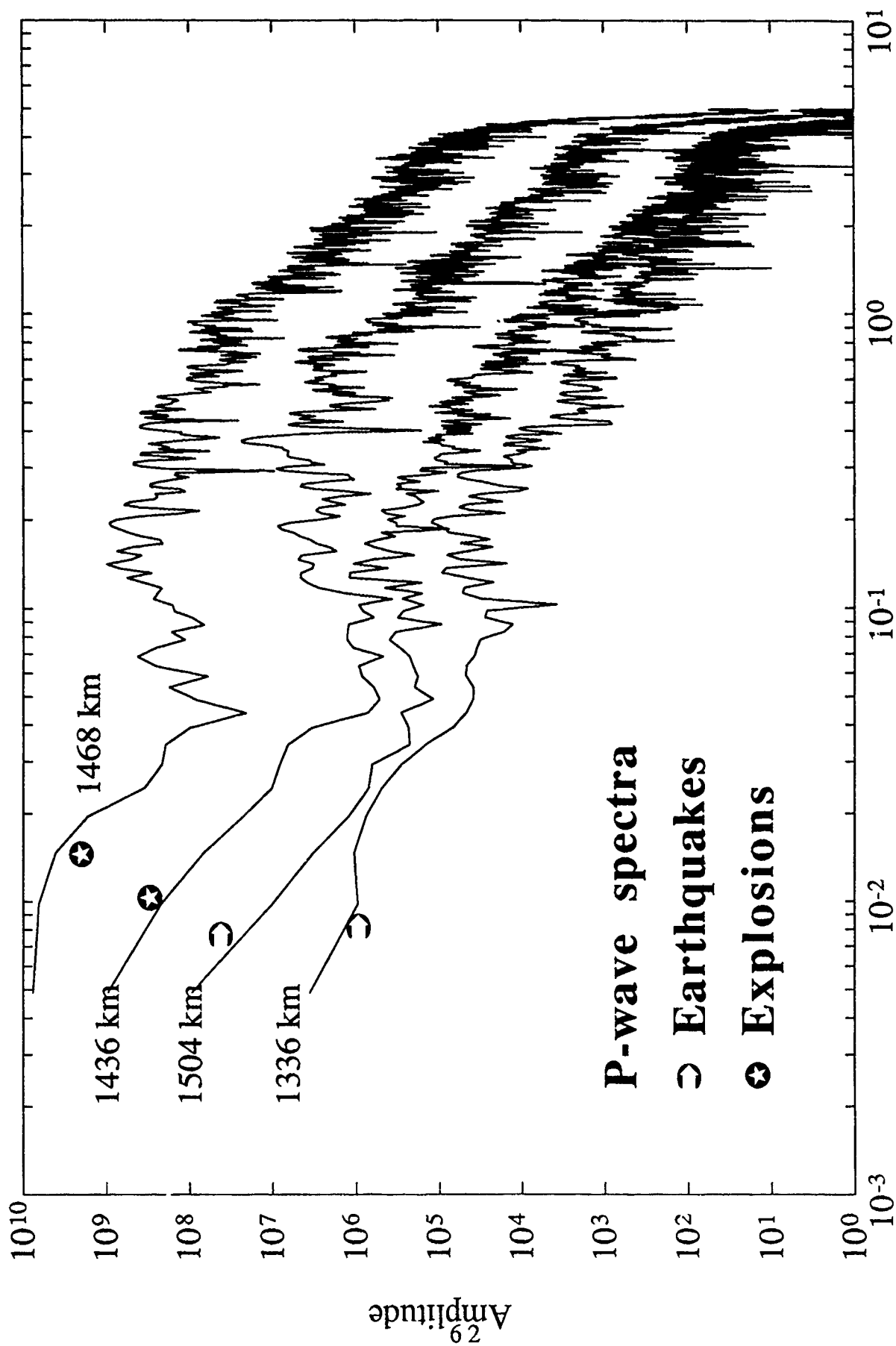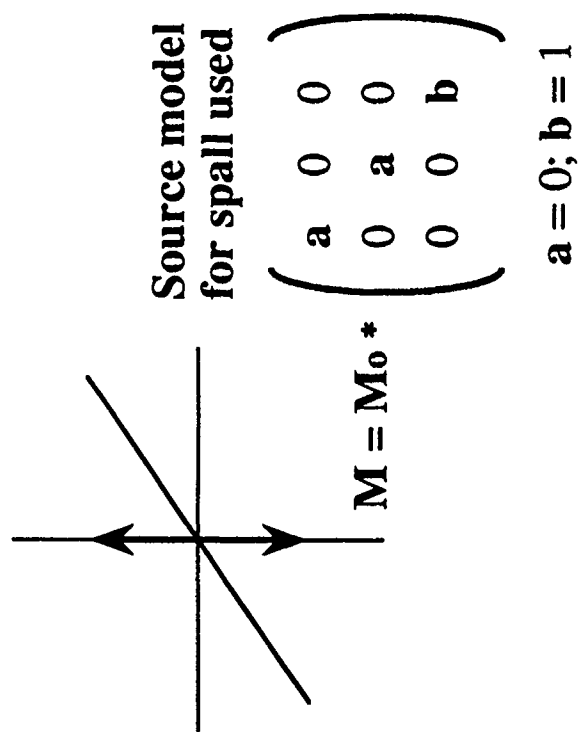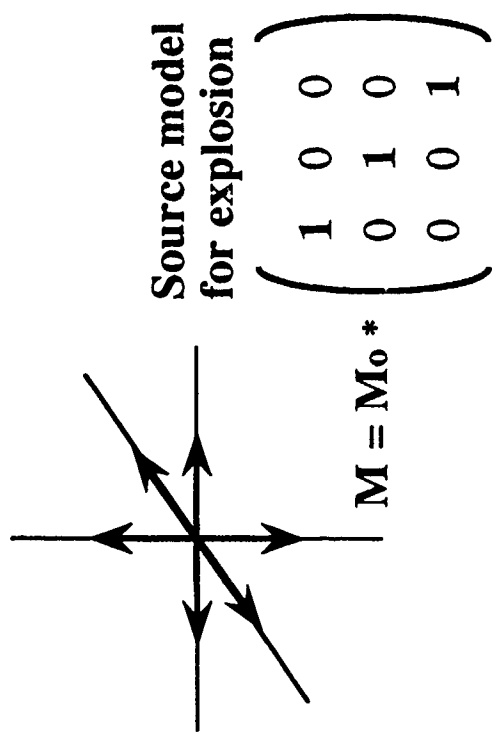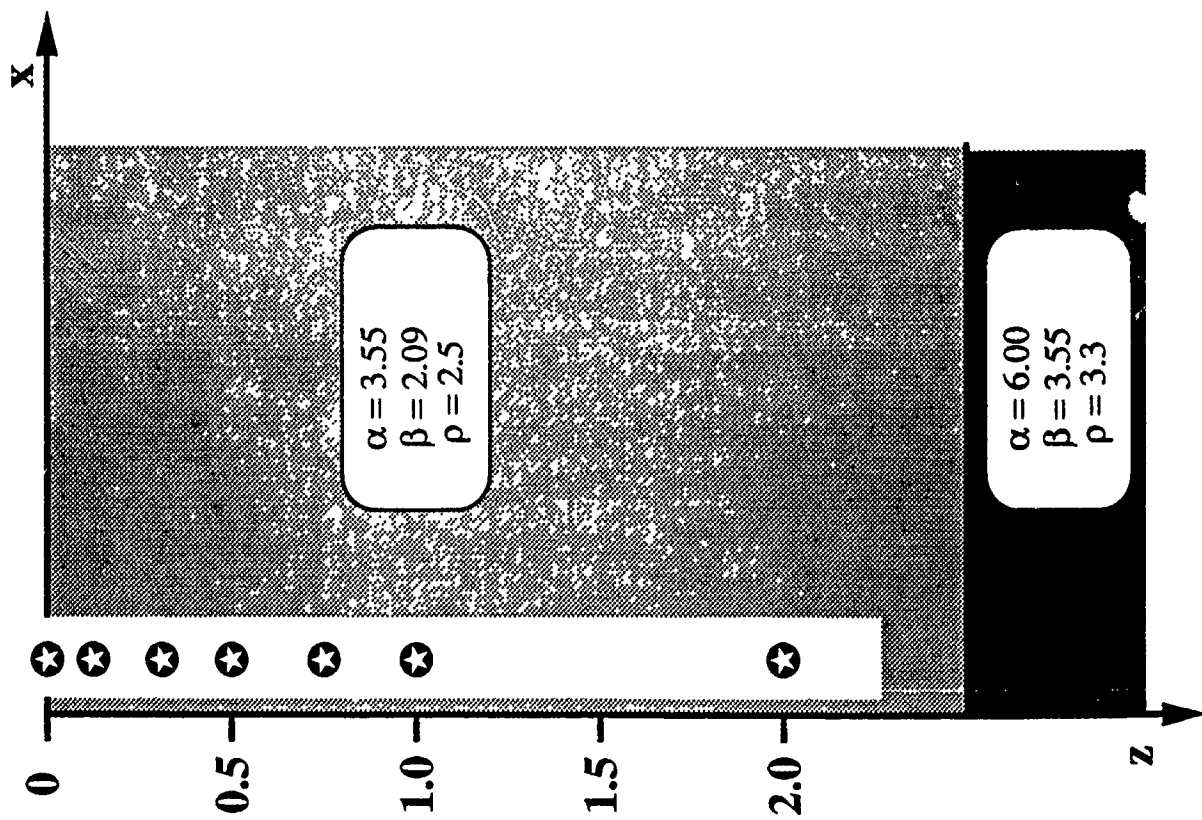
# Synthetic Seismograms * Explosion Source
## Vertical Component (0.05 - 2 Hz)



FIGURE 7a

Distance (km)

max. Amplitudes

LR - 0 m
Sg - 0 m
Pg - 0 m
Pn/Pm - 0 m
LR - 100 m
Sg - 100 m
Pg - 100 m
Pn/Pm - 100 m
LR - 300 m
Sg - 300 m
Pg - 300 m
Pn/Pm - 300 m
LR - 500 m
Sg - 500 m
Pg - 500 m
Pn/Pm - 500 m
LR - 750 m
Sg - 750 m
Pg - 750 m
Pn/Pm - 750 m
LR - 1 km
Sg - 1 km
Pg - 1 km
Pn/Pm - 1 km
LR - 2 km
Sg - 2 km
Pg - 2 km
Pn/Pm - 2 km

6 4
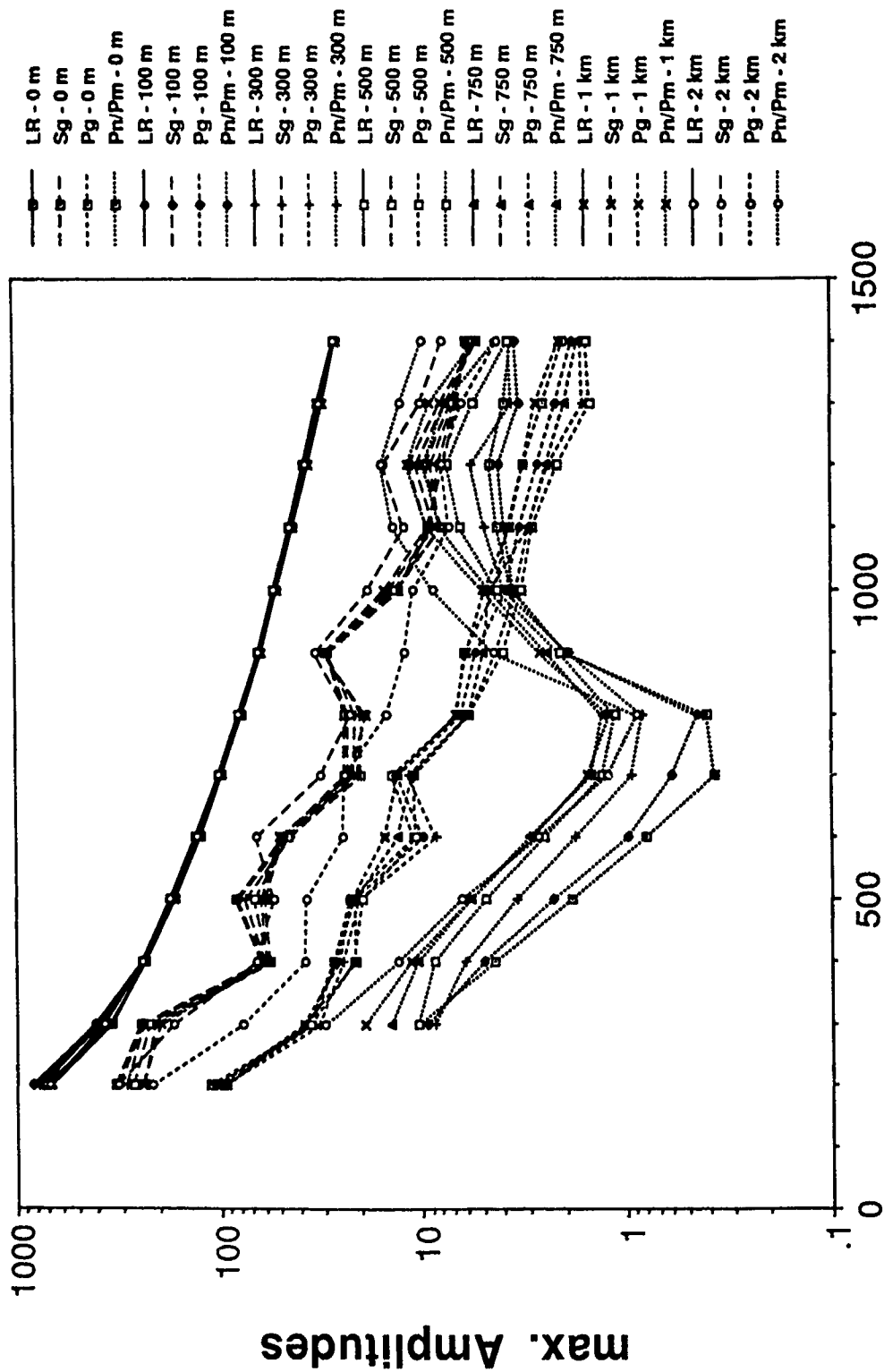
# Synthetic Seismograms * Spall Source
## Vertical Component (0.05 - 2 Hz)



**FIGURE 7b**

Legend:
- LR - 0 m
- Sg - 0 m
- Pg - 0 m
- Pn/Pm - 0 m
- LR - 100 m
- Sg - 100 m
- Pg - 100 m
- Pn/Pm - 100 m
- LR - 300 m
- Sg - 300 m
- Pg - 300 m
- Pn/Pm - 300 m
- LR - 500 m
- Sg - 500 m
- Pg - 500 m
- Pn/Pm - 500 m
- LR - 750 m
- Sg - 750 m
- Pg - 750 m
- Pn/Pm - 750 m
- LR - 1 km
- Sg - 1 km
- Pg - 1 km
- Pn/Pm - 1 km
- LR - 2 km
- Sg - 2 km
- Pg - 2 km
- Pn/Pm - 2 km

Distance (km)

max. Amplitudes

65
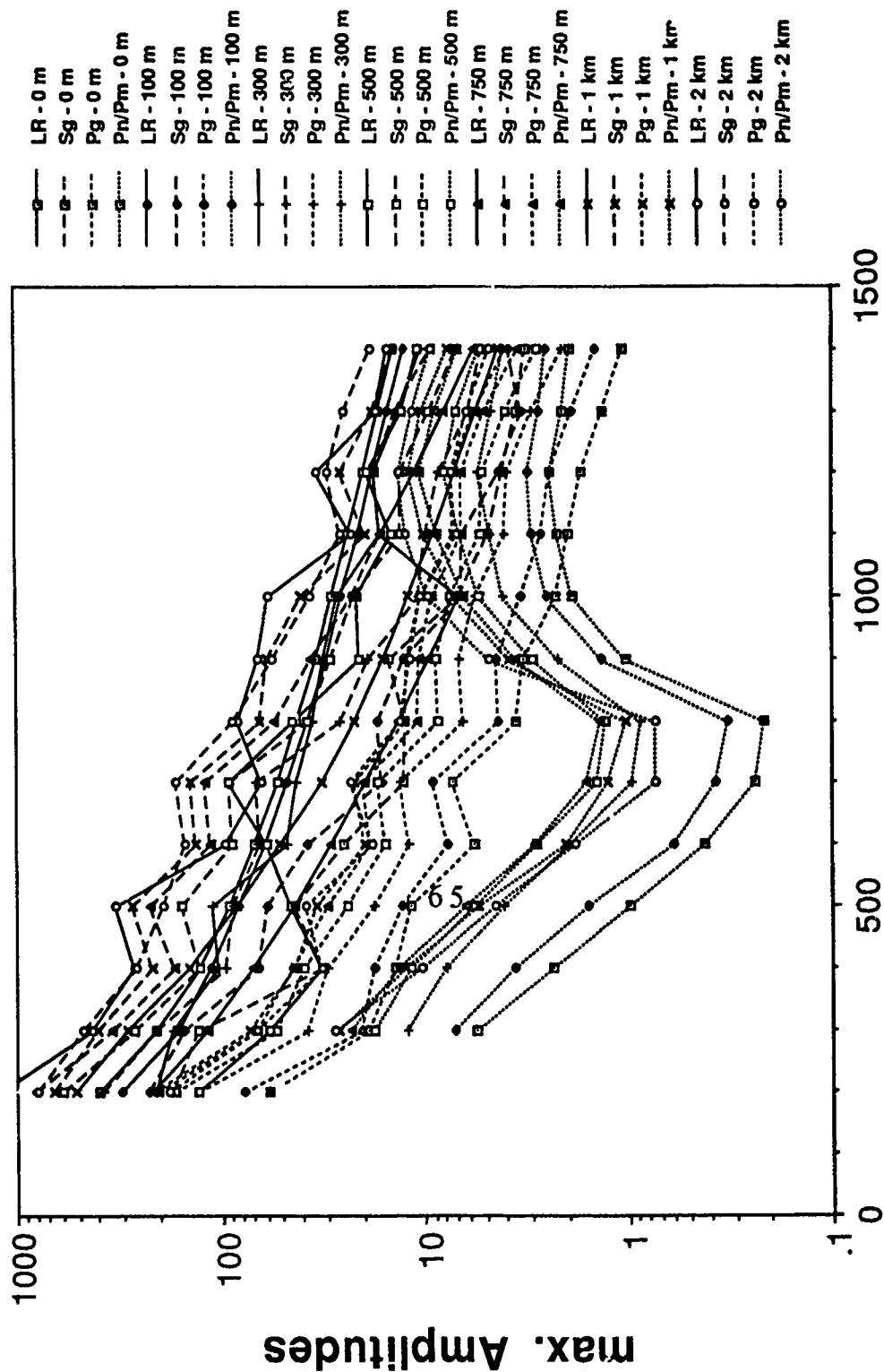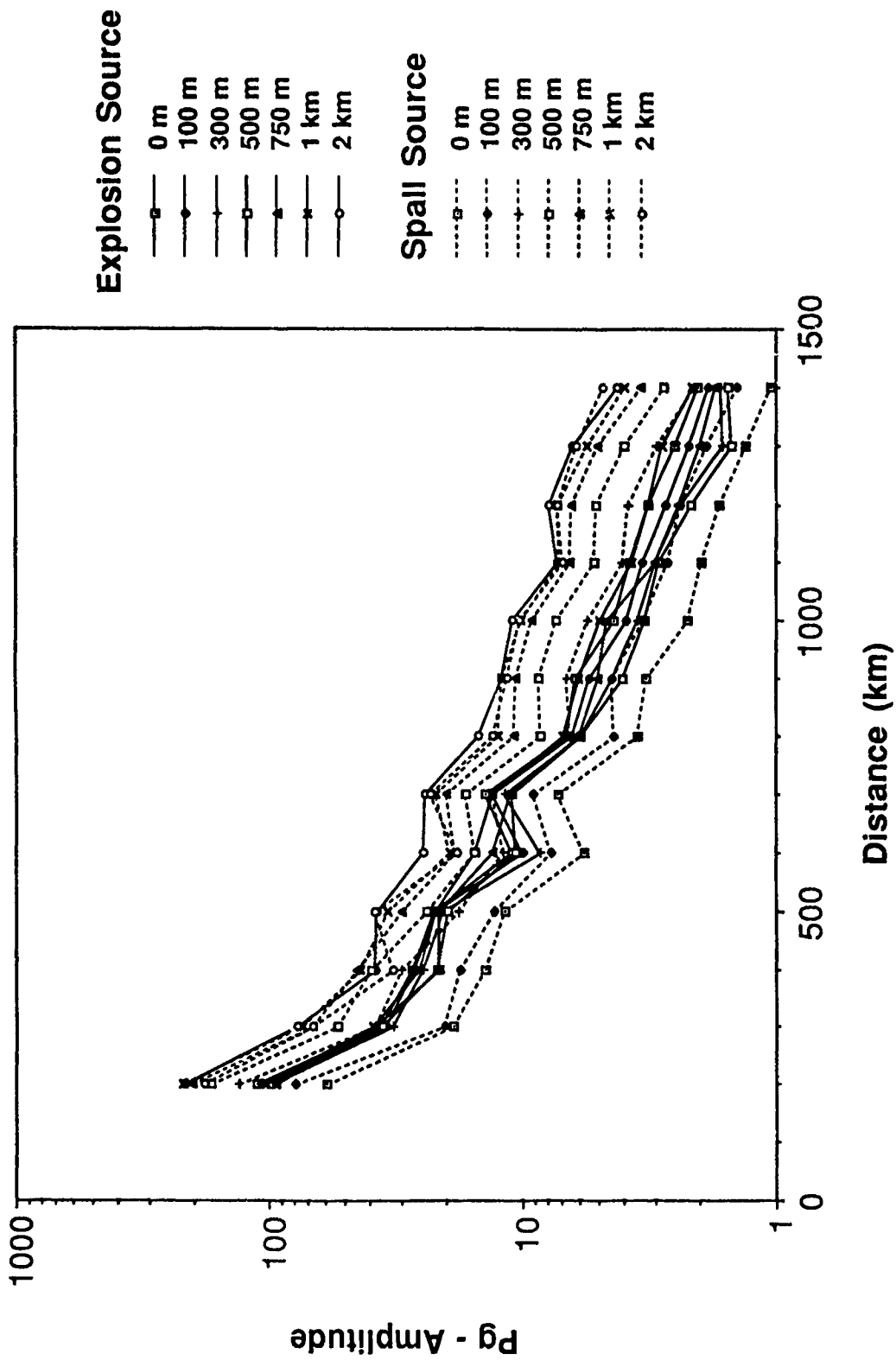
# Comparison of Amplitudes for Explosion and Spall Source



FIGURE 8a

66

# Comparison of Amplitudes for Explosion and Spall Source

**Explosion Source**

0 m
100 m
300 m
500 m
750 m
1 km
2 km

**Spall Source**

0 m
100 m
300 m
500 m
750 m
1 km
2 km

Lg - Amplitude

Distance (km)

FIGURE 8b

67

MISTY ECHO SEISMIC

2500'

Mesa Edge
tunnel LANL
surface LANL
surface AFWL, SMU
spall

FIGURE 9a

68
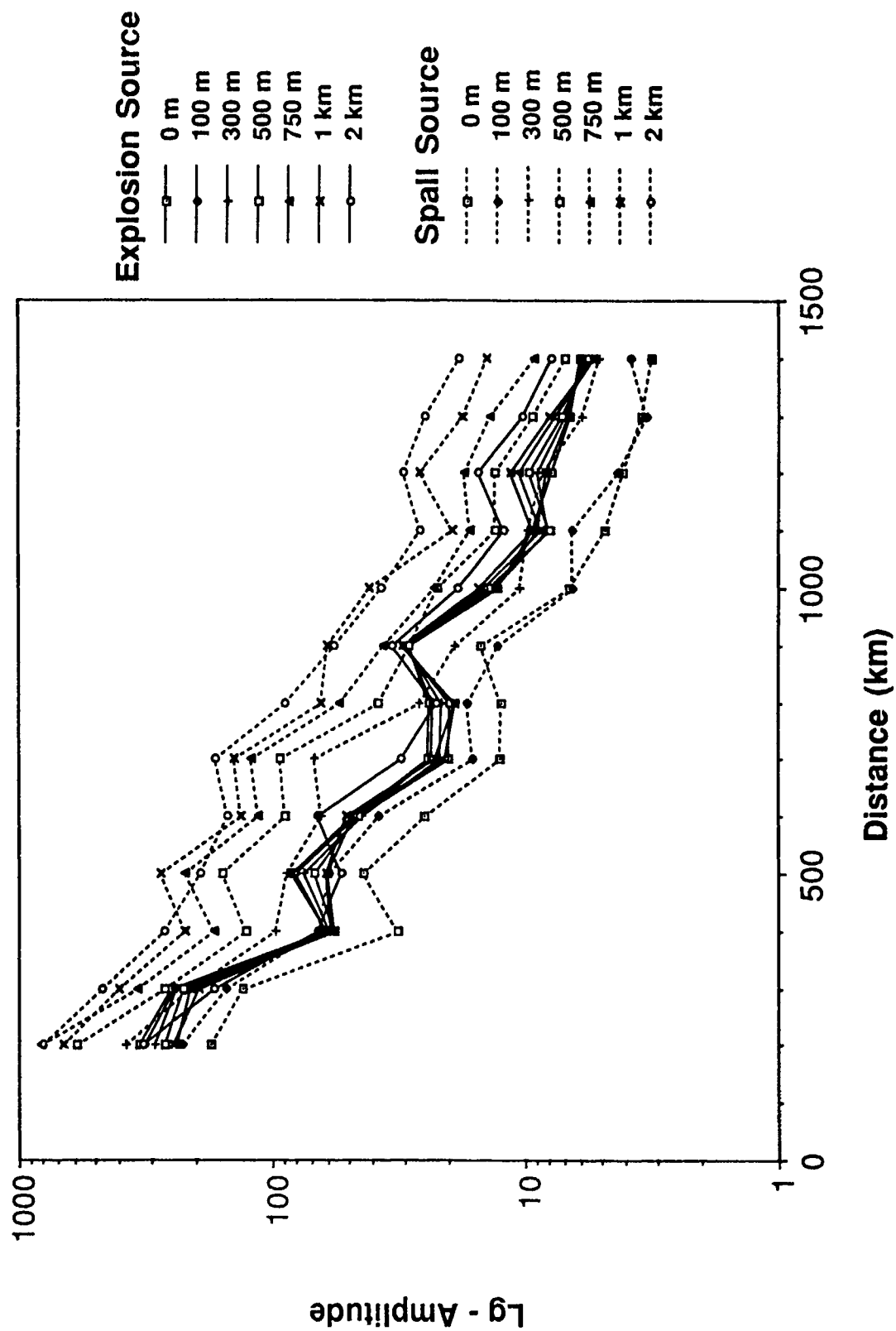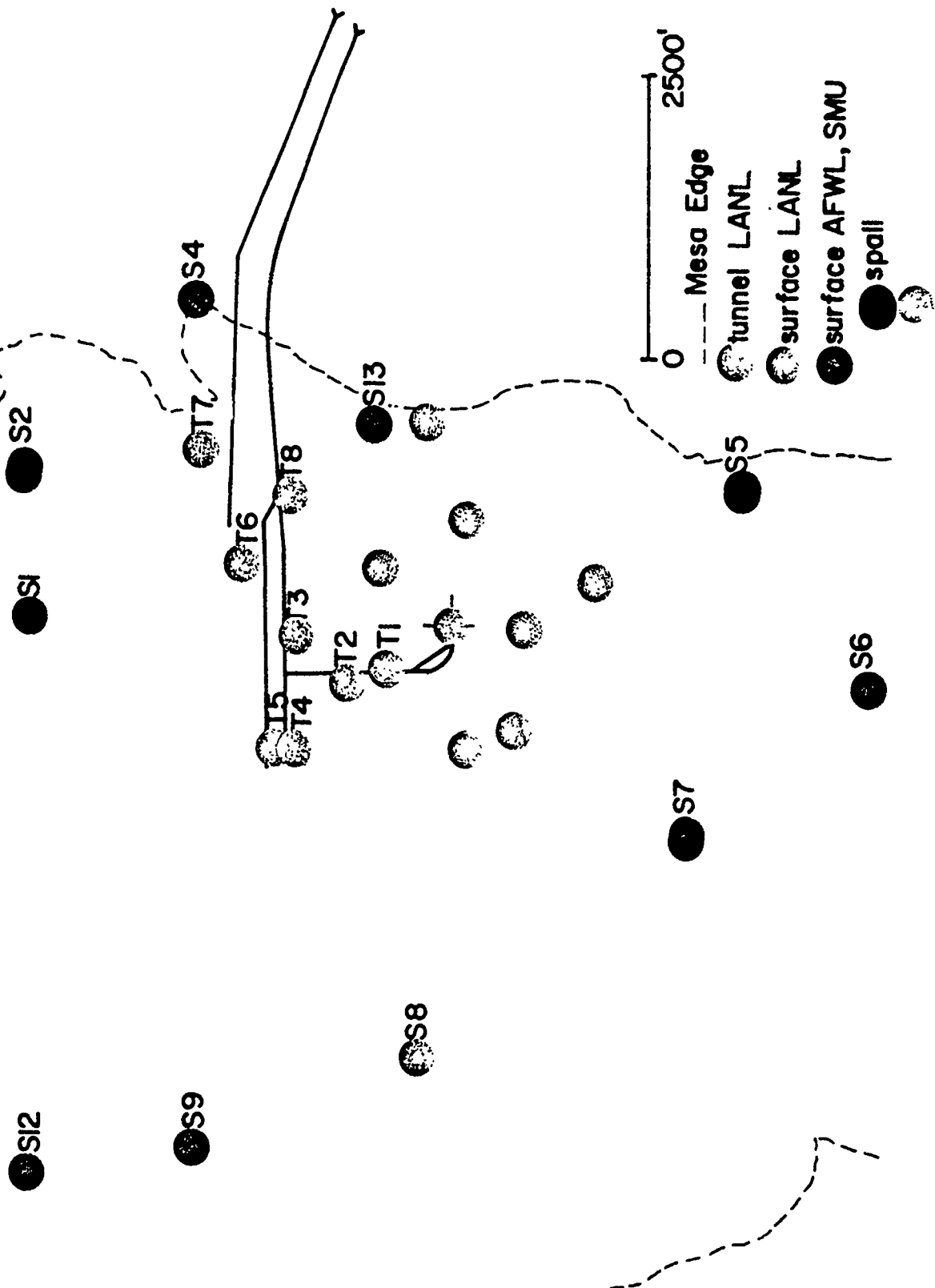
# MINERAL QUARRY FREE-FIELD
# AND FREE SURFACE EXPERIMENT

FIGURE 9b

GR5Z



GR5Zv



FIGURE 10

70

MQ/ME VERTICAL VEL (m/s)

Vertical Vel (m/s)

Slant Range (m)
FIGURE 11

Legend:
- MQ FF Vertical Vel (m/s)
- ME FF Vertical Vel (m/s)
- ME Spall Vertical Vel (m/s)
- MQ Spall Vertical Vel (m/s)
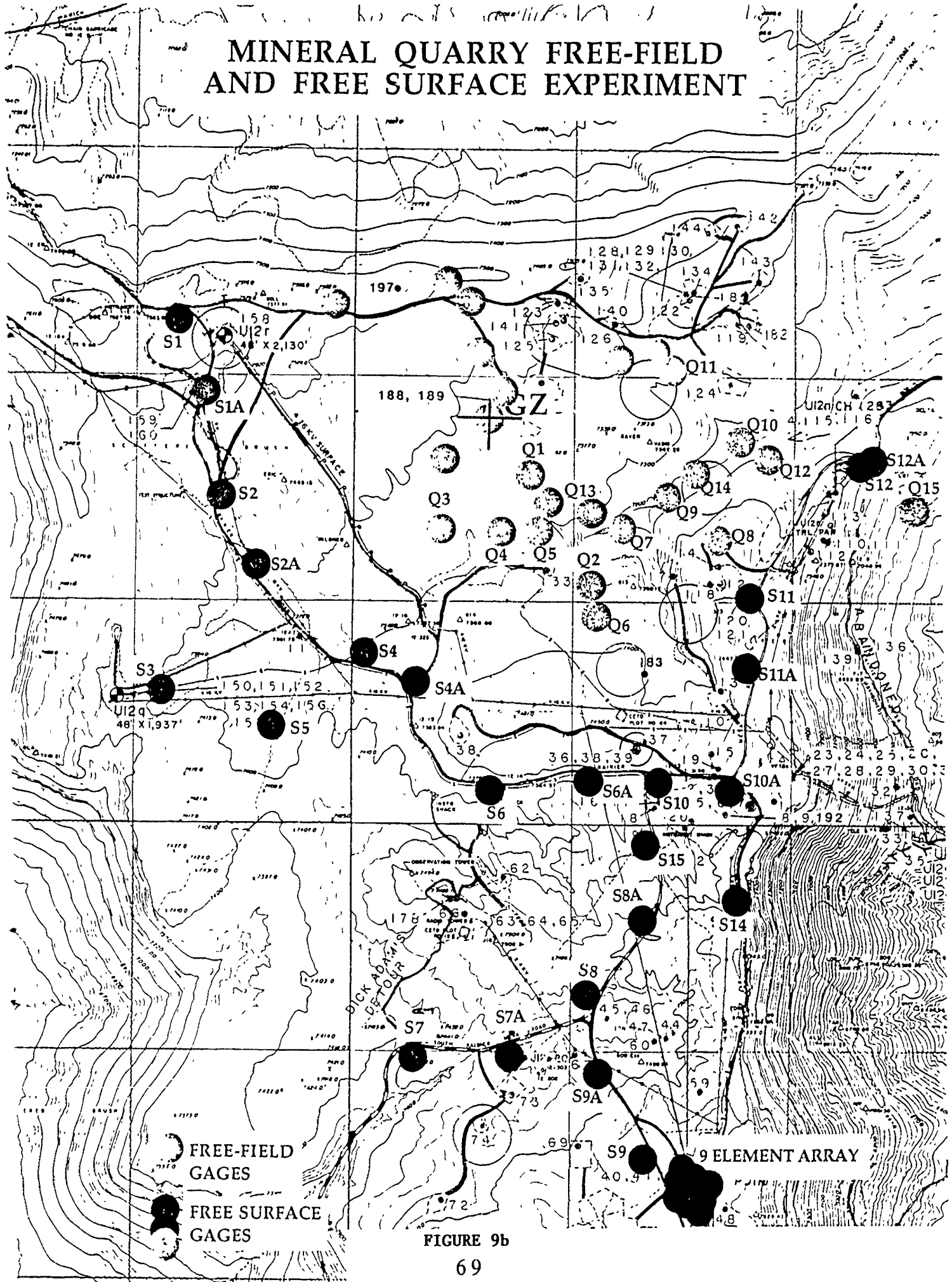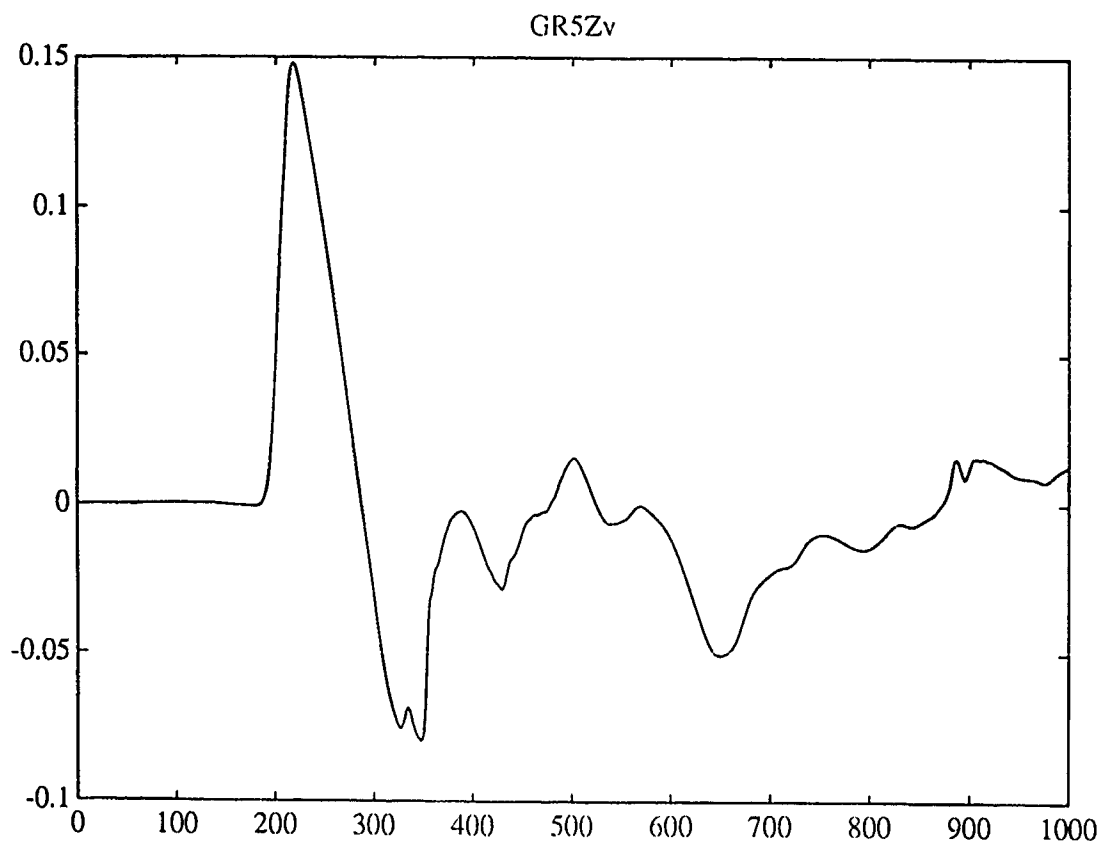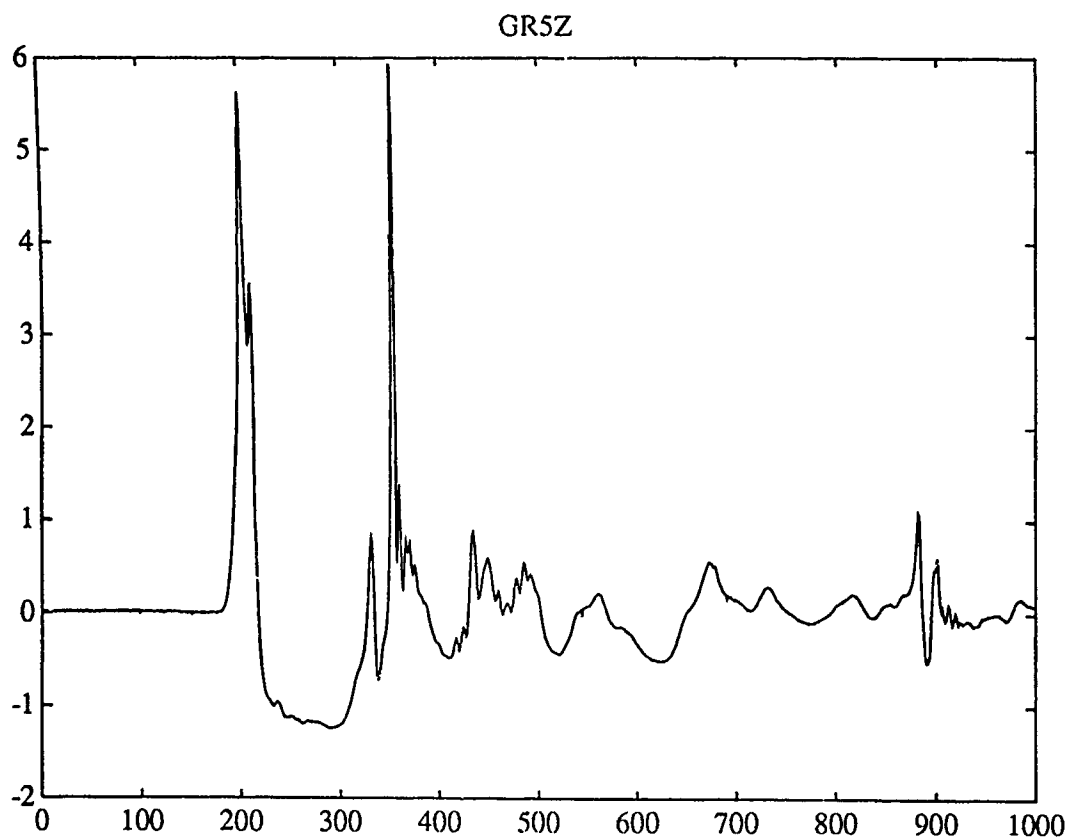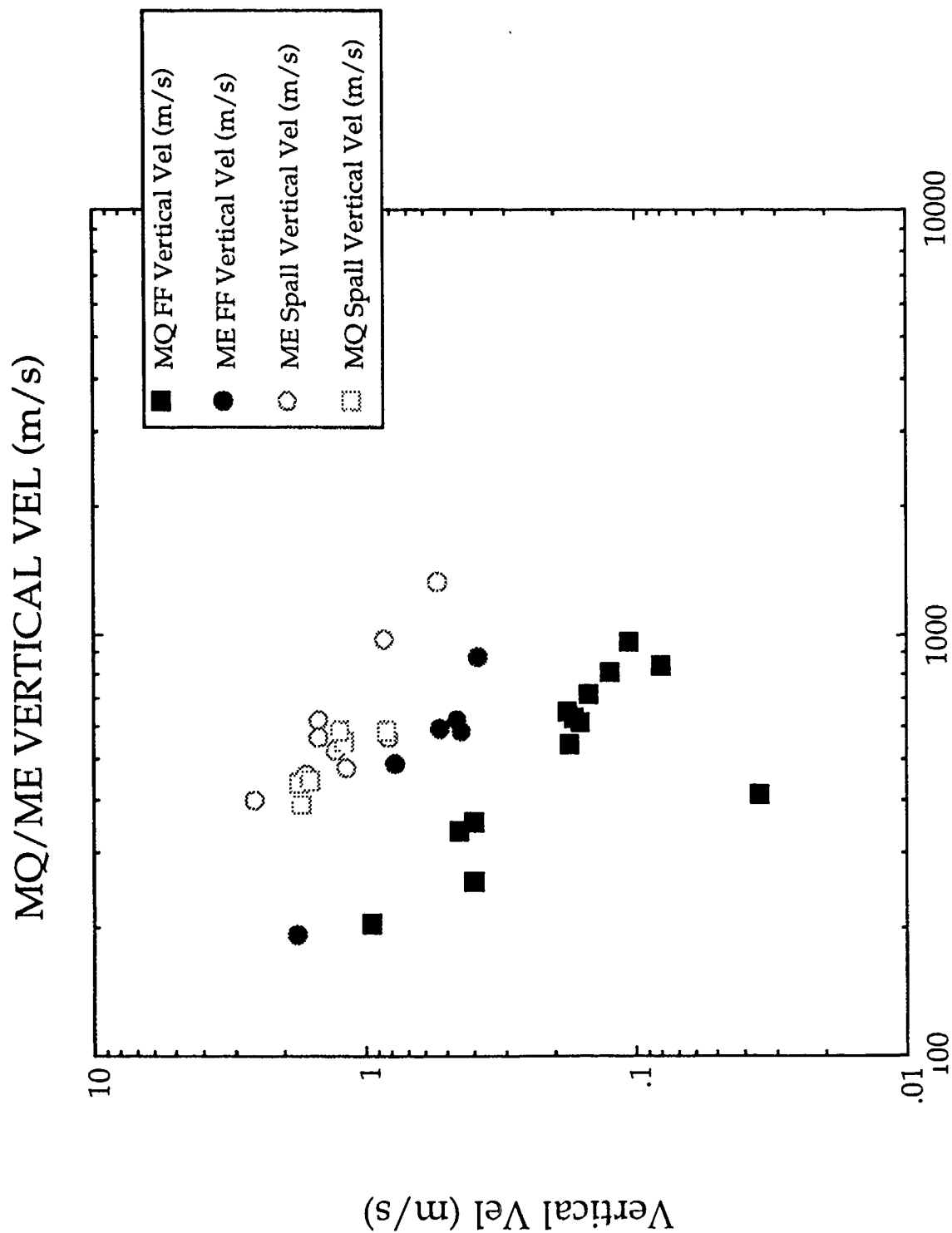
7 1
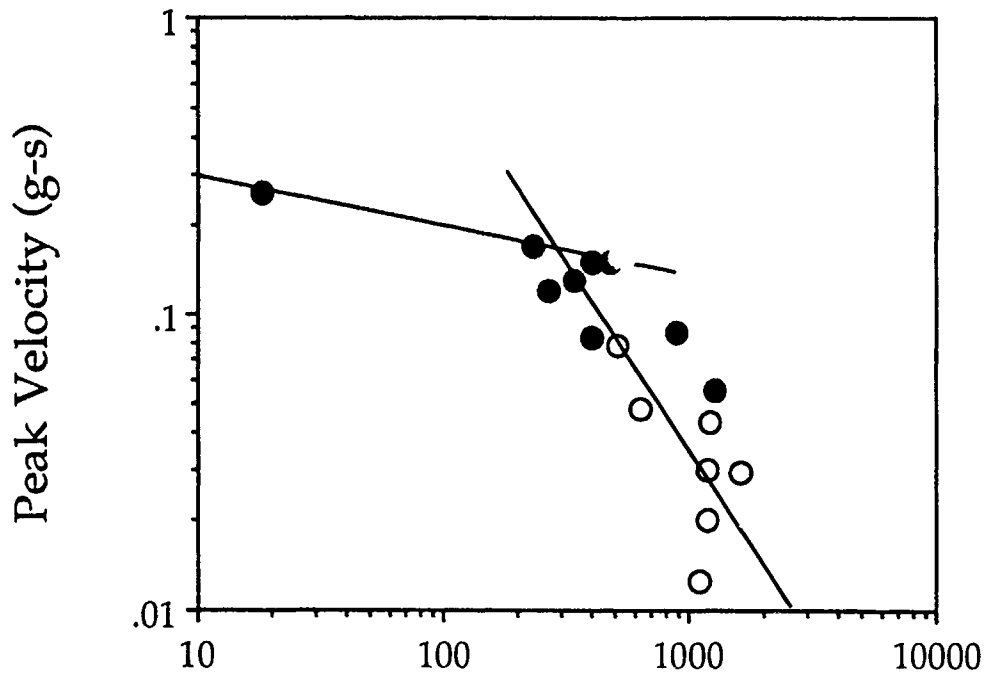
# MISTY ECHO SPALL



# MINERAL QUARRY SPALL



Free Surface Range (m)
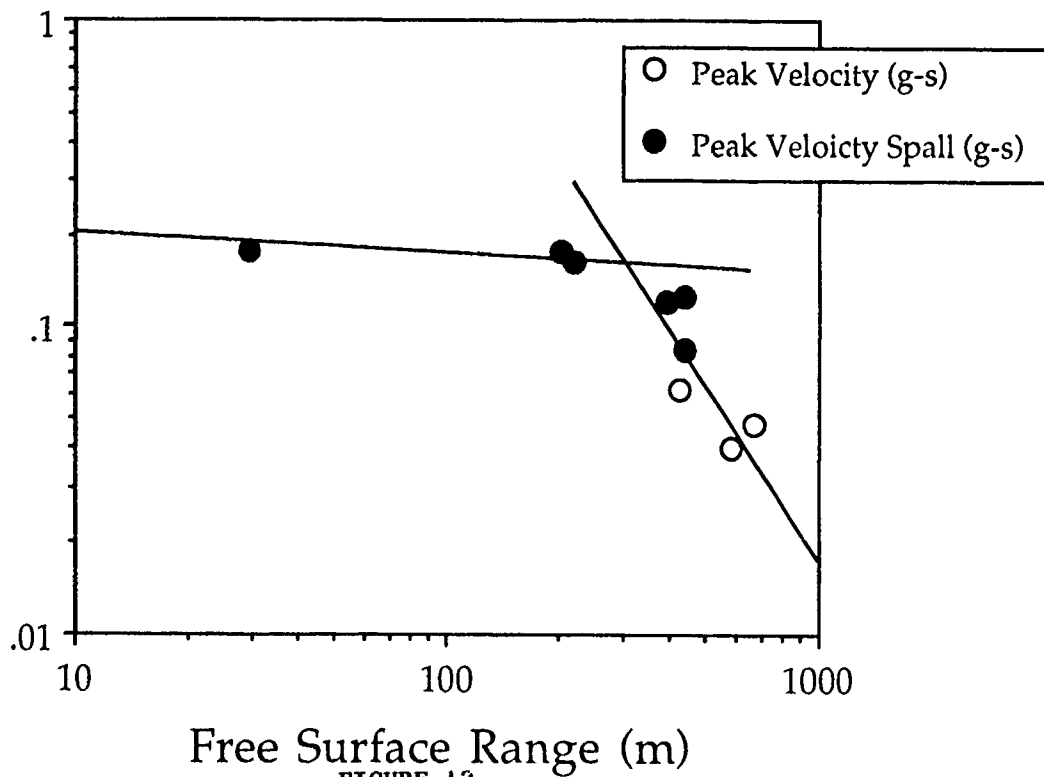
FIGURE 12

72

# MISTY ECHO SPALL ZONE
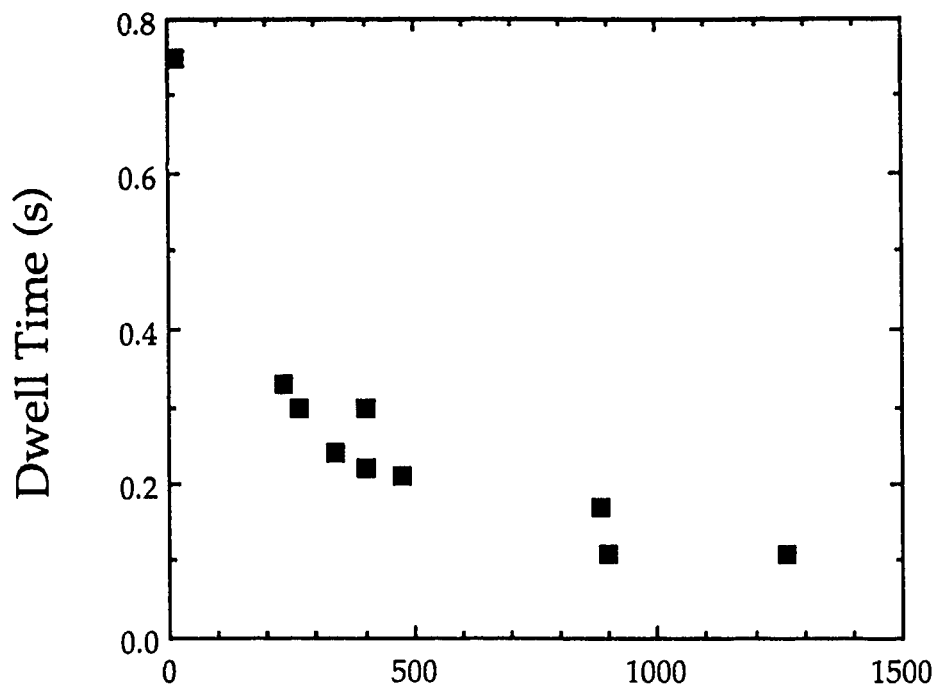


# MINERAL QUARRY SPALL ZONE



Free Surface Range (m)
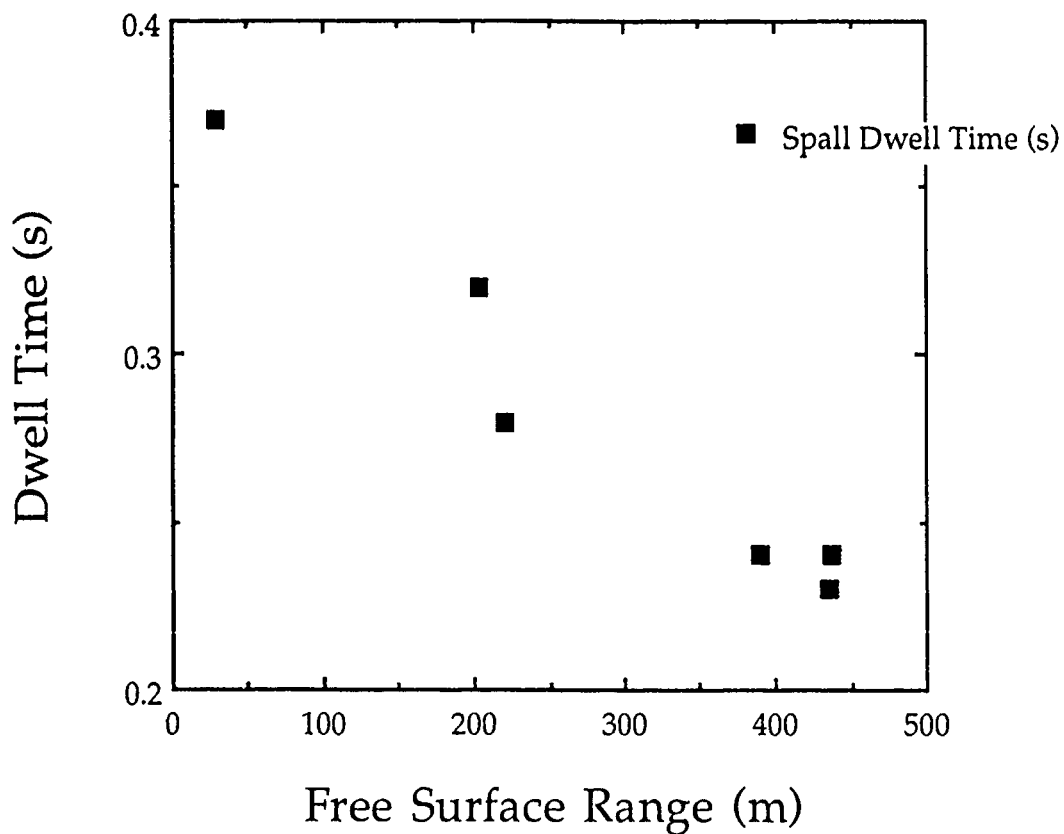
FIGURE 13

Station LTX (Epic. Distance 1455 km)



Z

NS

EW

Dec 10, 1988 20:33:11.810

Time (sec)
FIGURE 14

0    100    200    300    400    500    600
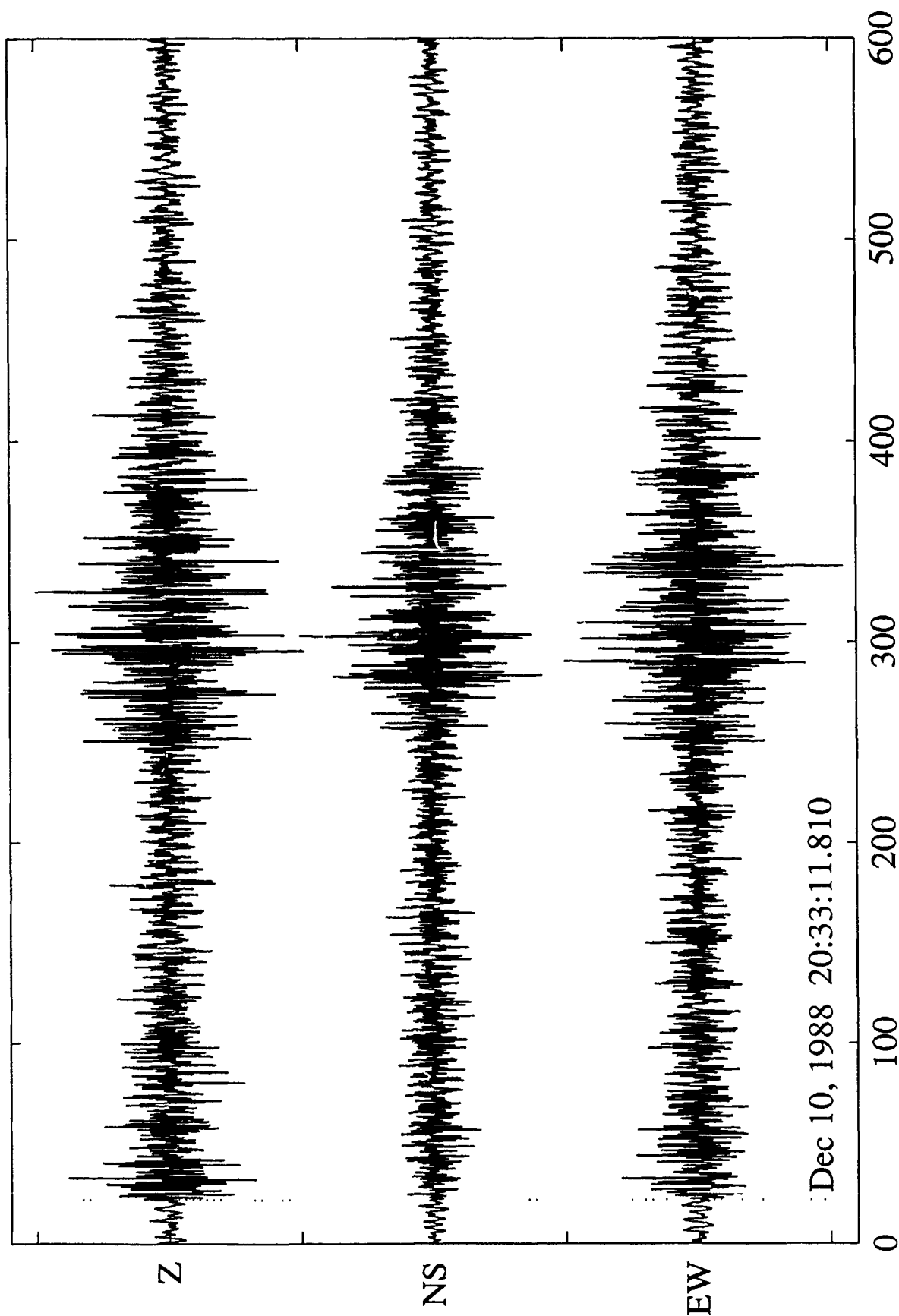
74

# MISTY ECHO



Von Seggern-Blandford source function
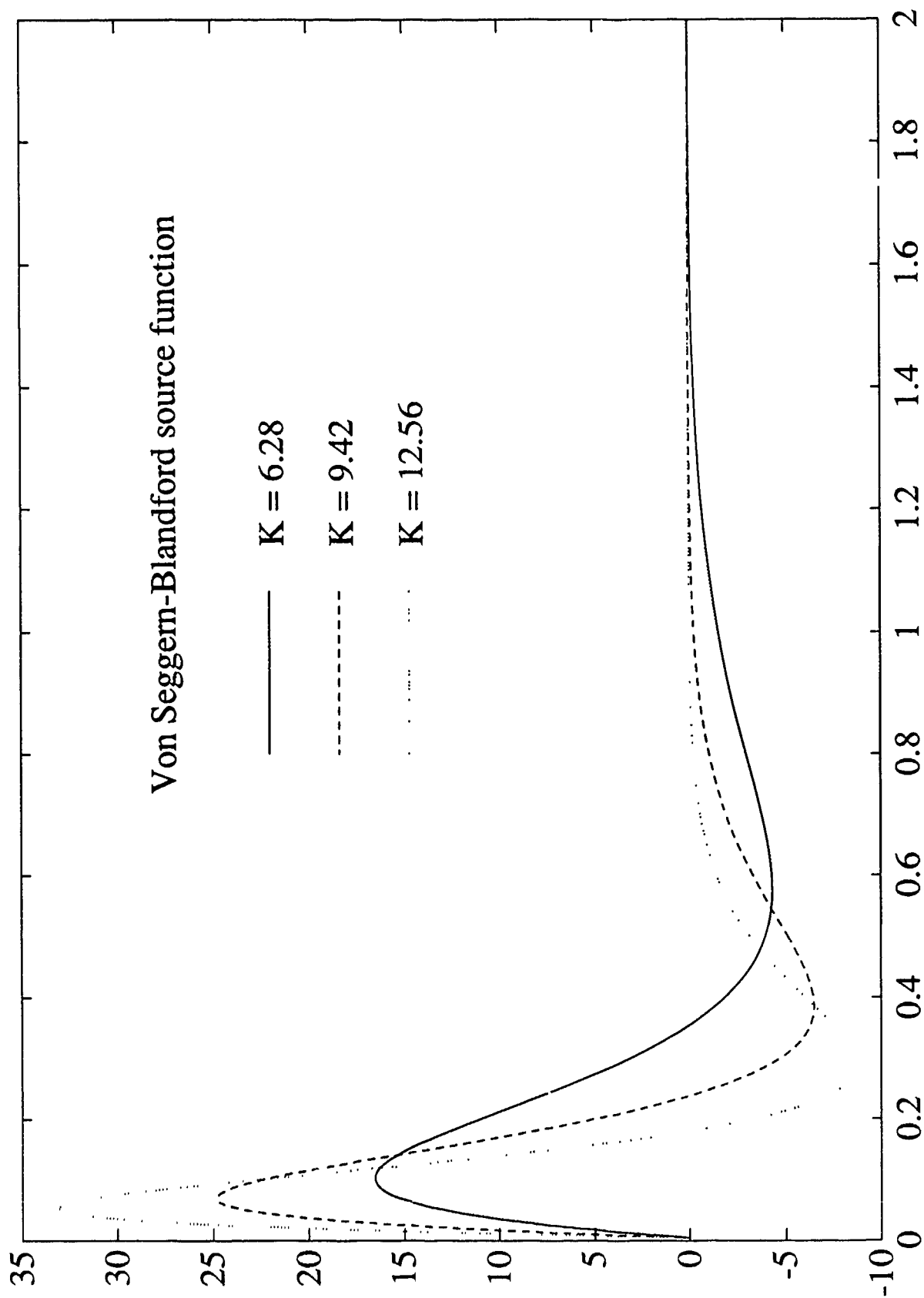
| | K = 6.28 |
| --- | --- |
| | K = 9.42 |
| | K = 12.56 |

Time (sec)
FIGURE 15a

75

MISTY ECHO



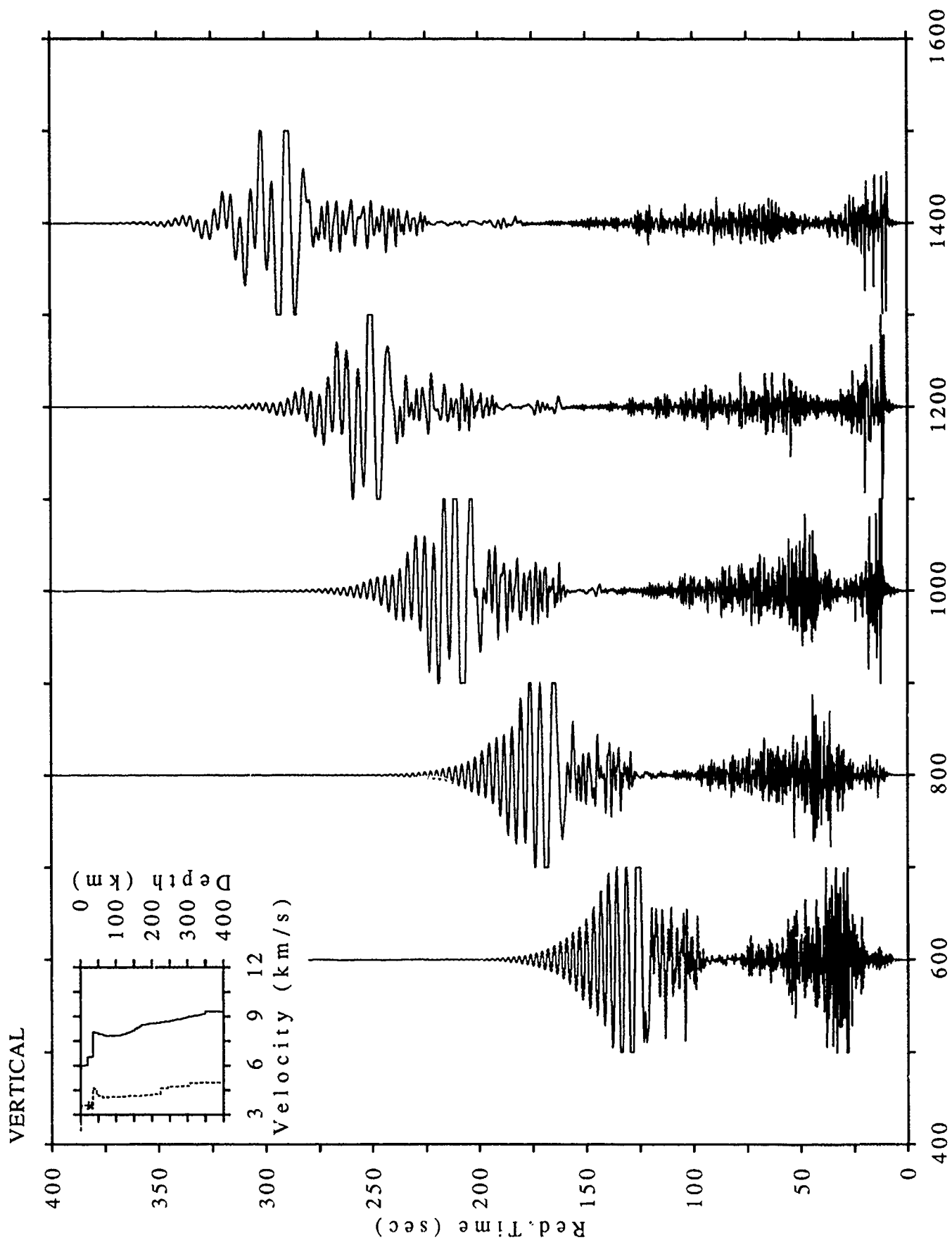| | Spall source function | |
|---|---|---|
| | dwell time | rise time |
| ⋯⋯ | 0.50 | 0.50 |
| - - - | 0.75 | 0.75 |
| —— | 0.50 | 0.375 |

Time (sec)
FIGURE 15b

Acceleration (g)

76

VERTICAL
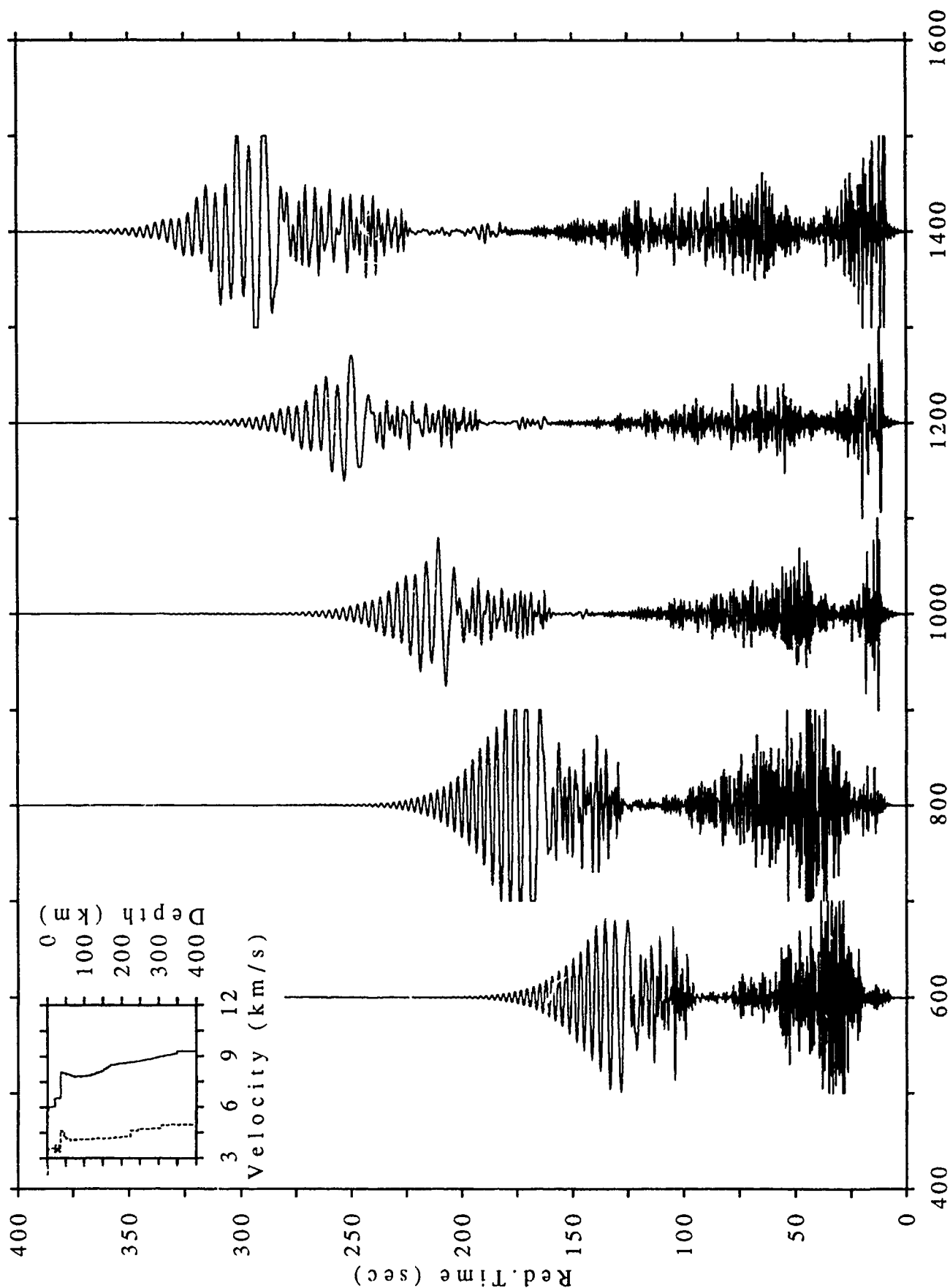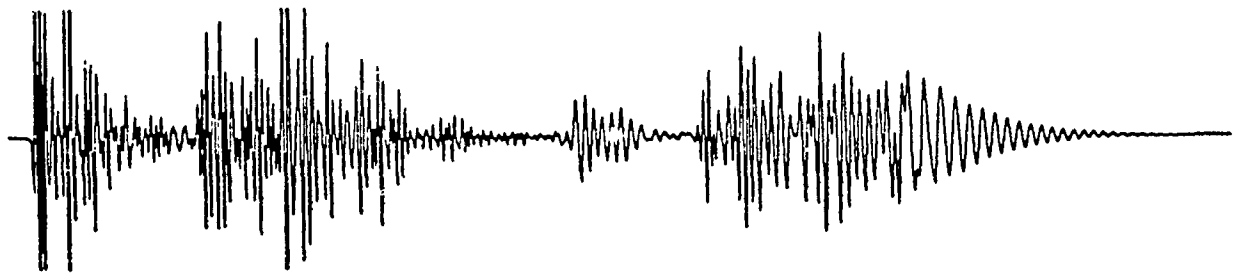
FIGURE 16

77

EXPLOSION SOURCE

VERTICAL

Range (km)
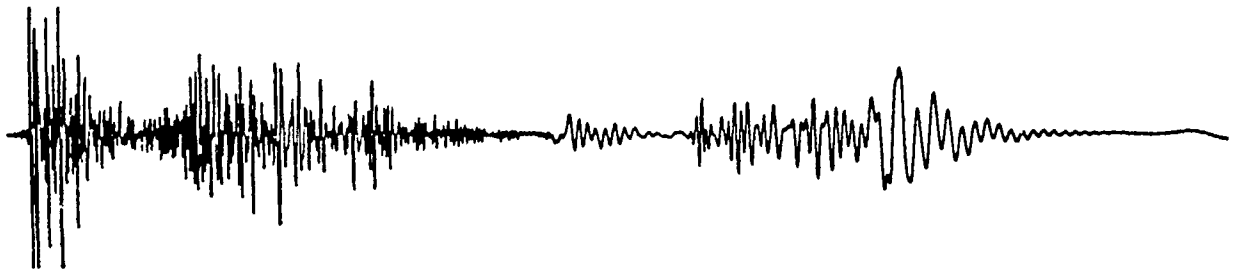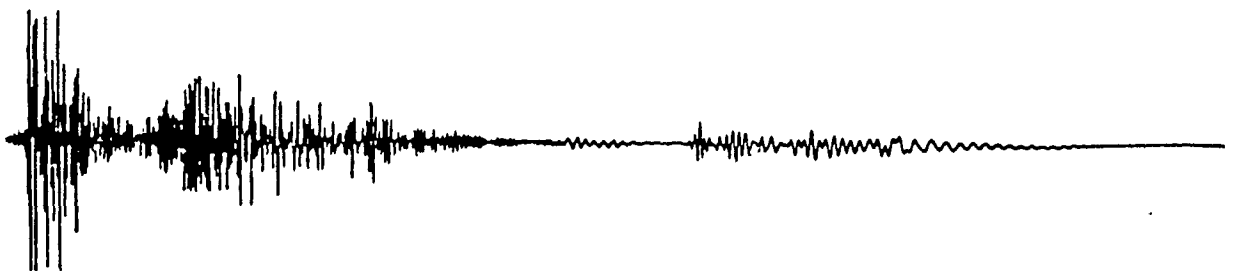
FIGURE 17

78
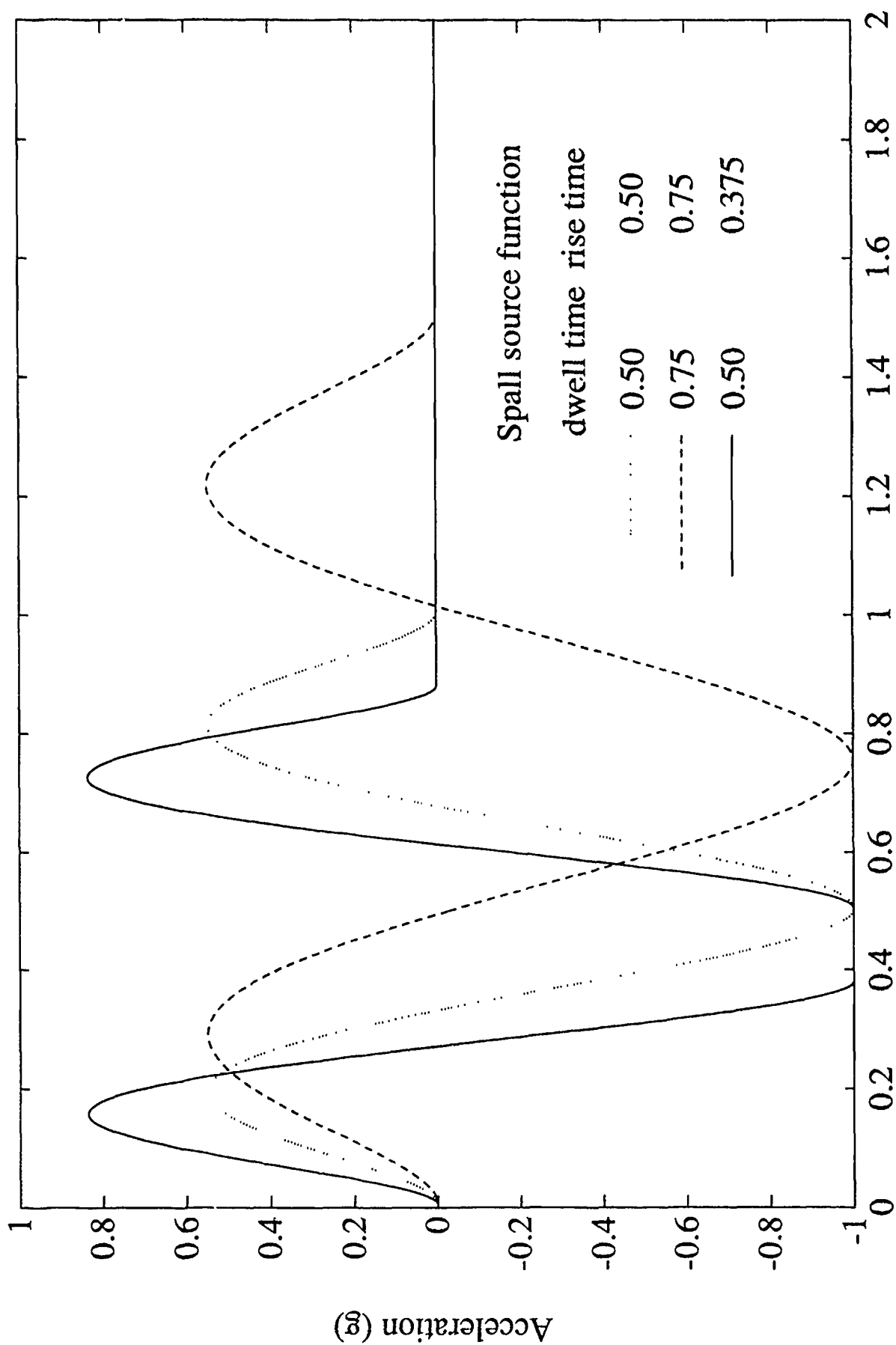
# REGIONAL SPALL SYNTHETICS (Z, 1400 km)

$T_{dwell} = 1.5 \text{ s} \quad T_{rise} = 1.5 \text{ s}$

$T_{dwell} = 0.5 \text{ s} \quad T_{rise} = 0.75 \text{ s}$

$T_{dwell} = 0.375 \text{ s} \quad T_{rise} = 0.50 \text{ s}$

0          200          400 s

FIGURE 18

79

# TELESEISMIC CODA ANALYSIS

WILLIAM L. SOROKA

# PAPER I

## SUMMARY

Spectra from teleseismic coda waves are used to estimate earth and source properties through Generalized Linear Inversion (GLI) techniques. High frequency teleseismic (66-98°) P-wave codas recorded by the Regional Seismic Test Network (RSTN) are analyzed. The spectra of the teleseismic coda were found to be described by the following two models: $(A/t^2+B)\exp(-Ct)$ and $(A/t+B)\exp(-Ct)$. A two-term model consisting of the sum of a time dependent and time independent part times an exponential term were required to fit the single and multiple scattering effects observed in the data. Two near-surface explosions (E. Kazakh) of magnitude 6.1 and one earthquake (N. Argentina-Chile, 559 km depth) of magnitude 5.8 are analyzed to evaluate near-source scattering. Five, three-component North America RSTN receiving stations are used to evaluate the effect of near-receiver scattering.

Coda-Q estimates from the inversions increased with frequency in the approximate range from 800 at 1 Hz to 1600 at 4 Hz. The same range of coda-Q values were obtained for both of the models tested; however, the $(A/t+B)\exp(-Ct)$ model results had higher variances suggesting poorer fit of this model to the data. Coda-Q estimates are higher at stations RSCP and RSNY compared to the other stations. The

coda-Q results from the GLI analyses are in agreement with Q values determined from the analysis of local coda. These results suggest that teleseismic coda-Q's are dominated by near-receiver scattering effects.

The coda analysis method outlined in this paper represent an alternative to normal single scattering analysis methods performed over small time windows early in the coda. This method, which accounts for multiple scattering effects, models the entire coda (500 to 600 seconds) where signal is above background noise. Good results were obtained for both earthquake and explosion data. While coda analysis on multiple scattered waves at teleseismic distances was the emphasis in this paper these methods should also work at local and regional distances.

## INTRODUCTION

Because it is not always possible to record data close to the source, coda analysis techniques have begun to be applied to data at teleseismic distances. At these large source-receiver separations multiple scattering effects play a dominant role in coda generation. As a result of this observation a study was undertaken to better understand how to deal with multiple scattering information in coda analysis. This is the first of three papers which address the issue of how to deal with multiple scattering effects in coda analysis. Coda-Q estimation is the main subject in this first paper. The second paper (Soroka, 1991), referred to as paper 2 in the text, covers the issue of solution bias due to model choice, type of scattering present in the data and random noise. The third paper

(Soroka, Stump and Dainty, 1991), referred to as paper 3 in the text, is an extension of the typical coda analysis and deals with the conversion of the A and B model parameters to earth turbidity and source spectral estimates.

Past work on seismic coda, the random energy that follows a body wave arrival, has focused on data at local and regional distances. This paper concentrates on coda following the direct P-wave arrival with large source to receiver separations in the range from 66 to 98 degrees. Three representative teleseismic waveforms from two explosions and one earthquake are given in figure 1. Shown are approximately 140 seconds of coda with their characteristic exponential decay. This energy travels from source to receiver via many ray paths and represents variations in material properties along the way. Because of their number and complexity the deterministic approach of locating and characterizing all acoustic impedance contrasts contributing to these waveforms is not feasible. A statistical approach to the analysis of seismic data can be applied by assuming that secondary waves are generated at the numerous random heterogeneities upon incidence of the primary wave. The scattered waves which form the coda will, therefore, be a superposition of these secondary waves and may be regarded as the sum of many independent small events (Aki, 1969).

Past studies (Aki, 1969; Aki and Chouet, 1975; Herraiz and Espinosa, 1987; and others) have demonstrated that coda characteristics for local earthquakes can be modeled as single backscattering processes. Application of
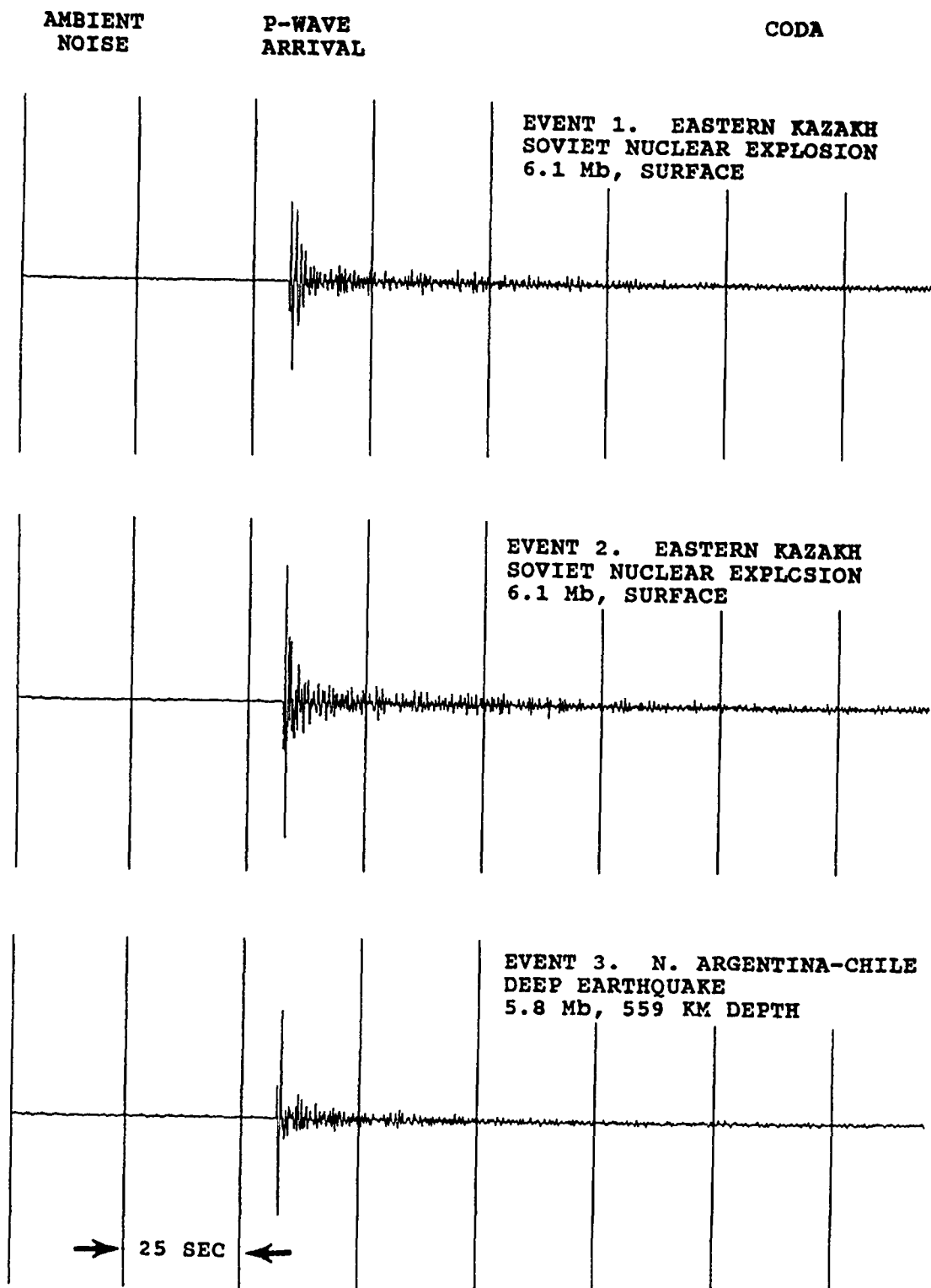
Figure 1.  Representative time series of the three events used in this study.  Shown is the pre-event ambient noise, direct P-wave arrival and approximately 140 sec. of coda.

the single backscattering model to local seismogram codas
has led to information concerning the propagation path and
the source (Herraiz and Espinosa, 1987). Singh and Herrmann
(1983) used the single backscattering model to evaluate the
regional characteristics of coda-Q in the United States.
Aki and Chouet (1975), and Aki (1980a,b) estimated the
turbidity coefficient to obtain information about the
heterogeneities responsible for coda generation. Aki and
Chouet (1975), Chouet et al., (1978) and Rautian and
Khalturin (1978) used the coda to obtain estimates of the
source.

Frankel and Clayton (1984) used finite difference
modeling techniques and found that the apparent attenuation
due to scattering was greatest when the scatterer size was
comparable to the seismic wavelength. Smaller scale
features were found to have an important but lesser effect
on coda generation. An estimate of the seismic wavelength
can be computed from the dominant frequency of the source
wavelet and the velocity of the material in which the wave
is propagating. For the data of this study, the estimated
wavelengths range from 1000 to 5000 meters for frequencies
from 1 to 3 Hz and velocities from 3 to 5 km/sec. Low
velocities are used because past coda work suggests shear
wave scattering is responsible for coda generation (Herraiz
and Espinosa, 1987).

Strong evidence for low apparent phase velocities
(3.5-4.5 km/sec) in teleseismic P-wave codas for deep
earthquakes and explosions were observed by Dainty (1985)
at NORSAR and NORESS. These phase velocities were

85

determined from wavenumber analysis of vertical component seismograms and interpreted as teleseismic P to Lg (trapped shear wave) scattering near the receiver. For the explosions Dainty (1985) also found an equal amount of high phase velocities that he interpreted as Lg to teleseismic P scattering near the source. The data analyzed in this study show a significant amount of energy on the radial and transverse components suggesting P to Lg scattering near the receiver.

The teleseismic coda analysis used in this paper is unique in a number of respects. The modeling includes both single and multiple scattering effects. Generalized Linear Inversion methods are applied so that the entire coda where signal is sufficiently above noise can be used. Inversion techniques are employed to handle large quantities of data to improve the resolution of model parameters as a function of frequency. The larger data set reduces the influence of localized data problems that might bias the final interpretations.

A review of pertinent past coda analysis work will be presented first. This is followed by a description of the methods used in this study. The results are described last and include comparisons to other independent measures of similar properties.

## BACKGROUND

Aki and Chouet (1975) successfully used single backscattering theory to model the codas of local seismic events. The wide applicability of the single backscattering coda model has been demonstrated by its use in local and

regional coda analysis (Herraiz and Espinosa, 1987). These studies include the use of codas to determine attenuation or coda-Q (Aki and Chouet (1975), Rovelli (1982), Singh and Herrmann (1983)), the source spectrum (Aki and Chouet (1975), Chouet et al., (1978), Rautian and Khalturin (1978)) and turbidity (Aki and Chouet (1975), Aki (1980a,b), Dainty et al., (1987)). The potential for using teleseismic coda in similar fashion was demonstrated by Aki (1982). The codas were found to be insensitive to the path and to have similar amplitude and spectral characteristics at different stations for the same source. The teleseismic codas were modeled as a superposition of many random independent single backscattered events similar to the methods used in local and regional coda analysis.

The single backscattering model describes the time (t) and frequency (f) variation of the power spectrum of the coda (P(f,t)), (Herraiz and Espinosa, 1987). The model parameters are the source term (S(f)), coda-Q (Q(f)) which includes intrinsic attenuation and scattering attenuation effects and turbidity (T(f)). Turbidity is a measure of the medium's ability to initiate scattering. It represents the wave path heterogeneity and is expressed as a cross-section per unit volume with units of 1/km. The mathematical expression for the power spectrum of single backscattered body waves (Gao et al., (1983b)) is:

$$P_1(f,t) = \frac{2\ T(f)\ S(f)}{V\ t^2}\ \exp\left(\frac{-2\pi ft}{Q(f)}\right) \qquad (1)$$

where: $P(f,t)$ = power spectrum

$S(f)$ = source term = $r^2\ P_0(f)\ \exp(4\pi fr/VQ)$

87

T(f)     =  turbidity

Q(f)     =  coda-Q

V        =  average crustal velocity

r        =  reference distance

The single backscattering coda model is not applicable to all seismic data. In some cases evidence for multiple scattering effects have been presented (Richards and Menke, 1983). In an attempt to better account for these multiple scattering effects the energy flux model has been applied (Frankel and Wennerberg (1987) and Langston (1989)). Gao et al., (1983b) extended the single backscattering model to multiple scattering and provided the mathematical expressions of higher order scattering models. They showed that single scattering effects dominate at early times in the coda and multiple scattering with its slower decay become important at longer times. The slower decay rate of multiple scattering is a result of the time delay of primary wave energy by scattering interactions. The slower decay rate associated with the multiple scattering process can explain the long coda durations which are characteristic of teleseismic observations (figure 1). The mathematical expressions for second and third order multiple backscattering (Gao et al., (1983b)) are:

$$P_2(f,t) = \frac{2.46\ S(f)\ V\ T(f)^2}{t} \quad \exp\left(\frac{-2\pi ft}{Q(f)}\right) \qquad (2)$$

$$P_3(f,t) = 0.716\ S(f)\ T(f)^3\ V\ \exp\left(\frac{-2\pi ft}{Q(f)}\right) \qquad (3)$$

A simple model which consists of a time dependent and

time independent term of the form $(A/t^2+B)\exp(-Ct)$ is seen to correspond to first and third order scattering in equations 1 and 3 above. Attempts were made to include second order scattering effects but, due to the extra degree of freedom the inversions were unstable on all but noise-free synthetics. First plus third order scattering was found to be a good average model to fit to the data. The results of these model tests are described in more detail in paper 2. Note that another simple model consisting of a time dependent and time independent term is of the form $(A/t+B)\exp(-Ct)$. This alternative model also describes the characteristics of the data.

Representative teleseismic coda spectral decay curves at a single frequency (2 Hz) are shown in figure 2. The data are seen to decay rapidly at early times and more slowly at later times. Superimposed on the data is the least-square best fit of the $(A/t^2+B)\exp(-Ct)$ model in the upper display and the $(A/t+B)\exp(-Ct)$ model in the lower display. The time independent multiple scattering term fits the data well at later times but has poor predictions at early times. The time dependent single scattering model curve fits the data well at early times and diverges at later times. Attempts to use the time dependent single scattering term to describe the entire data set failed because time-varying coda-Q's were required to effectively model the data (Soroka et al., (1985)). These results indicate that a two term model which includes a time dependent single and time independent multiple scattering term is necessary to describe coda when multiple scattering
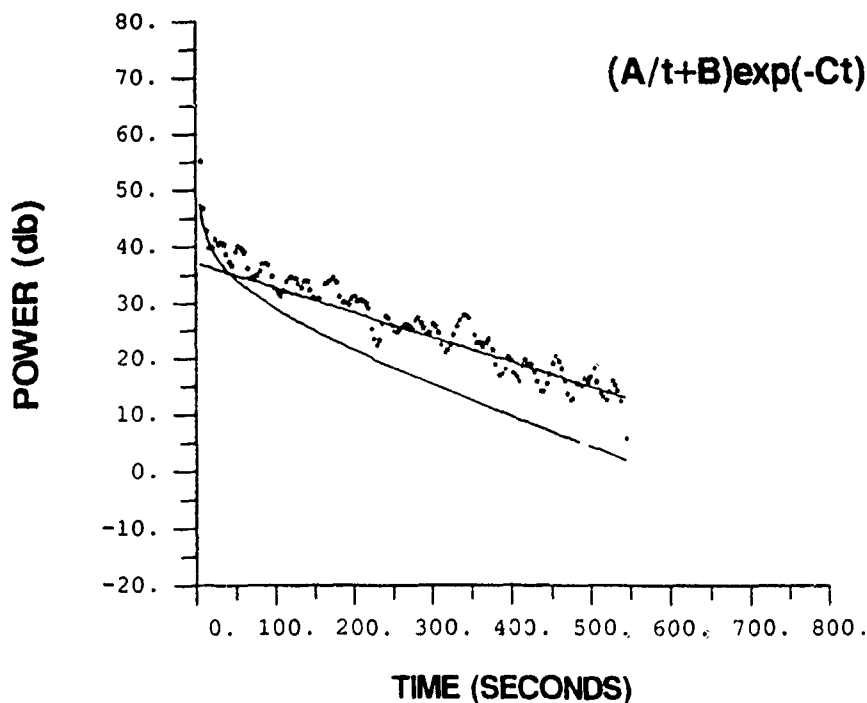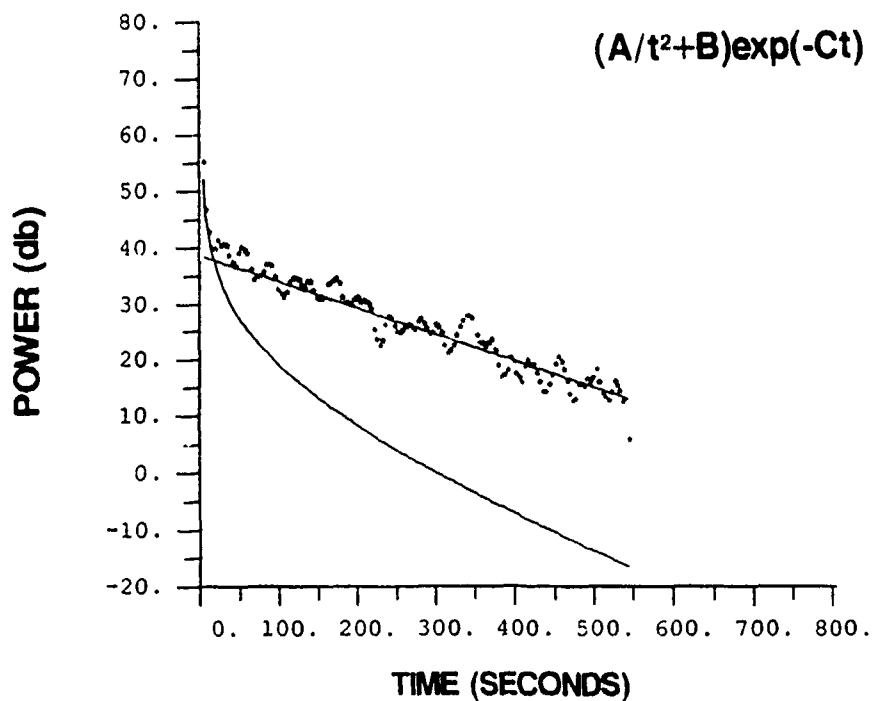
Figure 2. Representative $(A/t^2)$ and $(A/t)$ model fits to the data. The single and multiple models are plotted separately to illustrate that neither of the models alone can describe the data at all times. Analysis is for the vertical component at 2 Hz of event 2 at station RSON.

effects are present. This two-term model appears more appropriate than the single scattering model alone for describing teleseismic coda and probably seismic coda in general when long time windows which include multiple scattered energy are used (paper 2).

In summary the two models which adequately fit the time varying characteristics observed in the data are:

$$( \frac{A}{t^2} + B ) \exp(-Ct) \qquad (4)$$

and:

$$( \frac{A}{t} + B ) \exp(-Ct) \qquad (5)$$

These models will be referred to in the text as $(A/t^2)$ and $(A/t)$ respectively. The $(A/t^2)$ model is shown above to be the form of single and triple scattered body waves as derived by Gao et al., (1983b).

The $(A/t)$ model is the form of two different physical processes, one more and one less applicable to the teleseismic coda analysis problem. The time dependent and time independent terms in the $(A/t)$ model correspond to first and second order surface wave scattering (Gao et al., 1983a). Evidence presented later in this paper favors body wave over surface wave scattering in teleseismic coda generation. The time dependent term in the $(A/t)$ model is also the correct form of single scattered body waves that result from a plane wave encountering a layer of randomly distributed scatterers. The time independent term could represent trapped P-to-Lg waves that are generated when the plane wave hits the near surface layer under the receiver.

The plane wave model is discussed in more detail in paper 3. For the purposes of coda-Q estimation it is only important to note that the exponential term in both the $(A/t^2)$ and A/t) models (equations 4 and 5) are the same. Coda-Q estimates will be determined with both models and the results compared in the detailed result section.

## PROCEDURES

The coda analysis method used in this study involves fitting a model to time varying spectral estimates of teleseismic coda and then computing earth and source properties from the model parameters. Both of the proposed models (equations 4 and 5) are fit to the data using generalized linear inversion (GLI) techniques. The analysis procedure is divided into four steps:

1) TIME VARYING SPECTRAL CHARACTERIZATION
2) CODA MODEL VERIFICATION
3) INVERSION
4) INTERPRETATION

Each of these four topics will be discussed in turn. First however, the selection of an appropriate data set for analysis will be considered. The data chosen possessed the following characteristics:

1) Well developed codas following the direct P-wave
2) Events recorded at teleseismic distances
3) Coda uncorrupted by deterministic arrivals
4) Digitally recorded data with a sample rate that allows
   for high frequency (1-10 Hz) analysis

92

Data from the Regional Seismic Test Network (RSTN),
(Breding, 1983) seismic database (table 1) met these

Table 1. --Event and station information

EVENT LOCATIONS

| EVENT | TYPE | LOCATION |
|---|---|---|
| 1 | EXPLOSION | EASTERN KAZAKH, U.S.S.R. |
| 2 | EXPLOSION | EASTERN KAZAKH, U.S.S.R. |
| 3 | EARTHQUAKE | N. ARGENTINA-CHILE |

STATION LOCATIONS

| STATION | LOCATION |
|---|---|
| RSCP | CUMBERLAND PLATEAU, U.S.A. |
| RSNY | NEW YORK, U.S.A. |
| RSSD | SOUTH DAKOTA, U.S.A. |
| RSON | ONTARIO, CANADA |
| RSNT | NORTHWEST TERRITORY, CANADA |

SOURCE-TO RECEIVER DISTANCES IN DEGREES

| EVENT | MAGNITUDE | DEPTH | STATION | | | | |
|---|---|---|---|---|---|---|---|
| | | | RSNT | RSON | RSNY | RSSD | RSCP |
| 1 | 6.1 | NEAR-SURFACE | 68 | 79 | 83 | 86 | 94 |
| 2 | 6.1 | NEAR-SURFACE | 68 | 79 | 83 | 86 | 94 |
| 3 | 5.8 | 559 Km | 98 | 82 | 72 | 80 | 66 |

requirements. Two near-surface explosions ($m_b$=6.1) and one
deep earthquake (559 km depth, $m_b$=5.8) were selected for
analysis. Shallow earthquakes were not chosen because the
pP (surface reflection) occurs too soon after the direct
P-wave arrival and corrupts the coda decay. Two explosions
and one deep earthquake were selected for the purpose of
studying source differences and near-source versus
near-receiver scattering effects. Records from five North
American stations with source-to-receiver distances that
range from 60 to 98 degrees were used to study station

93

differences. The RSTN data were digitally recorded on three components (vertical, north and east) at a sample rate of 40 samples per second (Breding, 1983). Seismograms for the three events at all five North America RSTN stations (table 1) were analyzed. The north and east components are rotated to form radial and transverse components (to the source) prior to analysis.

## TIME VARYING SPECTRAL CHARACTERIZATION

The power spectra were computed using the Fast Fourier Transform (FFT) method on small, 3.75 second time windows (150 samples). To reduce edge effects, a Hanning window was applied to the selected data with zero padding prior to performing the FFT. Figure 3 is a representative 3-D display of the power spectral decay characteristics with frequency and time. Plotted is the signal-to-noise ratio computed from the data and average pre-event ambient noise spectral estimates. All 3-D displays of the time varying spectra have certain features in common. Maximum spectral power occurs at the direct arrival between 1 and 3 Hertz. Spectral amplitude decreases with time at all frequencies. The signal falls below background noise sooner at high and low frequencies relative to the spectral maximum.

## CODA MODEL SELECTION

Selection of the appropriate model for the teleseismic coda is not generally clear. The approach by some authors is to use the single backscattering model for the sake of consistency with previous work. While this
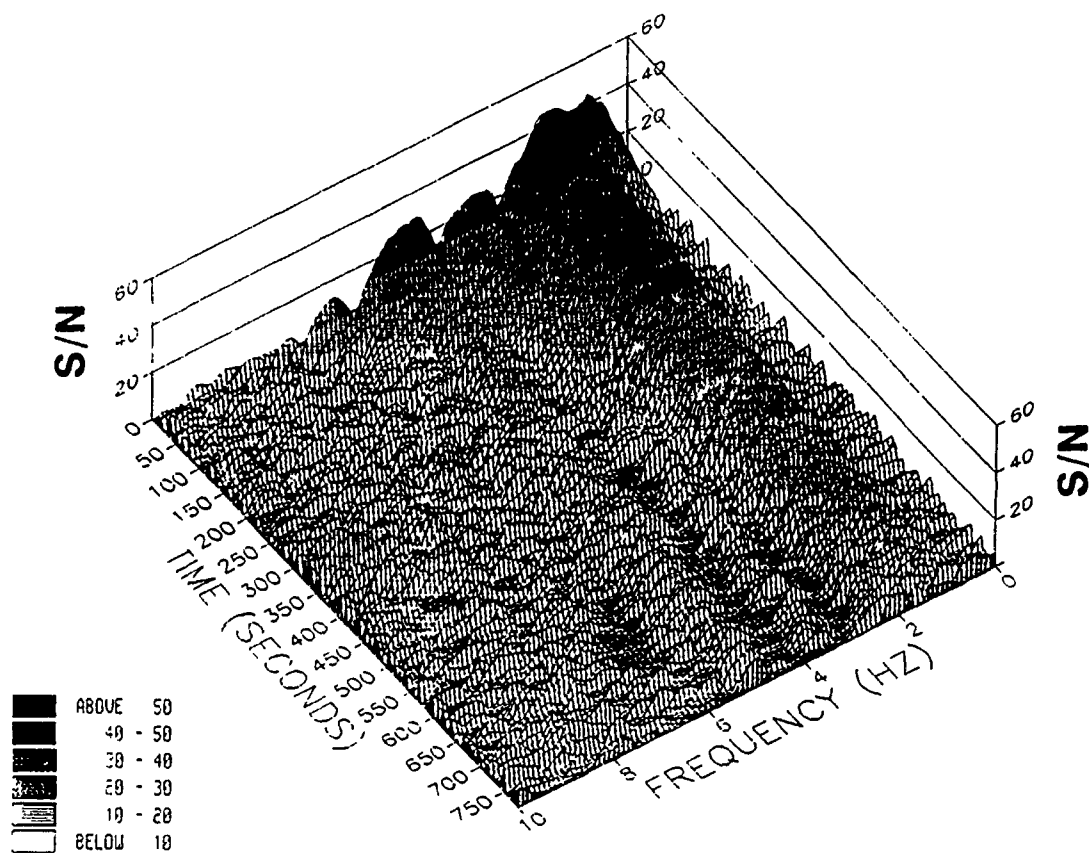
94

Figure 3. Time varying power spectra of Event 2. Shown is the signal-to-noise ratio in db for the vertical component at station RSNT.

approach is the simplest it can lead to biased solutions which may not reflect true earth properties. There are three main issues that need to be addressed when determining which model is most appropriate for the coda under analysis.

1- FORWARD -VERSUS- BACK-SCATTERING

2- SINGLE -VERSUS- MULTIPLE SCATTERING

3- SURFACE -VERSUS- BODY WAVE SCATTERING

FORWARD -VERSUS- BACK-SCATTERING

Menke and Chen (1984) and Richards and Menke (1983) have proposed criteria for distinguishing between forward and backscattering effects in coda. They include:

For forward scattered waves:
a) the coda has relatively higher frequencies than the
   initial wave. (Richards and Menke, 1983)
b) the coda power spectra decay rate with time is faster
   for lower frequencies than higher frequencies.
   (Menke and Chen, 1984; Frankel and Clayton, 1984)

For backscattered waves:
 a) at all frequencies the coda spectral power is lower
    than the initial wave. (Richards and Menke, 1983)
 b) the coda power spectra decay rate is faster for high
    frequencies then low frequencies.
    (Menke and Chen, 1984; Frankel and Clayton, 1984)
 c) estimates of apparent Q made from coda of backscattered
    waves increase with frequency, those from forward
    scattered waves do not (Richards and Menke, 1983).

Spectral ratios (Pizarenko, 1970) were used to characterize the changes in relative amplitude of the coda spectrum with time as a function of frequency. Figure 4 is a representative spectral ratio plot ($P_i$ / $P_{i-1}$ , where $P_i$ is the spectral power at a specific time) and shows that power decreases with time at all frequencies. There is no appreciable increase in power at high frequencies after the initial wave that cannot be attributed to high variance in the spectral estimates. The coda-Q solutions, reported later, are also found to increase with frequency in agreement with the backscattering model criteria. These observations lead to the conclusion that teleseismic coda, for the three events under analysis, are dominated by the backscattering processes.

## SINGLE -VERSUS- MULTIPLE SCATTERING

It was shown earlier for both the ($A/t^2$) and ($A/t$) models in figure 2 that neither the single or multiple model alone described the characteristics of the data. The time dependent single scattering curve fit the coda at early times and the time independent multiple scattering curve fit the data at later times. Figure 5 shows that good agreement is obtained between the data and both models when the single and multiple terms are added prior to being overlain on the data. The ($A/t^2$) and ($A/t$) models are plotted on top of the time varying spectral data and can be seen to follow the trend of the data at all times. The only exception might be at very early times where the ($A/t$) model with its gentler decay does not follow the data as well as the ($A/t^2$) model. This small difference between the
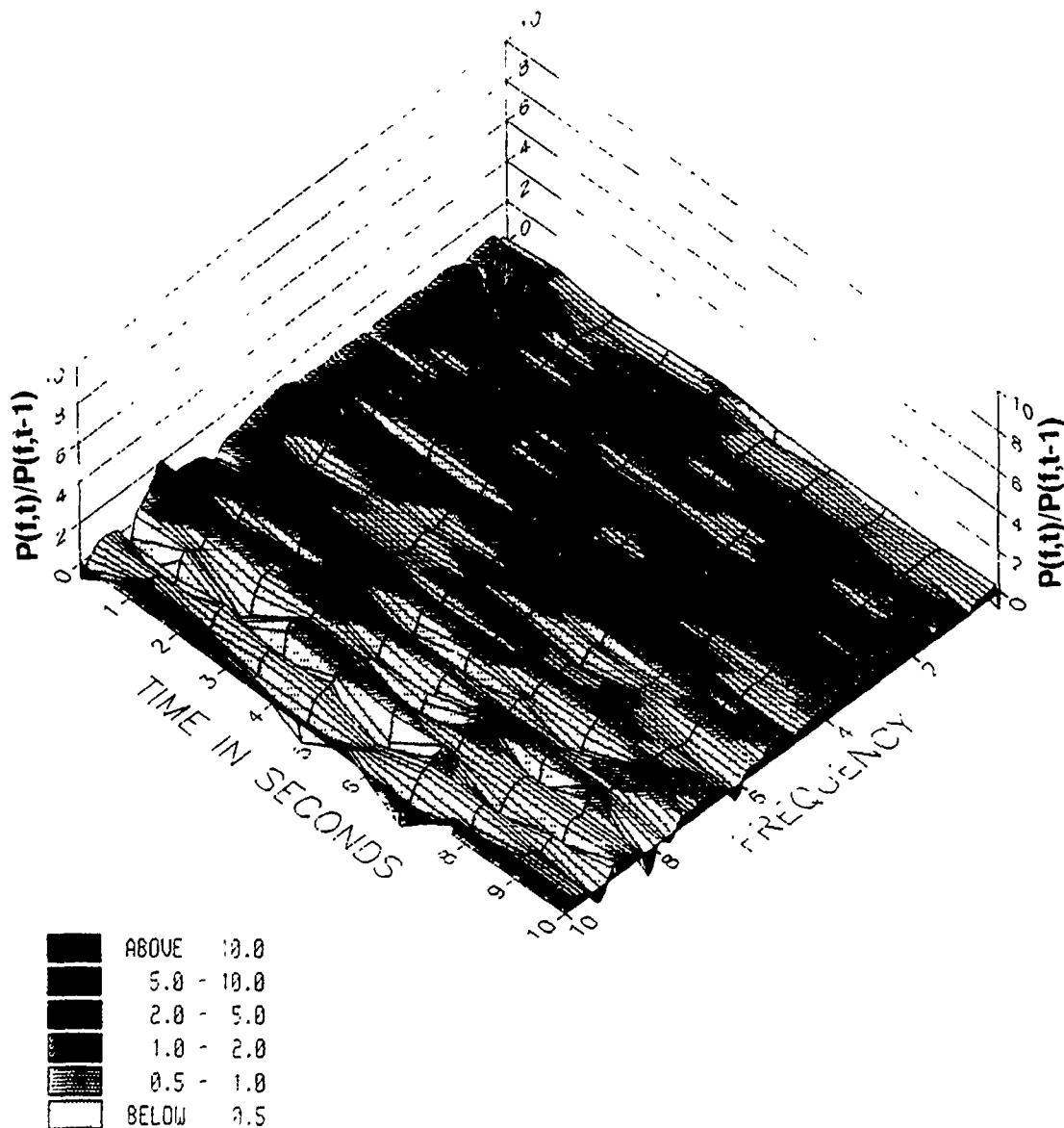
97

Figure 4. A representative spectral ratio plot. Computed
from the FFT solution as power at time t divided by power
at time t-1 for all frequencies. Analysis is for the
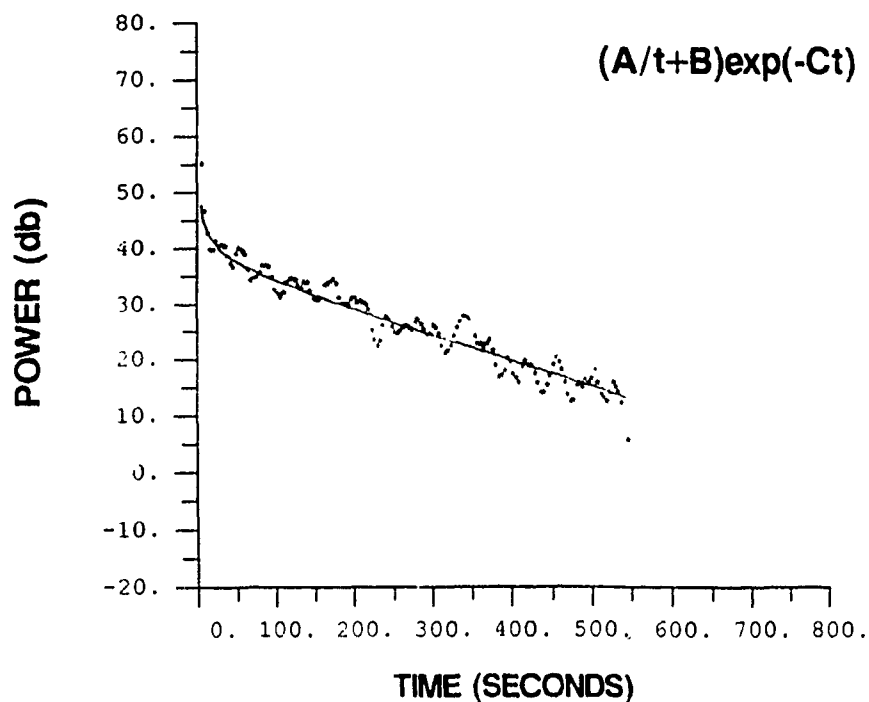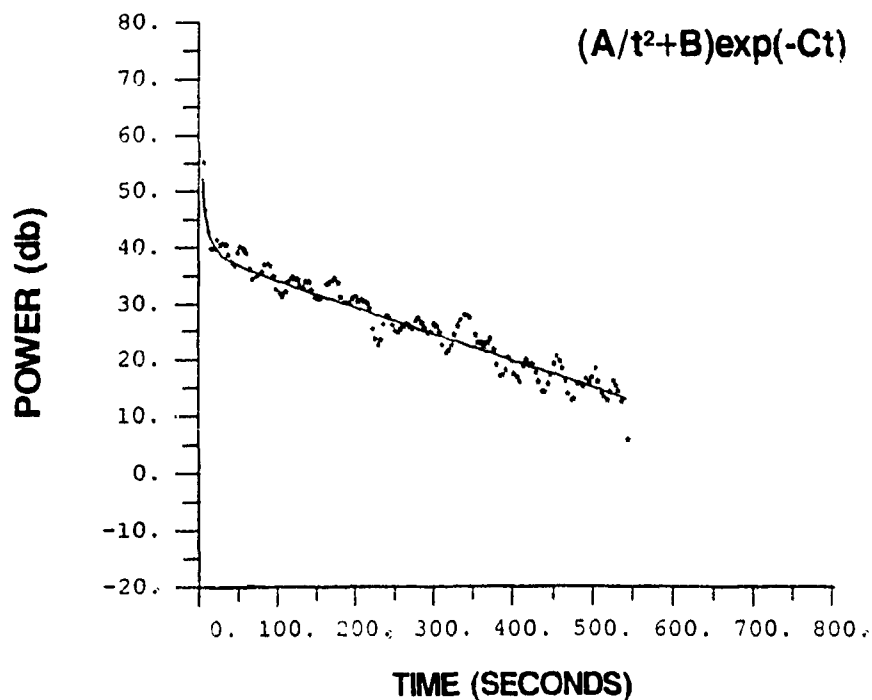vertical component of Event 2 at station RSNT.

Figure 5. Representative $(A/t^2)$ and $(A/t)$ final model fits (lines) to the data (points). The models plotted are the single plus multiple models discussed in the text. A five point smoothing function is applied to reduce the high frequency noise in the data. Analysis is for the vertical component at 2 Hz of Event 2 at station RSON.

two models at early times in the coda may not be resolvable. On the other hand, results from paper 2 indicate that this feature may make one model less stable than the other during the inversions. Based on these model fits to the data a model consisting of a time dependent single scattering term and a time independent multiple scattering term appears necessary to model coda with multiple energy present.

Attempts were made to perform the inversions with additional orders of scattering (or additional time dependent terms) in the hope that this would improve fits and reduce variances. The details of these tests are included in paper 2. These additional free parameters were found unstable on all but noise free synthetic data. The inversion technique is only able to resolve the steeply decaying early time coda from the gently sloping later time coda. The inversion was also found to be very unstable when the input data contained orders of scattering significantly different from the model being fit.

In summary, the decision to use the $(A/t^2)$ and $(A/t)$ models is based on:

1) the good agreement between data and models, the two-term models were found to be good average models to use

2) the necessity of keeping the model simple for use with the inversion techniques

3) the inability of the inversion tests using additional levels of scattering to improve the fits

SURFACE -VERSUS- BODY WAVE SCATTERING

Distinguishing surface from body wave scattering is

not something that is easily tested. The evidence in the literature appears to strongly favor body wave scattering as the mechanism for coda generation. Herraiz and Espinosa (1987) use the following three arguments in support of body wave scattering:

1) Coda waves corresponding to surface and a deep borehole (~3.5 km) site in Japan share the same features (Sato, 1978).

2) Coda and S-waves have similar site effects for a wide frequency range 1 to 25 Hz (Tsujiura, 1978).

3) Q for shear waves and coda-Q are similar over the frequency range 1 to 25 Hz (Aki, 1980a,b).

Based on the Gao et al., (1983a and b) theory the difference between the body and surface wave models is in the time dependence of the single scattering term. For body waves it's $A/t^2$ and for surface waves $A/t$. Both of these models fit the time varying spectra of teleseismic coda (figure 5) and produce stable solutions. Based on the above three pieces of evidence surface waves can be ruled out as a major contributor in teleseismic coda generation.

Surface wave coda-Q estimates would be identical to those determined by fitting the $(A/t)$ model which also describes a plane wave hitting a layer of random scatterers and is included in this study. The important difference between the surface wave and plane wave models is with the definition of the A and B model parameters which are different for each model. The exponential (C) term from which coda-Q is derived would be the same in each case

(paper 3). The coda-Q results from fitting the $(A/t^2)$ and $(A/t)$ models will be presented in the detailed results section for comparison. The conversion of the A and B model parameters to earth and source property estimates is the subject of paper 3.

## GENERALIZED LINEAR INVERSION

The scattering model parameters are determined from the time varying spectral data using the GLI technique (Aki and Richards, 1980 and Menke, 1984). Frequencies as high as 10 Hz are analyzed for each event, station and component. A signal-to-noise ratio of 10 db and a minimum of 10 data values were required for the inversion. The first of the two parametrized models used in the inversion is:

$$P = \left( \frac{A}{t^2} + B \right) \; EXP( -C\, t ) \qquad (6)$$

Comparison of this model to the Gao et al., (1983b) theory, equations (1) and (3) give the following relationship between the model parameters A and B and Earth and source properties described in the introduction:

$$A = 2\, S\, T\, /\, V\, , \quad B = 0.716\, S\, T^3\, V\, , \quad C = 2\pi f/Q \qquad (7)$$

The emphasis of this paper is on the estimation of coda-Q from teleseismic data where multiple energy is a dominant contributor to the coda. Equation 8 below gives the alternative model which also describes the characteristics of the data. The model parameter C in equation (8) from which coda-Q is computed is the same as for equation (6) (paper 3). Coda-Q is therefore obtained

from C in the same manner described above (C=2πf/Q).

$$P = ( A/t + B ) \exp(-C\ t) \qquad (8)$$

The A and B model parameters are not the same for the
$(A/t^2)$ and $(A/t)$ models. A detailed study of turbidity and
source spectral estimation from the A and B model
parameters is the subject of paper 3. Using the $(A/t^2)$
model, which appears to fit the data better, a limited test
was performed in which turbidity is computed from the ratio
of B/A and assuming a material velocity of 3.5 km/sec. The
source term is obtained from A. The results of this limited
test, shown in the result section, suggest that the simple
two-term representation of the complicated coda scattering
problem could provide a means of estimating turbidity and
source spectral properties. The reader is referred to paper
3 for more details on this work.

## ERROR ANALYSIS

An extensive study was undertaken to better
understand the significance of the coda analysis results
when multiple scattered energy is present. The details of
this study are the subject of paper 2. A brief summary of
the findings are presented below and the reader is referred
to paper 2 for more detail.

Using synthetics, paper 2 examines the effects of
multiple scattered energy, random noise and model parameter
magnitude on inversion stability and solution accuracy. The
popular models used in coda analysis are compared to better
understand their similarities, differences and limitations.
Also covered is the issue of solution bias which results

from using simple two-term models to represent different types of multiple scattered energy in the coda.

A Monte Carlo error analysis was run first to test the effect of random noise on the inversion results. If random noise effects severely corrupted the inversion solutions there was no point in proceeding. The test consisted of fitting the $(A/t^2)$ model 100 times to a known input model while adding different sets of random noise of a constant level to the input data. The noise added to the data was produced by generating a uniform distribution of random numbers. The four levels of noise tested are approximately 1, 10, 20 and 40 percent of signal maximum. The coda-Q, turbidity and source term results from the 100 runs were used to calculate a mean and standard deviation for each of these parameters. Figure 6 illustrates the solution uncertainty (% error=standard deviation in percent of mean) for larger values of coda-Q, turbidity, and source term as a function of random noise.

The difference between the Monte Carlo mean values and the known model is a measure of the bias expected in the inversions due to random noise. Table 2 gives the bias for each of the parameters and shows (similar to figure 6) that coda-Q and turbidity (T) can be computed with greater certainty than the source term (S).

A similar Monte Carlo test with low values of Q, turbidity and source term suggested that the results in figure 6 and table 2 are probably a worst case situation. The level of noise in the observational data varies from station to station and with frequency but was determined to
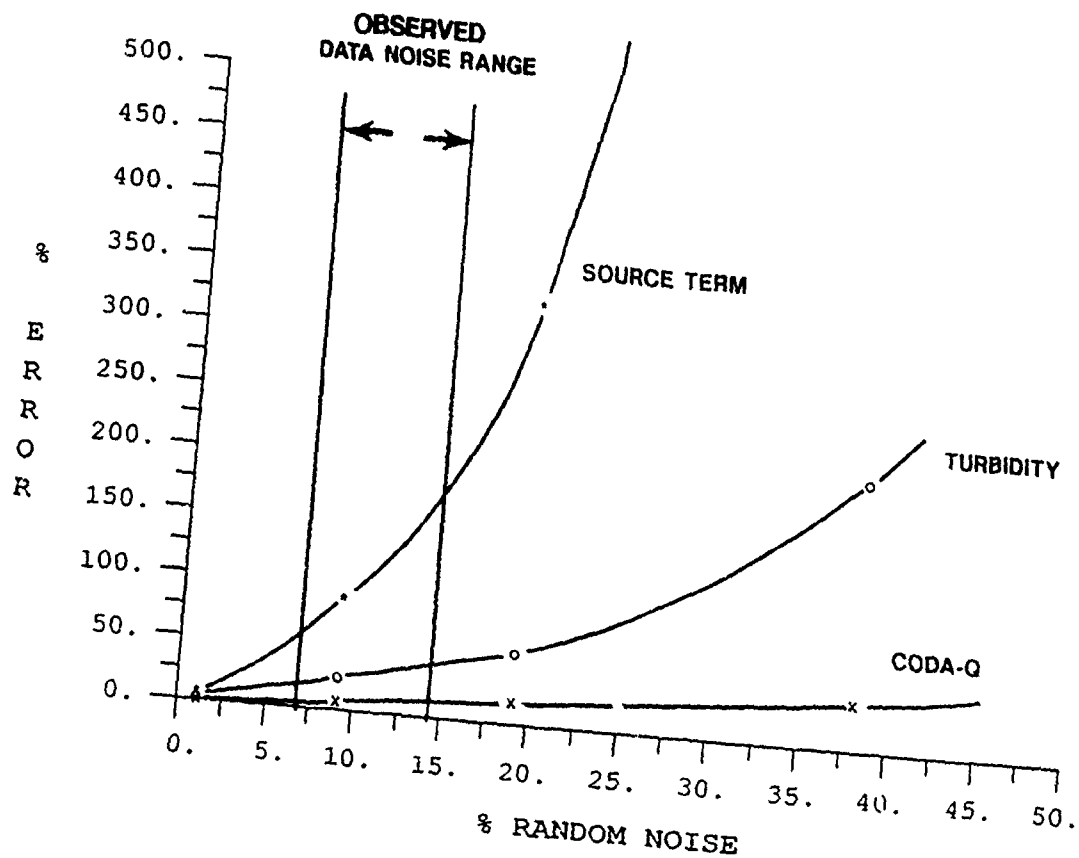
Figure 6. Monte Carlo error analysis results. The effect of random noise on the solution is shown. (% error = standard deviation in percent of mean)

be within the range indicated on figure 6 (7-14%). These random noise tests indicate that coda-Q can be determined more accurately then the other two parameters (T and S) and Q is relatively insensitive to even high levels of random noise. Turbidity can be determined more accurately then the source term and should produce relatively stable estimates. The source term should have the largest degree of uncertainty.

TABLE 2.--Solution bias due to random noise (percent difference between the Monte Carlo analysis mean and the known solution)

| MODEL PARAMETER | RANDOM NOISE LEVELS | | | |
|---|---|---|---|---|
| | 1% | 10% | 20% | 40% |
| Q | 0.0 | 0.5 | 3. | 10. |
| T | 0.0 | 3. | 10. | 115. |
| S | 0.1 | 30. | 200. | 2000. |

The Monte Carlo analysis indicated that the effects of random noise were tolerable and that stable coda analysis estimates could be determined. To better understand the applicability of the simple two-term models a comparison was made between the $(A/t^2)$, $(A/t)$ and energy flux models. The results of this comparison showed them to produce equivalent estimates of coda-Q. However, when the single scattering model was fit to data with single plus multiple scattered energy, the coda-Q solutions were strongly biased by as much as 280%. A similar situation was observed when the $(A/t^2)$ model was fit to data with only single scattered energy. The results of these tests tell us that poor coda-Q estimates are obtained when the model to

be fit to the data differs significantly from the scattering present in the data. The two term models $(A/t^2)$ and $(A/t)$ were found to be good average models of up to fourth order multiple energy. The $(A/t^2)$ model was observed to described steep decays at early times better than the $(A/t)$ model.

A comparison was also made between the A and B model parameters from the $(A/t^2)$ and $(A/t)$ models. These results showed large differences which suggests that model selection may be critical if useful information is to be extracted from the A and B model parameters. This is the subject of paper 3 to which the reader is referred for more detail.

## INTERPRETATION OF MODELING RESULTS

The $(A/t^2)$ and $(A/t)$ scattering models were applied to all RSTN data from the two explosions and one earthquake (table 1). Figures 7 and 8 are representative $(A/t^2)$ and $(A/t)$ model solutions of coda-Q versus frequency for the three events recorded at station RSON. Vertical, radial and transverse solutions are superimposed on each plot. In each case the results are observed to follow a linear increase of coda-Q with frequency. The $(A/t^2)$ and $(A/t)$ model results are similar but not equal. The increased scatter in coda-Q at low and high frequencies is due to low signal-to-noise ratios. Consistent coda-Q estimates from the three components support the conclusion that each component is measuring similar earth properties. The agreement in coda-Q estimates between the deep earthquake and the two shallow explosions suggests that near-receiver
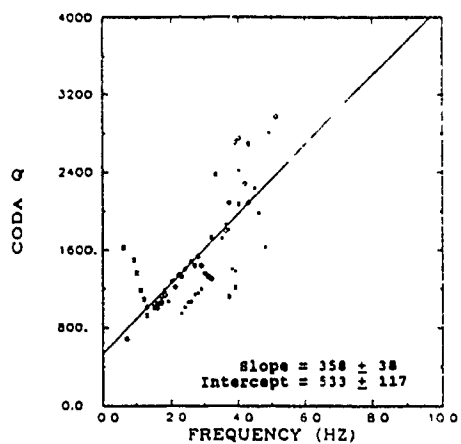
**EVENT 1**
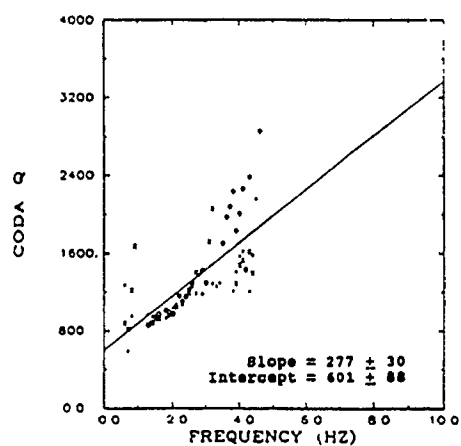
**EVENT 2**
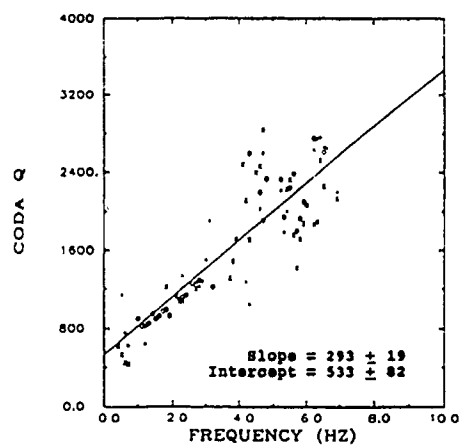
**EVENT 3**

Figure 7. $(A/t^2)$ model coda-Q versus frequency results for Events 1, 2 and 3 at station RSON. The slope and Y-intercept values for the least-square best fit lines are shown on the figures. Symbols represent the different components: vertical (+), radial (x) and transverse (o).
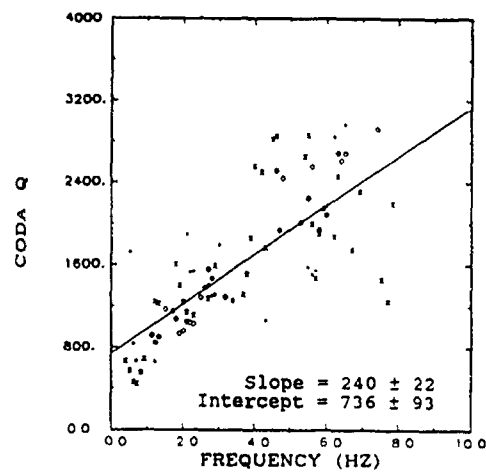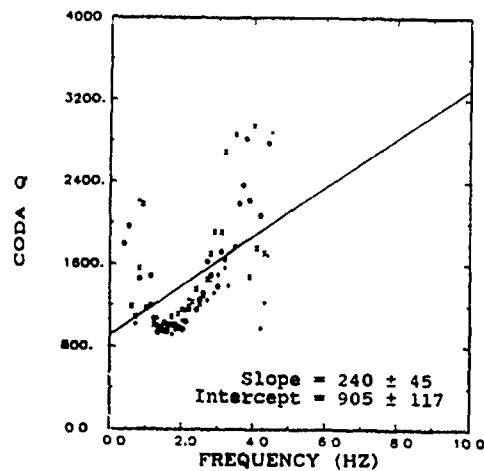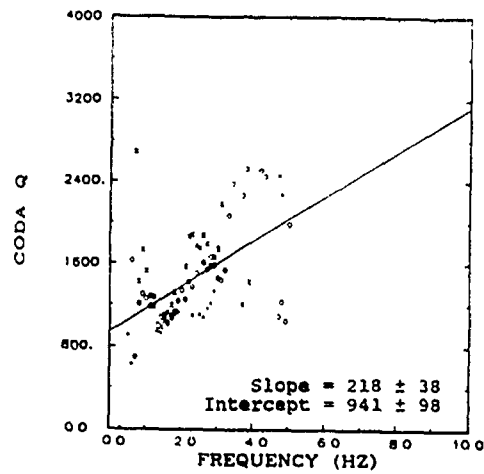
EVENT 1

EVENT 2

EVENT 3

Figure 8. (A/t) model coda-Q versus frequency results for Events 1, 2 and 3 at station RSON. The slope and Y-intercept values for the least-square best fit lines are shown on the figures. Symbols represent the different components: vertical (+), radial (x) and transverse (o).

109

scattering dominates over near-source scattering in these codas. The implications of this observation are that coda analysis reflect earth properties near the receiver.

Figure 9 is a representative display of both the A and B model parameters, from equation 4, as a function of frequency. These displays do not tell us about earth and source properties but suggest that some systematic changes are occurring in the data and are being measured by these parameters. To extract earth and source properties from A and B it is necessary to interpret A and B in terms of a scattering theory. Equations 1 and 3 provide a means of converting A and B into turbidity (T) and source spectra (S) by equating the A parameter to the single scattering amplitude term (in front of the exponential) and B to the triple scattering amplitude term. The extraction of earth and source information from the A and B model parameters is a potential new source of coda information. The issues of proper model, model assumptions and estimate reliability is discussed in detail in paper 3.

Because the $(A/t^2)$ model allows for the separation of the turbidity and source term, a small test was performed with a $(A/t^2)$ model to determine if additional work in this area was warranted. In this test turbidity and source spectra are computed from A and B for a representative data set. The resulting estimates are compared with other independent measures of these properties and evaluated in terms of general appearance.

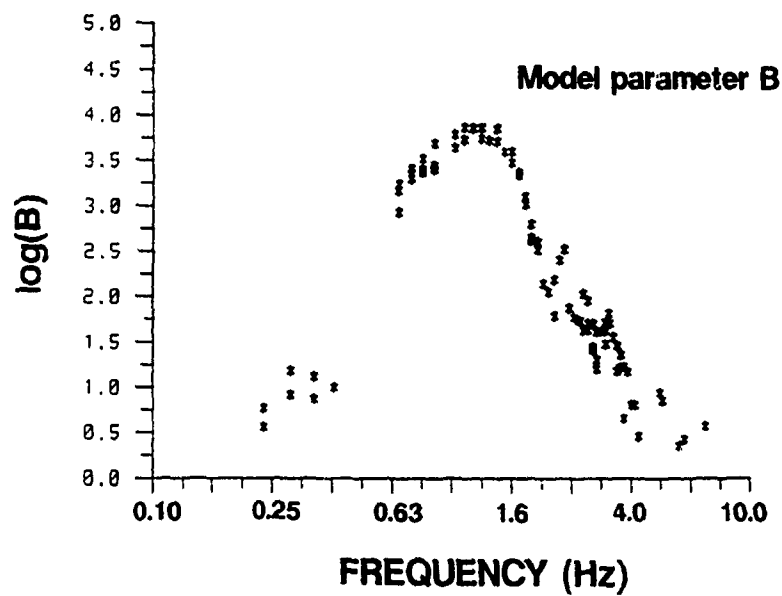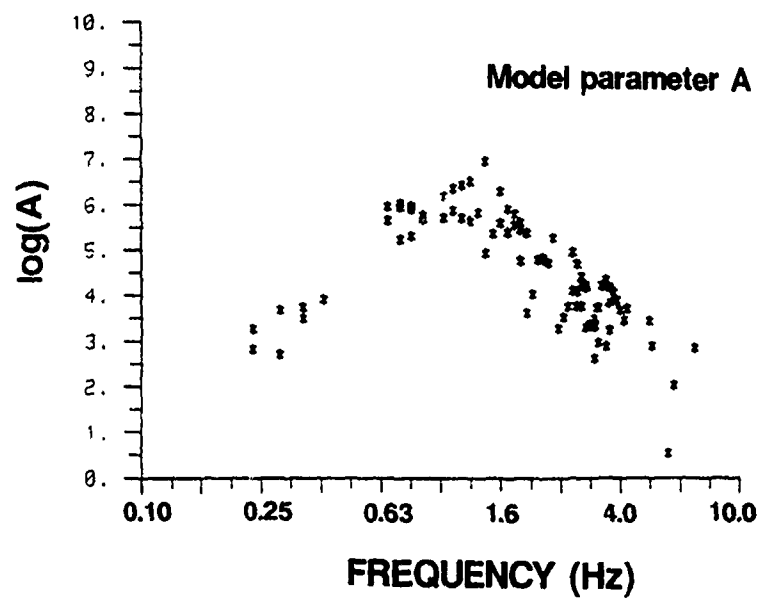Figure 10 is a representative plot of turbidity $(T(f))$ for all three events at station RSNT with the three

Figure 9. Representative A and B model parameter solutions from the $(A/t^2+B)\exp(-Ct)$ model.
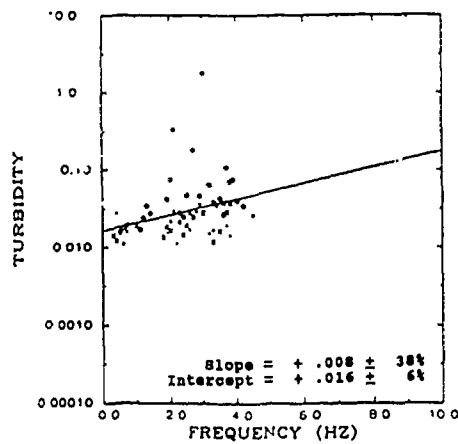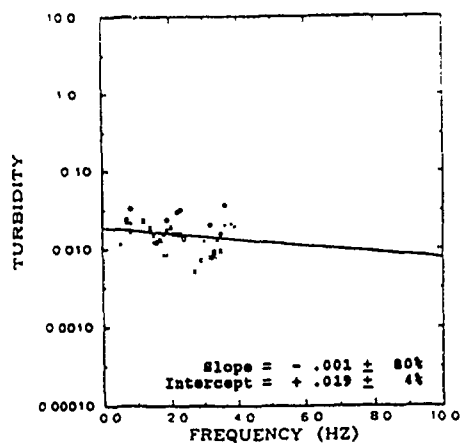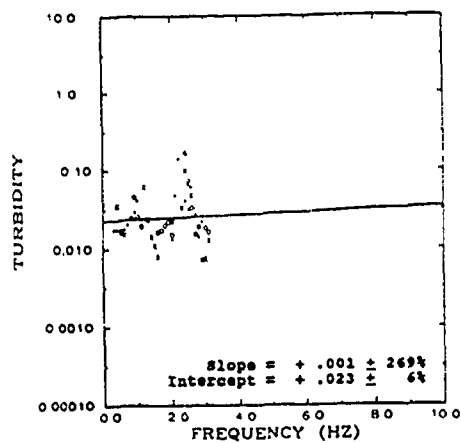
111

**EVENT 1**

**EVENT 2**

**EVENT3**

Figure 10. $(A/t^2)$ model turbidity versus frequency results for Events 1, 2 and 3 at station RSSD. The least-square best fit line is plotted. Symbols represent the three components: vertical (+), radial (x) and transverse (o).

components superimposed. Turbidity, which is a measure of a
medium's ability to initiate scattering, appears to be
relatively constant with frequency. The agreement among the
different components suggests they are again representative
of similar earth properties. The scatter in the turbidity
results tends to be higher then with the Q results as
predicted by the Monte Carlo error analysis. The values
fall consistently between .01 and .1 which is in agreement
with other published work (Aki, 1973, Dainty, 1988).
Because of the high variance the gentle slopes of the best
fit least-square lines are probably not significant.

Figure 11 is a representative display of the source
term result for the three events at station RSON (three
components superimposed). The vertical scale is spectral
power in db down from maximum. The maximum spectral value
used to compute the db spectrum is constant for a
pa... .icular source, receiver and component but varies
otherwise to make the results more comparable. The expected
high variance in the results has been suppressed because
log scales are used for both axes. Despite the noise
problems the source spectrums computed with the simplified
theory have the correct general appearance above 1 Hz where
the signal-to-noise ratio is better.

Since pre-event noise was subtracted from the data
prior to analysis, low signal-to-noise ratio values will
strongly effect the shape of the final source spectrums.
Pre-event noise was relatively flat above 1 Hz but rose to
high values below 1 Hz. As a result the source term
determinations below 1 Hz are strongly affected while those
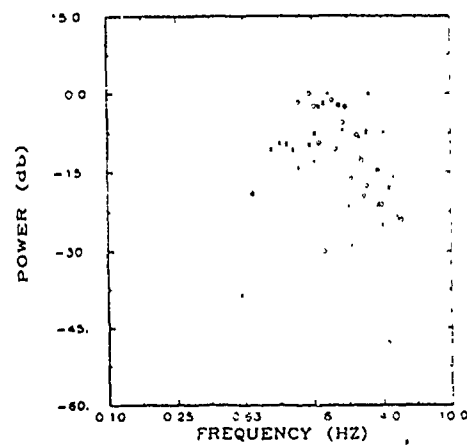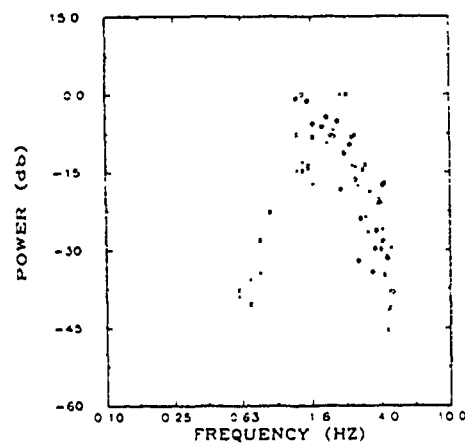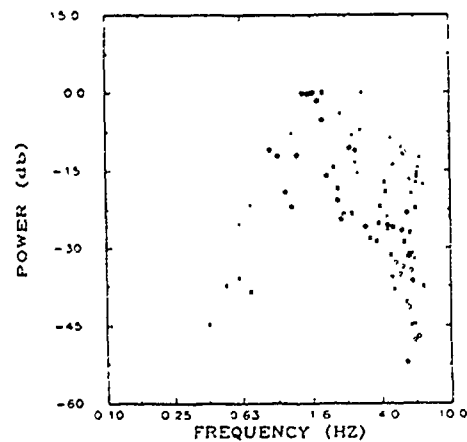
Figure 11. $(A/t^2)$ model source term solutions for Events 1, 2 and 3 at station RSON. Plot is spectral power in db down from maximum with the instrument response removed. Symbols represent the three components: vertical (+), radial (x) and transverse (o).

114

above 1 Hz are not.

Based on the encouraging results from this small test a more extensive study was undertaken in which both the inversion results from the $(A/t^2)$ and $(A/t)$ models are used. Details of this work can be found in paper 3 and will not be discussed any further here.

## DETAILED RESULT COMPARISONS

Three types of composite displays are provided for the coda-Q estimates. The first is a plot by common component (vertical, radial and transverse). The second is by common event (1, 2 and 3) and finally by common recei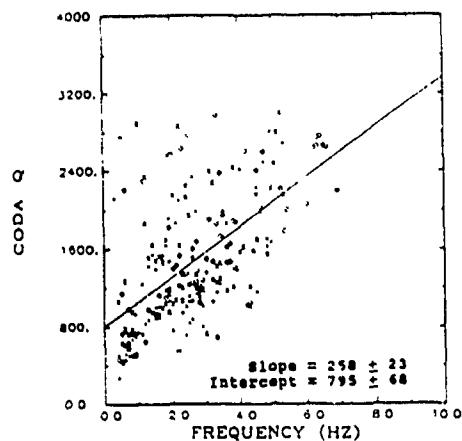ving station (RSON, RSNT, RSSD, RSCP and RSNY). The $(A/t^2)$ and $(A/t)$ model results for each of the 3 composite displays will be shown together for easier comparison.

The coda-Q versus frequency results are plotted by common component for the $(A/t^2)$ model in figure 12 and $(A/t)$ model in figure 13. In both cases a similar distribution in coda-Q is observed between the different components. This indicates that each component is providing a measure of similar earth properties. Coda-Q is seen to range between 400 and 2800 for both the $(A/t^2)$ and $(A/t)$ model results.

Shown in figures 14 and 15 are the $(A/t^2)$ and $(A/t)$ model results respectively for coda-Q versus frequency by event. These displays have a similar distribution and variance in coda-Q values as observed in the component sorted results. If large differences were observed between the two shallow explosions (events 1 and 2) and the deep earthquake, it could imply near-source scattering effects.

VERTICAL

Slope = 258 ± 23
Intercept = 795 ± 68

RADIAL

Slope = 269 ± 22
Intercept = 849 ± 62

TRANSVERSE

Slope = 246 ± 21
Intercept = 894 ± 63

Figure 12. $(A/t^2)$ model coda-Q versus frequency results by common component for all events and stations. The least-square best fit line is shown. Symbols represent the three events: Event 1 (+), Event 2 (x) and Event 3 (o).

VERTICAL

CODA Q

Slope = 200 ± 25
Intercept = 936 ± 69

FREQUENCY (HZ)

RADIAL

CODA Q

Slope = 163 ± 19
Intercept =1148 ± 57

FREQUENCY (HZ)

TRANSVERSE

CODA Q

Slope = 256 ± 18
Intercept = 903 ± 53

FREQUENCY (HZ)

Figure 13. (A/t) model coda-Q versus frequency results by
common component for all events and stations. The
least-square best fit line is shown. Symbols represent the
three events: Event 1 (+), Event 2 (x) and Event 3 (o).

117

EVENT 1

CODA Q — FREQUENCY (HZ)

Slope = 303 ± 25
Intercept = 667 ± 68

EVENT 2

CODA Q — FREQUENCY (HZ)

Slope = 218 ± 24
Intercept = 992 ± 65

EVENT 3

CODA Q — FREQUENCY (HZ)

Slope = 258 ± 19
Intercept = 849 ± 61
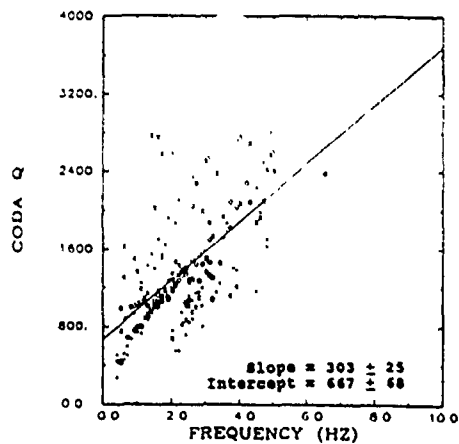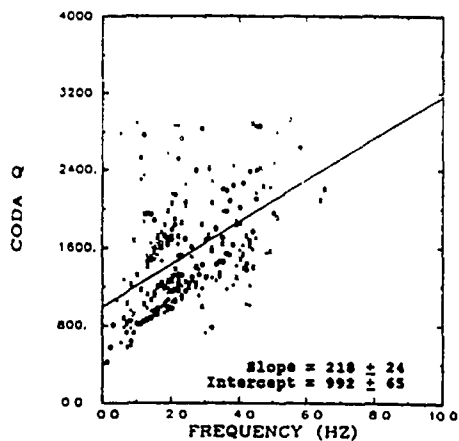
Figure 14. $(A/t^2)$ model coda-Q versus frequency results by common event for all stations and components. The least-square best fit line is shown. Symbols represent the 3 components: vertical (+), radial (x) and transverse (o).
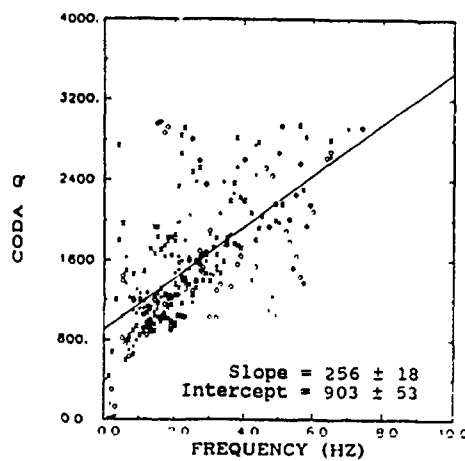
118

EVENT 1

EVENT 2

EVENT 3

Figure 15. (A/t) model coda-Q versus frequency results by common event for all stations and components. The least-square best fit line is shown. Symbols represent the 3 components: vertical (+), radial (x) and transverse (o).

119

No significant difference is observed suggesting that near-source scattering effects, if present, are poorly resolved.

Coda-Q versus frequency results plotted by common receiving station are given in figure 16 for the $(A/t^2)$ model and figure 17 for the $(A/t)$ model. For common receiver sorting the coda-Q solutions are observed to cluster along linear trends indicating a strong dependence on frequency and near-receiver earth properties. The large decrease in variability in both the $(A/t^2)$ and $(A/t)$ model displays with the common receiver sorting indicates that near-receiver scattering is the dominant contributor to teleseismic coda formation.

The $(A/t^2)$ model results in figure 16 for stations RSCP and RSNY between 1 and 2 Hz appears to have higher coda-Q values than the other receiving stations. The variance is also greater at RSCP indicating a lower signal-to-noise ratio for this station. RSCP and RSNY also appear to have anomalous slopes of coda-Q with frequency compared to RSON, RSNT and RSSD. To test if the slope of the coda-Q with frequency relationship at station RSCP is similar to that at RSNY the poor data at RSCP were edited and the least-square analysis repeated. The edited and unedited data are shown in figure 18. The least-square best fit line for station RSCP after editing is equal to that at station RSNY.

A similar argument for the RSCP and RSNY station is more difficult for the $(A/t)$ model results in figure 17. This is due to the very high variability in these displays

## RSON

## RSCP

## RSNT

## RSNY

## RSSD
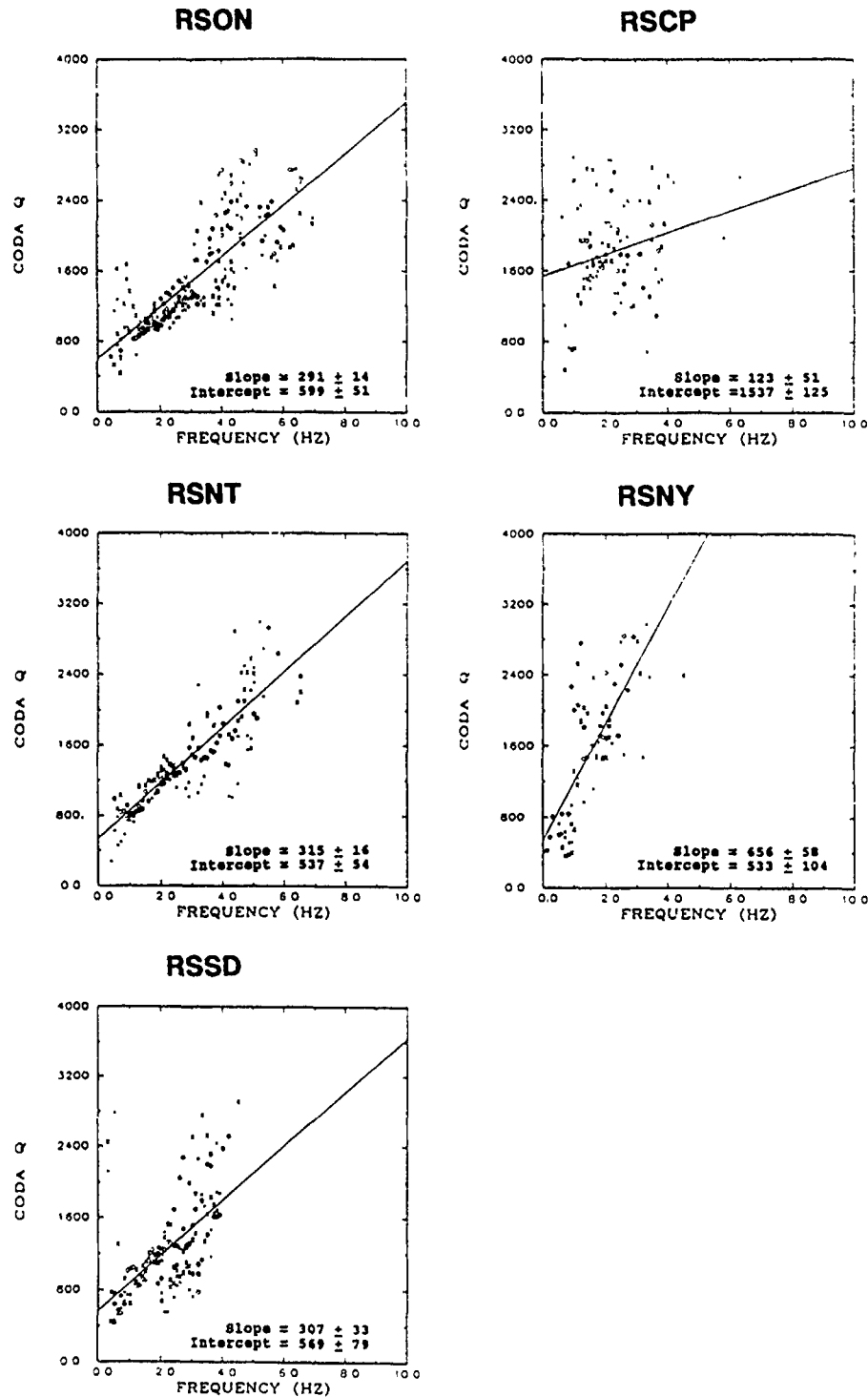
Figure 16. $(A/t^2)$ model coda-Q versus frequency results by common receiving station for all events and components. The least-square best fit line is shown. Symbols represent the 3 components: vertical (+), radial (x) and transverse (o).
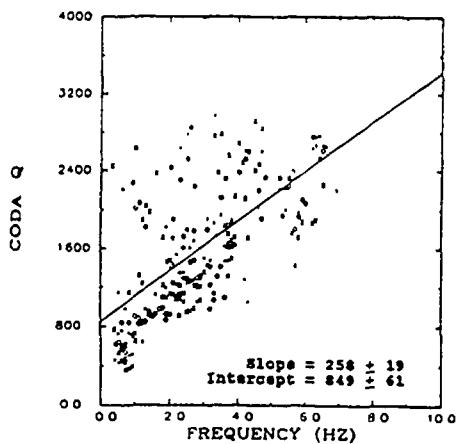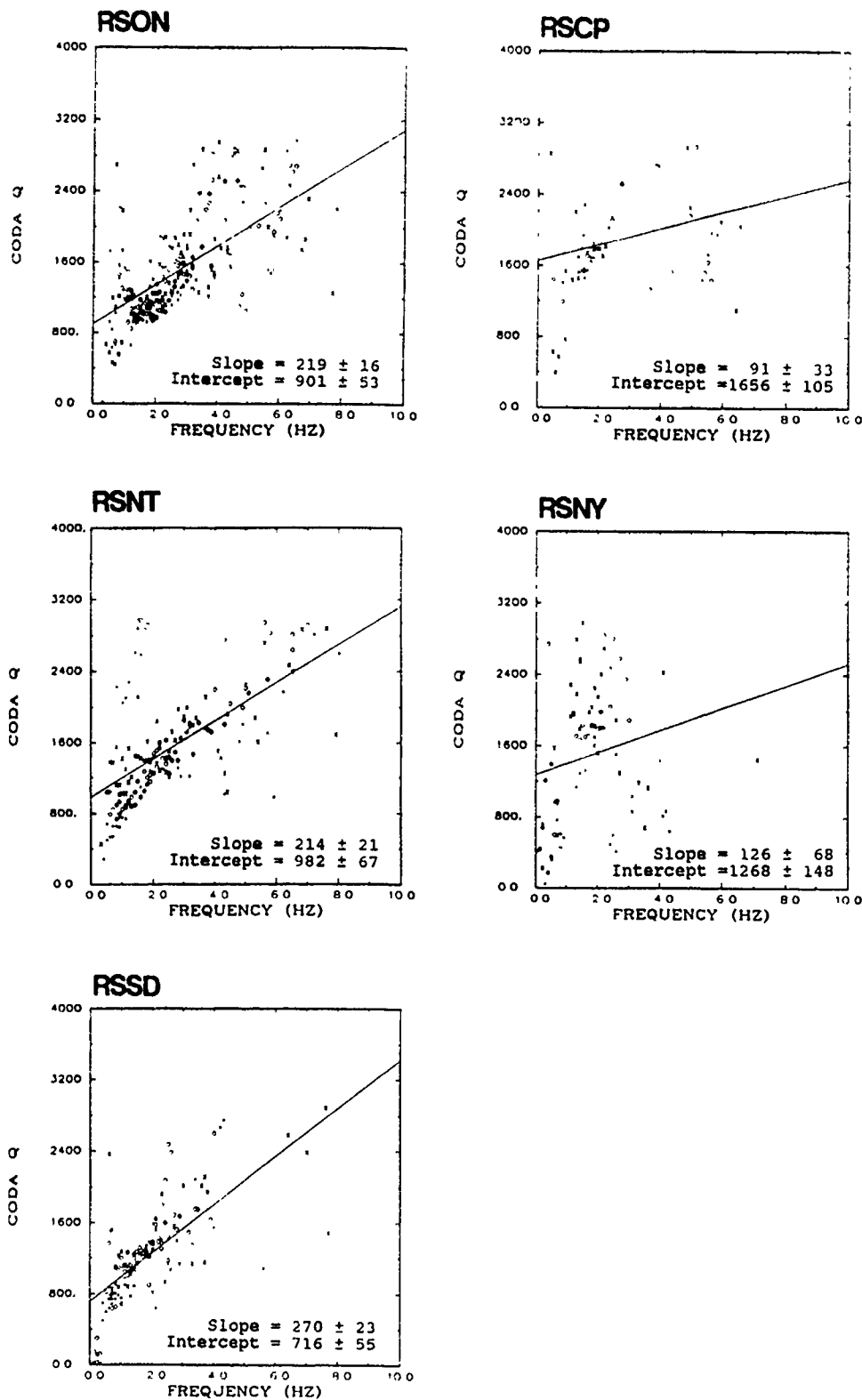
Figure 17. (A/t) model coda-Q versus frequency results by common receiving station for all events and components. The least-square best fit line is shown. Symbols represent the 3 components: vertical (+), radial (x) and transverse (o).

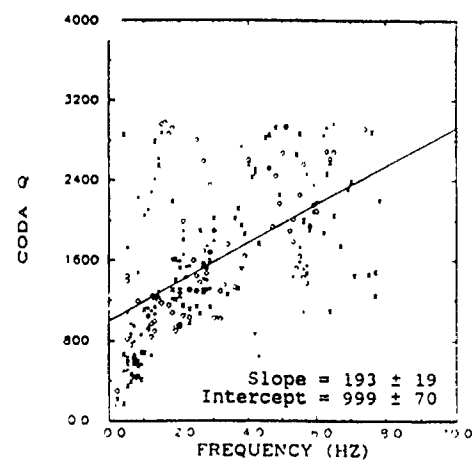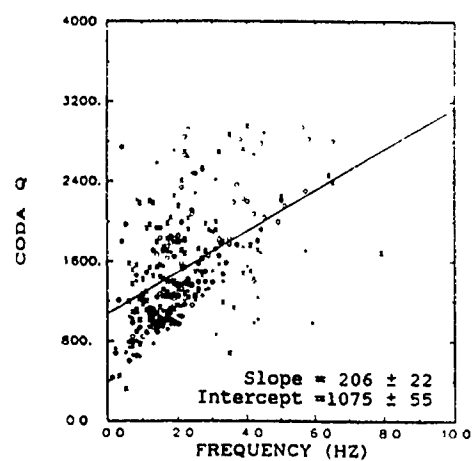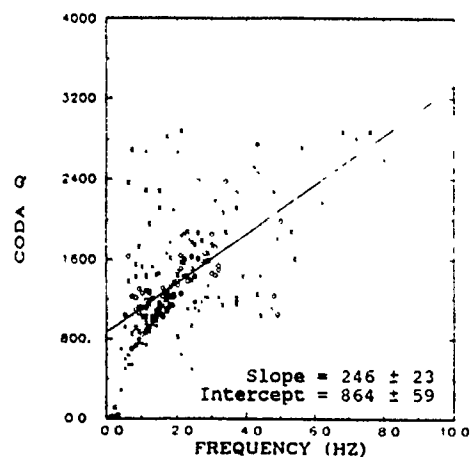122
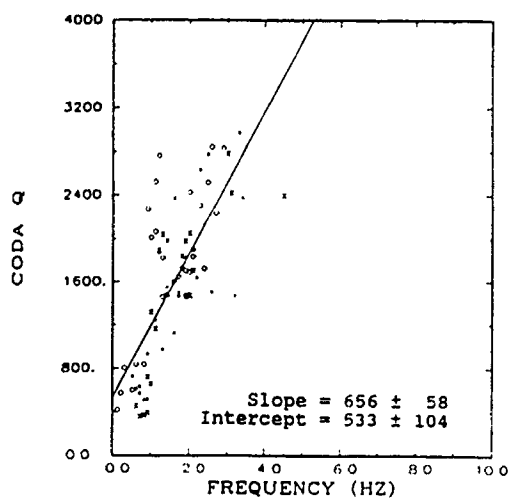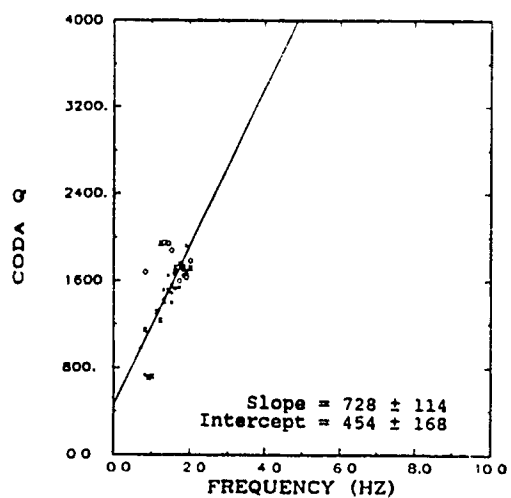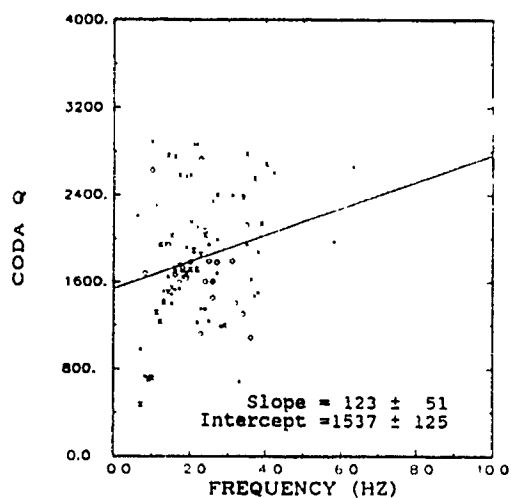
Figure 18. Edit test of $(A/t^2)$ model coda-Q solutions at station RSCP. Trend at station RSCP is similar to station RSNY after editing poor data.

123

which make the trends harder to interpret.

The observed range of coda-Q values for both the $(A/t^2)$ and $(A/t)$ model results are very similar in all the displays. The fact that both models produce similar coda-Q estimates is in agreement with the synthetic tests in paper 2. The $(A/t^2)$ model appears to produce results with lower variance compared to the $(A/t)$ model. The best fit lines in figure 17 for the $(A/t)$ model results do not follow the data trend as well as in the $(A/t^2)$ model results in figure 16. The large amount of scatter in the data points is corrupting the least-square fitting process.

The above observations suggest that qualitatively the $(A/t^2)$ model fits the data better than the $(A/t)$ model, but is that supported with quantitative evidence? One measure of which model fits the data better is the number of stable inversion solutions obtained by each model for the same data. Another measure of which model best fits the data is the sum of the square of the residuals (referred to as SSR in the text that follows). The SSR is a measure of how closely the data points follow the model curve. Table 3 gives the number of stable solutions and SSR for both models on a representative suite of the data.

To effectively use the number of stable inversions and the SSR as a measure of best model, it must be assumed that a stable inversion always implies a proper fit and therefore a good coda-Q estimate. Based on the high variances and evidence that the $(A/t)$ model appears to be finding more solutions above 5 Hz where the signal-to-noise ratio is poor (figures 16 and 17, station RSCP) this

assumption is probably not valid. It is therefore difficult
to draw any conclusions from table 3. The small magnitude
of the differences and the fact that no consistent trend is
observed suggests that both models fit the data equally
well.

Table 3.--Quantitative comparison of the $(A/t^2)$ and $(A/t)$
model fits to the data, shown are the number of stable
solutions and the SSR for a representative subset of data

| NUMBER OF SOLUTIONS BY EVENT (0-10 Hz, Z-component at RSON) | | | |
|---|---|---|---|
| MODEL | EVENT 1 | EVENT 2 | EVENT 3 |
| $(A/t^2)$ | 28 | 29 | 36 |
| $(A/t)$ | 22 | 26 | 27 |

| NUMBER OF SOLUTIONS BY COMPONENT (0-10 Hz, Event 2 at RSNT) | | | |
|---|---|---|---|
| MODEL | Z-COMPONENT | R-COMPONENT | T-COMPONENT |
| $(A/t^2)$ | 34 | 30 | 40 |
| $(A/t)$ | 23 | 40 | 53 |

| NUMBER OF SOLUTIONS BY STATION (0-10 Hz, Event 3, Z-comp.) | | | | | |
|---|---|---|---|---|---|
| MODEL | RSON | RSNT | RSSD | RSCP | RSNY |
| $(A/t^2)$ | 36 | 6 | 23 | 20 | 15 |
| $(A/t)$ | 27 | 11 | 26 | 19 | 18 |

| SUM OF THE SQUARE OF THE RESIDUALS BY EVENT (Station RSON) | | | | | |
|---|---|---|---|---|---|
| | EVENT 1 | | EVENT 2 | | EVENT 3 | |
| FREQUENCY | $(A/t^2)$ | $(A/t)$ | $(A/t^2)$ | $(A/t)$ | $(A/t^2)$ | $(A/t)$ |
| .8 | 626 | 651 | 307 | 306 | 611 | 640 |
| 1.4 | 861 | 834 | 1262 | 1254 | 1032 | 1051 |
| 2.1 | 1551 | 1536 | 1707 | 1726 | 543 | 518 |
| 3.0 | 624 | 624 | 361 | 338 | 561 | 561 |

Another means of quantifying which of the models is a
better fit to the data that is also sensitive to the
quality of the final results is the least-square best fit
line. The assumption is made that the coda-Q values follow
a linear trend increasing with frequency. The coda-Q
solutions from both models appear to suggest this type of

125

relationship. The standard deviation of the y-intercept and slope, the X-Y correlation coefficient and residuals from the least-square best fit line analysis is given in table 4. The standard deviations of the slope and y-intercepts are comparable for all stations between the two models. However, the X-Y correlation coefficients are higher and the residuals lower for the $(A/t^2)$ model results, except at station RSSD. These results are in agreement with the visual appearance of plotted coda-Q values.

Table 4.--The least-square best fit line analysis

$(A/t^2)$ MODEL

| STATION | STANDARD DEVIATION | | X-Y | |
| | Y-INTERCEPT | SLOPE | CORRELATION | RESIDUALS |
| --- | --- | --- | --- | --- |
| RSON | 50 | 14 | .81 | 346 |
| RSNT | 80 | 24 | .68 | 454 |
| RSSD | 79 | 33 | .60 | 427 |
| RSCP | 125 | 51 | .23 | 536 |
| RSNY | 125 | 69 | .73 | 501 |

$(A/t)$ MODEL

| STATION | STANDARD DEVIATION | | X-Y | |
| | Y-INTERCEPT | SLOPE | CORRELATION | RESIDUALS |
| --- | --- | --- | --- | --- |
| RSON | 53 | 16 | .64 | 437 |
| RSNT | 67 | 21 | .61 | 491 |
| RSSD | 55 | 23 | .69 | 389 |
| RSCP | 105 | 33 | .28 | 550 |
| RSNY | 148 | 68 | .20 | 756 |

The major difference between the $(A/t^2)$ and $(A/t)$ model results appears to be a larger degree of variance in the $(A/t)$ model result displays. This suggests that the $(A/t^2)$ model fits the data better and produced more

reliable coda-Q estimates than the (A/t) model. A possible explanation for this can be seen in figure 2. Because the time dependent term is not well separated from the time independent term the inversion explains some of the later part of the coda with the former. Note how the model curve drawn through the latter part of the coda in the lower display in figure 2 does not follow the data as well as in the upper display. However when the time dependent and independent terms are summed and the resulting model curves displayed over the data (figure 5) there is good agreement in both cases.

The inability of the (A/t) model to fit steep decays in the early part of the coda suggests that the (A/t) model is explaining mainly the later part of the coda. This splitting of the later coda energy between the two terms may result in biased coda-Q estimates which could explain the high variances in the displays. Comparison of the $(A/t^2)$ and (A/t) models in paper 2 using synthetics supports this interpretation. Based on this limited comparison the $(A/t^2)$ model appears to describe coda with a large multiple energy component at teleseismic distances better than the (A/t) model.

Because the $(A/t^2)$ model appears to produce more consistent results they will be used in the following quantitative comparisons to other studies of earth Q. To quantify the frequency dependence of coda-Q, $f^n$ is computed from the least-square best fit line for the $(A/t^2)$ model results sorted by receiving station. The value n is computed from results at two different frequencies by the

following relation:

$$( Q/Q_0 ) = ( f/f_0 )^n$$

| STATION = | RSNT | RSON | RSSD | RSNY | RSCP |
|-----------|------|------|------|------|------|
| n = | .56 | .52 | .54 | .72 | .16(.73) |

Stations RSON, RSNT and RSSD have very similar coda-Q versus frequency relations. Stations RSCP and RSNY appear to have anomalous slopes that could be due to the lower signal-to-noise ratios observed at these stations. Based on the discussion for figure 16, the results for RSCP may be in error due to low signal-to-noise ratio. A value of n =.73 similar to RSNY was computed for station RSCP when the poor data was edited prior to least-square fitting. Values of slope reported by Jin et al., (1985) ranged between .46-.61 for local events in old (stable) and young (active) oceanic areas respectively. The slopes computed in this study are in qualitative agreement with theirs.

Figure 19 is a comparison between coda-Q results of this study and those of Singh and Herrmann (1975) from local and near regional coda analysis. A similar relationship is observed between the coda-Q results from this study and their independent results using short source-to-receiver separations. With short source to receiver separations scattering processes near the source or receiver provide measures of similar earth properties. Agreement between local and teleseismic coda-Q results supports the conclusion that teleseismic coda-Q estimates are controlled by near receiver scattering and provide a measure of earth properties near the receiving station.

The frequency dependence of teleseismic coda-Q
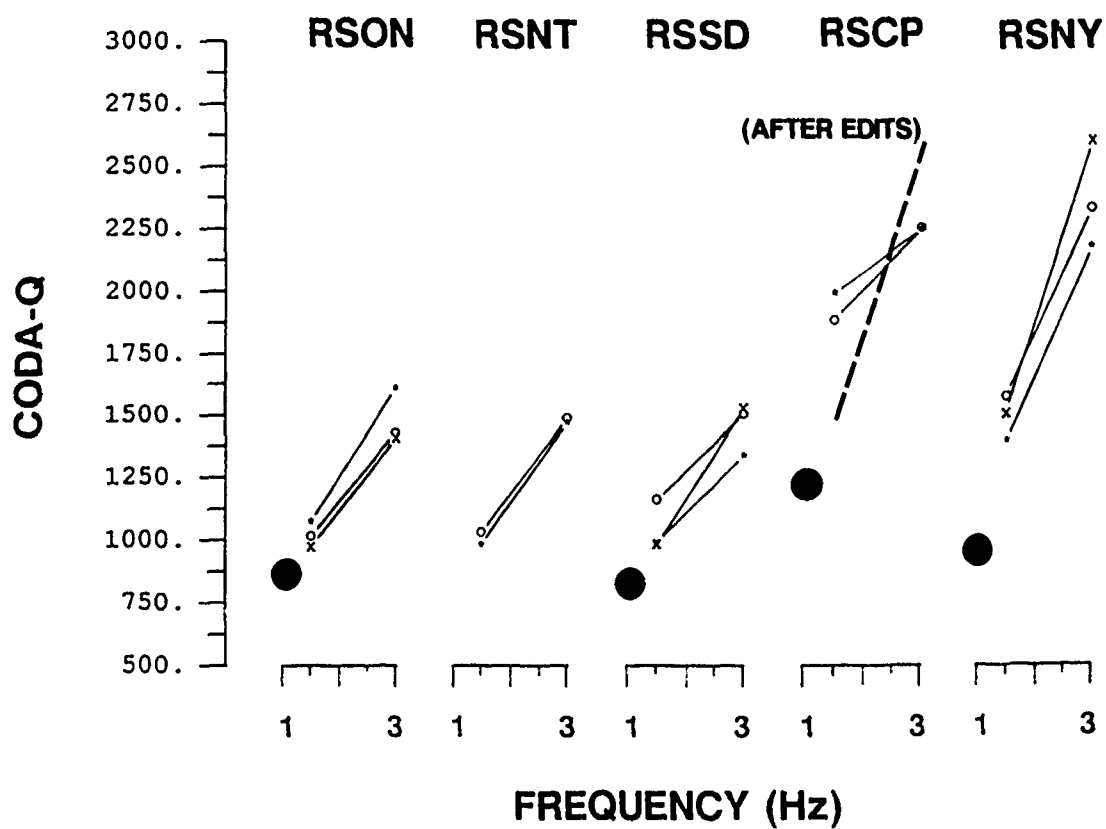
Figure 19. $(A/t^2)$ model coda-Q versus frequency solutions by common receiver. Plotted is the least-square best fit to the solutions from this study, event 1 (*), 2 (o) and 3 (x). The local coda-Q results from Singh and Herrmann (1983) are also shown (●).

estimates are compared to those from local coda-Q analysis in figure 20. Good agreement is observed between both the absolute magnitude and slope of the coda-Q with frequency relations.

## CONCLUSIONS

The GLI approach described in this paper is an alternative method for model fitting in coda analysis. It has the advantage of using the whole coda where signal is sufficiently above noise rather than small subsets of the coda.

The $(A/t^2+B)\exp(-Ct)$ model produced more consistent results than a $(A/t+B)\exp(-Ct)$ model. Application of the combined single plus triple body wave backscattering model (Gao et al., 1983b) with the $(A/t^2+B)\exp(-Ct)$ form provided a means of obtaining stable estimates of coda-Q when multiple scattering effects are present. Coda-Q determined from fitting the single scattering model alone when multiple scattering effects are present would produce biased solutions. A Monte Carlo error analysis indicates that reliable results are obtainable with the GLI coda analysis approach for levels of random noise observed in teleseismic data. The details of the Monte Carlo test and the bias test are the subject of paper 2.

For the teleseismic P-wave codas analyzed in this study a model which accounts for both single and multiple scattering effects was found to be necessary. Due to the strong multiple scattering effects the observational data could not be properly fit with the single scattering model alone. The results of a test to convert the A and B model
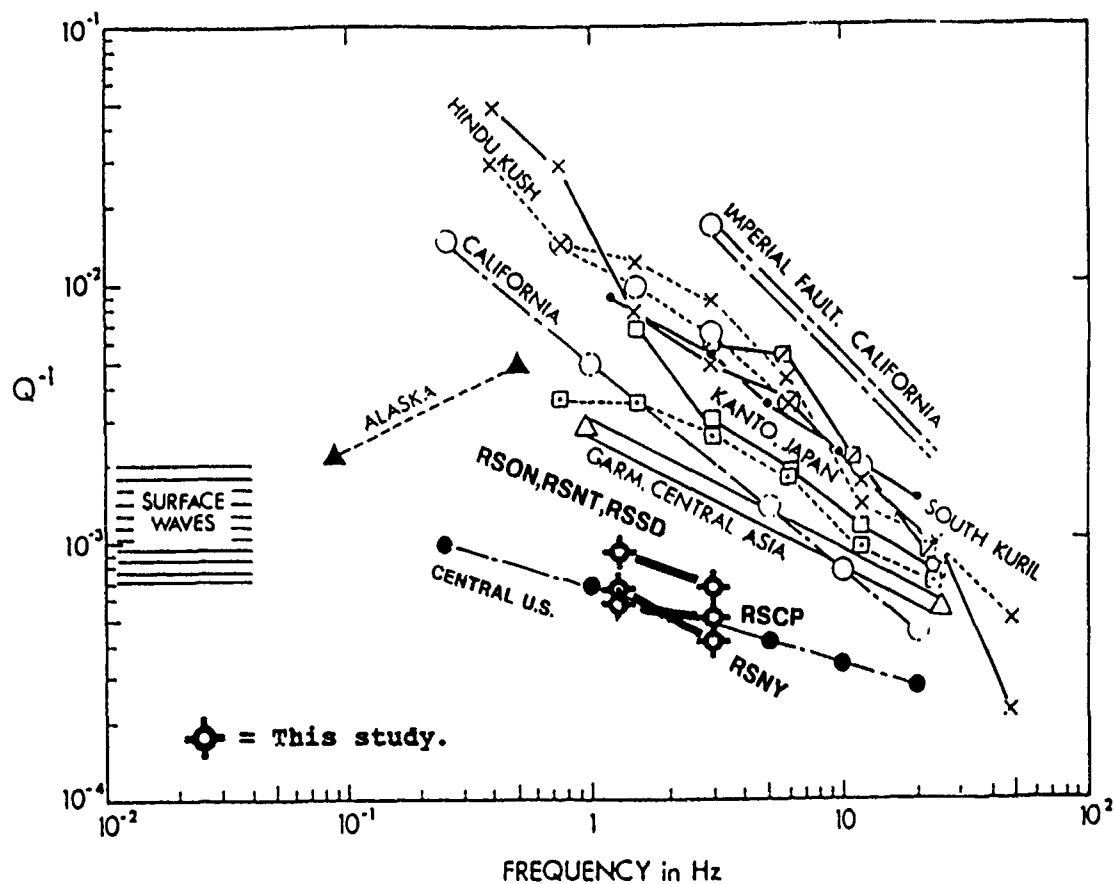
Figure 20. The frequency dependence of coda-Q for local earthquakes as summarized by Aki (1980a,b). The lowest frequency data are those from fundamental surface waves. The teleseismic coda-Q results from this study are plotted for comparison.

131

parameters into earth turbidity and source spectral
estimates were encouraging, a more detailed study of this
is the subject of paper 3.

The coda-Q values predicted in this study are found
to be in agreement with other estimates in the literature.
Coda-Q values increased with frequency in all cases in the
range from approximately 800 to 1600 from 1 to 4 Hz. Slopes
of the best fit lines ranged between $f^{.52}$ and $f^{.73}$. The
slope at station RSCP computed from the least-square best
fit line was questionable due to low signal-to-noise ratio,
but was found to be closer to that of station RSNY ($f^{.72}$)
when editing is performed prior to least-square fitting.
Higher coda-Q values of 1600 at 2 Hz were observed at
stations RSCP and RSNY, compared to 1100 at stations RSON,
RSNT and RSSD.

A strong relationship between coda-Q and near-
receiver scattering was observed. The coda-Q displays
have a large variance except when the results are plotted
by common receiving station. No near-source scattering
differences were observed between shallow explosions and a
deep earthquake. In fact, almost identical coda-Q estimates
were obtained for these two cases. There is good agreement
between the coda-Q results of this study and other
published Q values from local and regional work. These
agreements support the conclusion that the coda-Q values
estimated from teleseismic coda using the methods described
in this paper provide information about earth properties
near the receiver. Near-source scattering effects were not
found to be resolvable in this study.

# PAPER II

## SUMMARY

Two-term models of the form $(A/t^2+B)\exp(-Ct)$ and $(A/t+B)\exp(-Ct)$ where found to characterize both the single and multiple scattering effects in coda. Both of these models will estimate coda-Q values that are equal within error but the A and B model parameters are very different. Inversion stability may be useful in determining which of these models is the appropriate one to use for different data types. Instabilities occurred because the $(A/t+B)\exp(-Ct)$ model does not adequately describe steep decays at early times. The A and B model solutions were affected most by this deficiency. The two-term model parameter estimates were found to be consistent with respect to random noise, parameter magnitude and type of multiple scattered energy present in the data.

Strongly biased solutions were obtained when the scattering model used in the analysis differed significantly from the type of scattering present in the data. Bias is defined as the percent difference between a known solution and one computed from a coda analysis inversion. When the single scattering model was fit to data with multiple scattering, coda-Q values were biased by as much as 280% and the product of turbidity and source term by 267%. The bias in coda-Q was 29%, turbidity 55% and

source term 170%, when the $(A/t^2+B)\exp(-Ct)$ model was fit to data which contained only single scattering.

The two-term models were fit to data containing different orders of multiple scattering and the bias decreased as additional orders of multiple scattering, up to 4th order, were added to the input data. The bias to coda-Q in this case was 9%, turbidity 14% and source term 110%. This bias is similar in magnitude to that introduced by 10-20% random noise. Similar to the effects of random noise, the bias due to fitting inappropriate models was found to affect the source term parameter the most and coda-Q the least. No significant frequency dependent bias was observed.

Tests performed with the energy-flux model showed that the two-term models produced similar Q estimates when intrinsic Q effects dominated over scattering Q effects (scattering Q is large). Agreement between these models implies that two-term models can be used in place of the single scattering model for coda-Q estimation when multiple scattering effects are present in the data.

## INTRODUCTION

This is the second of three papers which address the issue of how to deal with multiple scattered energy in coda analysis. The first paper (Soroka and Stump, 1991) deals with coda-Q estimation and will be referred to as paper 1 in the following text. The third paper (Soroka, Stump and Dainty, 1991) referred to as paper 3 in the text, deals with earth turbidity and source spectral estimation in coda analysis. In this paper a study using synthetic data is

undertaken to determine if simple two-term models could be
used in coda analysis to describe single plus multiple
scattered coda energy. The effects of different types
of scattered energy, coda duration and random noise on coda
analysis solutions are described. Different scattering
theories are compared to better understand their
similarities, differences and limitations to help justify
the application of two-term models. The results of this
study also demonstrate the effect an incorrect model could
have on coda analysis estimates when it is difficult to
determine the correct model to use.

The analysis of coda, the random energy that
immediately follows a body wave arrival, has been shown to
provide useful estimates of earth and source properties
such as Q, turbidity and source spectrums (Aki and Chouet,
1975; Herraiz and Espinosa, 1988; Rautian and Khalturin,
1978; paper 1). A coda analysis involves fitting a model to
observational data and then computing earth and source
properties from the model parameters.

Because it is not always possible to record data
close to an event, coda analysis work has begun to be
extended to teleseismic distances where codas are dominated
by multiple scattering effects. The approach used by
some authors has been to fit the single scattering model in
the same manner as with local and regional studies, even
though multiple scattering effects were suspected in the
data. The approach used successfully in paper 1 is to fit a
two-term model to better account for the multiple scattered
energy. A two-term model approach would be equally

applicable at local and regional distances when multiple scattering effects are present in the data.

Selection of the appropriate model to fit to observational data in a coda analysis is a very important consideration. In paper 1 the $(A/t^2+B)\exp(-Ct)$ and $(A/t+B)\exp(-Ct)$ models hereafter referred to as the $(A/t^2)$ and $(A/t)$ models respectively were found to fit the spectra of coda dominated by multiple scattered energy. The $(A/t^2)$ model was found to produce coda-Q estimates with lower variances than the $(A/t)$ model in that study. Figure 1 is a representative fit of the $(A/t^2)$ model to time varying teleseismic P-wave coda spectra. In the upper display the time dependent and time independent terms are plotted separately and in the lower display the sum of the two terms is plotted. There is good agreement between the model and data. The time dependent term is necessary to describe the early single scattering effects and the time independent term is necessary to describe the later multiple scattering effects. The $(A/t)$ model was found to produce a similar match but was deficient in modeling steep decays at early times.

In this second paper an objective is to quantify the appropriateness of using simplified $(A/t^2)$ or $(A/t)$ models in coda analysis so that multiple scattered energy can be included in the analysis. To better understand the appropriateness of using these simple two-term models, comparisons are made between them and the commonly used single scattering model originally proposed by Aki (1969) and expanded to 3-D body waves by Gao et al. (1983b) and
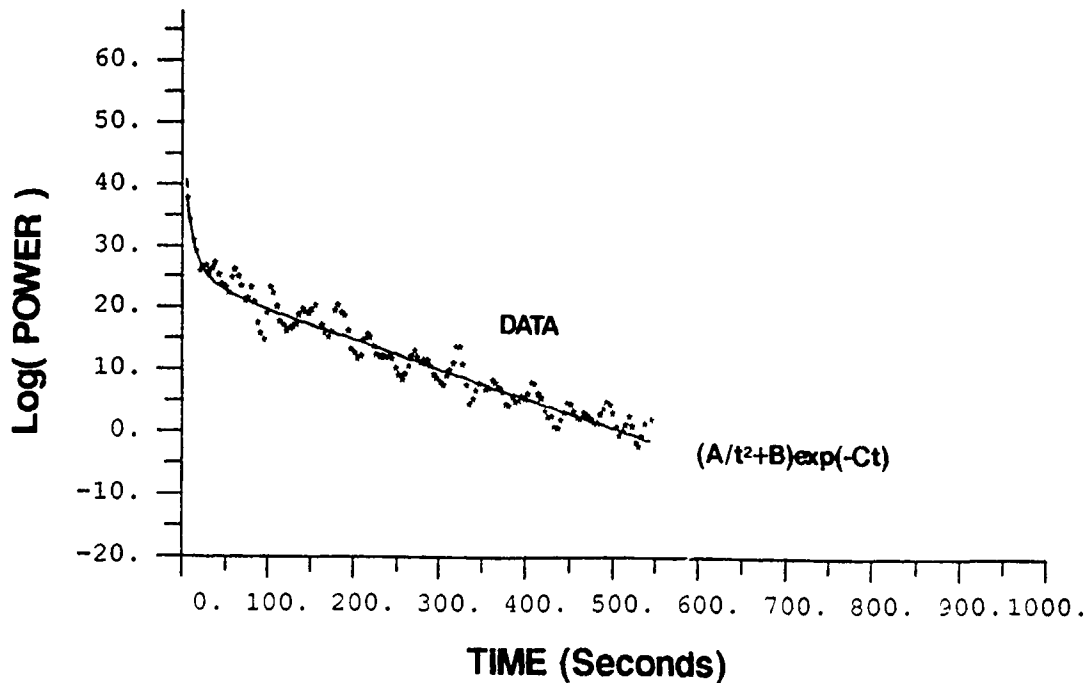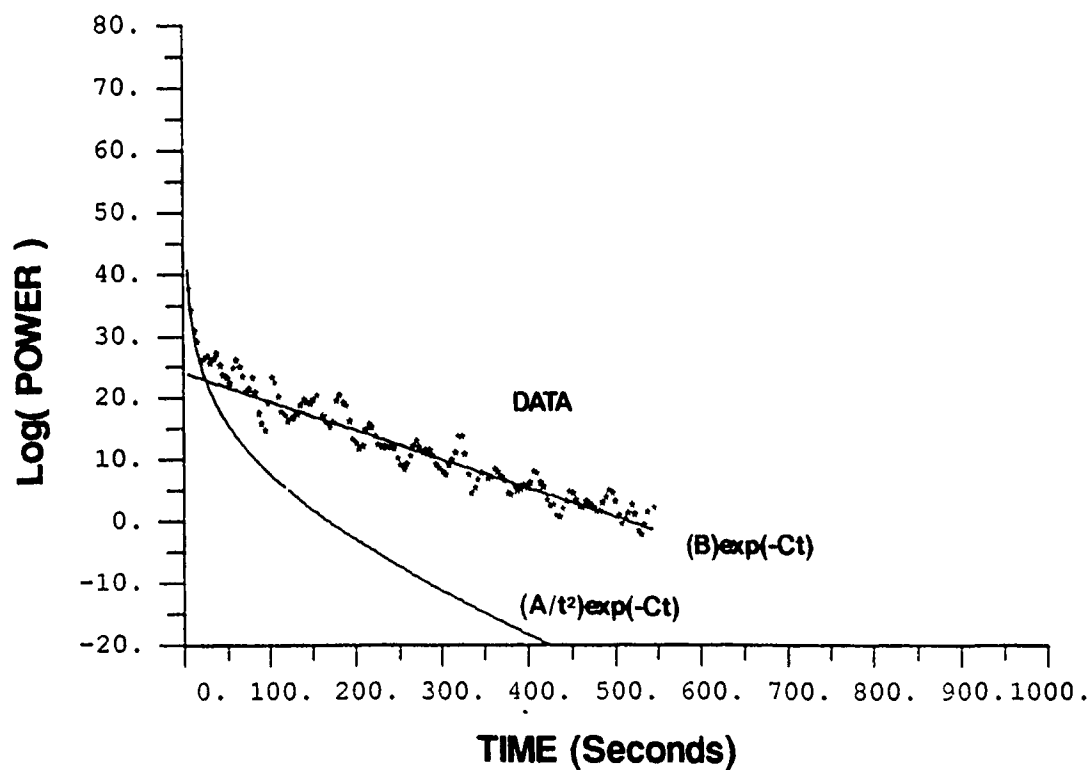
Figure 1. The $(A/t^2+B)\exp(-Ct)$ model fit to time varying spectral data (points). In the upper case the two terms are plotted seperatly and in the lower case their sum is plotted. The data is for Event 3 at station RSON, 2 Hz.

the energy-flux model of Frankel and Wennerberg (1987).

The approach that will be used to better understand the bias issues is to utilize synthetics where model parameters determined by inversion can be compared directly with known solutions. Synthetic tests give us insight into errors expected when observational data is analyzed. Bias is computed as the percent difference between the analysis estimate and the known value.

$$bias = \left( \frac{| known - estimate |}{known} \right) 100$$

Variance (standard deviation) by comparison is a measure of the amount a value can be expected to vary around the true value. Variance gives the uncertainty in a solution. The average from many experiments would yield the true solution if no bias were present.

## TWO-TERM MODEL ASSUMPTIONS

It is common practice to represent complicated geophysical processes by simplified models in the hope of gaining insight into the fundamentals of the problem. The wide use of Aki's, one term, single scattering model to estimate earth Q is just one example which demonstrates the validity of this approach. Extension of the one term single scattering model to two-terms so that multiple scattering effects can be used in a coda analysis is also a simplification of a complex problem.

In order to map the model parameters to more useful earth and source property estimates the $(A/t^2)$ and $(A/t)$ models must be equated to an appropriate scattering theory.

The $(A/t^2)$ model is the form of first and third order body wave backscattered energy (Gao et al., 1983b). This theory is based on elastic wave propagation with the following assumptions:

1) The seismic energy emanates from a point source
2) The source and receiver are located at the same position
3) The Born approximation is used and so energy is not conserved in the system of equations

The effect of the above assumptions is one of the issues of this study. These assumptions are minimized in the teleseismic problem if the scattered waves which form the coda can be regarded as the superposition of secondary waves which are the sum of many small independent events resulting from the scattering interactions (Aki, 1969). If the scattering occurs close to the receiver the effect of the coincident source-receiver and point source assumptions are therefore minimized. Strong evidence was found in paper 1 to suggest that near receiver scattering is responsible for most coda generation at teleseismic distances. The effect of the Born approximation is more difficult to resolve; however, coda-Q estimates in paper 1 are in agreement with other independent Q estimates. Comparison of the $(A/t^2)$, $(A/t)$ and energy-flux models later in this paper also shows that these assumptions may not present a significant problem, at least to the coda-Q estimates.

The above assumptions are not as serious at short source-receiver separations as they are at large

separations. In fact, to minimize the effect of the above
assumptions most coda analysis work has involved local and
regional distance data. With small source-receiver
separations the effects of both source-receiver coincidence
and the point source assumptions are thus minimized. The
fact that reasonable parameter estimates are obtained that
agree with other independent measures of the same
parameters suggests that the Born approximation is also not
a significant problem.

The (A/t) model represents an alternative two-term
model for describing coda which contains multiple scattered
energy. Like the $(A/t^2)$ model, the (A/t) model must be
equated to an appropriate scattering theory in order to
interpret the model parameters. The (A/t) model was shown
to be the correct form of scattered surface waves (Gao et
al., 1983a). Because of the supporting evidence that coda
generation is due to body wave scattered energy (paper 1),
surface waves have been ruled out as a significant
contributor to coda generation.

The (A/t) model also has the correct form of a plane
wave striking a layer of random scatterers plus P to Lg
(trapped shear) waves (paper 3). This alternative theory
provides a means of mapping the model parameters of the
(A/t) model to earth and source estimates. This plane wave
theory is more applicable to coda at teleseismic than local
distances. Because time is measured relative to the direct
arrival in this case and there are no assumptions regarding
source-receiver coincidence this theory is appealing.
However, higher order body wave scattering is assumed to be

negligible in this case.

In paper 1 it was shown that both the $(A/t^2)$ and $(A/t)$ models produced reasonable fits to coda spectral data which contained multiple scattered energy. The two theories will be compared quantitatively in the inversion results section to determine the degree of bias that would result if the wrong model was applied in the coda analysis.

## MODEL OVERVIEW

Because the $(A/t^2)$ model appeared to produce better coda-Q results in paper 1, it will be fit to the different data sets throughout this study and will serve as a basis for comparison. In order to determine the effect of the different tests on the inversion solutions the $(A/t^2)$ model parameters will be converted to earth and source property estimates using the Gao et al. (1983a and b) theory. Single scattering is defined as one scattering interaction between the source and receiver. Double scattering occurs when a wave undergoes a scattering interaction and the resulting scattered wave undergoes a second scattering interaction before reaching the receiver. Third and fourth order scattering are defined in similar fashion. Expressions for the first four orders of scattering are:

SINGLE

$$P_1(f,t) = \frac{2\ T\ S}{V\ t^2}\ \exp(-2\pi ft/Q) \tag{1}$$

DOUBLE

$$P_2(f,t) = \frac{2.46\ T^2\ S}{t}\ \exp(-2\pi ft/Q) \tag{2}$$

TRIPLE

$$P_3(f,t) = .716\ T^3\ V\ S\ \exp(-2\pi ft/Q) \tag{3}$$

141

**QUADRUPLE**

$$P_4(f,t) = .51 \, T^4 \, V^2 \, S \, t \, \exp(-2\pi f t/Q) \qquad (4)$$

Where:  P(f,t) = Spectral power with frequency and time

T = Turbidity

S = Source term

V = Average medium velocity

Q = Coda-Q

Coda-Q is the inverse of apparent attenuation and includes the effects of both intrinsic attenuation and attenuation due to scattering. Turbidity is a measure of a medium's ability to initiate scattering and the source term is an estimate of the source power spectrum (adapted from Gao et al. 1983a and b). Use of the single scattering model alone does not allow for the separation of turbidity and source term. However, with the $(A/t^2)$ model, which corresponds to single plus triple order scattering in the above equations, separation of the source and turbidity terms is possible.

The four types of scattering, equations 1-4, are displayed in figure 2 for comparison. Single scattering is seen to dominate the early part of the coda and decays quickly with time. Double scattering begins with lower magnitude than the single scattering model but decays more slowly. After a short time the double model curve rises above the single model curve indicating the dominance of double over single scattering in the coda decay curve. The triple scattering curve is a straight line on this log display because there is no time dependence other than the exponential term in this model. At long times third order
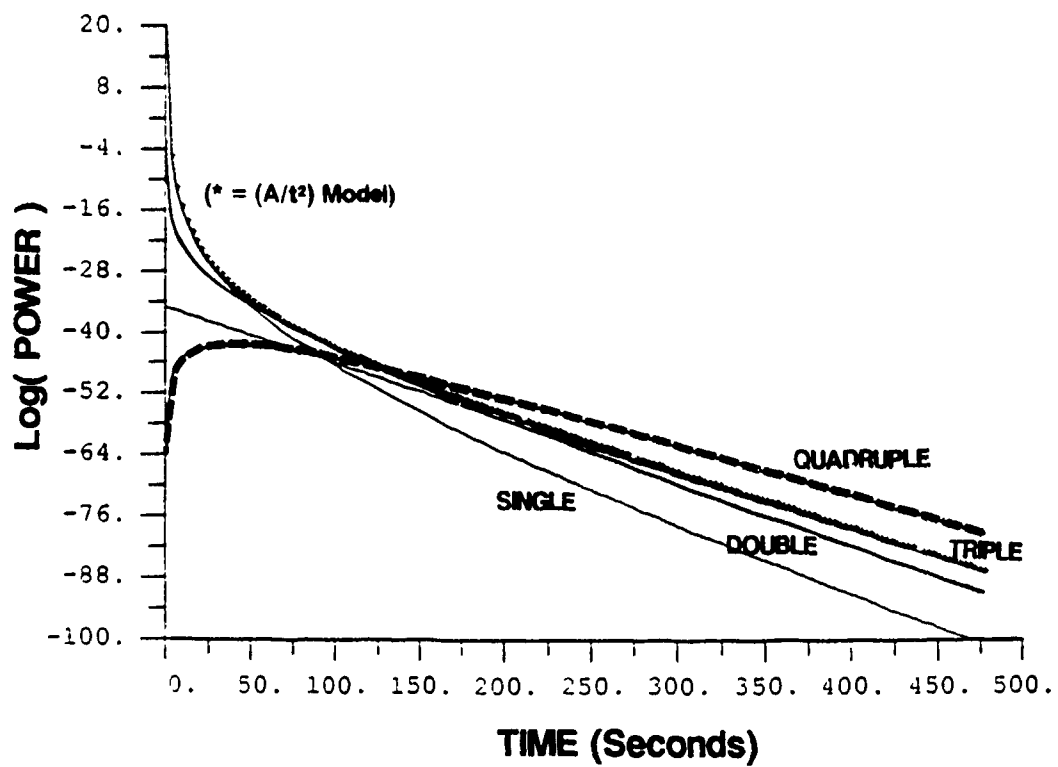
Figure 2. Comparison of different types of backscattered body wave models. Shown are the single through quadruple models and the combined single plus triple $(A/t^2)$ model.

scattering rises above the single and double model curves. Fourth order scattering has very low magnitude at early time but increases in amplitude until it rises above all the other models at longer times.

In summary the early part of the coda decay curve will be dominated by single scattering interactions. For a short transition time double scattering will dominate followed by triple and possibly quadruple order scattering very late in the coda. The single plus triple scattering model is also plotted in figure 2 for comparison. It is difficult to see because it is on or near the single scattering curve at early time, then the double scattering curve for a short time and finally the triple scattering curve at later time. The single plus triple model appears to represent a good average model of all these higher order scattering effects.

Because the $(A/t^2)$ model, equation 5, which includes first and third order scattering fits the data well a model that also included second order scattering, equation 6, might be even better.

$$( \frac{A}{t^2} + B ) \exp(-C\ t) \qquad (5)$$

$$( \frac{A}{t^2} + \frac{D}{t} + B ) \exp(-C\ t) \qquad (6)$$

Tests using a single plus double plus triple scattering model produced very unstable results. The extra free parameter "D" in equation (6) was not resolvable due to the short transition time in which this 2nd order scattering

144

term is the dominant contributor.

Since simple two-term models may not represent all types of scattering present in the data it is important to understand how the contributions of these other forms of scattered energy will affect the inversion solutions. The bias that results from ignoring double and quadruple scattering will be addressed latter in this paper.

## PARAMETER SENSITIVITY SYNTHETICS

By combining the four models discussed above (equations 1-4) five synthetics were created for input to the coda analysis program. The five models are listed below as well as the abbreviation that will be used throughout the remainder of this paper.

| SYNTHETIC DATA TYPES | ABBREVIATION |
|---|---|
| 1) Single | (single) |
| 2) Single + Double | (1+2) |
| 3) Single + Double + Triple | (1+2+3) |
| 4) Single + Double + Triple + Quadruple | (1+2+3+4) |
| 5) Single + Triple | (1+3) |

For coda analysis it is the combined effects of the individual models displayed in figure 2 that is important. Analysis of these synthetics can provide insight on the resolution of these different orders of scattering by the inversion. All five models include single scattering effects but differ in the type of higher order scattering added. The five models are compared in figure 3. The single scattering model is the lowest curve at long times on the display. This is due to the rapid decay of energy with time
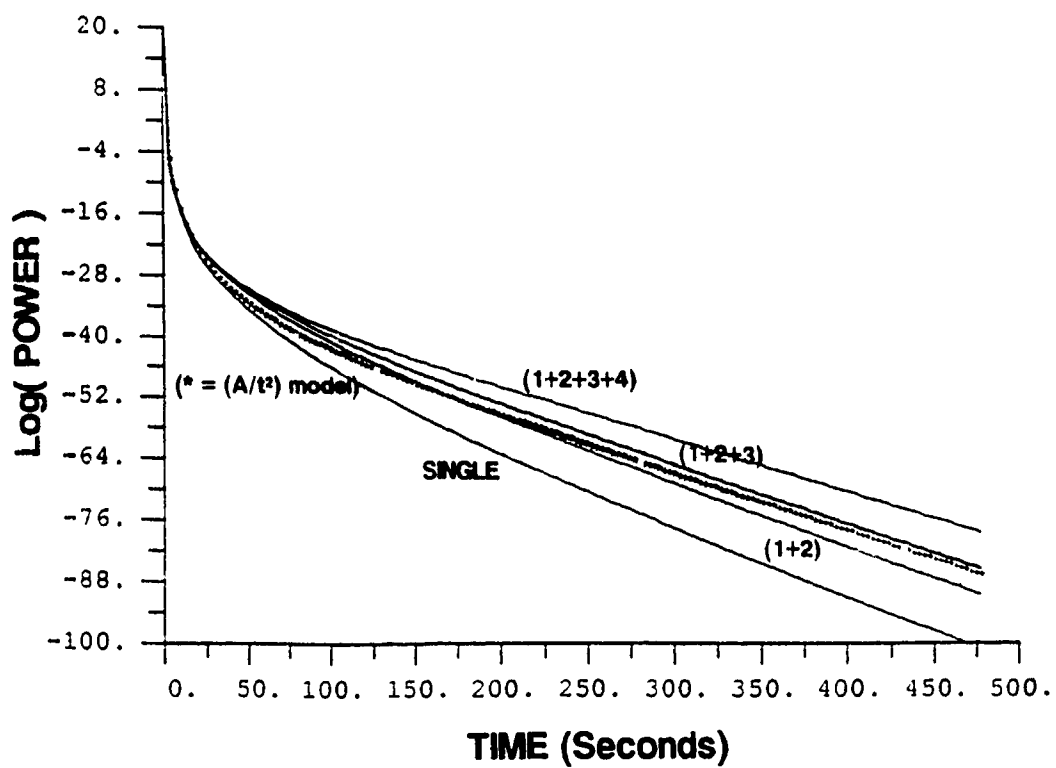
Figure 3. Comparison of the synthetic model data analyzed in this study. All the curves contain single scattering but different orders of multiple scattering.

when only first order scattering is present. As additional orders of scattering are added the decay with time becomes increasingly slower. The ($A/t^2$) model is equivalent to the 1+3 model and can be seen to fall between the 1+2 and 1+2+3 models. All the models converge toward the single scattering model at early times.

## INVERSION PROCEDURES

The five synthetic data sets described above were used as input to a coda analysis using Generalized Linear Inversion (GLI) techniques. Approximately 1% random noise was added to each data set to stabilize the inversion. Both the single scattering model, equation (1), of Gao et al. (1983b) and the ($A/t^2$) model, equations (1) plus (3), were fit to the synthetic data. For the single model fit coda-Q (Q) and the product of turbidity and source term (TS) are computed. With the ($A/t^2$) model fit it was possible to separate the turbidity and source term parameters. I. this case turbidity (T), source term (S) and coda-Q (Q) estimates are reported.

It was observed that the inversions would converge toward a reasonable solution for most input models. That is, the sum of the square of the residuals (referred to as SSR in the text that follows) between model and data would decrease in a systematic manner toward a minima. Low SSR's meant that the model and data were in good agreement, high SSR's meant poor agreement. If the input model was significantly different from the model being fit low SSR's may not be possible. In such cases unrealistic parameters (negative values) could be computed with eventual failure

of the inversion if the criteria to end the inversion was
not satisfied. For example, when fitting the $(A/t^2)$
two-term model to single scattering input the inversion
would be able to reduce the SSR's up to a point. To achieve
a better fit the amplitude of the time independent term
would have to go to zero so that only the time dependent
term would be fit to the input. This suggests that the
inversion approach, is model sensitive and a stable
solution is unlikely if the observational data are
significantly different from the model being fit. Rather
than reporting that the inversion failed or that a
parameter value of zero was obtained, the model fit with
the lowest SSR before the instability occurred is reported.

## INVERSION RESULTS

### THE $(A/t+B)\exp(-Ct)$ MODEL TESTS

In paper 1 both the $(A/t^2)$ and $(A/t)$ models were
found to describe coda dominated with multiple scattered
energy. Although the $(A/t^2)$ model solutions appeared better
because of lower variances in the displays there was still
room for debate. Because of the difficulty in determining
the appropriate model to use in a coda analysis these
models are compared here to better understand their
similarities and differences.

The $(A/t)$ model is the correct form of scattered
surface waves and scattered energy from a plane wave
striking a near surface layer. The time dependent term is
the correct form for single scattered events which result
when the plane wave strikes random scatterers. The time
independent term represents P to Lg energy trapped in the

layer under the receiver. The model parameters A and B in (A/t) model are interpreted differently depending upon whether the surface or plane wave model is assumed. The C term from which coda-Q is computed is however the same for all the models, including the $(A/t^2)$ model.

As a way of comparing the two models synthetic data are generated with the (A/t) model and the $(A/t^2)$ model is fit to that data. The A and B terms from the input model are compared to the inversion solutions to determine what effect the different time dependence of the single scattering term has on the model solutions. The known coda-Q value is also compared with the coda-Q inversion solution to determine the bias that would result from using these different models.

Table 1 gives the $(A/t^2)$ model coda-Q results for a range of different input model values. In each case the correct value of coda-Q was determined, within error, by fitting the $(A/t^2)$ model. Similar results were obtained when different values of A and B were used in the input model.

Table 1.--The 1+3 model Coda-Q solutions for a range of input model Q's

| KNOWN CODA-Q | INVERSION CODA-Q | % DIFFERENCE |
|---|---|---|
| 1000 | 998 | < 1% |
| 800 | 799 | < 1% |
| 600 | 599 | < 1% |
| 400 | 400 | 0% |
| 200 | 200 | 0% |

Shown in table 2 are the results of a test to

determine the effect of limiting the number of data points in the GLI analysis. The coda-Q solutions appear to be relatively robust in all cases tested. In the extreme case when only 10 samples were used only 12% difference was observed between the known and inversion coda-Q values. This could be attributed to the 1% random noise added to the synthetic data prior to analysis. These tests suggest that very similar coda-Q solutions would be obtained by fitting either the (A/t) or (A/t$^2$) models to observational data. In paper 1 these two models were fit to a suite of teleseismic coda and the range of coda-Q values obtained were the same in both cases. The results from fitting the (A/t$^2$) model had less variance than the (A/t) model suggesting the (A/t$^2$) model fit the characteristics of the data better. No evidence was found in the tests on synthetic to suggest a preference of one model over the other in coda-Q estimation.

Table 2.--(A/t$^2$) model coda-Q solutions as a function of number of analysis points, input data generated with the (A/t) model, 2 Hz case with 1% random noise

| Number of samples | KNOWN CODA-Q | INVERSION CODA-Q | PERCENT DIFFERENCE |
|---|---|---|---|
| 160 | 1000 | 999 | < 1% |
| 100 | 1000 | 998 | < 1% |
| 75 | 1000 | 979 | 2% |
| 40 | 1000 | 977 | 2% |
| 20 | 1000 | 910 | 9% |
| 10 | 1000 | 1123 | 12% |

The A and B model parameters will now be examined to

complete the comparison of the $(A/t^2)$ and $(A/t)$ models. The input model A and B parameters are compared to those determined by fitting the $(A/t^2)$ model in table 3. The results show significant differences between the A and B values. The low SSR's indicate that a good fit of the $(A/t^2)$ model to the data was obtained in each case. These good fits were obtained by decreasing the amplitude of the time dependent (A) term in the model and forcing the B term and exponential to explain the data. In other words, the $(A/t^2)$ term is inadequate to describe $(A/t)$ term effects early in the coda data but the later coda is described well with the B term. Higher levels of random noise or decreasing the number of analysis points did not change this situation.

Table 3.--Comparison of the input model and inversion solution A and B model parameters

| INPUT MODEL | | FINAL SOLUTION | | SSR |
|---|---|---|---|---|
| A | B | A | B | |
| 5.0 | 0.0875 | 1.3E-10 | 5.1 | 8.3 |
| 10.0 | 0.35 | 1.9E-17 | 10.5 | 8.3 |
| 50.0 | 8.75 | 7.9E-11 | 59.3 | 8.3 |
| 100.0 | 35.0 | 1.2E-10 | 136.2 | 8.3 |

The results of this test suggest that low residuals can be obtained by fitting either of these two models to observational data. Dramatically different values of the A and B model parameters will be obtained depending upon which model is used. Coda-Q estimates will be very similar regardless of which model is used. Selection of the

appropriate model to use is however important if the A and
B model parameters are to be properly converted to earth
and source property estimates. The subject of converting
the A and B model parameters into earth and source
properties is discussed in paper 3.

## $(A/t^2+B)\exp(-Ct)$ MODEL SENSITIVITY TESTS

The characteristics of data used in coda analysis can
be highly variable. For the results of a coda analysis to
be useful they must be reasonably consistent with changes
in signal-to-noise ratio, duration of the coda and types of
scattered energy present. The following tests are designed
to quantify the effect these types of changes will have on
parameter estimates when fitting the $(A/t^2)$ model to coda
spectra.

The following results were obtained by fitting the
$(A/t^2)$ model to the 5 synthetic data sets described above.
The sensitivity of the inversions to the order of
scattering present in the input data is quantified. Table 4
gives the coda-Q (Q), turbidity (T) and source term (S)
inversion solutions for the different input models. The
corresponding bias or percent difference between the known
answer and the inversion result and the SSR are also given.
An SSR value not equal to zero for the 1+3 model solution
is due to the random noise added to the synthetics. This
random noise effect will be similar for each of the models
tested. Based on the SSR a similar quality fit was made to
the 1+2 and 1+2+3 synthetic data. The large increase in SSR
when the single and 1+2+3+4 synthetics are used suggests
that the characteristics of these data are not well

represented by the $(A/t^2)$ model.

Table 4.--Inversion solutions and bias from fitting the $(A/t^2)$ model to data with different types of multiple scattering present, 2 Hz case

| MODEL PARAMETER | KNOWN SOLUTION | MODEL USED TO GENERATE INPUT | | | | |
|---|---|---|---|---|---|---|
| | | 1 | 1+2 | 1+3 | 1+2+3 | 1+2+3+4 |
| S (bias) | 100000 | 282547 (183%) | 263853 (164%) | 100781 (1%) | 174500 (75%) | 90952 (9%) |
| T (bias) | .01 | .004 (57%) | .007 (26%) | .01 (0%) | .01 (0%) | .014 (40%) |
| Q (bias) | 1000 | 777 (22%) | 764 (24%) | 1000 (0%) | 798 (20%) | 1210 (21%) |
| SSR | | 513 | 51 | 13 | 69 | 212 |

In the next series of tests the sensitivity of the coda analysis solutions to the magnitude of each model parameter is studied over their commonly observed range. The values of Q, T and S cover the ranges observed in papers 1 and 3. The results in table 5 show the effect of varying the number of data points used in the analysis.

Table 5.--Number of analysis points test. The $(A/t^2)$ model is fit to the 1+2+3 synthetic data at 2 Hz

| MODEL PARAMETER | known | NUMBER OF DATA POINTS USED | | | | |
|---|---|---|---|---|---|---|
| | | 160 | 100 | 50 | 30 | 10 |
| S (bias) | 100000 | 174499 (74%) | 146118 (46%) | 104151 (4%) | 81844 (18%) | 385405 (285%) |
| T (bias) | .01 | .01 (0%) | .011 (10%) | .014 (40%) | .017 (70%) | .002 (78%) |
| Q (bias) | 100 | 98 (2%) | 95 (5%) | 90 (10%) | 87 (13%) | 201 (101%) |
| SSR | | 69 | 40 | 13 | 28 | 32 |

153

The biases to S, Q and T were all observed to decrease with increasing number of analysis points. The source term had the most bias with the least number of analysis points. The bias however was a minimum with 50 points rather than with the maximum points as with Q and turbidity.

The effect of Q magnitude on solution bias is shown in table 6. Varying Q has no effect on the source term and turbidity estimates. Solution bias in coda-Q is observed to increase with increasing Q values. The observed range of coda-Q in paper 1 was between 400 and 2000. Values 100 and 5000 were included to test the extreme cases.

A similar test but with the 1+2 synthetic as input produced similar results to those shown in table 6: no change in T or S bias and Q bias decreasing with decreasing Q. These results suggest that a coda analysis which fits the $(A/t^2)$ model to data is more robust against bias when coda-Q values are low.

Table 6.--Q magnitude test, inversion results and bias from fitting the $(A/t^2)$ model, 2 Hz, 160 points case

| MODEL PARAMETER | known | Q VALUE USED IN 1+2+3 INPUT MODEL | | | |
| | | 100 | 1000 | 3000 | 5000 |
| --- | --- | --- | --- | --- | --- |
| S (bias) | 100000 | 174500 (75%) | 174500 (75%) | 174500 (75%) | 174500 (75%) |
| T (bias) | .01 | .01 (0%) | .01 (0%) | .01 (0%) | .01 (0%) |
| Q (bias) | -- | 98 (2%) | 798 (20%) | 1707 (43%) | 2210 (56%) |
| SSR | | 69 | 69 | 69 | 69 |

Changes in bias due to varying the magnitude of turbidity are shown in table 7. Turbidity controls the

crossover point from single to multiple scattering effects in the $(A/t^2)$ model. Lower values of turbidity result in greater separation of single and multiple scattering effects by delaying the crossover point in time. Values of turbidity were observed to range from approximately .01 to .1 in paper 3 but values less than .01 are published in the literature. Turbidity magnitude influences the S, Q and T estimates. Less bias appears to occur with lower values of T, although there appear to be exceptions to this general observation.

TABLE 7.--Turbidity magnitude test, shown is the $(A/t^2)$ model solutions and bias, 2 Hz, 160 data point case

| MODEL PARAMETER | T VALUE known | USED IN THE 1+2+3 INPUT MODEL .0001 | .001 | .01 | .05 |
|---|---|---|---|---|---|
| S (bias) | 100000 | 125209 (25%) | 117465 (17%) | 174500 (75%) | 351453 (251%) |
| T (bias) | -- | .00008 (20%) | .0009 (10%) | .01 (0%) | .035 (30%) |
| Q (bias) | 500 | 513 (3%) | 662 (32%) | 444 (11%) | 484 (3%) |
| SSR | | 13 | 92 | 69 | 33 |

Changes in bias due to varying the magnitude of the source term are shown in table 8. Source term magnitude does not influence the bias to the S, Q or T estimates significantly.

A test of the frequency dependence of the bias is shown in table 9. The $(A/t^2)$ model is fit to synthetic data generated with the 1+2 model at 1, 3 and 10 Hz. There is essentially no change in bias to the source term and

turbidity results. The coda-Q estimates improve with increasing frequency. Since frequency is in the numerator of the exponential term and coda-Q :⁻ in the denominator, an inverse relationship should exist between these two parameters. Based on the previous testing of Q magnitude, bias to Q should decrease with increasing frequency and there should be no effect to the T and S estimates.

Table 8.--Source term magnitude test, shown is the $(A/t^2)$ model solutions and bias, 2 Hz, 160 point case

| MODEL PARAMETER | known | S VALUE USED IN THE 1+2+3 INPUT MODEL | | | |
|---|---|---|---|---|---|
| | | 1000 | 10000 | 100000 | 500000 |
| S (bias) | -- | 1827 (82%) | 17450 (75%) | 174500 (75%) | 872497 (74%) |
| T (bias) | .01 | .0096 (4%) | .01 (0%) | .01 (0%) | .01 (0%) |
| Q (bias) | 500 | 478 (4%) | 444 (11%) | 444 (11%) | 444 (11%) |
| SSR | | 13 | 92 | 69 | 33 |

Table 9.--Frequency test, the $(A/t^2)$ model solutions at 1, 3 and 10 Hz with the 1+2 model used as input

| MODEL PARAMETER | KNOWN SOLUTION | FREQUENCY | | |
|---|---|---|---|---|
| | | 1Hz | 3Hz | 10Hz |
| S (bias) | 100000 | 263853 (164%) | 263853 (164%) | 263853 (164%) |
| T (bias) | .01 | .0075 (25%) | .0075 (25%) | .0075 (25%) |
| Q (bias) | 1000 | 618 (38%) | 829 (17%) | 942 (6%) |
| SSR | | 51 | 51 | 51 |

To sum up, parameter sensitivity tests have shown that bias varies depending upon the magnitude of Q and T but not S. The observed bias is less when Q and T are lower in magnitude (100, .001) and greater when Q and T are larger (1000, .05). Decreasing Q (or increasing frequency) produces faster coda decay rates which allow for better model parameter estimates. Small values of T cause the single to multiple scattering transition to occur at a later time; the additional single scattering information improves model parameter resolution. Bias in the estimates was also found to depend on the number of data points or duration of the coda. The more data available to fit the model, the less bias there is in the inversion estimates.

## MONTE CARLO ERROR ANALYSIS

A Monte Carlo error analysis was performed to determine the effects of random noise on the $(A/t^2)$ model solutions. Both the variance and bias in the presence of different levels of random noise were quantified. The test consisted of 100 coda analysis runs with the same input data but with different sets of random noise of a constant level added to the input data each time. A statistical analysis on the Q, T and S solutions from the 100 runs were used to calculate the bias and variance in each of the model parameters.

Two tests on the effects of random noise were made. In the first test the 1+3 model was used to generate the input and the $(A/t^2)$ model is fit to the data. In this case the model to be fit and the model used to generate the

157

synthetic data are the same. Figure 4 gives the expected variance (percent error or standard deviation) in coda-Q, turbidity and source term as a function of random noise. Also shown is a range of random noise observed in paper 1. Based on the sensitivity tests and the fact that high magnitude values of Q and T were used in this first test, the results in figure 4 represents a worst case.

In the second test (figure 5) the 1+2+3 model was used to generate input with low magnitude values of Q and T. As expected from the parameter sensitivity tests, the variances in the model parameter estimates were significantly reduced with lower coda-Q and turbidity values. The stronger decay of coda energy with time and better separation of single and multiple coda information allow for more robust inversions. Note that a significant scale change from that used in figure 4 was required to make figure 5.

Table 10 gives bias as a function of random noise for the coda-Q, turbidity and source term for both cases. In the first case the input model is the same as the model being fit and values of Q (1000) and T (.1) are at the high end of the typical range. Bias increases with increasing random noise magnitude. Q and T are relatively unaffected by even 20% random noise; however, S is strongly affected. In the second case the input model was different than the model being fit and values of Q (500) and T (.01) are closer to the low end of their range. The bias in this case is due primarily to the difference in scattering characteristics between the input and model being fit and
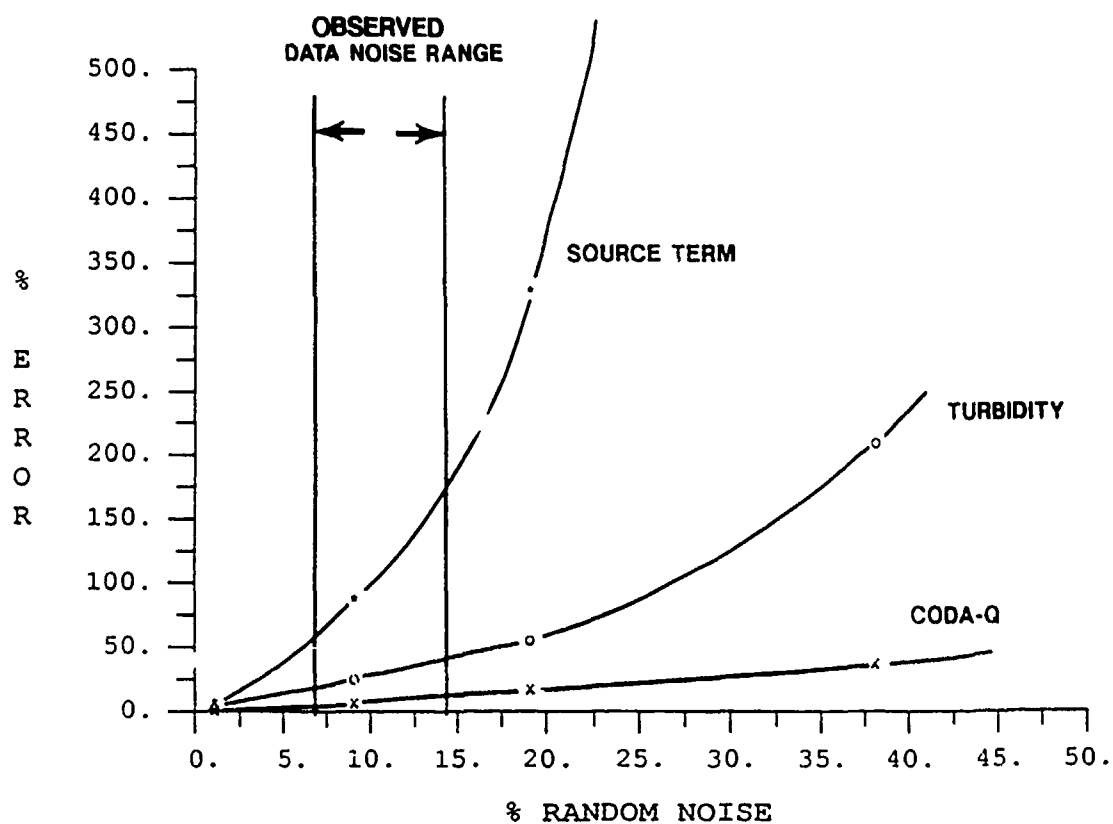
# MONTE CARLO ERROR ANALYSIS



Figure 4. Monte Carlo error analysis results with high magnitude parameter values. Shown is the variance (standard deviation) as percent error from the true value with different levels of random noise in the data. The range of random noise observed in teleseismic data is also shown.
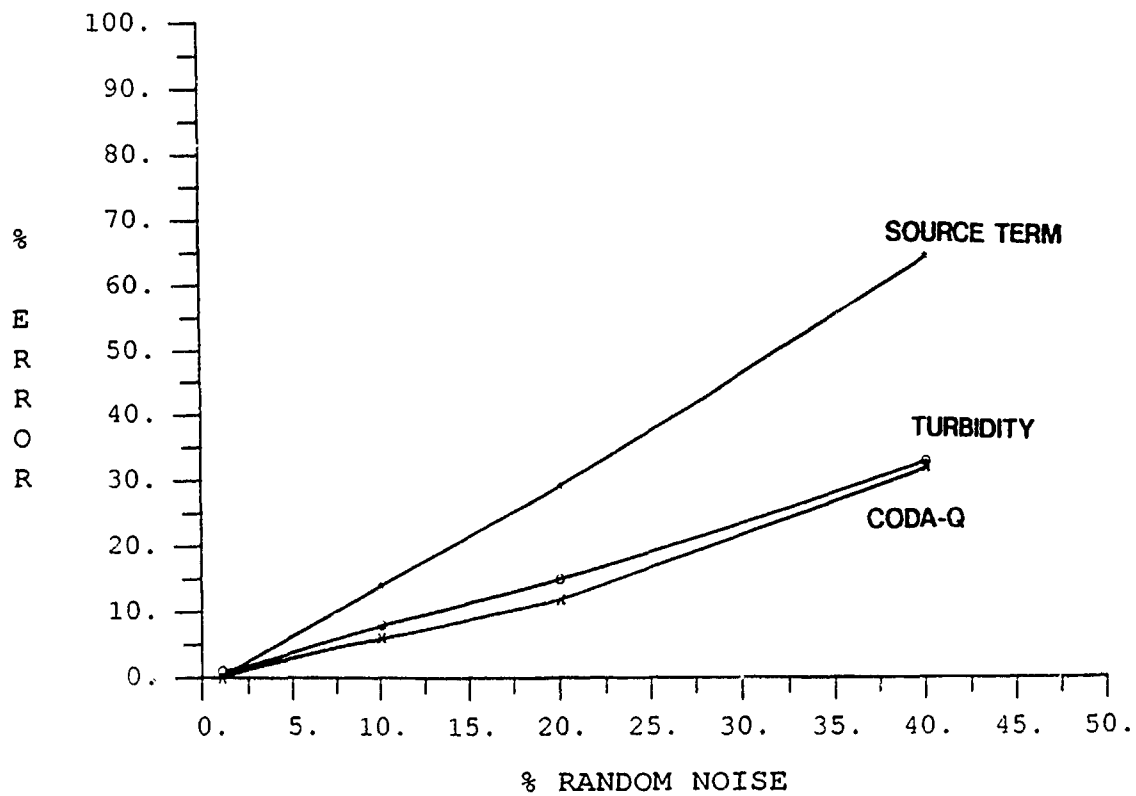
MONTE CARLO ERROR ANALYSIS



Figure 5. Monte Carlo error analysis results with low
magnitude parameter values. Shown is the variance (standard
deviation) as percent error from the true value with
different levels of random noise in the data.

not due to the random noise. Addition of random noise
actually improves the Q estimates slightly in this test.
Bias to T and S remains relatively constant except with the
40% random noise case which causes the bias to increase.

Table 10.--Bias computed as percent difference between
the known answer and the Monte Carlo test mean

| MODEL PARAMETER | RANDOM NOISE | | | |
|---|---|---|---|---|
| | 1 | 10 | 20 | 40% |
| 1+3 INPUT MODEL | | | | |
| S | 0% | 30% | 200% | 2000% |
| T | 0% | 3% | 10% | 115% |
| Q | 0% | 1% | 3% | 10% |
| 1+2+3 INPUT MODEL | | | | |
| S | 52% | 53% | 56% | 73% |
| T | 16% | 16% | 17% | 22% |
| Q | 27% | 27% | 26% | 21% |

The parameter sensitivity tests and Monte Carlo
analysis show that fitting the $(A/t^2)$ model to coda with
varying random noise, duration and orders of scattering
produces reasonably robust solutions. The bias problem is
less with smaller values of Q and turbidity. Table 11
compares the Monte Carlo analysis results to the results
from fitting the $(A/t^2)$ model to synthetic data with up to
4th order scattering. Only the results for low values of Q
and turbidity and 10 and 20% random noise are shown. The
magnitude of the bias due to using the wrong model is
equivalent to that due to 10% to 20% random noise. The
results in table 11 should be compared with those in table

4, which were determined with large Q and turbidity values.

Table 11.--Comparison of the bias due to random noise and
the effect of fitting an inappropriate model, 2 Hz case

| MODEL PARAMETER | | MODEL 1 | USED TO 1+2 | GENERATE 1+2+3 | INPUT 1+2+3+4 | RANDOM 10% | NOISE 20% |
|---|---|---|---|---|---|---|---|
| S | 1000 | 2% | 4% | 3% | 18% | 30% | 200% |
| T | .001 | 2% | 4% | 4% | 16% | 3% | 10% |
| Q | 200 | 1% | 5% | 5% | 8% | 1% | 3% |

## SINGLE SCATTERING MODEL TEST

The bias due to fitting the single scattering model
(equation 1) to data which include multiple scattering
information is included in this study because other authors
have demonstrated its inability to correctly model data
with multiple scattering effects (Frankel and
Wennerberg, 1987). The effect of incorrectly fitting the
$(A/t^2)$ model to data composed of only single scattering
information is also of interest. Table 12 gives the
inversion results obtained by fitting the single scattering
model to the 4 synthetic data sets which contain up to 3rd
order scattering. The inversion with the single model
failed when 4th order scattering was included.

Because there is only one amplitude term involved in
fitting the single model alone, it is not possible to
separate the turbidity and source terms. The product of
turbidity and source term is therefore reported in table
12. The bias is consistently higher than when the $(A/t^2)$
model was fit to these same data (table 4). This is due to

the fact that higher order scattering effects present in the data are not being properly accounted for when the single model is fit to these data. These results imply that coda-Q solutions computed by fitting the single scattering model can be strongly biased if the coda data being fit are dominated by multiple scattered energy.

Table 12.--Inversion results when a single scattering model is fit to the synthetic input data, 2 Hz case

| MODEL PARAMETER | KNOWN SOLUTION | MODEL USED TO GENERATE INPUT | | | |
|---|---|---|---|---|---|
| | | SINGLE | 1+2 | 1+2+3 | 1+3 |
| TS (bias) | 1000 | 1005 (1%) | 2907 (191%) | 3667 (267%) | 1965 (97%) |
| Q (bias) | 1000 | 1000 (0%) | 1618 (62%) | 2904 (190%) | 3804 (280%) |

## ENERGY-FLUX MODEL TEST

The Energy-Flux model has been used by Frankel and Wennerberg (1987) and Langston (1989) to model coda. The Energy-Flux model is based on the diffusion equation which accounts for multiple scattering and provides a means to separate scattering Q and intrinsic Q effects. While the $(A/t^2)$ model allows for the separation of the source, turbidity and coda-Q terms it cannot differentiate scattering Q from intrinsic Q. The Energy-Flux model from Langston (1989) is:

$$A(f,t) = \frac{(2 I_d t_d)^{1/2}}{t} \exp\left(\frac{2\pi f t_d\left(\frac{1}{Q_s} + \frac{1}{Q_i}\right)}{2}\right) \left(1 - \exp\left(\frac{-2\pi f t}{2 Q_s}\right)\right)^{1/2} \exp\left(\frac{-2\pi f t}{2 Q_i}\right) \tag{7}$$

Where:   $A(f,t)$   = coda spectral amplitude

$t_d$    = travel time of P-wave through layer

$Q_s$    = scattering Q parameter

$Q_i$    = intrinsic Q parameter

$I_d$    = integral of direct wave squared velocity

$f$      = frequency

$t$      = time

As a means of comparing the $(A/t^2)$ model to the
Energy-Flux model, test data were produced with the
Energy-Flux model and then analyzed. The quality factor is
computed from Qi and Qs using equation 8 for comparison to
the coda-Q estimates:

$$\frac{1}{\text{Quality factor}} = \frac{1}{Q_i} + \frac{1}{Q_s} \tag{8}$$

Table 13 compares the Energy-Flux model parameters to
the $(A/t^2)$ model estimates. At Q values of 1000 the $(A/t^2)$
model coda-Q was biased by only 2% from the correct answer
suggesting that the two models are similar in this case.
With Q values of 500 a 35% bias was observed and at Q
values of 200 a bias of 69% was observed. Figure 6 shows
the strong similarity between the $(A/t^2)$ model fit to the
Energy-Flux model data for both a low and high Q test.

Because the coda-Q estimates in table 13 appeared to
closely follow the values of Qi, two tests were performed
in which Qi and Qs were varied separately. In the first
test shown in table 14, Qs is kept constant at 1000 and Qi
is varied from 800 to 100. For all values of Q the coda-Q
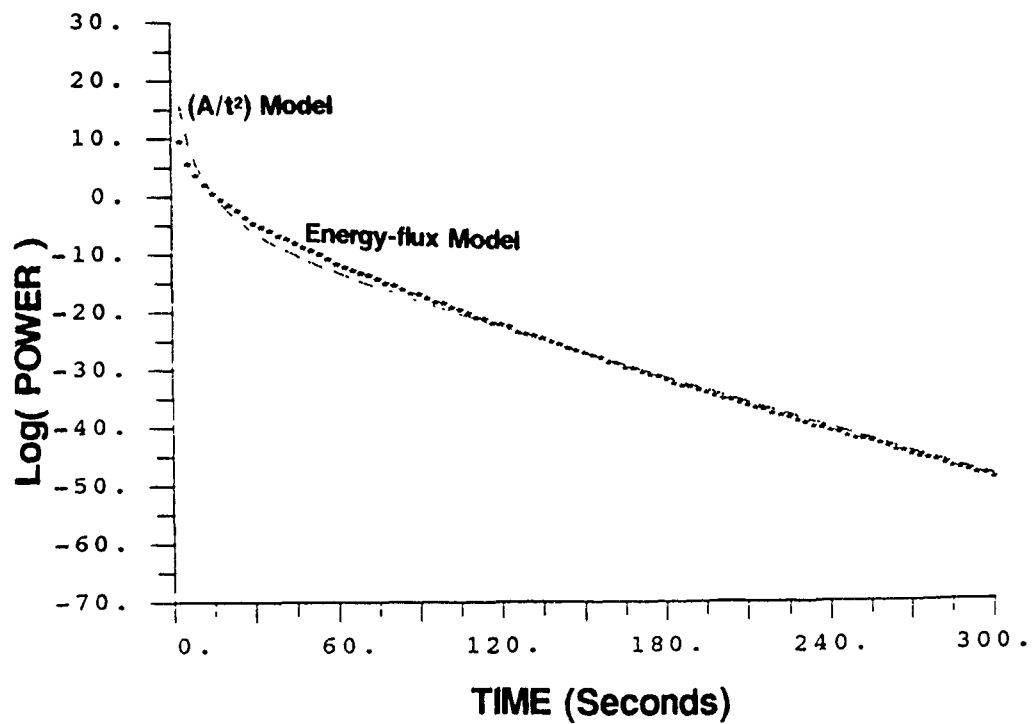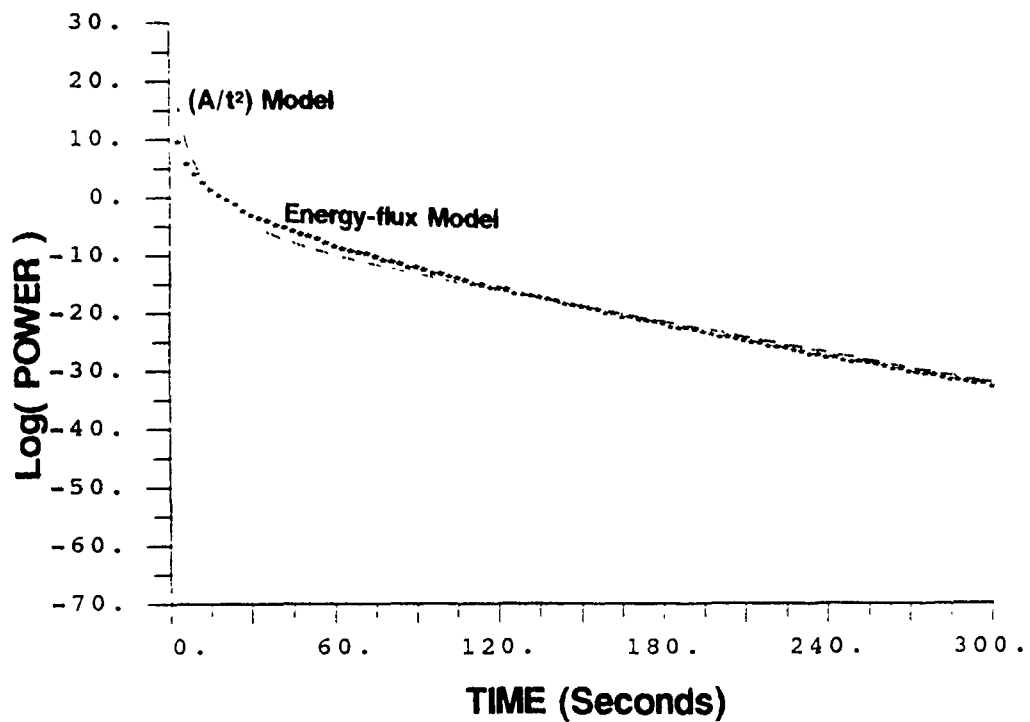estimates appear to agree very well with the quality factor

164

Figure 6. Comparison of the energy-flux model to the $(A/t^2+B)\exp(-Ct)$ model. The upper display is with coda-Q equal to 500 and the lower display is with coda-Q equal to 333. The $(A/t^2)$ model (line) is fit to data generated with the energy flux model plus 0.5% random noise (points).

computed from equation 8.


Table 13.--Energy-Flux model test with intrinsic and
scattering Q equal, the $(A/t^2)$ model results with the
the Energy-Flux model used as input, quality factor is
defined in equation 8

| Energy-Flux INPUT PARAMETERS | | | |
|---|---|---|---|
| Qs | 200 | 500 | 1000 |
| Qi | 200 | 500 | 1000 |
| Quality factor | 100 | 250 | 500 |
| | | | |
| GLI RESULTS | | | |
| coda-Q | 169 | 337 | 532 |
| (bias) | (69%) | (35%) | (6%) |
| | | | |
| Turbidity | .008 | .016 | .021 |
| Source term | 343988 | 56512 | 18324 |


Table 14.--Energy-Flux model test with intrinsic and
scattering Q different, the 1+3 model inversion
results when the Energy-Flux model is used as input,
quality factor is computed from equation 8

| INPUT PARAMETERS | | | | |
|---|---|---|---|---|
| Qs | 1000 | 1000 | 1000 | 1000 |
| Qi | 800 | 500 | 300 | 100 |
| | | | | |
| Quality factor | 444 | 333 | 230 | 91 |
| | | | | |
| GLI RESULTS | | | | |
| coda-Q | 470 | 344 | 233 | 92 |
| (bias) | (6%) | (3%) | (1%) | (1%) |


In the second case, shown in table 15, Qi is kept
constant at 1000 and Qs is varied from 800 to 100. The
coda-Q estimates in this case remain relatively constant at
approximately 500. Changing the magnitude of Qs does not
appear to significantly alter the rate of decay in time of
the Energy-Flux model. Although these tests are limited,
they suggest that it is intrinsic Q that controls the decay

of energy with time with scattering Q affecting the decay
to a much lesser degree in the Energy-Flux model. The
$(A/t^2)$ model appears to agree closely with the energy-flux
model except in the case were scattering Q is small
relative to intrinsic Q.

Table 15.--Energy-Flux model test with intrinsic and
scattering Q different, the 1+3 model inversion results
when the Energy-Flux model is used as input, quality
factor is computed from equation 8

| INPUT PARAMETERS | | | | |
|---|---|---|---|---|
| Qs | 800 | 500 | 300 | 100 |
| Qi | 1000 | 1000 | 1000 | 1000 |
| Quality factor | 444 | 333 | 233 | 91 |
| GLI RESULTS | | | | |
| coda-Q | 508 | 487 | 495 | 602 |
| (bias) | (14%) | (46%) | (112%) | (562%) |

## CONCLUSIONS

Two-term models were found to describe coda spectral
decay with time and therefore appear useful in modeling
multiple scattered energy in coda. The two term models
consisted of a time dependent term for the steep decays
early in the coda and the time independent term for the
gentle decays later in the coda. The two models studied in
this paper were: $(A/t^2+B)\exp(-Ct)$ and $(A/t+B)\exp(-Ct)$.
Comparison of the two models showed that similar coda-Q
values would be computed with either model. Large
differences were however observed between the A and B model
parameters and the $(A/t)$ model appeared deficient at
modeling steep spectral decays. These differences suggest
that model stability during inversion could help determine

the most appropriate model to use in a coda analysis.

Parameter sensitivity tests with the $(A/t^2)$ model showed that solution bias is dependent upon the magnitude of Q and T but not S. The bias was less when low Q (100) and T (.001) values were used and higher with large Q (1000) and T (.05) values. Bias in the estimates was also found to depend upon the number of data points or duration of the coda. The more data available the less bias there was in the inversion estimates. This observation suggests that better coda analysis estimates are possible if two-term models which use more of the coda are used instead of just a single scattering model applied to only the very early part of the coda.

Biased solutions were obtained when the models to be fit differed significantly from the scattering present in the data. The amount of bias was found to depend on the degree of difference. When a single scattering model was fit to data with multiple scattering effects coda-Q values were biased by as much as 280% and the product of turbidity and source term by as much as 267%. When the $(A/t^2)$ model was fit to data consisting of only single scattering, coda-Q values are found to be biased by 22%, turbidity by 57% and source term by 183%.

When the $(A/t^2)$ model, which includes multiple scattered effects, was fit to data with different orders of multiple scattered energy the amount of bias to the estimates was reduced. The $(A/t^2)$ model was found to be a good average model for data which contained up to 4th order multiple scattering. For large values of Q (1000), T (.01)

and S (100000). the maximum bias in coda-Q was 24%,
turbidity 40% and source term 164%. By comparison, the
bias due to approximately 20% random noise is 3% for
coda-Q, 10% for turbidity and 200% for the source term.
When small values of Q (200), T (.001) and S (1000) were
used the maximum biases were 8% for Q, 16% for T and 18%
for S.

The solution biases due to fitting inappropriate
models was found to be greatest for the source term and
least for coda-Q. Solution bias due to random noise was
also greatest for S and least for coda-Q. Coda-Q is
therefore the most reliable estimate from a coda analysis.
No frequency dependent bias was observed.

A marked reduction in stability of the inversions was
noticed when inappropriate models were fit to the data. The
analysis was found to be model sensitive. This observation
suggests that the GLI coda analysis technique is subject to
poor convergence or failure if an unreasonable model is
used.

When the Energy-Flux model was used to generate input
data for the GLI coda analysis the solutions indicated that
the two models were similar when scattering Q values were
high (1000). When intrinsic Q was high and scattering Q low
(100) the coda-Q solutions differed from the quality factor
by 562% indicating a divergence between the two models. In
each case coda-Q was computed to be larger than the true
value, probably due to the fact that higher order
scattering effects are included in the Energy-Flux model.

# PAPER III

## SUMMARY

Two-term models of the form $(A/t^2+B)\exp(-Ct)$ and $(A/t+B)\exp(-Ct)$ are fit to time varying spectra of coda and earth turbidity and source spectra estimated. The analysis is performed on teleseismic P-wave coda with lengths up to 700 seconds. The long durations suggest that the coda may contain significant multiple scattered energy. Separate estimates of turbidity and source spectrum were only possible with the $(A/t^2+B)\exp(-Ct)$ model which assumes that coda generation is due to single and multiple scattered body waves. Turbidity values ranged from .007 to .2, in agreement with other published values. Turbidity was also found to be constant with frequency. The estimated source spectra had well developed corner frequencies and decay of energy at high frequencies. Comparison of turbidity and source spectra products from both models after normalization showed them to be equal within error. This similarity suggests that the methods used in this study may not be as model sensitive as originally believed. For both models, the fall off of high frequency energy was observed to be greater for the explosion data than for the deep earthquake, in agreement with other published work. While the results of this feasibility study are encouraging, additional work on larger data sets is necessary to better

evaluate the significance of the turbidity and source spectra estimates.

## INTRODUCTION

This paper is the last of three which document research conducted to better understand how to treat multiple scattered energy in a coda analysis, with primary emphasis on teleseismic observations. Coda is the random energy that immediately follows a direct body wave arrival. In the first paper (Soroka and Stump, 1991), hereafter referred to as paper 1, coda-Q estimation using two-term models and an inversion approach was developed. In the second paper (Soroka, 1991), referred to as paper 2, the results of an error analysis study designed to better understand the applicability of simple two-term models in coda analysis are given. Based on the encouraging results in papers 1 and 2, the study was expanded to determine if additional earth and source information could be estimated from the two-term model fits to the coda.

This third paper deals with estimating the source spectrum and earth turbidity from the two-term model parameters determined in paper 1. Source spectra play an important part in the earthquake-explosion discrimination problem and the coda method has potential for producing a more stable spectrum than by using the direct arrival alone. Turbidity is a difficult property to estimate but provides useful information about how homogeneous it is in the subsurface. Turbidity values have the potential for being an indicator of tectonic activity in an area (Herraiz

and Espinosa, 1987).

Because it is not always possible to record data close to an event, coda analysis work has begun to be extended to teleseismic distances where multiple scattering and crustal structure effects may be more dominant contributors to the coda. The approach used by some researchers has been to fit the single scattering model in the same manner as with local and regional studies (Novelo-Casanova and Butler, 1986). More recently the energy flux model has been used to describe coda (Langston, 1989; Frankel and Wennerberg, 1987). The alternative approach developed in paper 1 is to fit a two term model to better account for multiple scattering and crustal structure effects that occur later in the coda. A two-term model approach would also be applicable at local and regional distances when crustal structure and multiple scattering effects are present in the coda. Use of additional coda information in a coda analysis could in some cases produce a better, more stable solution.

In current coda analysis a model is fit to coda spectral power as a function of time. Then estimates of earth and source properties are computed from the model parameters. Two important assumptions in this approach are first that a proper model is being fit and second that the coda contains earth and source information. Papers 1 and 2 discuss the issue of model choice in detail. There is strong evidence in the literature that coda-Q estimates are a measure of earth Q (Aki and Chouet, 1975 and Herraiz and Espinosa, 1989). Useful information about the source has

also been obtained by analyzing coda (Rautian and Khalturin, 1978). In addition, Aki (1982) found that coda for a particular event at different receiving stations has similar amplitude and spectral characteristics. These observations suggest that the coda does contain information about the source that initiated the seismic event and about the earth material through which the seismic energy has traveled.

The principal earth information contained in the coda is Q and turbidity. Earth Q is the inverse of attenuation and is a measure of the loss of primary wave energy due to scattering and absorption. Local and regional coda analysis work has been aimed primarily at Coda-Q estimation (Aki and Chouet, 1975; Herraiz and Espinosa, 1989). Turbidity is a measure of the earth's ability to scatter seismic energy (Dainty et al., 1987). Work on turbidity is not as abundant as coda-Q probably because of the greater difficulty in making this estimate.

The principal source information in the coda is the spectrum of the source wavelet and the source magnitude. Estimates of the source spectrum from coda have been used to calculate seismic moments, corner frequencies and stress drops (Rautian and Khalturin, 1978). Source spectra are also used in earthquake-explosion discrimination and event magnitude estimation studies.

A strong motivation for using the coda to obtain the source spectrum is the potential for producing a more stable spectrum than if the direct arrival is used alone. The difficulty lies in extracting this information from the

coda in a meaningful manner. In traditional coda analysis a one term, single scattering model is fit to a subset of the coda shortly after the direct arrival. In this case it is not possible to easily separate the source spectrum and earth turbidity information because they appear as a product. The two-term coda analysis approach described in paper 1 models the whole coda and has the potential for separating source spectrum and earth turbidity information. This implies that source spectral estimation from coda may be possible when multiple scattering effects are included in the analysis.

In this paper, estimates of source spectrum and earth turbidity, or their product are determined from model parameters after fitting the models to a set of teleseismic data. These results are evaluated to determine if they represent reasonable estimates using general appearance and comparison to other independent measures of the estimated properties.

## ASSUMPTIONS

Coda generation is a complex process which can involve back- and forward-scattered waves, mode-converted waves, single- and multiple-scattered waves as well as numerous other sources. Arriving at a theoretical description which explains all these processes and yet is relatively simple to apply is a difficult if not impossible problem. It is common practice to represent complicated geophysical processes by simplified models in the hope of gaining insight into the fundamentals of the problem. The wide use of Aki's one-term model to estimate earth Q at

local and regional distances (Herraiz and Espinosa, 1987) is one example which demonstrates the validity of this approach. The one-term model assumes an infinite random scattering medium and accounts for only single backscattered body waves.

Extension of the one-term single scattering model to two terms is yet another simplification of the complex coda problem. However, with the two-term model the later part of the coda dominated by multiple scattering effects can be used in the coda analysis. In this study two-term models of the form:

$$(A/t^2+B)\exp(-Ct) \text{ and } (A/t+B)\exp(-Ct),$$

hereafter referred to as the $(A/t^2)$ and $(A/t)$ models respectively, are fit to coda spectra with time (papers 1 and 2). In both cases the two-term models involve the sum of a time dependent and time independent term times an exponential term. Coda-Q is computed from the exponential term which is the same for both models. In papers 1 and 2 it was shown that coda-Q estimation is not greatly affected by which of the two-term models is fit to the coda spectra.

The difficulty in using simple models to represent complex processes has to do with interpreting the model parameters in terms of physical properties of the process under study. A simple model which cannot be equated with a reasonable physical process to provide a way to map the model parameters to physical properties is of very little use. On the other hand if several models are found to fit the data or if a simple model describes more than one

physical process, some way must be found to choose among the different models and theory.

The $(A/t^2)$ and $(A/t)$ models represent different scattering processes. Depending upon the data set under analysis one model may be more applicable than the other. In paper 2 the $(A/t^2)$ model was shown to represent reasonably single and multiple backscattered body waves in the theory of Gao et al. (1983b). Because of a coincident source and receiver assumption this model is more applicable to coda with small source-to-receiver separations. At larger separations the physical justification of this model is more difficult even if coda generation is due to scattering processes close to the receiver. In this case it is assumed that a new point source equal in strength and spectral properties to the incident wave is placed near the receiving station. The fact that reasonable coda-Q values in close agreement to the $(A/t)$ model results were obtained in paper 1 suggests that the infinite random scattering medium or other assumptions imposed by the theory are not violated.

The $(A/t)$ model represents scattered body waves plus P-to-Lg (trapped shear) waves that result when a plane wave hits a layer of random scatterers beneath the receiver (Appendix). Because of the plane wave assumption this model appears more applicable to coda with very large source-to-receiver separations. The $(A/t)$ model can however have applications at small source-to-receiver separations if surface wave scattering is responsible for the coda generation (papers 1 and 2).

Because it is not clear how sensitive the desired earth and source property estimates are to the choice of model this work should be looked on as a feasibility study. The main objective is to determine if the coda analysis technique can be extended to extract more than just coda-Q from data when two-term models are used. The encouraging results of this work should be considered a beginning with more detailed studies performed on larger data sets to establish the stability of the estimates.

## SCATTERING MODEL THEORY

In paper 1 the $(A/t^2)$ and $(A/t)$ models were successfully fit in a least-square manner to up to 500 seconds of teleseismic coda. The difference between the two models, shown in equations 1 and 2 below, is the time dependence of the first term. A, B and C are model parameters that depend on frequency. $P(f,t)$ is spectral power of the coda as a function of both frequency and time. Time begins with the direct arrival.

$$P(f,t) = ( A/t^2 + B )\ \exp(-C\ t) \qquad (1)$$
$$P(f,t) = ( A/t + B )\ \exp(-C\ t) \qquad (2)$$

Figure 1 gives the A, B and C model parameters determined by both models for the same event and station. In both cases the model parameters appear to be measuring systematic changes in the data that are potentially related to earth and source properties. The $(A/t^2)$ model results have similar variances to the $(A/t)$ model suggesting that both fit the data well.

After the models are fit to the data and the A, B and
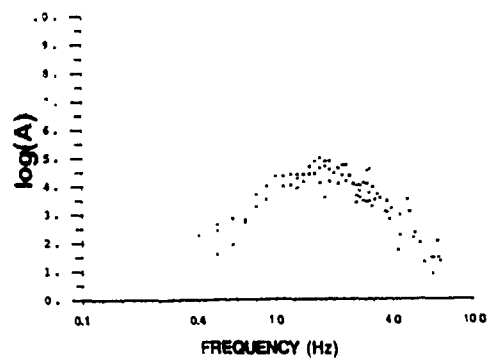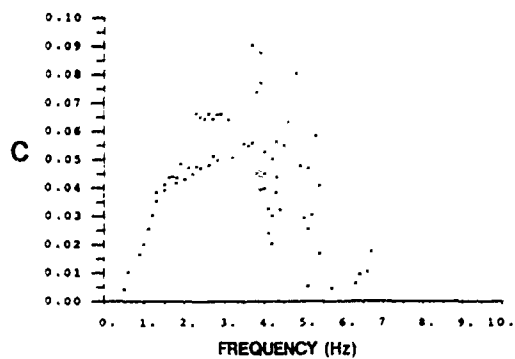
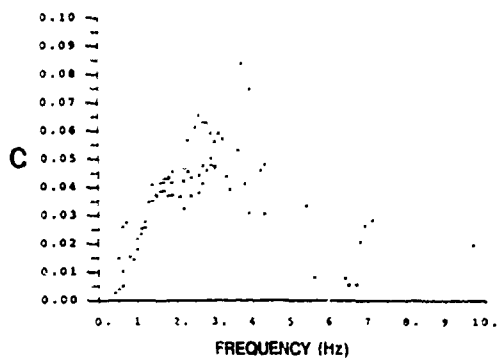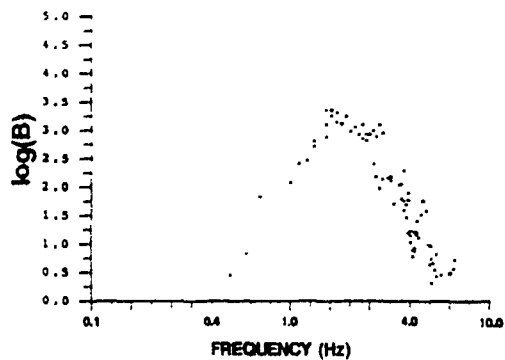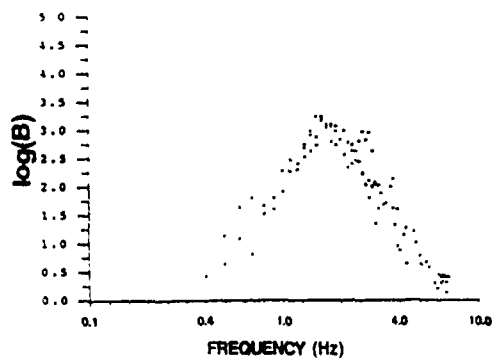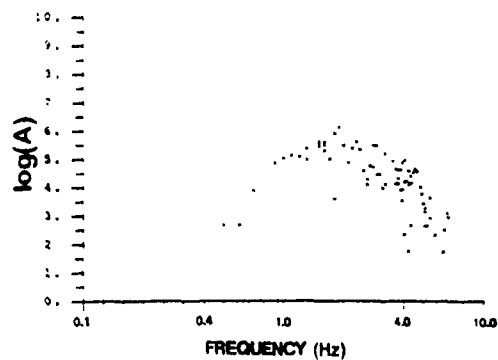Figure 1. Comparison between the A, B and C model parameters determined by fitting the $(A/t^2)$ and $(A/t)$ models. Results are for all components at station RSON for event 1.

C model parameters have been determined the next step is to equate these parameters to earth and source properties with an appropriate scattering theory. The 3-D body wave backscattering model of Gao et al. (1983b), which describes coda spectral power variation with time and frequency has been used to interpret the $(A/t^2)$ model parameters in equation 1. In paper 2 the $(A/t^2)$ model was found to be a good average model for single plus multiple backscattered body waves. The $A/t^2$ time-dependent term has the form appropriate for single backscattering and the time-independent B term has the form of triple order backscattering as shown below:

$$P(f,t) = (\frac{S\ T}{t^2} + .716\ S\ T^3\ V\ )\ \exp(\frac{-2\ \pi\ f\ t}{Q}) \tag{3}$$

where:  S = Source power spectrum

T = Turbidity

V = Average earth velocity

Q = Coda-Q

f = Frequency

t = Time

The $(A/t)$ model, equation 2, has a form corresponding to two different types of scattered energy. The first is scattered surface waves (Gao et al. 1983a) with a coincident source-receiver assumption. Pg waves are generally not considered a dominant contributor to coda generation but Lg waves are in local and regional seismograms (Herrmann, 1980; Dainty and Toksoz, 1990). The second is scattered energy that results from a plane wave

striking a layer of random scatterers (Appendix). For the
plane wave case, the time dependent term represents
scattered body wave energy of all orders (but with single
scattering dominant for small values of turbidity) and the
time independent term represents P-to-Lg (trapped shear
wave) energy near the receiver. The plane wave model can be
expressed mathematically as:

$$P(f,t) = \left( \frac{S\,T\,h}{2\,t} + \frac{S\,T\,V}{2} \right) \exp\left( \frac{-2\,\pi\,f\,t}{Q} \right) \qquad (4)$$

where S, T, Q and V are as defined above and h is the
thickness of the layer.

For both models the exponential term, from which
coda-Q is determined, is the same. In paper 2 it was shown
that similar coda-Q estimates would be determined with
either of these models. In paper 1, where both these models
were fit to the same data, the $(A/t^2)$ model was found to
produce results with better clustering and lower
variability. Figure 2 gives the coda-Q results obtained by
fitting both the $(A/t)$ and $(A/t^2)$ models to the same data.
The faster falloff with time of the $(A/t^2)$ model seemed to
fit the early part of the coda better, suggesting that the
$(A/t^2)$ model fits the data better.

In paper 2 it was shown that the A and B model
parameters can be significantly different depending upon
which model is fit to the data. Both models are used in
this study to help establish the applicability of these
different theories in coda analysis where multiple
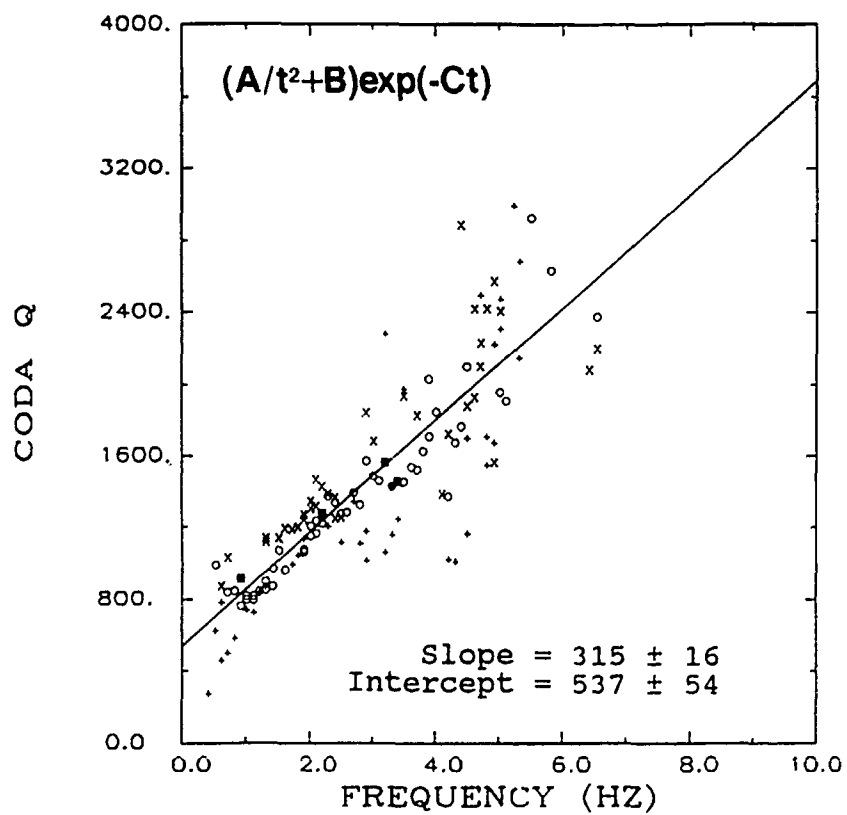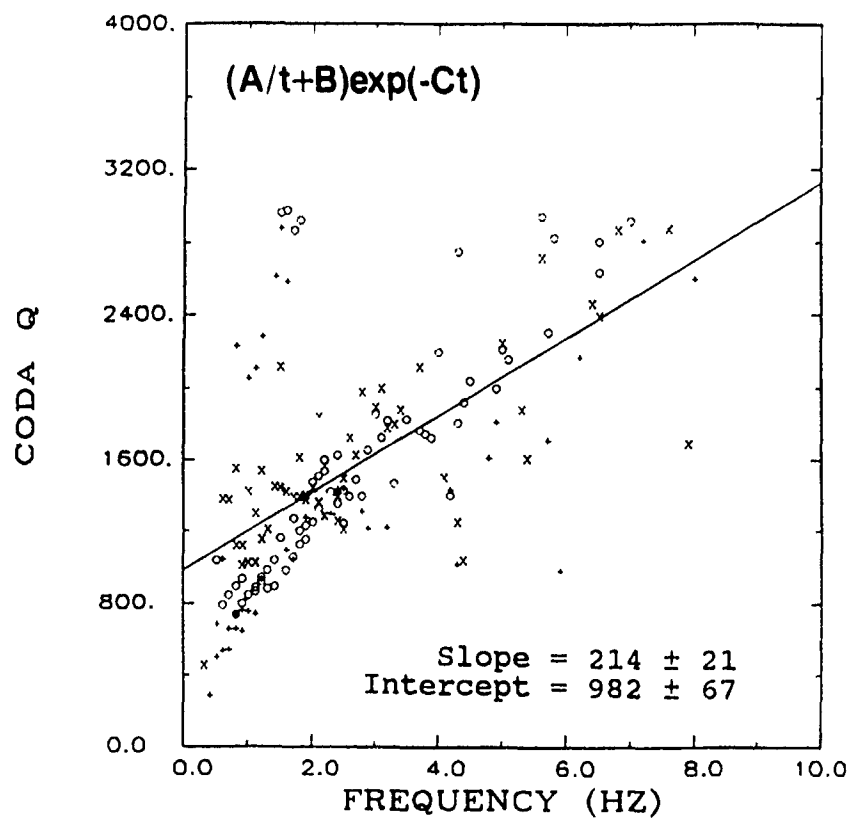scattered energy and structure effects are important.

Figure 2. Coda-Q versus frequency for station RSNT. Comparison between the (A/t²) and (A/t) model solutions.

# ANALYSIS PROCEDURES

The A and B model parameters determined with the inversion procedures described in papers 1 and 2 were used to generate the results in this paper. A generalized linear inversion (GLI) approach was used to fit the two-term models to the data in a least-square manner. The A, B and C parameters are then converted to earth and source estimates using the appropriate theories.

For the $(A/t^2)$ model, the 3-D body wave theory of Gao et al. (1983b) is used. Equating equation 1 and 3 gives:

$$A = \frac{2\ S\ T}{V}\ , \quad B = .716\ S\ T^3\ V\ , \quad C = \frac{2\ \pi\ f}{Q}$$

Dividing B by A allows turbidity (T) to be computed. A value of V=3.5 km/s is used in the calculations. Once T is determined S is computed from A. The same value for S can also be calculated from B.

For the $(A/t)$ model, the plane wave theory (appendix) is used. Equating equations 2 and 4 gives:

$$A = \frac{S\ T\ h}{2}\ , \quad B = \frac{S\ T\ V}{2}\ , \quad C = \frac{2\ \pi\ f}{Q}$$

To compute the product of T and S in this case A and B are summed and ST calculated by assuming values for V and h (V=3.5 km/s and h=35 km). When ST is computed using only A or B, the solutions are similar in shape but considerably different in magnitude. It is not clear that turbidity should be the same for the A and B terms since different types of scattering are involved.

As the above parametrization indicates the $(A/t^2)$ model leads to separation of the source spectrum (S) and earth turbidity (T). In the $(A/t)$ model, separation of source spectra and earth turbidity is not possible unless an independent measure of either the source spectrum or turbidity is available.

The teleseismic P-wave data analyzed in this study consisted of two near-surface explosions and one deep earthquake to contrast near-source scattering effects. The shallow explosions may contain near-source crustal scattering effects but the earthquake does not. Each of the three events were digitally recorded at five 3-component North American Regional Seismic Test Network (RSTN) stations. All five receiving stations were used to contrast near-receiver scattering effects. Table 1 lists the characteristics of the data set used in this study. For more detail the reader is referred to paper 1.

Two inversions were performed on the three events recorded at the five 3-component North American RSTN stations. In one case the $(A/t^2)$ model was fit to the data; in the other the $(A/t)$ model was fit. Estimates of coda-Q from the two inversions are reported in paper 1. The A and B model parameters computed in both inversions were converted to earth and source estimates usin  the appropriate equations described above. These solutions are compared and discussed in detail below.

## RESULTS

Three types of composite displays have been assembled from the results. First all solutions are sorted by common

component to determine if similar or different information
has been recorded in the vertical, radial and transverse
directions. Second the solutions are sorted by common event
to determine the significance of near-source scattering in
coda generation. Third the solutions are sorted by common
receiving station to emphasize near-receiver effects.

Table 1.--Event and station information

**EVENT LOCATIONS**

| EVENT | TYPE | LOCATION |
|---|---|---|
| 1 | EXPLOSION | EASTERN KAZAKH, U.S.S.R. |
| 2 | EXPLOSION | EASTERN KAZAKH, U.S.S.R. |
| 3 | EARTHQUAKE | N. ARGENTINA-CHILE |

**STATION LOCATIONS**

| STATION | LOCATION |
|---|---|
| RSCP | CUMBERLAND PLATEAU, U.S.A. |
| RSNY | NEW YORK, U.S.A. |
| RSSD | SOUTH DAKOTA, U.S.A. |
| RSON | ONTARIO, CANADA |
| RSNT | NORTHWEST TERRITORY, CANADA |

**SOURCE-TO RECEIVER DISTANCES IN DEGREES**

| EVENT | MAGNITUDE | DEPTH | RSNT | RSON | RSNY | RSSD | RSCP |
|---|---|---|---|---|---|---|---|
| 1 | 6.1 | NEAR SURFACE | 68 | 79 | 83 | 86 | 94 |
| 2 | 6.1 | NEAR SURFACE | 68 | 79 | 83 | 86 | 94 |
| 3 | 5.8 | 559 Km | 98 | 82 | 72 | 80 | 66 |

$(A/t^2+B)\exp(-Ct)$ MODEL RESULTS

In this case it is possible to separate the source
term from turbidity. These two estimates will be presented
in turn beginning with turbidity, which is a measure of the
medium's ability to scatter. An average crustal velocity of
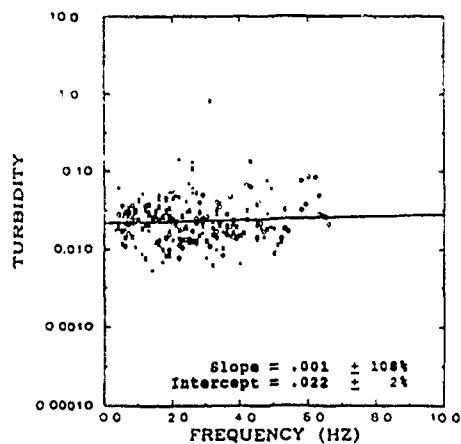3.5 km/s was used in the calculations.

The turbidity versus frequency results are plotted by

common component in Figure 3. A similar distribution is observed in each case with the data values falling approximately in the range from .007 to .2. Even though the scatter is high in these displays the similar range in the results for each component suggests they are measuring similar earth properties.
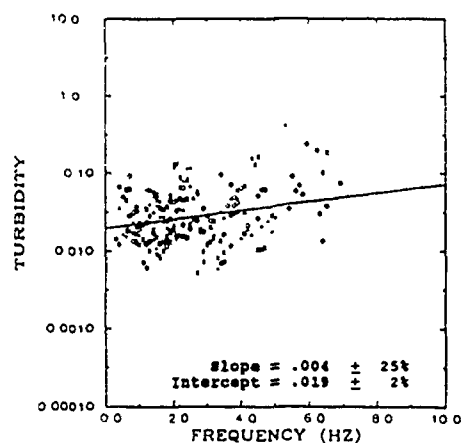
Turbidity versus frequency results are plotted by common event in Figure 4. These displays again show a similar distribution of the turbidity values in the range from .007 to 0.2. Turbidity estimates do not appear significantly different between events.

Turbidity versus frequency results are plotted by receiving station in Figure 5. The reduction of scatter in these displays is not as apparent as with the coda-Q results (paper 1), possibly because of the higher variances predicted for the turbidity solutions by the Monte Carlo error analysis (paper 2). Note that only the receiving station results show significant differences in the level of the turbidity, consistent with the idea of near-receiver scattering. The turbidity solutions are relatively constant over the frequency range analyzed. These displays suggest that scattering will occur equally at all frequencies analyzed in this study. This could be interpreted as an indication that scattering responsible for coda formation is a relatively uniformly random process with only minor subtle differences between the different locations evaluated in this study.
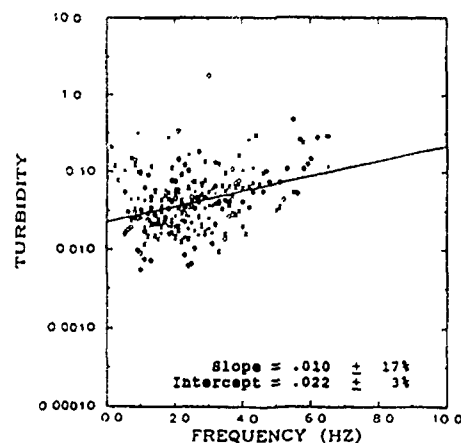
Dainty et al. (1987) report turbidity values for local events in South Carolina that range in magnitude from

**VERTICAL**

Slope = .001 ± 108%
Intercept = .022 ± 2%

**RADIAL**

Slope = .004 ± 25%
Intercept = .019 ± 2%

**TRANSVERSE**

Slope = .010 ± 17%
Intercept = .022 ± 3%

Figure 3. (A/t$^2$) model, turbidity versus frequency by common component for all events and stations. The least-square best fit line is shown. The symbols represent the three events: Event 1 (+), Event 2 (x) and Event 3 (o).
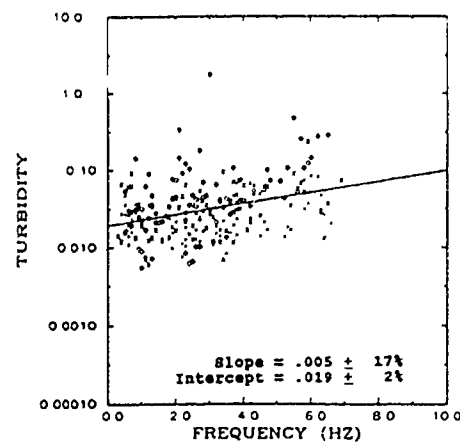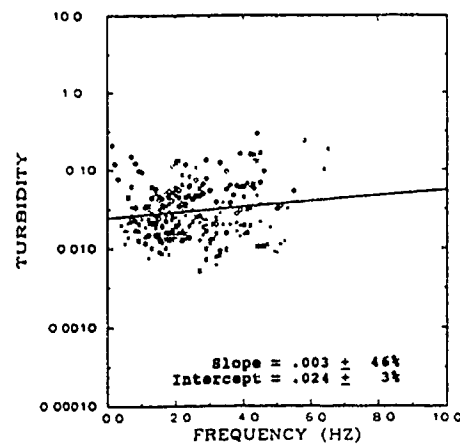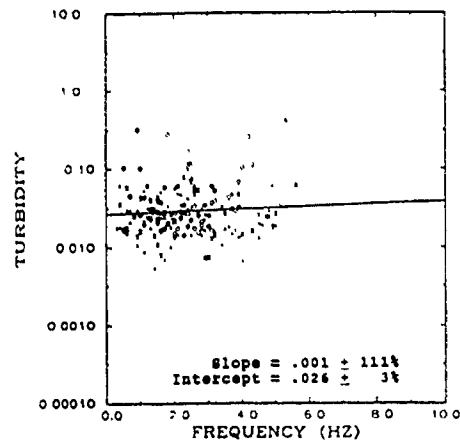
186

EVENT 1

EVENT 2

EVENT 3

Figure 4. (A/t$^2$) model, turbidity versus frequency by common event for all stations and components. The least-square best fit line is shown. Symbols represent the three components: vertical (+), radial (x) and transverse (o).
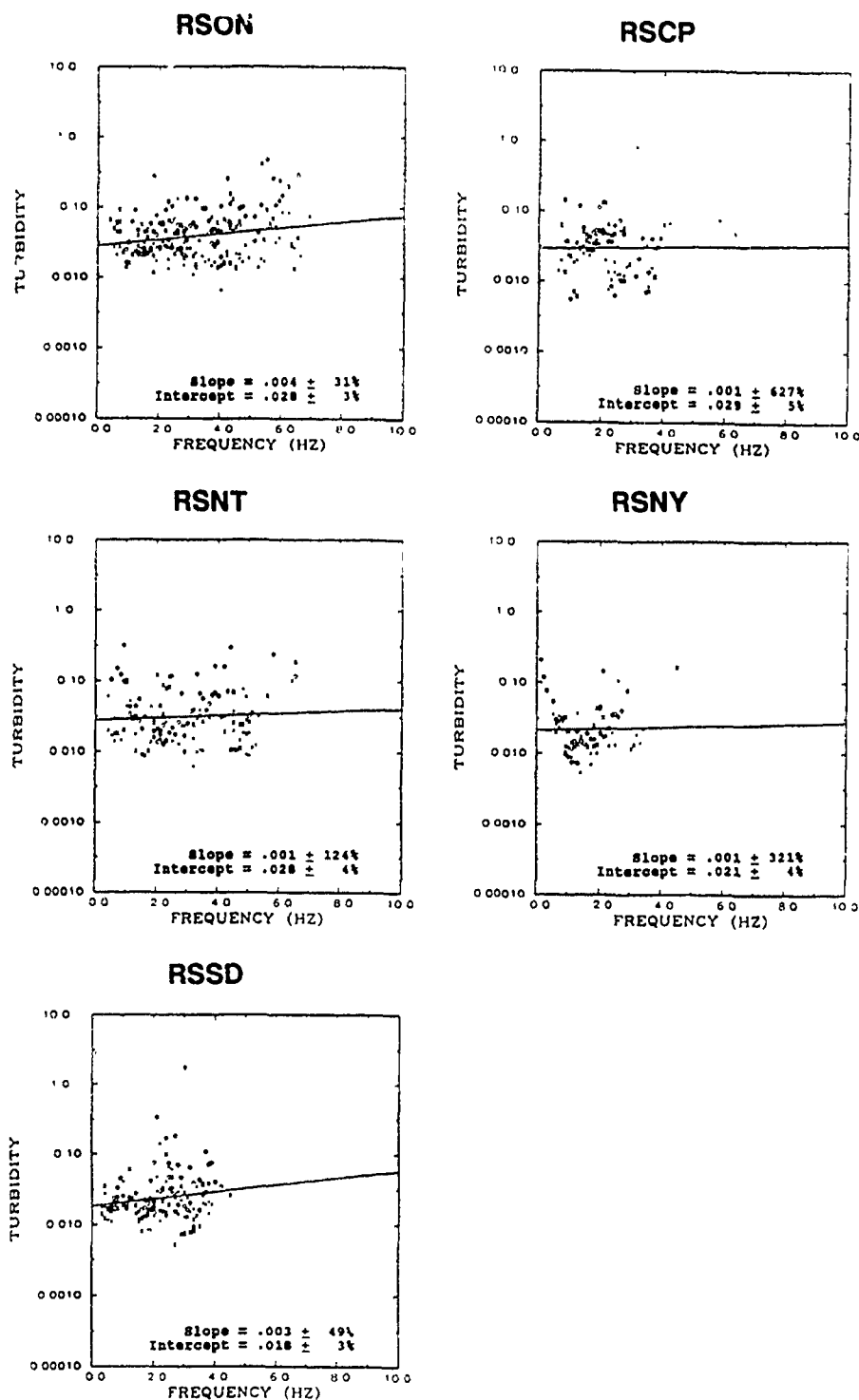
187

Figure 5. $(A/t^2)$ model, turbidity versus frequency by common receiver for all events and components. The least-square best fit line is shown. Symbols represent the three components: vertical (+), radial (x) and transverse (o).

188

.007 to .1 at 3 Hz. These values determined from local events are in agreement with this study, where the values were determined at teleseismic distances.

The source term is an estimate of the source wavelet spectrum. Prior to analysis the spectrum of the pre-event ambient noise was subtracted from the coda spectrum. The shape of the source term results will therefore be a signal-to-noise ratio distribution. Shown in Figure 6 for the $(A/t^2)$ model are the source term results, spectral power (db down from maximum) versus frequency, plotted by common component. The source term results appear to be similar for each component.

Source spectrum results plotted by common event are given in Figure 7. The displays are similar to those plotted by component but show less scatter when plotted by common event. If the source spectral estimates represent a true measure of source properties these displays should have better continuity than those sorted by component or receiving station. The two explosions, events 1 ($m_b$=6.1) and 2 ($m_b$=6.1) appear to have a faster high frequency decay than event 3, the smaller magnitude ($m_b$=5.8) earthquake. These spectral differences between the earthquake and explosion sources are consistent with other published studies (Taylor et al., 1988; Murphy and Bennett, 1982).
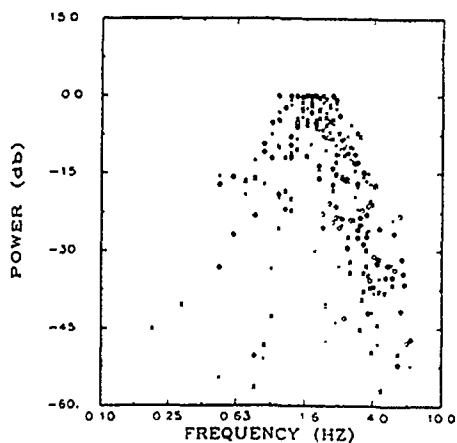
The faster decay of high frequency energy for a shallow explosion is attributed to passage through low Q material both at the source and receive locations. Energy from the 559 km deep earthquake used in this study would only pass through low Q crust near the receiver. This
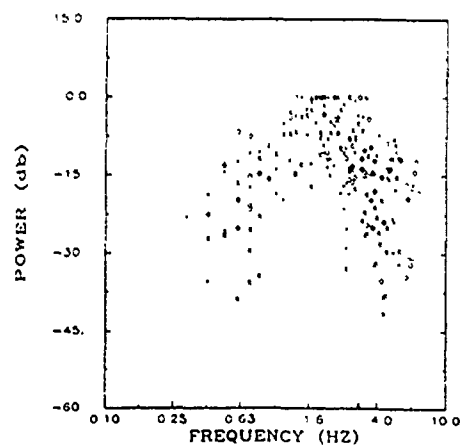
**VERTICAL**
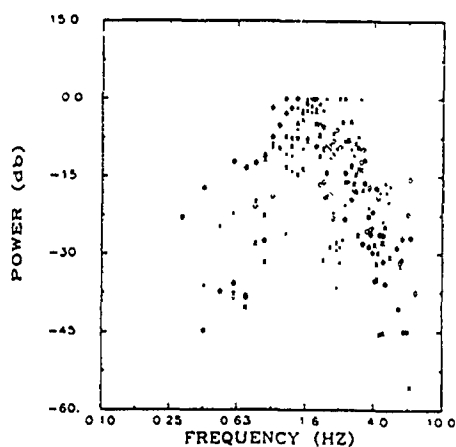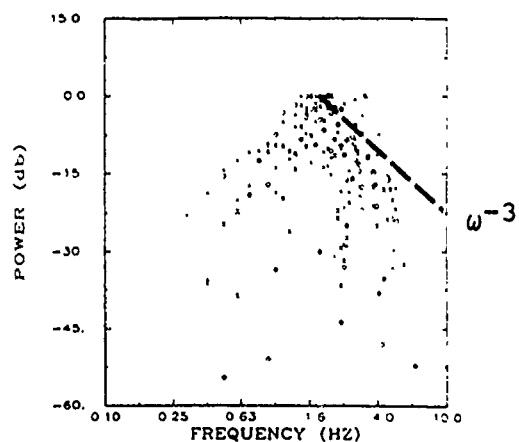
**RADIAL**

**TRANSVERSE**

Figure 6. (A/t$^2$) model, source term solution by common component for all events and stations. Values plotted are db down from maximum. Symbols represent the three events: Event 1 (+), Event 2 (x) and Event 3 (o).
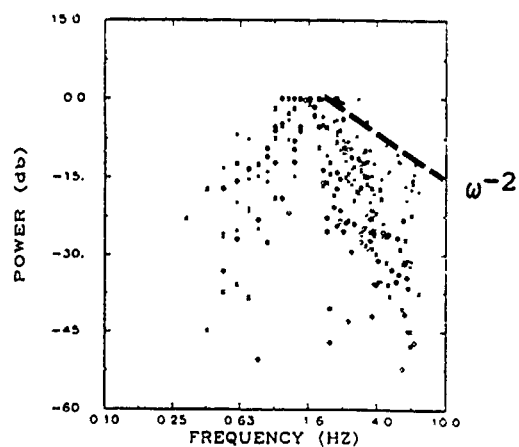
EVENT 1
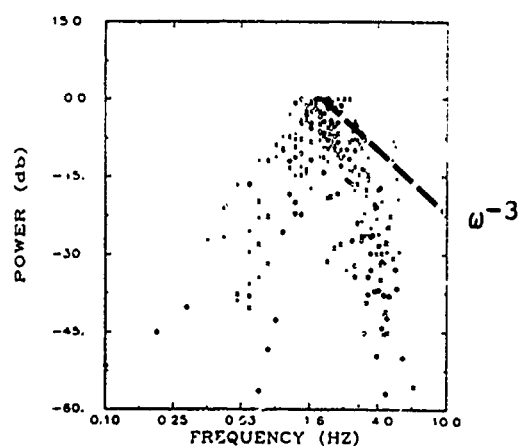
EVENT 2

EVENT 3

Figure 7. (A/t$^2$) model, source term solution by common event for all stations and components. Values plotted are db down from maximum. Symbols represent the three components: vertical (+), radial (x) and transverse (o).

191

spectral characteristic is less apparent for events with magnitudes above 4.5 to 5.0 (Taylor et al., 1988). The fact that the effect is clearly observed on magnitude 5.8 and 6.1 events in this study is quite interesting and merits extended investigation with a larger data set. One possible explanation is that the source spectrum computed for 500 to 700 seconds of coda is more stable than one computed from the direct arrival alone. Alternatively the source-to-receiver distance may be an important factor, teleseismic in this study versus regional for Taylor et al., (1988).

Source depth can also affect the decay of energy at high frequency (Taylor et al., 1988). Deep explosion models involving a sudden pressurization of a spherical cavity result in an $\omega^{-2}$ spectral decay at high frequencies (cf. Sharpe, 1942 and Aki and Richards, 1980). Shallow explosions involving nonlinear effects such as crushing and plastic flow can result in an $\omega^{-3}$ decay at high frequencies. Superimposed on figure 7 for the shallow events 1 and 2 is the $\omega^{-3}$ model and for the deep event 3 the $\omega^{-2}$ model. These models appear to fit the high frequency decay of energy observed in the solutions. Due to the high amount of scatter and the limited data set analyzed it is difficult to draw any definite conclusions from this comparison. This comparison would be more meaningful in a study with a larger data set.

For the sake of completeness Figure 8 shows the source spectrum results from the three events plotted by common receiving station. The motivation for this sorting of the source term results was to determine if near-
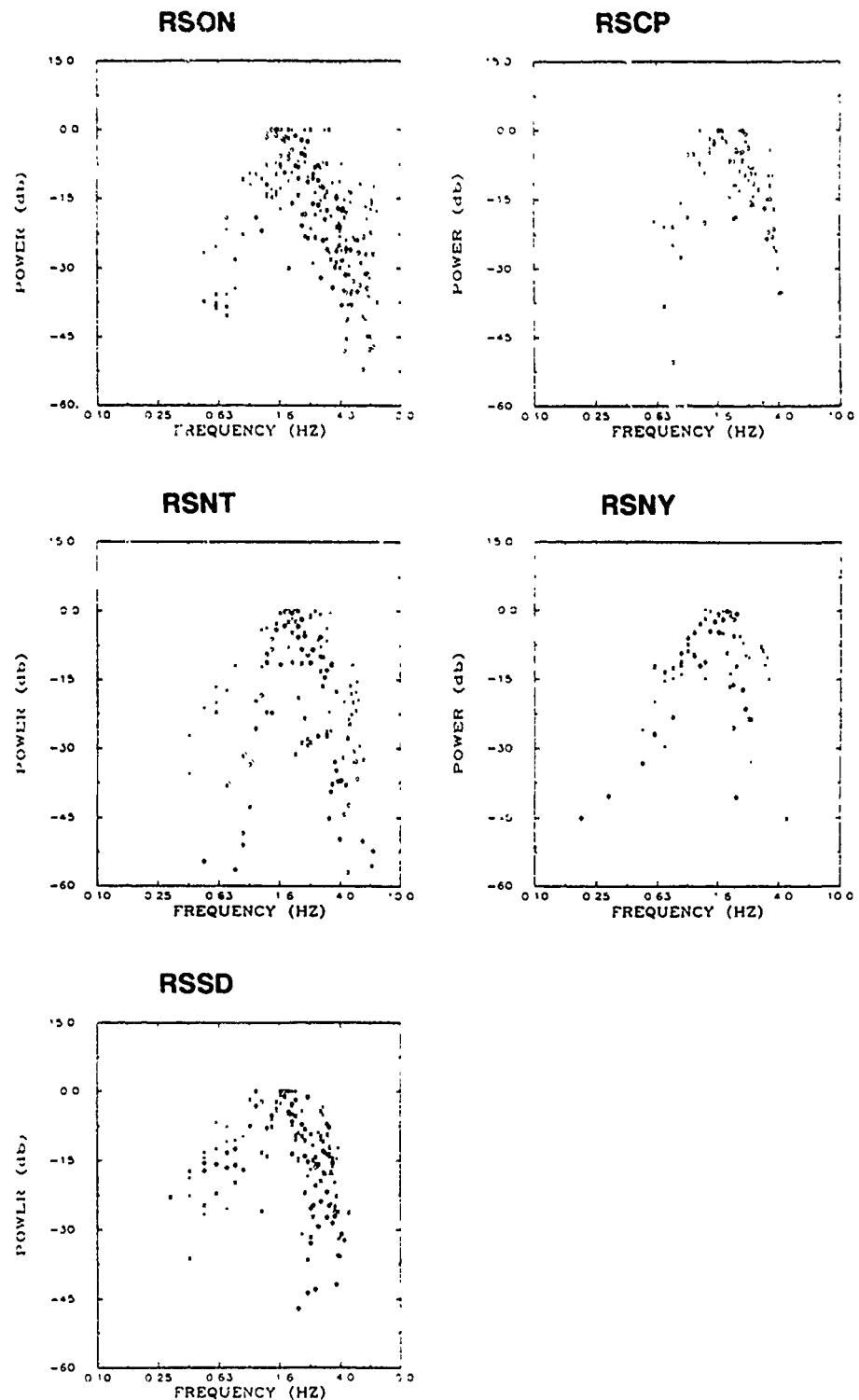
Figure 8. (A/t²) model, source term solution by common receiver for all events and components. Values plotted are db down from maximum. Symbols represent the three components: vertical (+), radial (x) and transverse (o).

receiver effects were affecting the source spectral
estimates and therefore corrupting the source information.
No strong receiver dependence is observed for the source
term.

## (A/t+B)exp(-Ct) MODEL RESULTS

It is not possible to separate the source term from
turbidity with the (A/t) model results. In this case the
product of turbidity and source spectra (TS) is shown in
the displays that follow. The same average crustal velocity
used in the analysis of the $(A/t^2)$ results is used here
(3.5 km/s). The value of crustal thickness used in the
calculations is 35.0 km. The TS results shown below were
determined from the sum of the A and B model parameters.
When TS was computed from A and B independently, the
results had similar shapes but magnitude differed by as
much as 1000. These magnitude differences suggest that
turbidity may be different for the two types for scattering
represented by the plane wave model.

Shown in Figure 9 is log(TS) versus frequency by
common component. The displays are similar in each case
suggesting that each component is measuring similar earth
and source information. The least-square best fit line is
also shown in TS result displays. Although the shape
suggests that the source term is influencing the results
and thus a best fit line may not be meaningful, the lines
were left because they act as reference points for
comparisons.

Figure 10 is log(TS) versus frequency plotted by
common event. Large variances are still observed in the
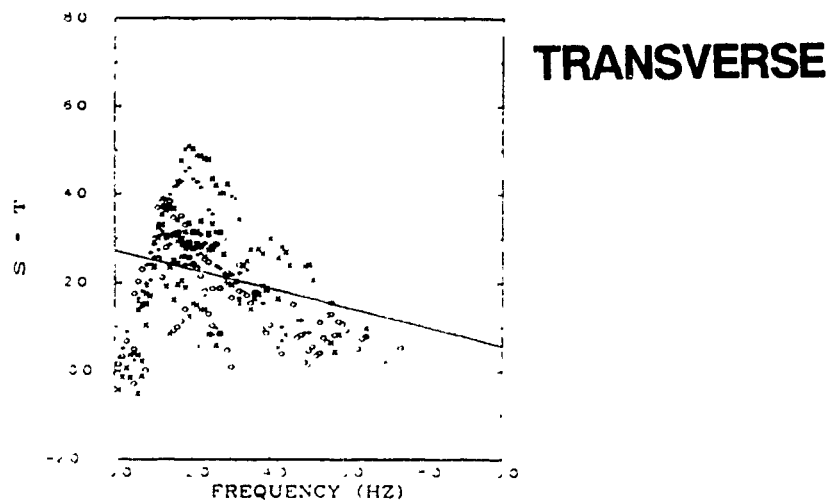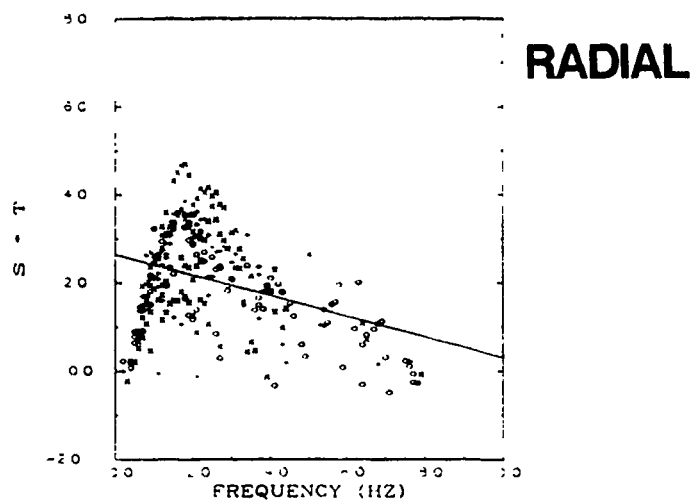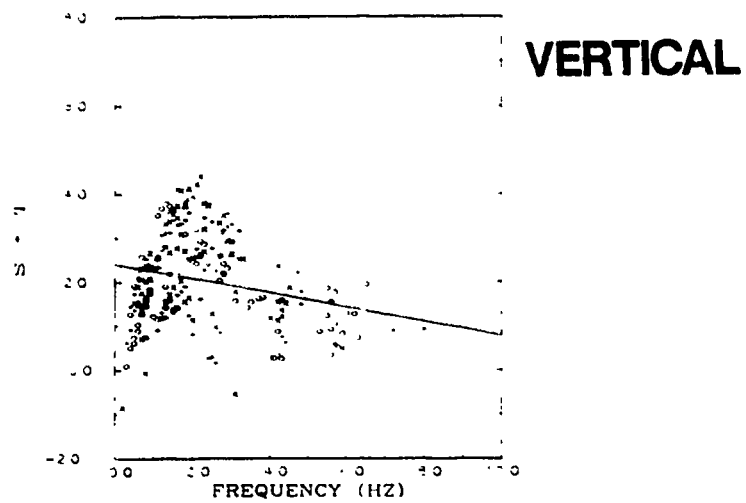
Figure 9. (A/t) model, product of turbidity and source term versus frequency by common component. Symbols represent the three events, event 1 (+), event 2 (X) and event 3 (O).

195
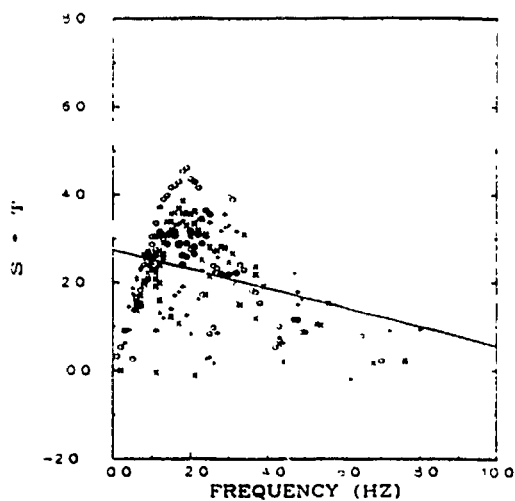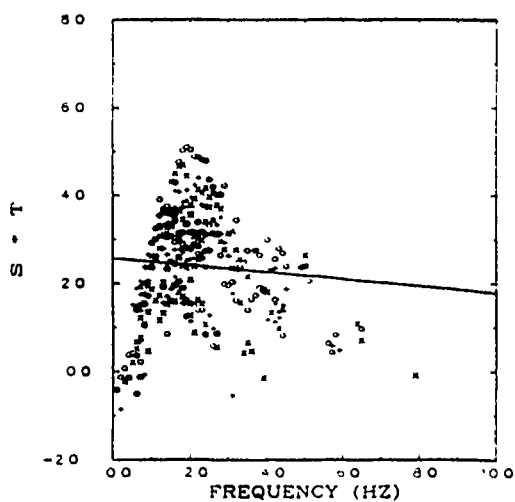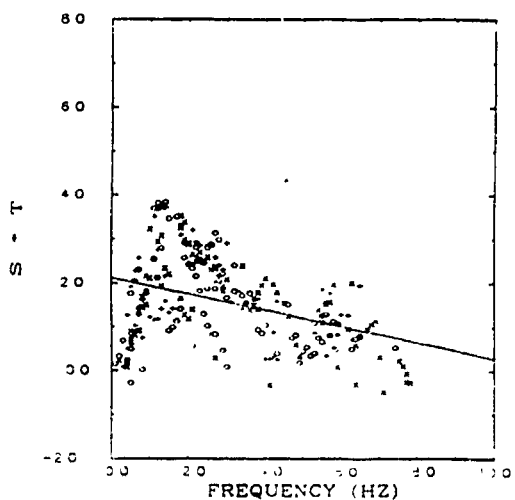
Figure 10. (A/t) model, turbidity and source term product versus frequency by common event. Symbols represent the 3-components, vertical (+), radial (X) and transverse (O).

196

solutions with this sorting. It's interesting that the results for the two explosions (event 1 and 2) have strong similarities. The decay of energy at high frequency appears to be slower for the earthquake than the explosions. If turbidity is relatively constant with frequency these shapes could represent estimates of the source spectra.

Figure 11 is log(TS) versus frequency plotted by common receiving station. There appears to be less variability in the solutions when sorted by common receiving station. This again suggests that processes near the receiving station are dominant contributors to these solutions. While this is reasonable for the turbidity term it is not expected for the source term.

An additional comparison between the two models was made by computing the product of turbidity and source term (TS) for the $(A/t^2)$ model. In Figure 12 the $(A/t^2)$ and $(A/t)$ model TS solutions are plotted. In all cases the results are displayed as db down from maximum versus frequency. The solutions are for each of the three events at station RSON. The $(A/t)$ model solutions appear to have slightly lower variability than the $(A/t^2)$ model results. There is however good agreement between the two sets of solutions. For example, the corner frequency for each event occurs at approximately the same frequency (1.5-2.0 Hz) for both models. The fall off of energy at high frequency is also similar. For each event a reference line, which follows the high frequency decay of energy, is drawn for easier comparison. These similarities suggest that the two-term coda analysis approach is not as model sensitive

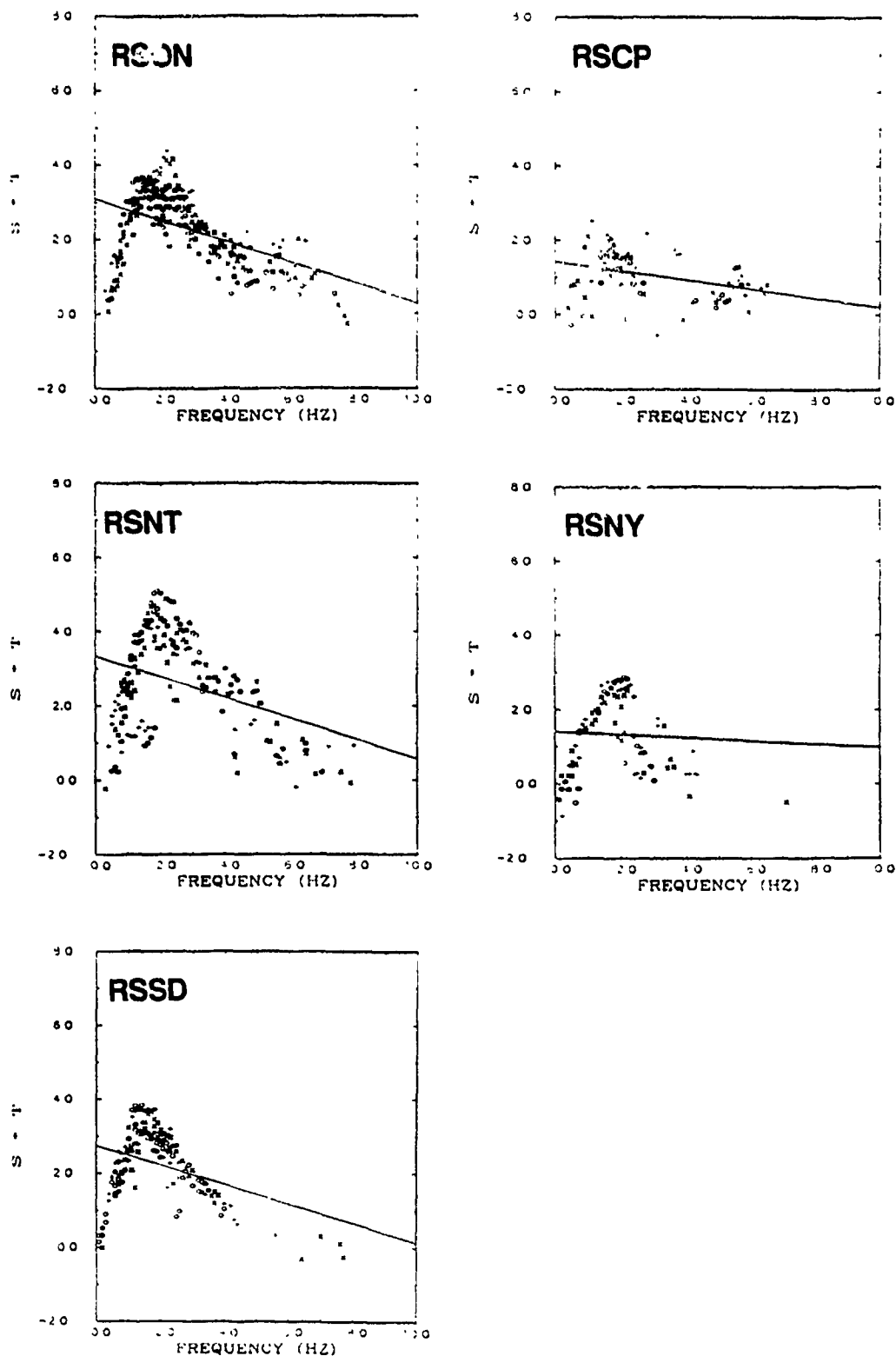Figure 11. (A/t) model, product of turbidity and source term versus frequency by common receiving station. Symbols represent the 3-components, vertical (+), radial (x) and transverse (o).
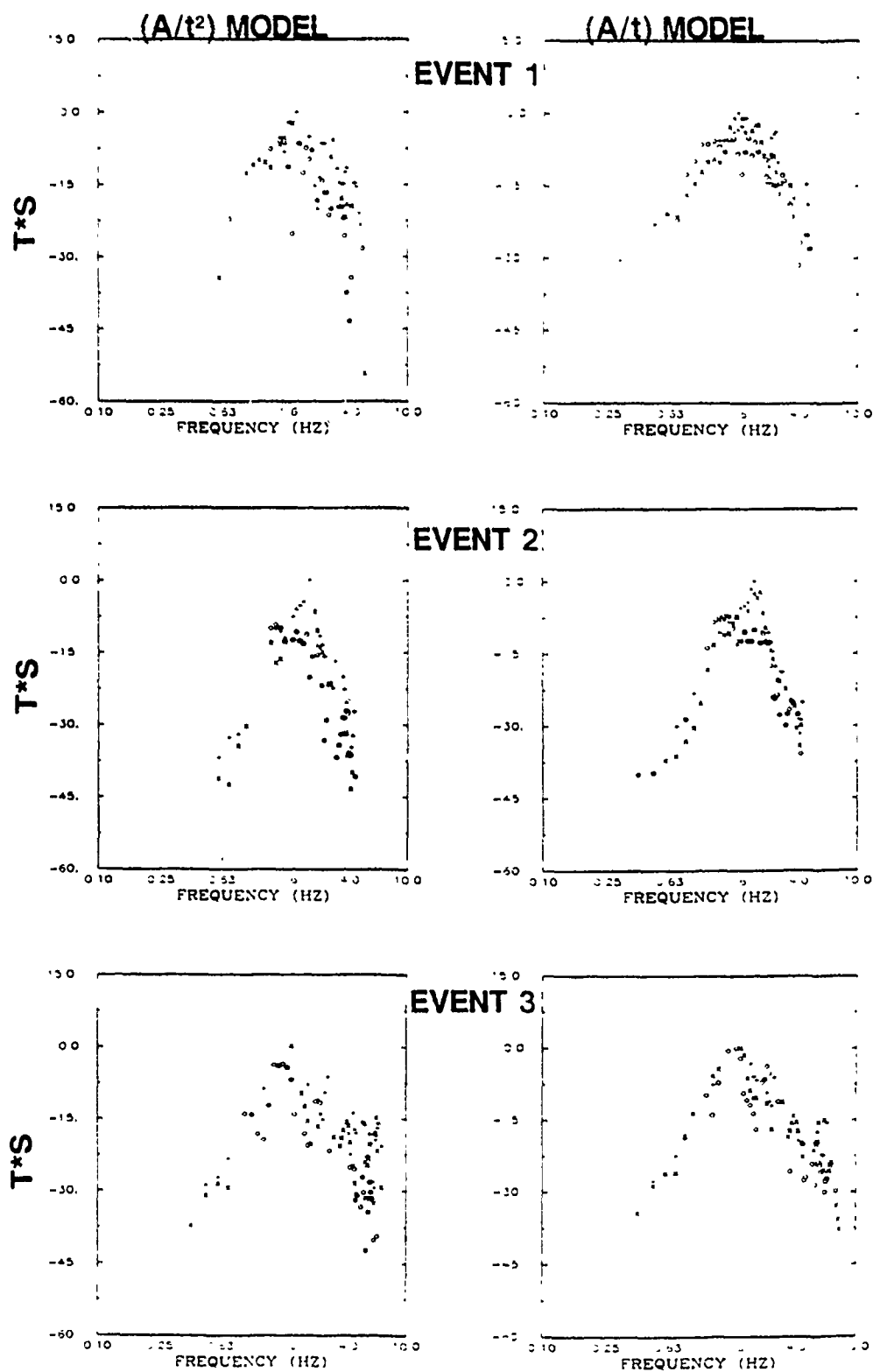
Figure 12. Product of turbidity and source term versus frequency for both the $(A/t^2)$ and $(A/t)$ models. Comparison of all three events at station RSON. Symbols represent the 3-components, vertical (+), radial (x) and transverse (o).

199

as was originally thought.

## CONCLUSIONS

The results of this feasibility study are encouraging. The use of two-term models in coda analysis was shown to be a valid approach to obtaining source and earth property estimates. Source spectrum and earth turbidity information was obtained from the A and B model parameters.

Turbidity estimates were found to be in agreement with other estimates in the literature (Dainty et al., 1987) and ranged in value from .007 to 0.2. Turbidity in this study appears to be dominated by near-receiver properties. Much lower variability was observed in the results when they were sorted by common receiver than by common component or event. Turbidity estimates were only possible with the $(A/t^2)$ model. They were found to be nearly constant with frequency.

Although turbidity could not be uniquely separated with the $(A/t)$ model, the source spectrum shape was estimated by assuming that turbidity was constant with frequency. Both the $(A/t^2)$ and $(A/t)$ model results show that all three components (vertical, radial and transverse) contain similar information. The explosion events had faster decay of energy at high frequency than the earthquake. Source spectrum estimation from coda analysis was shown to be a potentially new way of obtaining spectral information about the source that could be useful in discriminating between earthquakes and explosions.

The $(A/t)$ model solutions were found to have a strong

near-receiver component. Better clustering and lower variability was observed when the (A/t) model results were plotted by common receiver. When the solutions were sorted by common event the explosion results were observed to decay faster at high frequency than the earthquake. This type of difference has been reported in the literature as a means of discriminating between explosions and earthquakes at local and regional distances.

In paper 1 lower variability was observed in the coda-Q solutions with the $(A/t^2)$ model results suggesting that this model fit the data better. In this paper the (A/t) model solutions were observed to have the same or slightly lower variability than the $(A/t^2)$ model. Based on the results of this study, including papers 1 and 2, it is not possible to conclude that the $(A/t^2)$ or (A/t) model was best. On the contrary the results suggest that the two-term coda analysis approach is not as model sensitive as was originally suspected and either model will generate similar solutions.

The results of this study suggest that multiple scattering effects can be modeled in coda and additional earth and source information can be extracted from a coda analysis. While these preliminary results using two-term models demonstrate the potential benefits of such an approach, they also suggest that additional studies with larger data sets are required to better understand the significance of the solutions.

# APPENDIX

# APPENDIX

## CODA DUE TO SCATTERING OF A PLANE WAVE
## WITHIN A LAYER

(By: A. M. Dainty, Earth Resources Laboratory, M.I.T.)

## MODEL, ASSUMPTIONS AND SIMPLIFICATIONS

The physical model is shown in Figure A-1a and consists of a layer of scatterers of thickness h underneath the receiver. Where a more specific model is required, the layer will be assumed to be the crust. Two types of propagation will be considered, propagation in a half space ("body wave scattering") and in the layer after the manner of Lg ("surface wave scattering"). The source is considered to be a plane wavelet, short in time but nonetheless with a narrow frequency content around a center frequency f. By this means we introduce the frequency-dependent amplitude of the primary wave $S_o(f)$. The source spectrum $S = S_o^2$.

The following assumptions and simplifications are made:

1. The scatterers are parametrized by a turbidity $T(f)$ where $T(f)/(4\pi)$ is the scattering cross-section per unit volume per unit solid angle, and the scattering is considered to be isotropic. Then the scattered amplitude $s_1$ at distance $r_1$ from a scattering volume dV is

$$s_1 = \frac{S_o2 \; dV \; T}{4 \; \pi \; r_1^2} \qquad (1)$$
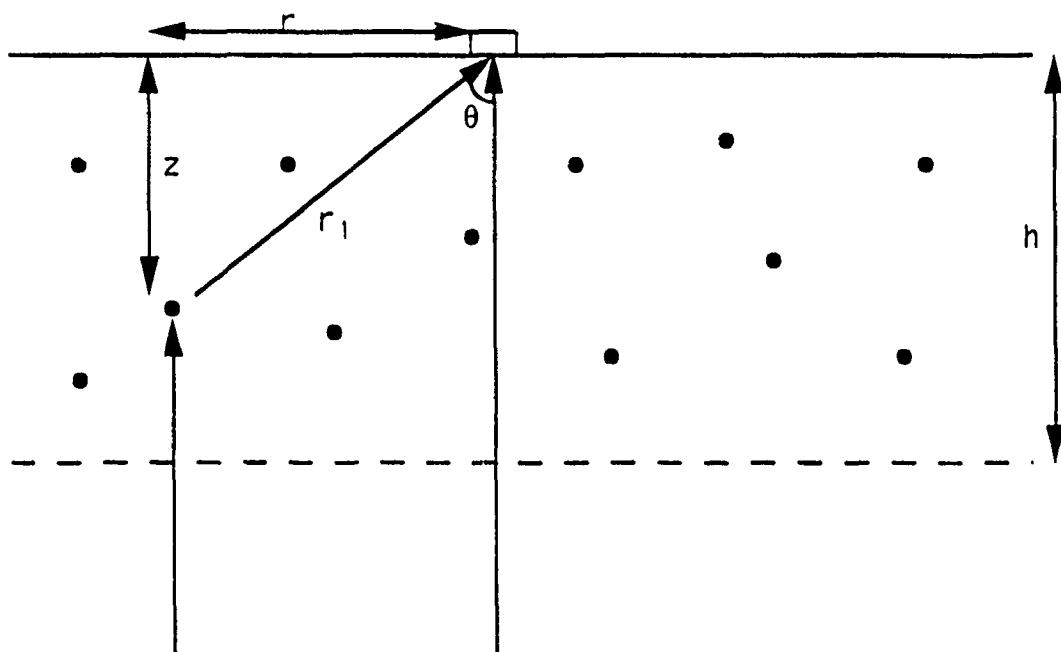
Figure A-1a. Scattering geometry, single scattering.
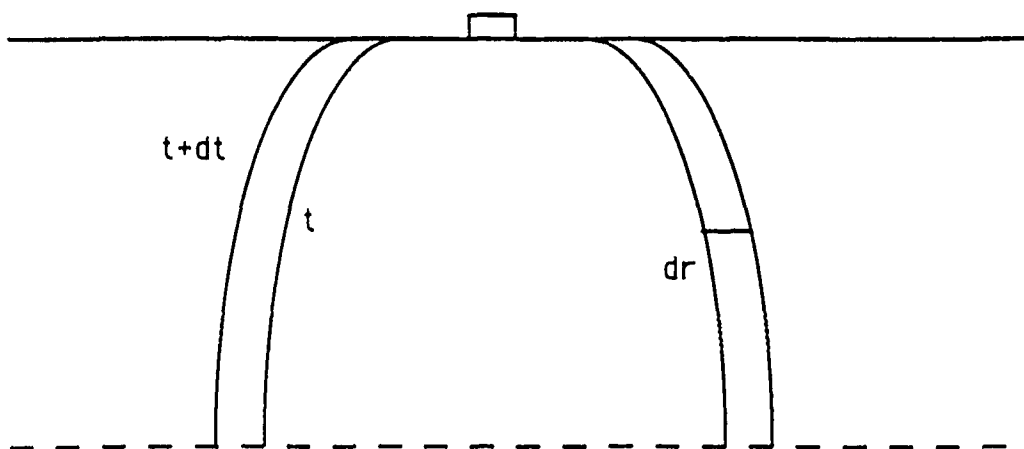


Figure A-1b. Integration geometry, single scattering.
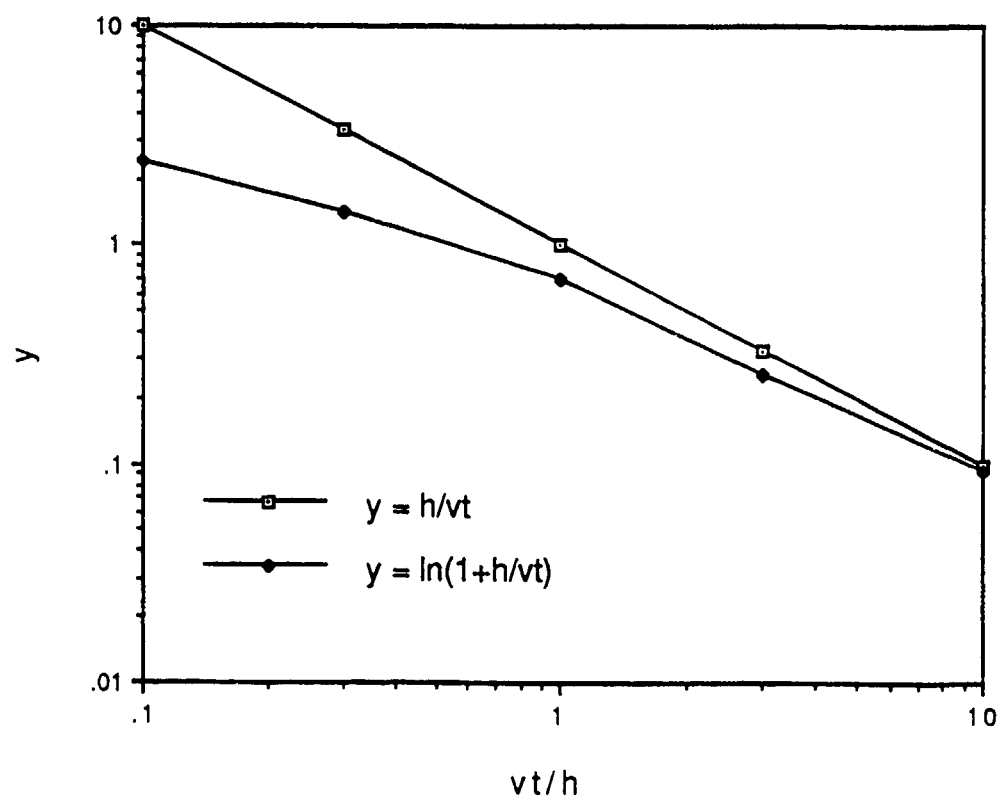
Figure A-1c. Comparison of h/vt with ln(1+h/vt).

for body wave scattering and

$$s_1 = \frac{S_o2 \, dV \, T}{4 \, \pi \, h \, r_1} \qquad (2)$$

for surface wave scattering (i.e., dispersion is ignored, as appears reasonable for Lg; Herrmann and Kijko, 1983). The factor of 1/h corrects for the spreading of the energy over the thickness of the layer.

2. The total scattered amplitude $S_1$ between lag times t and t+dt after first arrival time is given by

$$S_1{}^2 = \int s_1{}^2 \, dV \qquad (3)$$

$$= P(f,t) \, dt \qquad (4)$$

where the volume of integration is taken between the surfaces of constant lag time t and t+dt and it is assumed that the relative phase between scattered arrivals is random, thus the squared amplitudes are summed (integrated). The relation (4) between amplitude and coda power $P(f,t)$ is taken from Aki and Chouet (1985).

3. The effect of attenuation after the first arrival is given by $\exp(-2\pi ft/Q)$.

4. The acoustic problem with a mean velocity v is solved.

5. The incident wave is assumed to be vertically incident.

## SINGLE SCATTERING

BODY WAVE SCATTERING

Refer to Figure A-1a for the geometry and the definition of cylindrical polar coordinated $r,z,\phi$, where $\phi$ is the azimuth angle. The lag time t for a wave scattered at r,z is

$$t = \frac{(h - z)}{v} + \frac{r_1}{v} - \frac{h}{v} = (r_1 - z) / v \qquad (5)$$

Using

$$r_1^2 = r^2 + z^2,$$

we obtain for the surface of constant scattering lag time

$$\frac{r^2}{v^2} - \frac{2\,t\,z}{v} = t^2,$$

which is a paraboloid of revolution truncated at $z = 0$ and $z = h$. The volume of integration is sketched in Figure A-1b. The volume element: $dV = r\, d\phi\, dr\, dz$, but we may immediately integrate over $\phi$ to give

$$dV = 2\,\pi\, r\, dr\, dz.$$

The differential $dr$ may be expressed in terms of $dt$ by noting that at constant $z$, from (5) and Figure A-1a,

$$dr = \frac{dr_1}{\sin\theta} = \frac{r_1}{r}\, dr_1 = \frac{r_1}{r}\, v\, dt \qquad (6)$$

Then combining (3),(1) and (6),

$$S_1^2 = v\, dt \int_0^h \frac{S_o^2\, T}{2\, r_1}\, dz = v\, dt \int_0^h \frac{S_o^2\, T}{2(vt+z)}\, dz,$$

using (5). Integrating, using (4) and adding attenuation,

$$P_1(f,t) = -\frac{1}{2} S_o^2\, T(f)\, v\, \ln\left( 1 + \frac{h}{vt} \right) \exp\left( \frac{-2\,\pi\, f\, t}{Q} \right) \qquad (7)$$

There are two extreme cases. For $h > vt$, the constant 1 in the logarithm may be neglected ("thick layer"). More interesting is the case $h < vt$ ("thin layer"). Then the logarithm in (7) may be expanded to give

$$P_1(f,t) = S_o^2\, T\, h\, \frac{1}{2\, t}\, \exp\left( \frac{-2\,\pi\, f\, t}{Q} \right) \qquad (8)$$

which is identical with Equation (10) of Dainty (1985)

allowing for a difference in the definition of turbidity. In fact, this formula may be derived directly by means of the approximations $r_1=r$, $vt=r$ and $dV=hdA=2\pi hrdr=2\pi hrvdt$ used in (1) and (3). Physically, this is equivalent to saying that the depth of the scatterer may be neglected and the scattering volume approximated by the volume between two cylinders of depth h; dA is the area on the surface between the two cylinders. This will be referred to as the "thin layer approximation". Figure A-1c compares h/vt with $\ln(1+h/vt)$; we see that for $vt/h \geq 1$, the thin layer approximation is quite accurate.

SURFACE WAVE SCATTERING

First, we note for Lg scattering the thin layer approximation must hold because the scatterer must be sufficiently far away to allow the phase to develop. Since Lg is a collection of higher modes that may be viewed as post-critical crustal S bounces, this implies distances of at least two crustal thicknesses, i.e., 2h. For the fundamental mode (Rg) there is no such limitation on distance, but this mode is confined to the upper 5 km for frequencies greater than 0.5 Hz and only scatterers in this depth range are important. Subsequent discussion shall refer to Lg.

Under the thin layer approximation, we substitute $r_1 = r$ and $dV = 2\pi hrdr = 2\pi hrvdt$ in (2) and (3) and using (4) obtain:

$$P_1(f,t) = \frac{1}{2} S_0^2 T v \exp\left( \frac{-2\pi f t}{Q} \right) \qquad (9)$$

This is identical to Equation (8) of Dainty (1985) after

correcting for a factor of $1/h$ as discussed in (2).

## DOUBLE SCATTERING

### BODY WAVE SCATTERING, THIN LAYER APPROXIMATION

The geometry is shown in Figure A-2a in map view;

$$r_2 + r_3 = v\,t = 2\,a$$

where $a$ is the semimajor axis of the ellipse, and $r_1 = 2c$, where $c$ is half the distance between foci of the ellipse; the receiver is one focus and the first scattering volume at $dA_1$ is the other. Then the scattered amplitude at $dA_2$ from $dA_1$ is

$$s_1{}^2 = \frac{S_o{}^2\; T\; h\; d\; A_1}{4\;\pi\; r_2{}^2},$$

and the scattered amplitude at the receiver from double scattering is

$$s_2{}^2 = \frac{s_1{}^2\; T\; h\; d\; A_2}{4\;\pi\; r_3{}^2} = \frac{S_o{}^2\; T^2\; h^2\; dA_1\; dA_2}{16\;\pi^2\; r_2{}^2\; r_3{}^2}$$

from (1) and the thin layer approximation. Thus

$$S_2 = S_o{}^2\; T^2\; h^2 \int \frac{dA_1\; dA_2}{16\;\pi^2\; r_2{}^2\; r_3{}^2}, \tag{10}$$

The differential $dA_1 = 2\pi r_1 dr_1$. Following Gao et al. (1983), the following relations may be use:

$$dA_2 = r_3\; dr_3\; d\theta$$

$$r_2 = vt - r_3 = \frac{a^2 + c^2 - 2\,a\,c\,\cos\theta}{a - c\,\cos\theta}, \quad r_3 = \frac{a^2 - c^2}{a - c\,\cos\theta}$$

$$dr_3 = \frac{a^2 + c^2 - 2ac\,\cos\theta}{(a - c\,\cos\theta)^2}\; da = \frac{a^2 + c^2 - 2ac\,\cos\theta}{(a - c\,\cos\theta)^2}\; \frac{v\,dt}{2}$$

Using these relations and (4),

$$P_2(f,t) = \frac{1}{8\,\pi}\; S_o{}^2\; T^2\; h^2\; K_2 \exp\left(\frac{-2\,\pi\,f\,t}{Q}\right),$$
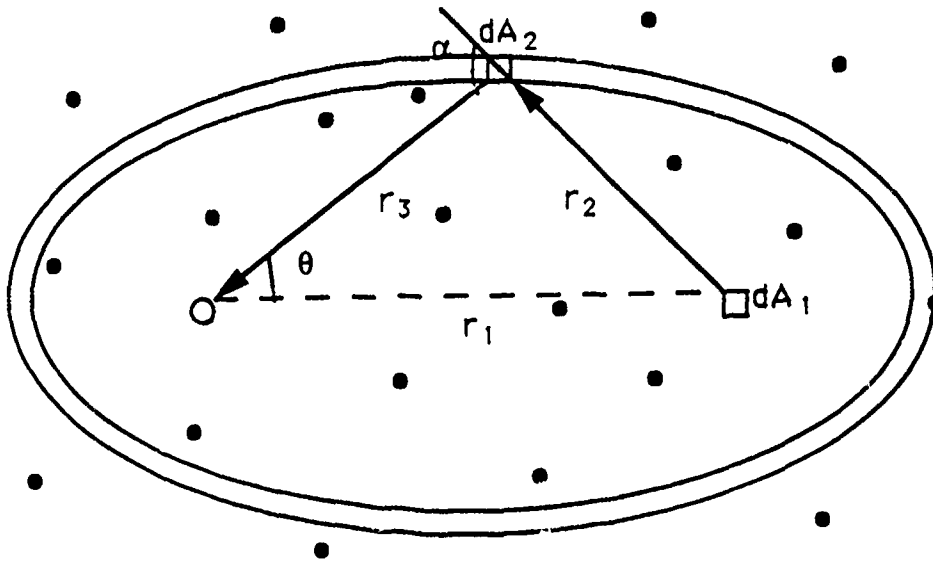
209

**Figure A-2a.** Integration geometry, double scattering, thin layer.
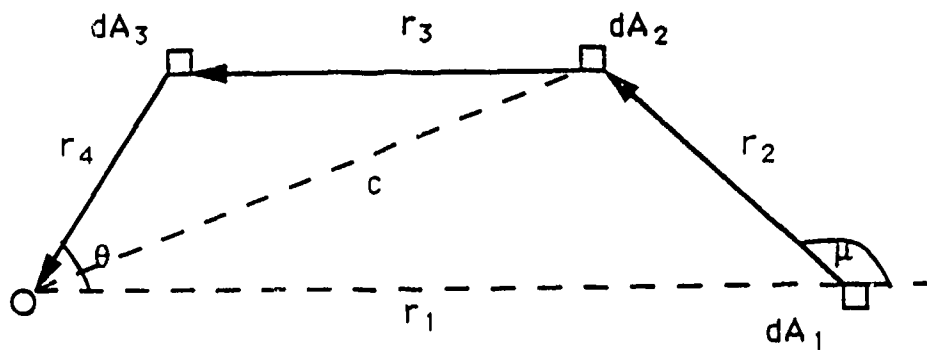


**Figure A-2b.** Integration geometry, triple scattering, thin layer.

where

$$K_2 = v \int_0^{r_m} \frac{r_1 \, dr_1}{a^2 - c^2} \int_0^{\pi} \frac{a - c \cos\theta}{a^2 + c^2 - 2ac \cos\theta} \, d\theta$$

Substituting $r_1 = uvt$, $a = vt/2$, $c = uvt/2$,

$$K_2 = \frac{8}{t} \int_0^{u_m} \frac{u \, du}{1 - u^2} \int_0^{\pi} \frac{1 - u \cos\theta}{1 + u^2 - 2 ac \cos\theta} \, d\theta$$

$$= \frac{8\pi}{t} \int_0^{u_m} \frac{u \, du}{1 - u^2} = \frac{4\pi}{t} [ -\ln( 1 - u_m^2 ) ]$$

We must now consider the question of the proper value of $u_m$. At first sight it is $u_m = 1$, corresponding to $r_1 = vt$. This however leads to a logarithmic singularity in $K_2$. This problem occurs because the limit $r_1 = vt$ is the case where the scattering angle $\alpha$ (Figure A-2a) is 0, the ellipse degenerates to a line, and there are second scatterers infinitely close to the receiver, leading to a singularity of order $1/r_2^2$ in the integrand of (10). However, Sato (1982) points out that waves scattered at angles $\alpha \le 30^{\circ}$ do not form separate scattered waves in the coda but interfere with the incident wave to cause fluctuations. To exclude such waves, take $\alpha = 30^{\circ}$, and $r_2 = r_3$ to give $r_m = vt \cos 15^{\circ}$, $u_m = \cos 15^{\circ} = 0.965$, and $K_2 = 10.8\pi/t$. Then

$$P_2(f,t) = 1.35 \, S_o^2 \, T^2 \, h^2 \, \frac{1}{2\, t} \, \exp(\frac{-2\pi f t}{Q}) = 1.35 \, T \, h \, P_1$$

Dainty (1985) found (Th) to be of the order of $10^{-1}$ (correcting for the error in Equation (8)) for Semipalatinsk explosions, giving $P_2 \approx 0.1 \, P_1$.

The case of triple scattering in this approximation has also been solved, giving (refer to Figure A-2b for the

geometry)

$$P_3 = \frac{1}{32\ \pi^2}\ S_o{}^2\ T^3\ h^3\ K_3\ \exp(\frac{-2\ \pi\ f\ t}{Q}),$$

where

$$K_3 = \frac{1}{t}\int_0^{u_m} u\,du \int_0^{w_m} \frac{dw}{w} \int_0^\pi \frac{d\mu}{1-u^2-2w-2uw\ \cos\ \mu} \int_0^\pi \frac{1-w-B\ \cos\theta\ \ d\theta}{1+u2-2w(w+1)+2C\ \cos\theta}$$

with $B^2 = u^2+w^2+2uw\ \cos\ \mu$, $C = uw+(1-w)B$ and $u_m=w_m=0.965$.

SURFACE WAVE SCATTERING, THIN LAYER APPROXIMATION

Refer again to Figure A-2a for the geometry. The scattered amplitude at $dA_2$ from $dA_1$ is

$$s_1{}^2 = \frac{S_o{}^2\ T\ dA_1}{4\ \pi\ r_2}$$

and the scattered amplitude at the receiver from double scattering is

$$s_2{}^2 = \frac{s_1{}^2\ T\ dA_2}{4\ \pi\ r_3} = \frac{S_o{}^2\ T^2\ dA_1\ dA_2}{16\ \pi^2\ r_2\ r_3}$$

from (2). Thus

$$S_2 = S_o{}^2\ T^2 \int \frac{dA_1\ dA_2}{16\ \pi^2\ r_2\ r_3} \tag{11}$$

Expressing $dA_1$, $dA_2$, $r_2$ and $r_3$ in the same manner as before and using (4),

$$P_2(f,t) = \frac{1}{8\ \pi}\ S_o{}^2\ T^2\ v\ K_2\ \exp(\frac{-2\ \pi\ f\ t}{Q}),$$

where

$$K_2 = \frac{1}{2}\int_0^{r_m} r_1\ dr_1 \int_0^{2\pi} \frac{d\theta}{a-c\ \cos\theta}.$$

Writing as before $r_1 = uvt$, $a = vt/2$, $c = uvt/2$,

$$K_2 = vt \int_0^{u_m} u\ du \int_0^{2\pi} \frac{d\theta}{1 - u\ \cos\theta}.$$

212

The definite integral over $\theta$ has the value (CRC Math Tables, Integral # 645) $2\pi/\sqrt{(1-u^2)}$, leading to

$$K_2 = 2 \pi v t ( 1 - \sqrt{(1-u_m^2)} ).$$

We see that in this case we may take $r_m = vt$, $u_m = 1$; this is because the singularity in (11) is only of the order of $1/r_2$. Then $K_2 = 2 \pi v t$ and

$$P_2(f,t) = \frac{1}{4} S_o^2 T^2 v^2 t \exp(\frac{-2 \pi f t}{Q}) = \frac{1}{2} T v t P_1$$

BODY WAVE SCATTERING, THICK LAYER APPROXIMATION

Refer to Figure A-3 for the geometry.

$$P_2(f,t) = \frac{1}{8 \pi} S_o^2 T^2 v K_2 \exp(\frac{-2 \pi f t}{Q})$$

where

$$K_2 = 2\pi vt \int_0^{u_m} u\,du \int_0^{\pi/2} \frac{\sin \psi \, d\psi}{1+u \cos \psi} \ln[ \frac{(1+u \cos\psi)^2+u^2 \sin\psi}{(1+u \cos\psi)^2-u^2 \sin\psi} ].$$

REMARKS

It will be seen that in the thin layer approximation, for body wave scattering

$$P_b(f,t) = \frac{A}{t} \exp(\frac{-2 \pi f t}{Q})$$

for single scattering and all higher orders of scattering. For surface wave scattering,

$$P_s(f,t) = ( B + C t + \cdots ) \exp(\frac{-2 \pi f t}{Q})$$

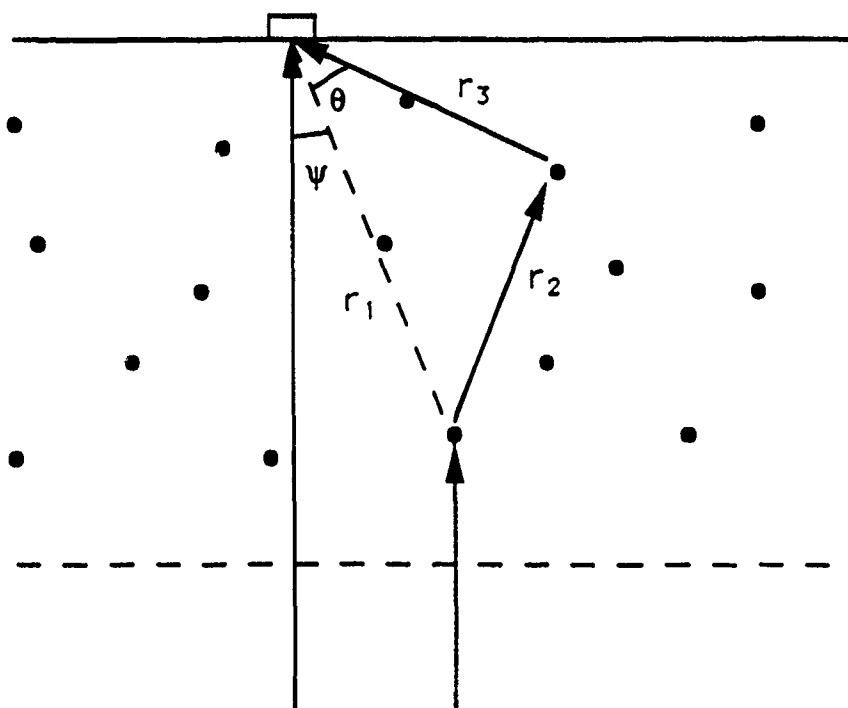where B is single scattering, C is double scattering.

Figure A-3. Scattering geometry, double scattering, thick layer.

# REFERENCES

## PAPER I

Aki, K. (1969), Analysis of the seismic coda of local earthquakes as scattered waves. J. Geophys. Res. 74, 615-631.

Aki, K. (1973), Scattering of P waves under the Montana LASA. J Geophys. Res. 78, 1334-1346.

Aki, K. (1980a), Attenuation of shear-waves in the lithosphere for frequencies from 0.05 to 25 Hz. Phys. Earth Planet. Interiors 21, 50-60.

Aki, K. (1980b), Scattering and attenuation of shear waves in the lithosphere. J. Geophys. Res. 85, 6496-6504.

Aki, K. (1982), Scattering and attenuation. Bull. Seism. Soc. Am. 72, 319-330.

Aki, K. and B. Chouet (1975), Origin of coda waves: source, attenuation and scattering effects. J. Geophys. Res. 80, 3322-3342.

Aki, K. and P. Richards (1980), Quantitative Seismology, I and II (W. H. Freeman and Co., San Francisco).

Breding, D. R. (1983), Data user's guide for the Regional Test Network (RSTN), Rep SAND82-2935, Sandia Lib., Albuquerque, N.M.

Chouet, B., K. Aki, and M. Tsujiura (1978), Regional variations of the scaling law of earthquake source spectra. Bull. Seism. Soc. Am. 68, 49-79.

Dainty, A. M. (1985), Coda observed at NORSAR and NORESS. Air Force Geophysics Laboratory. report no. AFGL-TR-85-0199. ADA164424

Dainty, A. M., R. M. Duckworth and A. Tie (1987), Attenuation and Backscattering from local Coda. Bull Seism. Soc Am. 77, 1728-1747.

Frankel, A. and L. Wennerberg (1987), Energy-Flux model of Seismic Coda: Separation of Scattering and Intrinsic Attenuation. Bull. Seism. Soc. Am. 77, 1223-1251.

Frankel, A. and R. W. Clayton (1984), A finite difference

simulation of wave propagation in two-dimensional random media. Bull Seis. Soc. Am. 74, 2167-2186.

Gao, L. S., N. N. Biswas, L. C. Lee and K. Aki (1983a), Comparison of the effects between single and multiple scattering on coda waves for local earthquakes. Bull. Seism. Soc. Am. 73, 377-389.

Gao, L. S., N. N. Biswas, L. C. Lee and K. Aki (1983b), Effects of multiple scattering on coda waves in three-dimensional medium. Pure Appl. Geophys. 121, 3-15.

Herraiz, M. and A. F. Espinosa (1987), Coda waves: A review. PAGEOPH. Vol 125, No 4.

Jin, A., T. Cao and K. Aki (1985), Regional change of coda Q in the oceanic lithosphere. J. Geophys. Res. 90, 8651-8659.

Langston, C. A. (1989), Scattering of teleseismic body waves under Pasadena, California. J. Geophys. Res. 94, 1935-1951.

Menke, W. (1984), Geophysical data analysis: Discrete inverse theory. (Academic Press Inc., Orlando, Florida.)

Menke, W. and R. L. Chen (1984), Numerical studies of the coda fall-off rate of multiply scattered waves in randomly layered media. Bull. Seism. Soc. Am. 74, 1605-1614.

Pizarenko V. F. (1970), Statistical Estimates of Amplitude and Phase Corrections. Geophys. J. R. astr. Soc. 20, 89-98.

Rautian, T. G. and V. I. Khalturin (1978), The use of the coda for determination of the earthquake source spectrum. Bull. Seism. Soc. Am. 68, 923-943.

Richards, P. and W. Menke (1983), The apparent attenuation of a scattering medium. Bull. Seism. Soc. Am. 73, 1005-1022.

Rovelli, A. (1982), On the frequency dependence of Q in Friuli from short-period digital records. Bull. Seism. Soc. Am. 72, 2369-2372.

Sato, H. (1978), Mean free path of Ss-waves under the Kanto District of Japan. J. Phys. Earth 26, 185-198.

Singh, S. and R. B. Herrmann (1983), Regionalization of crustal coda Q in the continental United States. J. Geophys. Res. 88, 527-538.

Soroka, W. L., B. W. Stump and P. W. Golden (1985), Temporal and spectral characterization of high frequency teleseismic body waves. EOS Vol. 66, No. 46.

Soroka, W. L., Paper 2, A study on the applicability of two-term models to characterize multiple scattered energy in coda.

Soroka, W. L., B. W. Stump and A. M. Dainty, Paper 3, Source spectral estimation and earth turbidity estimation in coda analysis.

Tsujiura, M. (1978), Spectral analysis of the coda waves from local earthquakes. Bull. Earthquake Res. Inst., Tokyo Univ. 53, 1-48.


PAPER II

Aki, K. (1969), Analysis of the seismic coda of local earthquakes as scattered waves. J. Geophys. Res. 74, 615-631.

Aki, K. and B. Chouet (1975), Origin of coda waves: source, attenuation and scattering effects. J. Geophys. Res. 80, 3322-3342.

Dainty, A. M. (1981), A scattering model to explain seismic Q observations in the lithosphere between 1 and 30 Hz. Geophys. Res. Lett. 8, 1126-1128.

Frankel, A. and L. Wennerberg (1987), Energy-Flux model of seismic coda: separation of scattering and intrinsic attenuation. Bull. Seism. Soc. Am. 77, 1223-1251.

Gao, L. S., N. N. Biswas, L. C. Lee and K. Aki (1983a), Comparison of the effects between single and multiple scattering on coda waves for local earthquakes. Bull. Seism. Soc. Am. 73, 377-389.

Gao, L. S., N. N. Biswas, L. C. Lee and K. Aki (1983b), Effects of multiple scattering on coda waves in three-dimensional medium. Pure Appl. Geophys. 121, 3-15.

Herraiz, M. and A. F. Espinosa (1987), Coda waves: A review. PAGEOPH. Vol 125, No 4.

Langston, C. A. (1989), Scattering of teleseismic body waves under Pasadena, California. J. Geophys. Res. 94, 1935-1951.

Rautian, T. G. and I. V. Khalturin (1978), The use of the coda for determination of the earthquake source spectrum. Bull. Seism. Soc. Am. 68, 923-943.

Soroka, W. L. and B. W. Stump Paper 1: Teleseismic coda analysis with simultaneous modeling of single and multiple scattering.

Soroka, W. L., B. W. Stump and A. M. Dainty Paper 3: Source

spectrum and earth turbidity estimates in coda
analysis.

## PAPER III

Aki, K. (1982), Scattering and attenuation, Bull. Seism.
    Soc. Am. 72, 319-330.

Aki, K. and B. Chouet (1975), Origin of coda waves: source,
    attenuation and scattering effects, J. Geophys. Res.
    80, 3322-3342.

Aki, K. and P. Richards, (1980), Quantative Seismology, II
    (W. H. Freeman and Co., San Francisco).

Dainty, A. M. (1985), Coda observed at NORAS and NORESS.
    Report AFGL-TR-85-0199, Air Force Geophysics
    Laboratory, Hanscom AFB MA. ADA164424

Dainty, A. M., R. W. Duckworth and A. Tie (1987),
    Attenuation and backscattering from local coda, Bull.
    Seism. Soc. Am. 77, 1728-1747.

Dainty, A. M. and M. N. Toksoz (1981), Seismic codas on the
    earth and moon: A comparison, Phys. Earth Planet. Int.
    26, 250-260.

Dainty, A. M. and M. N. Toksoz (1990), Array analysis of
    seismic scattering. Bull. Seis. Soc. Am. 80,
    2242-2260.

Frankel, A. and L. Wennerberg (1987), Energy-Flux model of
    seismic coda: Separation of scattering and intrinsic
    attenuation, Bull. Seism. Soc. Am. 77, 1223-1251.

Gao, L. S., N. N. Biswas, L. C. Lee and K. Aki (1983a),
    Comparison of the effects between single and multiple
    scattering on coda waves for local earthquakes, Bull.
    Seism. Soc. Am. 73, 377-389.

Gao, L. S., N. N. Biswas, L. C. Lee and K. Aki (1983b),
    Effects of multiple scattering on coda waves in
    three-dimensional medium, Pure Appl. Geophys. 121,
    3-15.

Herrmann, R. B. (1980), Q estimates using the coda of local
    earthquakes. Bull. Seis. Soc. Am. 70, 447-468.

Herrmann, R. B. and A. Kijko (1983), Modeling some
    empirical vertical component Lg relations. Bull. Seis.
    Soc. Am. 73, 157-171.

Herraiz, M. and A. F. Espinosa (1987), Coda waves: A
    review, Pageoph. Vol 125, No 4.

Langston, C. A. (1989), Scattering of teleseismic body

waves under Pasadena, California, J. Geophys. Res. 94, 1935-1951.

Murphy, J. R. and J. J. Bennett (1982), A discrimination analysis of short-period regional seismic data recorded at Tonto Forest Observatory, Bull. Seism. Soc. Am. 72, 1351-1366.

Novelo-Casanova, D. A. and R. Butler (1986), High-frequency seismic coda and scattering in the Northwest Pacific, Bull. Seism. Soc. Am. 76, 617-629.

Rautian, T. G. and I. V. Khalturin (1978), The use of the coda for determination of the earthquake source spectrum, Bull. Seism. Soc. Am. 68, 923-943.

Sato, H. (1977), Energy propagation including scattering effect: single isotropic scattering approximation. J. Phys. Earth 25, 27-41.

Sato, H. (1982), Amplitude attenuation of impulsive waves in random media based on travel time corrected mean wave formalism. J. Acous. Soc. Am., 71, 559-564.

Sharpe, J. A. (1942), The production of elastic waves by explosion pressures. Part 1. Theory and empirical field observations. Geophysics 7, 144-154.

Soroka, W. L. and B. W. Stump, paper 1, Teleseismic coda analysis with simultaneous modeling of single and multiple scattering.

Soroka, W. L., paper 2, A study on the applicability of two-term models to characterize multiple scattered energy in coda.

Taylor, S. R., N. W. Sherman and M. D. Denny (1988), Spectral discrimination between NTS explosions and western united states earthquakes at regional distances. Bull. Seism. Soc. Am. 78, 1563-1579.

Zeng, Y., F. Su and K. Aki (1991), Scattering wave energy propagation in a random isotropic medium 1. Theory. J. Geophys. Res. 96, 607-619.

Prof. Thomas Ahrens
Seismological Lab, 252-21
Division of Geological & Planetary Sciences
California Institute of Technology
Pasadena, CA 91125

Prof. Charles B. Archambeau
CIRES
University of Colorado
Boulder, CO 80309

Dr. Thomas C. Bache, Jr.
Science Applications Int'l Corp.
10260 Campus Point Drive
San Diego, CA 92121    (2 copies)

Prof. Muawia Barazangi
Institute for the Study of the Continent
Cornell University
Ithaca, NY 14853

Dr. Jeff Barker
Department of Geological Sciences
State University of New York
  at Binghamton
Vestal, NY 13901

Dr. Douglas R. Baumgardt
ENSCO, Inc
5400 Port Royal Road
Springfield, VA 22151-2388

Prof. Jonathan Berger
IGPP, A-025
Scripps Institution of Oceanography
University of California, San Diego
La Jolla, CA 92093

Dr. Gilbert A. Bollinger
Department of Geological Sciences
Virginia Polytechnical Institute
21044 Derring Hall
Blacksburg, VA 24061

Dr. Lawrence J. Burdick
Woodward-Clyde Consultants
566 El Dorado Street
Pasadena, CA 91109-3245

Dr. Jerry Carter
Center for Seismic Studies
1300 North 17th St., Suite 1450
Arlington, VA 22209-2308

Prof. Vernon F. Cormier
Department of Geology & Geophysics
U-45, Room 207
The University of Connecticut
Storrs, CT 06268

Professor Anton W. Dainty
Earth Resources Laboratory
Massachusetts Institute of Technology
42 Carleton Street
Cambridge, MA 02142

Prof. Steven Day
Department of Geological Sciences
San Diego State University
San Diego, CA 92182

Dr. Zoltan A. Der
ENSCO, Inc.
5400 Port Royal Road
Springfield, VA 22151-2388

Prof. Lewis M. Duncan
Dept. of Physics & Astronautics
Clemson University
Clemson, SC 29634-1901

Prof. John Ferguson
Center for Lithospheric Studies
The University of Texas at Dallas
P.O. Box 830688
Richardson, TX 75083-0688

Dr. Mark D. Fisk
Mission Research Corporation
735 State Street
P. O. Drawer 719
Santa Barbara, CA 93102

Prof. Stanley Flatte
Applied Sciences Building
University of California
Santa Cruz, CA 95064

Dr. Alexander Florence
SRI International
333 Ravenswood Avenue
Menlo Park, CA 94025-3493

Dr. Clifford Frohlich
Institute of Geophysics
8701 North Mopac
Austin, TX 78759

Dr. Holy K. Given
IGPP, A-025
Scripps Institute of Oceanography
University of California, San Diego
La Jolla, CA 92093

Prof. Henry L. Gray
Vice Provost and Dean
Department of Statistical Sciences
Southern Methodist University
Dallas, TX 75275

Dr. Indra Gupta
Teledyne Geotech
314 Montgomery Street
Alexandria, VA 22314

Prof. David G. Harkrider
Seismological Laboratory
Division of Geological & Planetary Sciences
California Institute of Technology
Pasadena, CA 91125

Prof. Danny Harvey
CIRES
University of Colorado
Boulder, CO 80309

Prof. Donald V. Helmberger
Seismological Laboratory
Division of Geological & Planetary Sciences
California Institute of Technology
Pasadena, CA 91125

Prof. Eugene Herrin
Institute for the Study of Earth and Man
Geophysical Laboratory
Southern Methodist University
Dallas, TX 75275

Prof. Bryan Isacks
Cornell University
Department of Geological Sciences
SNEE Hall
Ithaca, NY 14850

Dr. Rong-Song Jih
Teledyne Geotech
314 Montgomery Street
Alexandria, VA 22314

Prof. Lane R. Johnson
Seismographic Station
University of California
Berkeley, CA 94720

Dr. Richard LaCoss
MIT-Lincoln Laboratory
M-200B
P. O. Box 73
Lexington, MA 02173-0073   (3 copies)

Prof Fred K. Lamb
University of Illinois at Urbana-Champaign
Department of Physics
1110 West Green Street
Urbana, IL 61801

Prof. Charles A. Langston
Geosciences Department
403 Deike Building
The Pennsylvania State University
University Park, PA 16802

Prof. Thorne Lay
Institute of Tectonics
Earth Science Board
University of California, Santa Cruz
Santa Cruz, CA 95064

Prof. Arthur Lerner-Lam
Lamont-Doherty Geological Observatory
of Columbia University
Palisades, NY 10964

Dr. Christopher Lynnes
Teledyne Geotech
314 Montgomery Street
Alexandria, VA 22314

Prof. Peter Malin
Department of Geology
Old Chemistry Bldg.
Duke University
Durham, NC 27706

Dr. Randolph Martin, III
New England Research, Inc.
76 Olcott Drive
White River Junction, VT 05001

Prof. Thomas V. McEvilly
Seismographic Station
University of California
Berkeley, CA 94720

Dr. Keith L. McLaughlin
S-CUBED
A Division of Maxwell Laboratory
P.O. Box 1620
La Jolla, CA 92038-1620

2

Prof. William Menke
Lamont-Doherty Geological Observatory
of Columbia University
Palisades, NY 10964

Stephen Miller
SRI International
333 Ravenswood Avenue
Box AF 116
Menlo Park, CA 94025-3493

Prof. Bernard Minster
IGPP, A-025
Scripps Institute of Oceanography
University of California, San Diego
La Jolla, CA 92093

Prof. Brian J. Mitchell
Department of Earth & Atmospheric Sciences
St. Louis University
St. Louis, MO 63156

Mr. Jack Murphy
S-CUBED, A Division of Maxwell Laboratory
11800 Sunrise Valley Drive
Suite 1212
Reston, VA 22091 (2 copies)

Prof. John A. Orcutt
IGPP, A-025
Scripps Institute of Oceanography
University of California, San Diego
La Jolla, CA 92093

Prof. Keith Priestley
University of Cambridge
Bullard Labs, Dept. of Earth Sciences
Madingley Rise, Madingley Rd.
Cambridge CB3 OEZ, ENGLAND

Dr. Jay J. Pulli
Radix Systems, Inc.
2 Taft Court, Suite 203
Rockville, MD 20850

Prof. Paul G. Richards
Lamont Doherty Geological Observatory
of Columbia University
Palisades, NY 10964

Dr. Wilmer Rivers
Teledyne Geotech
314 Montgomery Street
Alexandria, VA 22314

Prof. Charles G. Sammis
Center for Earth Sciences
University of Southern California
University Park
Los Angeles, CA 90089-0741

Prof. Christopher H. Scholz
Lamont-Doherty Geological Observatory
of Columbia University
Palisades, NY 10964

Thomas J. Sereno, Jr.
Science Application Int'l Corp.
10260 Campus Point Drive
San Diego, CA 92121

Prof. David G. Simpson
Lamont-Doherty Geological Observatory
of Columbia University
Palisades, NY 10964

Dr. Jeffrey Stevens
S-CUBED
A Division of Maxwell Laboratory
P.O. Box 1620
La Jolla, CA 92038-1620

Prof. Brian Stump
Institute for the Study of Earth & Man
Geophysical Laboratory
Southern Methodist University
Dallas, TX 75275

Prof. Jeremiah Sullivan
University of Illinois at Urbana-Champaign
Department of Physics
1110 West Green Street
Urbana, IL 61801

Prof. Clifford Thurber
University of Wisconsin-Madison
Department of Geology & Geophysics
1215 West Dayton Street
Madison, WS 53706

Prof. M. Nafi Toksoz
Earth Resources Lab
Massachusetts Institute of Technology
42 Carleton Street
Cambridge, MA 02142

Prof. John E. Vidale
University of California at Santa Cruz
Seismological Laboratory
Santa Cruz, CA 95064

Prof. Terry C. Wallace
Department of Geosciences
Building #77
University of Arizona
Tucson, AZ 85721

Dr. William Wortman
Mission Research Corporation
8560 Cinderbed Rd.
Suite # 700
Newington, VA 22122

Prof. Francis T. Wu
Department of Geological Sciences
State University of New York
at Binghamton
Vestal, NY 13901

Dr. Monem Abdel-Gawad
Rockwell International Science Center
1049 Camino Dos Rios
Thousand Oaks, CA 91360

Prof. Keiiti Aki
Center for Earth Sciences
University of Southern California
University Park
Los Angeles, CA 90089-0741

Prof. Shelton S. Alexander
Geosciences Department
403 Deike Building
The Pennsylvania State University
University Park, PA 16802

Dr. Kenneth Anderson
BBNSTC
Mail Stop 14/1B
Cambridge, MA 02238

Dr. Ralph Archuleta
Department of Geological Sciences
University of California at Santa Barbara
Santa Barbara, CA 93102

Dr. Susan Beck
Department of Geosciences
Bldg. # 77
University of Arizona
Tucson, AZ 85721

Dr. T.J. Bennett
S-CUBED
A Division of Maxwell Laboratory
11800 Sunrise Valley Drive, Suite 1212
Reston, VA 22091

Mr. William J. Best
907 Westwood Drive
Vienna, VA 22180

Dr. N. Biswas
Geophysical Institute
University of Alaska
Fairbanks, AK 99701

Dr. Stephen Bratt
Center for Seismic Studies
1300 North 17th Street
Suite 1450
Arlington, VA 22209

Michael Browne
Teledyne Geotech
3401 Shiloh Road
Garland, TX 75041

Mr. Roy Burger
1221 Serry Road
Schenectady, NY 12309

Dr. Robert Burridge
Schlumberger-Doll Research Center
Old Quarry Road
Ridgefield, CT 06877

Dr. W. Winston Chan
Teledyne Geotech
314 Montgomery Street
Alexandria, VA 22314-1581

Dr. Theodore Cherry
Science Horizons, Inc.
710 Encinitas Blvd., Suite 200
Encinitas, CA 92024 (2 copies)

Prof. Jon F. Claerbout
Department of Geophysics
Stanford University
Stanford, CA 94305

Prof. Robert W. Clayton
Seismological Laboratory
Division of Geological & Planetary Sciences
California Institute of Technology
Pasadena, CA 91125

Prof. F. A. Dahlen
Geological and Geophysical Sciences
Princeton University
Princeton, NJ 08544-0636

Mr. Charles Doll
Earth Resources Laboratory
Massachusetts Institute of Technology
42 Carleton St.
Cambridge, MA 02142

Prof. Adam Dziewonski
Hoffman Laboratory, Harvard Univ.
Dept. of Earth Atmos. & Planetary Sciences
20 Oxford St
Cambridge, MA 02138

Prof. John Ebel
Department of Geology & Geophysics
Boston College
Chestnut Hill, MA 02167

Eric Fielding
SNEE Hall
INSTOC
Cornell University
Ithaca, NY 14853

Dr. John Foley
Phillips Laboratory/LWH
Hanscom AFB, MA 01731-5000

Prof. Donald Forsyth
Department of Geological Sciences
Brown University
Providence, RI 02912

Dr. Anthony Gangi
Texas A&M University
Department of Geophysics
College Station, TX 77843

Dr. Freeman Gilbert
IGPP, A-025
Scripps Institute of Oceanography
University of California
La Jolla, CA 92093

Mr. Edward Giller
Pacific Sierra Research Corp.
1401 Wilson Boulevard
Arlington, VA 22209

Dr. Jeffrey W. Given
SAIC
10260 Campus Point Drive
San Diego, CA 92121

Prof. Stephen Grand
University of Texas at Austin
Department of Geological Sciences
Austin, TX 78713-7909

Prof. Roy Greenfield
Geosciences Department
403 Deike Building
The Pennsylvania State University
University Park, PA 16802

Dan N. Hagedorn
Battelle
Pacific Northwest Laboratories
Battelle Boulevard
Richland, WA 99352

Dr. James Hannon
Lawrence Livermore National Laboratory
P. O. Box 808
Livermore, CA 94550

Prof. Robert B. Herrmann
Dept. of Earth & Atmospheric Sciences
St. Louis University
St. Louis, MO 63156

Ms. Heidi Houston
Seismological Laboratory
University of California
Santa Cruz, CA 95064

Kevin Hutchenson
Department of Earth Sciences
St. Louis University
3507 Laclede
St. Louis, MO 63103

Dr. Hans Israelsson
Center for Seismic Studies
1300 N. 17th Street, Suite 1450
Arlington, VA 22209-2308

Prof. Thomas H. Jordan
Department of Earth, Atmospheric
  and Planetary Sciences
Massachusetts Institute of Technology
Cambridge, MA 02139

Prof. Alan Kafka
Department of Geology & Geophysics
Boston College
Chestnut Hill, MA 02167

Robert C. Kemerait
ENSCO, Inc.
445 Pineda Court
Melbourne, FL 32940

William Kikendall
Teledyne Geotech
3401 Shiloh Road
Garland, TX 75041

Prof. Leon Knopoff
University of California
Institute of Geophysics & Planetary Physics
Los Angeles, CA 90024

Prof. Jack Oliver
Department of Geology
Cornell University
Ithaca, NY 14850

Prof. John Kuo
Aldridge Laboratory of Applied Geophysics
Columbia University
842 Mudd Bldg.
New York, NY 10027

Dr. Kenneth Olsen
P. O. Box 1273
Linwood, WA 98046-1273

Prof. L. Timothy Long
School of Geophysical Sciences
Georgia Institute of Technology
Atlanta, CA 30332

Prof. Jeffrey Park
Department of Geology and Geophysics
Kline Geology Laboratory
P. O. Box 6666
New Haven, CT 06511-8130

Dr. Gary McCartor
Department of Physics
Southern Methodist University
Dallas, TX 75275

Howard J. Patton
Lawrence Livermore National Laboratory
L-205
P. O. Box 808
Livermore, CA 94550

Prof. Art McGarr
Mail Stop 977
Geological Survey
345 Middlefield Rd.
Menlo Park, CA 94025

Prof. Robert Phinney
Geological & Geophysical Sciences
Princeton University
Princeton, NJ 08544-0636

Dr. George Mellman
Sierra Geophysics
11255 Kirkland Way
Kirkland, WA 98033

Dr. Paul Pomeroy
Rondout Associates
P.O. Box 224
Stone Ridge, NY 12484

Prof. John Nabelek
College of Oceanography
Oregon State University
Corvallis, OR 97331

Dr. Norton Rimer
S-CUBED
A Division of Maxwell Laboratory
P.O. Box 1620
La Jolla, CA 92038-1620

Prof. Geza Nagy
University of California, San Diego
Department of Ames, M.S. B-010
La Jolla, CA 92093

Prof. Larry J. Ruff
Department of Geological Sciences
1006 C.C. Little Building
University of Michigan
Ann Arbor, MI 48109-1063

Dr. Keith K. Nakanishi
Lawrence Livermore National Laboratory
L-205
P. O. Box 808
Livermore, CA 94550

Dr. Richard Sailor
TASC Inc.
55 Walkers Brook Drive
Reading, MA 01867

Prof. Amos Nur
Department of Geophysics
Stanford University
Stanford, CA 94305

Dr. Susan Schwartz
Institute of Tectonics
1156 High St.
Santa Cruz, CA 95064

John Sherwin
Teledyne Geotech
3401 Shiloh Road
Garland, TX 75041

Dr. Matthew Sibol
Virginia Tech
Seismological Observatory
4044 Derring Hall
Blacksburg, VA 24061-0420

Dr. Albert Smith
Lawrence Livermore National Laboratory
L-205
P. O. Box 808
Livermore, CA 94550

Prof. Robert Smith
Department of Geophysics
University of Utah
1400 East 2nd South
Salt Lake City, UT 84112

Dr. Stewart W. Smith
Geophysics AK-50
University of Washington
Seattle, WA 98195

Donald L. Springer
Lawrence Livermore National Laboratory
L-205
P. O. Box 808
Livermore, CA 94550

Dr. George Sutton
Rondout Associates
P.O. Box 224
Stone Ridge, NY 12484

Prof. L. Sykes
Lamont-Doherty Geological Observatory
of Columbia University
Palisades, NY 10964

Prof. Pradeep Talwani
Department of Geological Sciences
University of South Carolina
Columbia, SC 29208

Dr. David Taylor
ENSCO, Inc.
445 Pineda Court
Melbourne, FL 32940

Dr. Steven R. Taylor
Lawrence Livermore National Laboratory
L-205
P. O. Box 808
Livermore, CA 94550

Professor Ta-Liang Teng
Center for Earth Sciences
University of Southern California
University Park
Los Angeles, CA 90089-0741

Dr. Gregory van der Vink
IRIS, Inc.
1616 North Fort Myer Drive
Suite 1440
Arlington, VA 22209

Professor Daniel Walker
University of Hawaii
Institute of Geophysics
Honolulu, HI 96822

William R. Walter
Seismological Laboratory
University of Nevada
Reno, NV 89557

Dr. Raymond Willeman
Phillips Laboratory/LWH
Hanscom AFB, MA 01731-5000

Dr. Gregory Wojcik
Weidlinger Associates
4410 El Camino Real
Suite 110
Los Altos, CA 94022

Dr. Lorraine Wolf
Phillips Laboratory/LWH
Hanscom AFB, MA 01731-5000

Dr. Gregory B. Young
ENSCO, Inc.
5400 Port Royal Road
Springfield, VA 22151-2388

Dr. Eileen Vergino
Lawrence Livermore National Laboratory
L-205
P. O. Box 808
Livermore, CA 94550

J. J. Zucca
Lawrence Livermore National Laboratory
P. O. Box 808
Livermore, CA  94550

Dr. Ralph Alewine III
DARPA/NMRO
1400 Wilson Boulevard
Arlington, VA 22209-2308

Mr. James C. Battis
Phillips Laboratory/LWH
Hanscom AFB, MA 01731-5000

Harley Benz
U.S. Geological Survey, MS-977
345 Middlefield Rd.
Menlo Park, CA 94025

Dr. Robert Blandford
AFTAC/TT
Center for Seismic Studies
1300 North 17th St. Suite 1450
Arlington, VA 22209-2308

Eric Chael
Division 9241
Sandia Laboratory
Albuquerque, NM 87185

Dr. John J. Cipar
Phillips Laboratory/LWH
Hanscom AFB, MA 01731-5000

Cecil Davis
Group P-15, Mail Stop D406
P.O. Box 1663
Los Alamos National Laboratory
Los Alamos, NM 87544

Mr. Jeff Duncan
Office of Congressman Markey
2133 Rayburn House Bldg.
Washington, DC 20515

Dr. Jack Evernden
USGS - Earthquake Studies
345 Middlefield Road
Menlo Park, CA 94025

Art Frankel
USGS
922 National Center
Reston, VA 22092

Dr. Dale Glover
DIA/DT-1B
Washington, DC 20301


Dr. T. Hanks
USGS
Nat'l Earthquake Research Center
345 Middlefield Road
Menlo Park, CA 94025

Dr. Roger Hansen
AFTAC/TT
Patrick AFB, FL 32925


Paul Johnson
ESS-4, Mail Stop J979
Los Alamos National Laboratory
Los Alamos, NM 87545


Janet Johnston
Phillips Laboratory/LWH
Hanscom AFB, MA 01731-5000


Dr. Katharine Kadinsky-Cade
Phillips Laboratory/LWH
Hanscom AFB, MA 01731-5000


Ms. Ann Kerr
IGPP, A-025
Scripps Institute of Oceanography
University of California, San Diego
La Jolla, CA 92093

Dr. Max Koontz
US Dept of Energy/DP 5
Forrestal Building
1000 Independence Avenue
Washington, DC 20585

Dr. W.H.K. Lee
Office of Earthquakes, Volcanoes,
& Engineering
345 Middlefield Road
Menlo Park, CA 94025

Dr. William Leith
U.S. Geological Survey
Mail Stop 928
Reston, VA 22092

Dr. Richard Lewis
Director, Earthquake Engineering & Geophysics
U.S. Army Corps of Engineers
Box 631
Vicksburg, MS 39180

James F. Lewkowicz
Phillips Laboratory/LWH
Hanscom AFB, MA 01731-5000

Mr. Alfred Lieberman
ACDA/VI-OA'State Department Bldg
Room 5726
320 - 21st Street, NW
Washington, DC 20451

Stephen Mangino
Phillips Laboratory/LWH
Hanscom AFB, MA 01731-5000

Dr. Robert Masse
Box 25046, Mail Stop 967
Denver Federal Center
Denver, CO 80225

Art McGarr
U.S. Geological Survey, MS-977
345 Middlefield Road
Menlo Park, CA 94025

Richard Morrow
ACDA/VI, Room 5741
320 21st Street N.W
Washington, DC 20451

Dr. Carl Newton
Los Alamos National Laboratory
P.O. Box 1663
Mail Stop C335, Group ESS-3
Los Alamos, NM 87545

Dr. Bao Nguyen
AFTAC/TTR
Patrick AFB, FL 32925

Dr. Kenneth H. Olsen
Los Alamos Scientific Laboratory
P. O. Box 1663
Mail Stop D-406
Los Alamos, NM 87545

Mr. Chris Paine
Office of Senator Kennedy
SR 315
United States Senate
Washington, DC 20510

Colonel Jerry J. Perrizo
AFOSR/NP, Building 410
Bolling AFB
Washington, DC 20332-6448

Dr. Frank F. Pilotte
HQ AFTAC/TT
Patrick AFB, FL 32925-6001

Katie Poley
CIA-ACIS/TMC
Room 4X16NHB
Washington, DC 20505

Mr. Jack Rachlin
U.S. Geological Survey
Geology, Rm 3 C136
Mail Stop 928 National Center
Reston, VA 22092

Dr. Robert Reinke
WL/NTESG
Kirtland AFB, NM 87117-6008

Dr. Byron Ristvet
HQ DNA, Nevada Operations Office
Attn: NVCG
P.O. Box 98539
Las Vegas, NV 89193

Dr. George Rothe
HQ AFTAC/TTR
Patrick AFB, FL 32925-6001

Dr. Alan S. Ryall, Jr.
DARPA/NMRO
1400 Wilson Boulevard
Arlington, VA 22209-2308

Dr. Michael Shore
Defense Nuclear Agency/SPSS
6801 Telegraph Road
Alexandria, VA 22310

12

Mr. Charles L. Taylor
Phillips Laboratory/LWH
Hanscom AFB, MA 01731-5000

Phillips Laboratory
Attn: XO
Hanscom AFB, MA 01731-5000

Dr. Larry Turnbull
CIA-OSWR/NED
Washington, DC 20505

Phillips Laboratory
Attn: LW
Hanscom AFB, MA 01731-5000

Dr. Thomas Weaver
Los Alamos National Laboratory
P.O. Box 1663, Mail Stop C335
Los Alamos, NM 87545

DARPA/PM
1400 Wilson Boulevard
Arlington, VA 22209

Phillips Laboratory
Research Library
ATTN: SULL
Hanscom AFB , MA 01731-5000

Defense Technical Information Center
Cameron Station
Alexandria, VA 22314 (2 copies)

Phillips Laboratory
ATTN: SUL
Kirtland AFB, NM 87117-6008 (2 copies)

Defense Intelligence Agency
Directorate for Scientific & Technical Intelligence
Attn: DT1B
Washington, DC 20340-6158

Secretary of the Air Force
(SAFRD)
Washington, DC 20330

AFTAC/CA
(STINFO)
Patrick AFB, FL 32925-6001

Office of the Secretary Defense
DDR & E
Washington, DC 20330

TACTEC
Battelle Memorial Institute
505 King Avenue
Columbus, OH 43201 (Final Report Only)

HQ DNA
Attn: Technical Library
Washington, DC 20305

DARPA/RMO/RETRIEVAL
1400 Wilson Boulevard
Arlington, VA 22209

DARPA/RMO/Security Office
1400 Wilson Boulevard
Arlington, VA 22209

Dr. Ramon Cabre, S.J.
Observatorio San Calixto
Casilla 5939
La Paz, Bolivia


Prof. Hans-Peter Harjes
Institute for Geophysik
Ruhr University/Bochum
P.O. Box 102148
4630 Bochum 1, FRG

Prof. Eystein Husebye
NTNF/NORSAR
P.O. Box 51
N-2007 Kjeller, NORWAY


Prof. Brian L.N. Kennett
Research School of Earth Sciences
Institute of Advanced Studies
G.P.O. Box 4
Canberra 2601, AUSTRALIA

Dr. Bernard Massinon
Societe Radiomana
27 rue Claude Bernard
75005 Paris, FRANCE        (2 Copies)


Dr. Pierre Mecheler
Societe Radiomana
27 rue Claude Bernard
75005 Paris, FRANCE


Dr. Svein Mykkeltveit
NTNF/NORSAR
P.O. Box 51
N-2007 Kjeller, NORWAY     (3 copies)

Dr. Peter Basham
Earth Physics Branch
Geological Survey of Canada
1 Observatory Crescent
Ottawa, Ontario, CANADA K1A 0Y3

Dr. Eduard Berg
Institute of Geophysics
University of Hawaii
Honolulu, HI 96822

Dr. Michel Bouchon
I.R.I.G.M.-B.P. 68
38402 St. Martin D'Heres
Cedex, FRANCE

Dr. Hilmar Bungum
NTNF/NORSAR
P.O. Box 51
N-2007 Kjeller, NORWAY

Dr. Michel Campillo
Observatoire de Grenoble
I.R.I.G.M.-B.P. 53
38041 Grenoble, FRANCE

Dr. Kin Yip Chun
Geophysics Division
Physics Department
University of Toronto
Ontario, CANADA M5S 1A7

Dr. Alan Douglas
Ministry of Defense
Blacknest, Brimpton
Reading RG7-4RS, UNITED KINGDOM

Dr. Manfred Henger
Federal Institute for Geosciences & Nat'l Res.
Postfach 510153
D-3000 Hanover 51, FRG

Ms. Eva Johannisson
Senior Research Officer
National Defense Research Inst.
P.O. Box 27322
S-102 54 Stockholm, SWEDEN

Dr. Fekadu Kebede
Geophysical Observatory, Science Faculty
Addis Ababa University
P. O. Box 1176
Addis Ababa, ETHIOPIA

Dr. Tormod Kvaerna
NTNF/NORSAR
P.O. Box 51
N-2007 Kjeller, NORWAY

Dr. Peter Marshall
Procurement Executive
Ministry of Defense
Blacknest, Brimpton
Reading FG7-4RS, UNITED KINGDOM

Prof. Ari Ben-Menahem
Department of Applied Mathematics
Weizman Institute of Science
Rehovot, ISRAEL 951729

Dr. Robert North
Geophysics Division
Geological Survey of Canada
1 Observatory Crescent
Ottawa, Ontario, CANADA K1A 0Y3

Dr. Frode Ringdal
NTNF/NORSAR
P.O. Box 51
N-2007 Kjeller, NORWAY

Dr. Jorg Schlittenhardt
Federal Institute for Geosciences & Nat'l Res.
Postfach 510153
D-3000 Hannover 51, FEDERAL REPUBLIC OF
GERMANY

Universita Degli Studi Di Trieste
Facolta Di Ingegneria
Istituto Di Miniere E. Geofisica Applicata, Trieste,
ITALY

Dr. John Woodhouse
Oxford University
Dept of Earth Sciences
Parks Road
Oxford OX13PR, ENGLAND

,